Universidad
de La Laguna

Escuela de Doctorado
y Estudios de Posgrado

TÍTULO DE LA TESIS DOCTORAL

Preparation and characterization of rare earth molybdates: structure-property relation

AUTOR/A

MARIA CANDELARIA	GUZMAN	AFONSO

DIRECTOR/A

VICTOR	LAVIN	DELLA VENTURA

CODIRECTOR/A

MARIA CRISTINA	GONZALEZ	SILGO

DEPARTAMENTO O INSTITUTO UNIVERSITARIO

FECHA DE LECTURA

10/04/15

VÍCTOR LAVÍN DELLA VENTURA, MANUEL EULALIO TORRES BETANCORT y MARÍA CRISTINA GONZÁLEZ SILGO, profesores titulares adscritos al departamento de Física de la Universidad de La Laguna
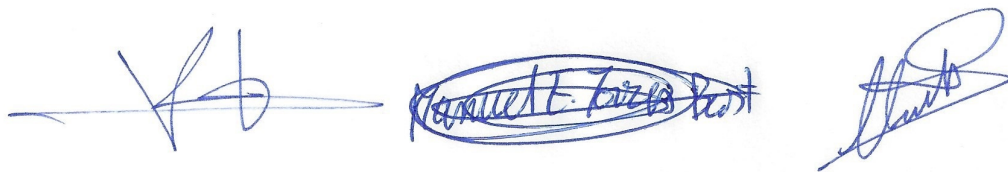
CERTIFICAN

que MARÍA CANDELARIA GUZMÁN AFONSO ha realizado bajo nuestra dirección y surpervisión los trabajos conducentes a su Tesis Doctoral titulada:

"PREPARATION AND CHARACTERIZATION OF RARE EARTH MOLYBDATES:
STRUCTURE–PROPERTY RELATION"

Examinada la presente memoria, nos declaramos conformes con su contenido y consideramos que cumple los requisitos académicos y científicos para optar al título de Doctor en Física y, por consiguiente, ser sometida al juicio del tribunal que proponga la Comisión de Doctorado de la Universidad de La Laguna.

Y para que así conste donde convenga y surta los efectos oportunos, expedimos el presente certificado en La Laguna, a 3 de febrero de 2015.

VÍCTOR LAVÍN   MANUEL E. TORRES   Mª CRISTINA GONZÁLEZ

DEPARTAMENTO DE FISICA

Universidad de La Laguna

Preparation and characterization of rare earth molybdates:

structure–property relation

Thesis submitted by

María Candelaria Guzmán Afonso

as a requirement for the degree of

Doctor of Philosophy.

ULL

**Universidad
de La Laguna**

February 3, 2015

Abstract

The work presented in this thesis focuses on the experimental study of rare earth molybdates with chemical formula $RE_2(MoO_4)_3$ (RE=La–Lu, Y). These compounds crystallize in three structural types at ambient conditions: modulated scheelite–type structure (divided in two: $La_2(MoO_4)_3$ and α–phase) and β'- and γ–phases. We have characterized these compounds under different conditions of temperature and pressure by using several experimental techniques, such as powder diffraction, impedance, optical and Raman spectroscopies, and thermal analysis. In addition, we complemented the high–pressure experiments using theoretical calculations.

For rare earth molybdates with α–phase three transport mechanisms have been found: semiconductor, polaronic and ionic; in three temperature regions. These transport mechanisms were correlated with an anomalous temperature dependence of the crystal structure. Moreover, high–pressure studies revealed that the α–phase reaches the pressure–induced amorphization without any intermediate structural phase transition. Furthermore, the mechanisms of structural compression and amorphization were proposed.

Rare earth molybdates with β'–phase were also studied under high pressures. These materials have a phase transition to a new δ–phase and their lattice parameters were found. On the other hand, we conducted a preliminary study of the β'–phase in several rare earth molybdates at ambient conditions, looking for correlations between the rare–earth ionic radius and their ferroelectric–ferroelastic properties. In addition, we obtained the phase diagram varying the temperature in the $Ho_2(MoO_4)_3$ polymorphous with β'– and γ–phases in order to identify their phase transitions.

Finally, we analysed the negative thermal expansion in several compounds with γ–phase. We evaluated their crystal structures as a function of the temperature and the rare–earth ionic radius, proposing the structural mechanisms that explain the compression of the lattice parameters when the temperature increases.

Resumen

El trabajo presentado en esta tesis se centra en el estudio experimental de los molibdatos de tierras raras con fórmula química $RE_2(MoO_4)_3$ (RE=La–Lu, Y). Estos compuestos cristalizan en tres tipos estructurales en condiciones ambientales: estructura tipo chelita modulada (dividida en dos: $La_2(MoO_4)_3$ y fase α) y fases β' y γ. Hemos caracterizado estos compuestos bajo diferentes condiciones de temperatura y presión usando varias técnicas experimentales, tales como difracción de polvo, espectroscopias de impedancia, óptica y Raman, y análisis térmico. Además, complementamos los experimentos de alta presión usando cálculos teóricos.

Para los molibdatos de tierras raras con fase α tres mecanismos de transporte fueron encontrados: semiconductor, polarónico y iónico; en tres regiones de temperatura. Estos mecanismos de transporte fueron correlacionados con una dependencia anómala de la estructura cristalina con la temperatura. Además, los estudios de alta presión revelaron que la fase α alcanza la presión de amorfización inducida sin ninguna transición de fase estructural intermedia. También, se propusieron los mecanismos de la compresión estructural y de la amorfización.

Los molibdatos de tierras raras con fase β' fueron también estudiados bajo altas presiones. Estos materiales tienen una transición de fase a una nueva fase δ y sus parámetros de celda fueron encontrados. Por otro lado, realizamos un estudio preliminar de la fase β' en varios molibdatos de tierras raras en condiciones ambientales, buscando correlaciones entre el radio iónico de la tierra rara y sus propiedades ferroeléctricas-ferroelásticas. Además, obtuvimos el diagrama de fases variando la temperatura en el polimorfo $Ho_2(MoO_4)_3$ con fases β' y γ para identificar sus transiciones de fase.

Finalmente, analizamos la expansión térmica negativa en varios compuestos con fase γ. Evaluamos sus estructuras cristalinas como función de la temperatura y del radio iónico de la tierra rara, proponiendo los mecanismos estructurales que explican la compresión de los parámetros de celda cuando la temperatura aumenta.

Agradecimientos

Me gustaría agradecer a todas las personas que me han ayudado en este trabajo, tanto investigadores como familia y amigos, gracias a todos ellos he podido llevar a cabo esta tesis doctoral.

En particular me gustaría agradecerles a mis directores de tesis Cristina, Manolo y Víctor por inculcarme sus ganas de investigar desde el primer día. Además, por ofrecerme su ayuda y guía durante estos años. Me habéis hecho sentir como una investigadora más trabajando junto a ustedes.

También me gustaría agradecer a las entidades que han subvencionado esta tesis, por medio de las becas doctorales de Investigación para Posgraduados de la Universidad de La Laguna y de la Agencia Canaria de Investigación, Innovación y Sociedad de la Información (ACIISI); y también a los proyectos de investigación nacionales MAT2007-65990-C03-02, MAT2010-21270-C04-02 y MAT2013-43319-P por financiar esta investigación. Además, se agradece la financiación concedida a la ULL por la Agencia Canaria de Investigación, Innovación y Sociedad de la Información, cofinanciada en un 85% por el Fondo Social Europeo para los gastos de la edición de la tesis doctoral.

Gracias a Diamond Light Source (DLS; Oxford, Inglaterra) y al Instituto Laue Langevin (ILL, Grenoble, Francia) he podido realizar varios experimentos en sus instalaciones, que han permitido realizar parte de los estudios de esta tesis doctoral. Además, gracias a la ayuda de estancias breves de la ACIISI realice una estancia en DLS. También, me gustaría agradecerles a Heribert Wilhelm, Dominik Daisenberger y Annette Kleppe por ayudarme durante esa estancia.

Quiero dar las gracias a los siguientes investigadores: Miguel Castro, Jolanta Stankiewicz, Rafael Valiente y Daniel Errandonea por invitarme a colaborar en sus respectivas universidades y ayudarme en mi investigación. Me gustaría también reconocer su colaboración y ayuda prestada a los profesores de la Universidad de La Laguna: Nanci Sabalisck, Andrés Mujica, Javier González, Plácida Rodríguez, Alfonso Muñoz, Silvana Radescu, Ulises Rodríguez, Carlos Yanes, Fernando Lahoz, Jorge Méndez, Catalina Ruiz y Vicente Rodríguez.

Además, extender estos agradecimientos a los investigadores de la Universidad de La Laguna: Javier López, Sergio León, Diego Lozano, Víctor Sánchez, Ana Hernández, José Velázquez, Virginia Monteseguro, Carla Pérez, Jorge Pasán y Emmanuel Lalla por su colaboración y buena disposición para enseñarme todo lo que saben. También agradecer a muchos investigadores externos a la Universidad de La Laguna que han colaborado en esta tesis como: Emilio Matesanz, Juan Rodríguez, Lourdes Mestres, Elena Cerdeiras, Xavier Vendrell, Francisco Manjón y Shahed Rasekh.

Por último, y no en menor importancia, me gustaría dar las gracias a Carlos por sus infatigables ganas de ayudarme y animarme a realizar este trabajo. Él siempre ha sido mi ejemplo a seguir como investigador y como persona. A mis padres Juan y Yaya por su apoyo en las decisiones más importantes de mi vida. A mi hermana Clary, y mis sobrinas Claudia y Carla que me lo paso genial con ellas. A mi segunda familia: Ángeles, Juan, Yesi, Jonay y Ainhoa que cada fin de semana hacen que mis pilas se recarguen para empezar el lunes con muchas ganas. A todos los demás familiares: abuelos, tíos, primos, ... gracias por ser una familia tan unida.

Contents

Contents

One day, I was teaching my niece Claudia the Archimedes' principle. At that time, she was a child. I started to explain to her, "All submerged body..." However, I could not finish the sentence because she stopped me, saying "...gets wet". Then, I realised that it was also right.

Chapter 1

Introduction

This work is presented to the University of La Laguna to fulfil the requirements for the Degree of Doctor in Physical Science. It has been written according to the Official Rules of the University of La Laguna to apply to the modality of *"Compendium of Publications"*. This modality implies that the manuscript should be constituted by a minimum of three article published in scientist journals belonging to the list of Journal Citations Reports. This manuscript includes a general introduction divided in four chapters. In the first one, we include a general introduction where we present the papers included in this work, we justify their common topic and we also summarize the state of the art and the aims of our investigation. In the two next chapters, we synthesise the methods that we used during this work to obtain the data for our analysis and the results and discussion that we inferred from our studies. After that, we present the most relevant conclusions in the chapter 4.

The different papers that constitute the work presented in this thesis, and also, the position of each journal into its field are listed below:

1. Electrical transport and anomalous structural behavior of α–$Eu_2(MoO_4)_3$ at high temperature. *Solid State Communications* 151, 1654 (2011). **C. Guzmán–Afonso**, M. E. Torres, C. González–Silgo, N. Sabalisck, J. González–Platas, E. Matesanz and A. Mujica.

PHYSICS, CONDENSED MATTER 31/69, Q2 (2011, IF 1.649)

2. Structural anomalies related to changes in the conduction mechanisms of α–$Sm_2(MoO_4)_3$. *Journal of Physics: Condensed Matter* 25, 035902 (2013). **C. Guzmán–Afonso**, C. González–Silgo, M. E. Torres, E. Matesanz and A. Mujica.

   PHYSICS, CONDENSED MATTER 22/67, Q2 (2013, IF 2.223)

3. Pressure evolution of two polymorphs of $Tb_2(MoO_4)_3$. *High Pressure Research* 34, 184 (2014). **C. Guzmán–Afonso**, J. López–Solano, C. González–Silgo, S. F. León–Luis, E. Matesanz and A. Mujica.

   PHYSICS, MULTIDISCIPLINARY 51/78, Q3 (2013, IF 0.926)

4. Crystal structure and non–linear properties of $A_2(MoO_4)_3$ (A=Eu, Gd, Tb, Dy and Ho) *Materials Letters* 65, 2731 (2011). **C. Guzmán–Afonso**, C. González–Silgo, M. E. Torres, N. Sabalisck, A. D. Lozano–Gorrín, J. González–Platas and E. Matesanz.

   MATERIALS SCIENCE, MULTIDISCIPLINARY 47/232, Q1 (2011, IF 2.307)

   PHYSICS, APPLIED 30/125, Q1 (2011, IF 2.307)

5. Polymorphism in $Ho_2(MoO_4)_3$. *Powder Diffraction* 28, S33 (2013). C. González–Silgo, **C. Guzmán–Afonso**, V. M. Sánchez–Fajardo, S. Acosta–Gutiérrez, A. Sánchez–Soares, M. E. Torres, N. Sabalisck, E. Matesanz and J. Rodríguez–Carvajal.

   MATERIALS SCIENCE, CHARACTERIZATION & TESTING 19/33, Q3 (2013, IF 0.586)

6. Structural investigation of the negative thermal expansion in yttrium and rare earth molybdates. *Journal of Physics: Condensed Matter* 23, 325402 (2011). **C. Guzmán–Afonso**, C. González–Silgo, J. González–Platas, M. E. Torres, A. D. Lozano–Gorrín, N. Sabalisck, V. M. Sánchez–Fajardo, J. Campo and J. Rodríguez–Carvajal.

   PHYSICS, CONDENSED MATTER 18/69, Q2 (2011, IF 2.546)

These papers are included in chapter 5, in the same order as they appear in the previous list. They are presented with the original format of their respective editorials. We have added an additional work in the appendices of this manuscript. This work, entitled "Experimental and theoretical study of α–Eu$_2$(MoO$_4$)$_3$ under compression", has been submitted to *The Journal of Chemical Physics*. We believe that this work strongly complements the results presented in the third article of the list and, for this reason, we decided to include this article in the appendix 6.1. We also added the supplementary material of the sixth article of the list in the appendix 6.2. And finally, the thermodynamic relations used in this work have been compiled in appendix 6.3.

The common topic of all these papers is the preparation and characterization of rare earth (RE) molybdates, with chemical formula RE$_2$(MoO$_4$)$_3$. We choose to study these compounds because they present an unusual polymorphism and phase transitions, when they are subjected to changes in temperature, pressure and RE substitution. This gives them a great interest for technological applications, regarding their physical properties, for instance: ferroelectricity, ferroelasticity, piezoelectricity, ionic conduction, negative thermal expansion, fluorescence, and second harmonic generation, among others. In the next section, we will review the most significant contributions that make up the state of the art in this family of compounds from its preparation, crystallographic description, typical physical properties until their most common applications.

1.1   Rare earth molybdates RE$_2$(MoO$_4$)$_3$

The first RE molybdates represented by the formula RE$_2$(MoO$_4$)$_3$ were prepared by Hitchcock in 1895. In particular, he synthesized lanthanum, praseodymium and neodymium molybdates. However, the study of RE molybdates did not improved in the next years until almost a century later, in 1966, when Borchardt et al. prepared Gd$_2$(MoO$_4$)$_3$ and found that this compound is ferroelectric. This discovery promoted the interest on the studies of the RE$_2$(MoO$_4$)$_3$ series until the present day, the researchers now focus on finding new crystals with applications in

lasers (Suzuki et al. 2014).

The RE molybdate series, $RE_2(MoO_4)_3$, can crystallize in three structural groups depending on the RE cation size and the synthesis conditions. These three structures are known as modulated scheelite–type structure, the β'- and γ–phases, without any symmetry relation among them. This rich polymorphism of RE molybdates is also made evident under changes of pressure and temperature, i.e. nine different crystal structures are known for these compounds from ambient temperature to their respective melting points (Brixner et al. 1979), and from ambient pressure (AP, 1 atm) to their respective pressure–induced amorphization (Maczka et al. 2012). This variety of crystal structures makes them appropriate to develop new concepts about the physics of phase transitions and amorphization processes under high pressures, as well as related physical properties and their potential applications.

In the following subsections we summarize some remarkable aspects of the three structural–types of RE molybdates with an emphasis on structure–property relation. We also highlight the interest of these properties and some features that we want to study in deep.

1.1.1 Modulated scheelite–type ($La_2(MoO_4)_3$ and α–phase)

The modulated scheelite structure is a cation deficient structure with formula $RE_{2/3}\square_{1/3}MoO_4$, where $\square$ indicates vacant sites. A vacancy defect is formed when an atom is missing from a normal atomic site in a crystalline structure. The $RE_2(MoO_4)_3$ series with RE ions from lanthanum to dysprosium crystallize in two substructures related to the scheelite–type structure through the vacancy ordering of one third of the calcium positions (Brixner et al. 1979). The original scheelite structure of $CaWO_4$ possesses the tetragonal space group (SG) $I4_1/a$ with Z=4 and three atoms in the asymmetric unit (Zalkin et al. 1964). In this structure, calcium ions are in a polyhedral environment with eight–fold coordination and Wyckoff symbol *4b* which corresponds to the site symmetry S_4, whereas the tungsten ions are surrounded by four oxygen ions in a tetrahedral site with Wyckoff symbol *4a* and the same site symmetry (see Figure 1.1 (left)).
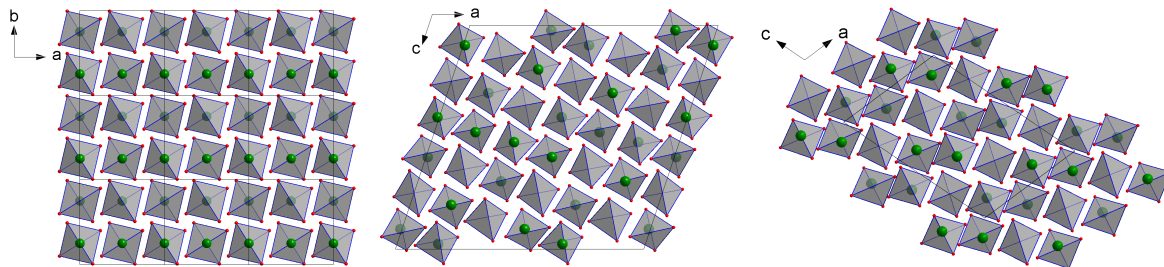
Figure 1.1: Projection of the CaWO$_4$ (left), La$_2$(MoO$_4$)$_3$ (center) and Eu$_2$(MoO$_4$)$_3$ (right) structures along the c axis of the scheelite–structure. Calcium and RE ions are showed in green. The tetrahedral coordination of molybdenum and tungstates ions are in grey. Oxygen ions are showed in red.

We can distinguish two substructures in RE molybdates with different ordering of the vacancies depending on the RE ion. The first substructure appears for the following ions: La^{3+}, Ce^{3+}, Pr^{3+}, and Nd^{3+}. This structure denominated as La$_2$(MoO$_4$)$_3$–type is monoclinic with SG *C2/c* and Z=12 formula units per conventional cell (see Figure 1.1 (center)). Its volume is nine times the scheelite volume. Its asymmetric unit consist in 23 atoms with non–equivalent positions, all of them in general positions 8f, excepting one Mo occupying a Wyckoff position *4e* with the site symmetry C_2 (Templeton et al. 1963). The second substructure, known as the α–phase (see Figure 1.1 (right)), occurs for the Sm^{3+}, Eu^{3+}, Gd^{3+}, Tb^{3+} and Dy^{3+} ions. This crystal structure with SG *C2/c* and Z=4 comprises three scheelite–like subcells. Its asymmetric unit consist in 9 atoms with non–equivalent positions, all of them in general positions 8f, excepting one Mo occupying a Wyckoff position *4e* with the site symmetry C_2 (Boulahya et al. 2005). An additional possible ordering has been recently found for Pr$_2$(MoO$_4$)$_3$ as an incommensurable structure. This structure is described by a SG *I2/b*($\alpha\beta$0)00 and Z=7 (Logvinovich et al. 2010). These authors proposed that "the main structure motif is similar to that La$_2$(MoO$_4$)$_3$–type, but it contains regularly spaced stacking faults defects related with the incommensurate character of its structure".

The materials with related scheelite symmetry, for instance, molybdates and tungstates,

are excellent host materials for solid–state lasers (Neeraj et al. 2004) and phosphors (Yen et al. 2007), as well as Raman shifter (Brenier et al. 2004) and scintillators (Globus et al. 2005). Because of their specific spectroscopic properties, specially the luminescence of the RE ions, high energy conversion efficiency, large thermal conductivity, and high thermal stability are very interesting properties for developing optical devices. In particular, $CaWO_4$ (scheelite) was the first material found for efficient conversion from X–ray to visible light (Röntgen 1896). It is generally accepted that the high–energy band is due to the radiative recombination of a self–trapped electron, localised at the oxyanion complex $[WO_4]^{2-}$. This material has been the most used in X–ray intensifying screens for over 80 years until RE phosphors have overtaken its dominant position in the last years (Shionoya et al. 2006). On the other hand, Raman spectra of tungstate and molybdate single crystals consist of intensive and narrow lines corresponding to symmetrical vibrations of $[WO_4]^{2-}$ and $[MoO_4]^{2-}$ groups, making this type of compound promising Raman active crystals (Basiev et al. 2000).

Respect to their application as phosphors, RE molybdates as stoichiometric solid solution or doped materials are widely studied both for the important applications they have in optics and electronics, as well as for the fundamental physics underlying those processes (Gai et al. 2014; Mason 1990). The optical properties of RE ions are basically influenced by the spin–forbidden character of the intra–configurational 4f $\rightarrow$ 4f electronic transitions, that produce relatively small absorption cross–sections and long radiative lifetime (Ofelt 1963). In particular, the lanthanum ion demonstrates to be an exceptional host for other RE ions in modulated scheelites due to its large ionic radius, for instance: A study in ytterbium- and erbium–co–doped lanthanum molybdates revealed that these materials have an efficient near–IR to visible light up–conversion, where ytterbium acts as an absorber and erbium as an emitter in the crystal lattice (Yi et al. 2002). On the other hand, a study in solid solutions of $RE_{0.8}Eu_{1.2}(MoO_4)_3$ (RE=La, Y, and Gd) was performed by Guo et al. in 2008. In that case, $La_{0.8}Eu_{1.2}(MoO_4)_3$ was the only one that adopted the $La_2(MoO_4)_3$–type phase. As it was recently demonstrated by Atuchin et al. 2014, the luminescence of each compound differs from others because this

17

property depends on the RE ion and the crystal structure.

Finally, the design and functioning of solid–state lasers as new advanced devices for optoelectronic applications are the focus of increasing attention (Cerny et al. 2002; Pask et al. 2000; Volkov et al. 2005). The compounds with scheelite and related scheelite structures are considered as interesting solid–state laser host materials. The advantages of these crystals are their high quantum efficiency, broad absorption and emission bands, as well as relatively low upper–level lifetime. As a consequence of the possibility to have a locally variable position of the active ion on the crystal structure, the line widths of the electronic transitions for the RE elements are found to be broader in disordered than in ordered materials. For that reason, the ordering degree of the materials is studied through the intra–configurational optical transitions of active ion (Lavín et al. 2002). Moreover, in RE doped crystals, the crystallographic positions of RE ions may not be evident, and it is difficult to see clearly the relation between the photoluminescence spectrum and crystallographic environment of the RE ions. The compounds with stoichiometric RE content are more suitable for this purpose because the RE ion position can be reliably defined from crystal structure analysis.

Besides the possible applications in optical devices, studies on scheelites and related materials have shown that these crystals have good prospects as heterogeneous catalysts (Paski et al. 1988), ionic conductors (Takai et al. 1999), and possible to replace the graphite materials currently used in lithium ion batteries (Sharma et al. 2004). In particular, the electric characterization of the modulated scheelite–type structure was performed by Gaur et al. 1993, using DC conductivity (σ_{dc}) and Seebeck coefficient (S) in the temperature range 450–1200 K. These molybdates were described as electrical insulators: materials whose internal electric charges do not flow freely, and therefore make it very hard to conduct an electric current under the influence of an electric field. These materials have a band gap that increases slowly going down the RE molybdate series from 2.30 eV for La molybdate to 3.20 eV for Eu molybdate. They observed, in general, three linear regions with two break temperatures, occurring due to changes in the conduction mechanism. At lower temperatures, electrical conduction is mainly

extrinsic, that is, the impurities play the significant role. And at higher temperatures, the charge carriers would become polarons. The polaron formation occurs when the interaction between electrons and optical phonons is strong enough and at sufficiently high temperature this will move through the material, taking place the polaronic–type conduction. Despite that study, the conduction mechanisms are unknown. In another study, $RE_2(MoO_4)_3$ (RE=La, Nd) were proposed as promising candidates for microwave substrate applications, considering them as easy preparation samples with simple phase composition, fine microstructure, low sintering temperature, and good microwave dielectric properties (Pang et al. 2011).

Molybdates and tungstates (AMO_4 and $ABMO_4$ materials, M=Mo or W) with scheelite structures constitute important class of materials that exhibit various functional properties, which depends on the structure. In the last years, its evolution under pressure has arisen renewed interest (Errandonea et al. 2008; Maczka et al. 2012). However, less works have been developed for $A_2(MO_4)_3$ compounds with modulated scheelite–structure. High–pressure Raman spectroscopy studies have been performed in $Nd_2(MoO_4)_3$ and $Tb_2(MoO_4)_3$ by Jayaraman et al. 1997, and in $Eu_2(MoO_4)_3$ by Le Bacq et al. 2011. No pressure–induced phase transitions were observed for $Nd_2(MoO_4)_3$ and $Tb_2(MoO_4)_3$ but in the case of $Eu_2(MoO_4)_3$, a splitting of the high–frequency modes was observed suggesting a minor structural change. Additionally, the pressure–induced amorphization was found for $Nd_2(MoO_4)_3$, $Eu_2(MoO_4)_3$ and $Tb_2(MoO_4)_3$ at 15.5 GPa, 19.9 GPa and 25 GPa, respectively. Those compounds constitute interesting examples where the ambient pressure phase undergoes pressure–induced amorphization without an intermediate phase. However, in spite of these works, the mechanisms for the compression of these structures are still unknown, particularly the pressure dependence of their crystal structure has not be well studied.

All these interesting electric and optical properties of modulated scheelite–related compounds and, in particular, the possibility to study their crystal structure evolution with the temperature, pressure and RE ionic radius, has motivated our interest in this family. Also, these compounds exhibit high stability, easy preparation and some advantages in their men-
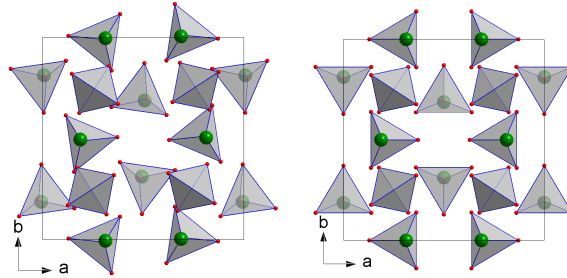
Figure 1.2: View along the c axis of the β'- (left) and β–phases (right) of $Gd_2(MoO_4)_3$. RE ions are showed in green. The tetrahedral coordination of molybdenum ions are in grey. Oxygen ions are showed in red.

tioned physical properties regarding other materials with related–scheelite structure. Moreover, the creation of cationic vacancies in the crystal lattice and the ordering of these cations and vacancies may be a new factor in controlling the structural and physical properties.

1.1.2 β'–phase

The molybdate series with RE from samarium to holmium can crystallize in the β'–phase (Brixner et al. 1979) and the representative compound of this structural–type is $Gd_2(MoO_4)_3$. This phase is particular of the molybdates family because of it does not appear in any family of similar compounds as tungstates, chromates, phosphates, vanadates or sulphates. The β'– phase is an orthorhombic structure with SG *Pba2* and Z=4 (Borchardt et al. 1966; Keve 1971; Svensson et al. 1979). In this structural–type, the RE ions are in a polyhedral environment, without site symmetry (general positions *4c*) and build by seven oxygen ions, whereas the molybdenum ions are surrounded by four oxygen ions in a distorted tetrahedral site (see in Figure 1.2 (left)). There are two independent sites for the RE ions, three sites for the Mo ions and twelve sites for the oxygen ions.

The main properties of molybdates with β'–phase are their ferroelectricity and ferroe-lasticity (Cross et al. 1968; Keve 1971; Ponomarev 2002) due to the possibility to develop a spontaneous polarization in the direction of the polar axis, parallel to the c axis (as can

be inferred from the space group) and also may exhibit a spontaneous strain. Both spontaneous polarization and strain disappear after the phase transition ferroelectric–paraelectric and ferroelastic–paraelastic, at the same temperature. Compounds with this β'–phase are known as improper ferroelectrics because the distortion responsible for the spontaneous polarization and the strain is a secondary mode, that is unstable in the paraelectric–paraelastic phase. In addition, the appearance of this secondary mode in the ferroelectric–ferroelastic phase is induced by its coupling with a primary unstable non–polar distortion mode (Toledano et al. 1987). The spontaneous electric polarization and the spontaneous strain in these materials is usually small compared with that in proper ferroelectrics, as expected from its secondary role in the stabilization of the phase.

The corresponding paraelectric–paraelastic phase, called β–phase, belongs to the SG *P-42_1m* and shows up after a phase transition at about 450 K. This high–temperature phase is a tetragonal structure (see in Figure 1.2 (right)) and it is more symmetric than the β'–phase, i.e., the sites for RE ions are reduced to one, for the Mo ions to two sites and four sites for the oxygen ions (Jeitschko 1972). The RE, one Mo and one O ions are located on a mirror plane C_S with Wyckoff symbol *4e*, while another Mo ion is located on a fourfold inverse axis S_4, with Wyckoff symbol *2a*. Thus, the tetragonal form around the more symmetric Mo is due to disordered positions of a first O atom in a general position *8f*. The less symmetric tetrahedron is formed by a second O atom at the mirror plane, with Wyckoff position *4e* and split positions for the third O and the fourth O atom, both at a general position. The crystal structure of β–$Gd_2(MoO_4)_3$ is formed by corner–sharing MoO_4 tetrahedra and RE polyhedra coordinated by seven oxygen atoms. Each oxygen atom has either two or three nearest metal atoms.

In addition, both β'- and β–phases are non–centrosymmetric with potential non–linear properties, specially optical ones. For that reason, $Gd_2(MoO_4)_3$ is an efficient frequency doubling medium for laser diode pumping because it displays second order harmonic generation (Kojima et al. 1978). In particular, the β'–$Gd_2(MoO_4)_3$:Nd crystals are very appealing non–linear materials for the creation of various laser frequency doublers and also Raman shifters, due to MoO_4

vibrations (Kaminskii et al. 1997). The spontaneous polarization, second order non–lineal susceptibility tensor values (responsible for second order harmonic generation), the piezoelectric and optoelectronic coefficients of Gd$_2$(MoO$_4$)$_3$ and Tb$_2$(MoO$_4$)$_3$ have been obtained by Keve 1971 and Svensson et al. 1979. They found the value of the non–lineal susceptibility tensor for gadolinium molybdate is just the 7.5% of the values showed by more common compounds used in optoelectronic devices, as titanates and niobates (structural families of Pb[Zr$_x$Ti$_{1-x}$]O$_3$ (PZT) or LiNbO$_3$) (Kojima et al. 1978). However, at the same time, the β'–phase displayed the largest piezoelectric and optoelectronic coefficients ever found. The optical properties of this structural phase have been also analysed as phosphor hosts, due to their RE components. For instance, Bubb et al. 2005 studied the near–IR to visible light up–conversion of LaEr(MoO$_4$)$_3$. In other study, β'–Sm$_2$(MoO$_4$)$_3$ crystals were written at the surface of Sm$_2$O$_3$–MoO$_3$–B$_2$O$_3$ glasses by YAG laser irradiation. This work demonstrated that the samarium atom heat processing is a technique for the writing of RE containing optical non–linear/ferroelectric crystal lines in glasses (Abe et al. 2005).

The electrical transport properties of Gd$_2$(MoO$_4$)$_3$ and Tb$_2$(MoO$_4$)$_3$ were reported at the temperature range 650–1075 K (Tripathi et al. 1980). These compounds showed three linear regions with two break temperatures, due to changes in the conduction type, for example, a change from an extrinsic to an intrinsic conductivity. This result is similar to the one found in the modulated scheelite–type structure (Gaur et al. 1993). In addition, the band gap energies are related to the RE ionic radius, decreasing those energies when the RE ionic radius diminishes. These authors concluded that the conduction below 805 K is due to thermally activated charge carriers in localized impurity levels. Moreover, they observed some instabilities in the phases of those crystals from 805 to 880 K. Therefore, a possible phase transition β–α must be considered, since this transition could affect the properties temperature dependent. And finally, the intrinsic conduction is dominating beyond 880 K.

On the other hand, the less density of the β'–phase compared to the α–phase (about 20% denser) prompted several high–pressure studies on the β'–phase, due to an opener structure

allows more structural changes under high pressures. The first high–pressure study with this characteristic phase was performed on $Gd_2(MoO_4)_3$ using X–ray diffraction (Brixner 1972). In this study was found that the β–phase transformed to the α–phase when the sample was subjected to high pressure and high temperature (3.0 GPa and 828 K). However, the β–phase transformed to an amorphous phase when pressure was applied at temperatures below 673 K. This means that at low temperatures the kinetics of this reaction are very slow and therefore an intermediate structural disarray is frozen, becoming an amorphous form. The next study under high pressures was performed in the β'–phase of $Tb_2(MoO_4)_3$ using Raman spectroscopy and X–ray diffraction (Jayaraman et al. 1993). In this analysis, the Raman peaks were classified by their origin and a pressure–induced phase transition was found from the dramatic changes in the Raman profile collected at 2.3 GPa. The resulting new phase was called δ–phase. Beyond 2.3 GPa, the δ–phase reached the pressure–induced amorphization at 6.6 GPa. However, the quality of the X–ray diffraction data were not good enough for obtaining the new structure. Other X–ray diffraction study on Sm, Eu and Gd molybdates with β'–phase confirmed the same phase transition for these isostructural compounds (Dmitriev et al. 2003). However, in spite of the efforts performed, the δ–phase has not been properly characterized. Later on, another six pressure–induced transformations (including the transition to the δ–phase) were identified using fluorescence spectroscopy of Eu^{3+} ions (Machon et al. 2004). The mechanisms proposed for these sequences of transformations were related to a progressive distortion of the MoO_4 tetrahedra followed by a coordination change of Mo atoms (Lucazeau et al. 2009; Lucazeau et al. 2011).

With respect to some members of this large family of polymorphs, in particular, $Y_2(MoO_4)_3$ can exist in two stable phases at ambient temperature (Gates et al. 2007): β' and γ(hydrated). Moreover, $Ho_2(MoO_4)_3$ crystallizes in both structures too (Brixner et al. 1979). Ionic radii of yttrium and holmium are between dysprosium, which possesses the β'–phase, and erbium, which possesses the γ–phase, but this crystal structure is difficult to determine because is hydrated (see the following subsection). However, in the case of $Ho_2(WO_4)_3$, this compound

23
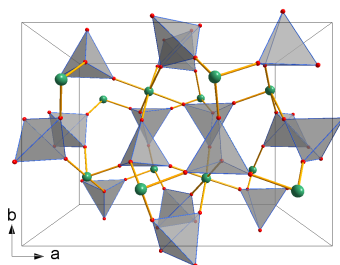
Figure 1.3: View along the c–axis of the γ–phase of Sc$_2$(WO$_4$)$_3$. Scandium ions are showed in green. The tetrahedral coordination of tungstates ions are in grey. Oxygen ions are showed in red.

adopts the monoclinic α–phase (Xiao et al. 2008) and the orthorhombic γ–phase, because the β'–phase is particular of molybdates, as aforementioned. This fact makes holmium compounds very interesting for us, although, in this work we are more interested in the molybdate family.

1.1.3 γ–phase

Molybdates with RE=Y, Ho–Lu can crystallize in the orthorhombic SG *Pbcn* with Z=4, known as γ–phase. This structure corresponds to isostructural Sc$_2$(WO$_4$)$_3$ (Abrahams et al. 1966) and its unit–cell is formed for an scandium (or RE), two tungstens (or molybdenums), and six oxygen atoms. One of the two tungstens is in a Wyckoff position *4c*, with site symmetry C_2 that consist in a two–fold rotation parallel to the b–axis. The other one is located in a general position *8d* without site symmetry. All the other atoms are situated in general position *8d*. Then, two tetrahedra are formed. The more symmetric tungsten or molybdenum W2 (or Mo2) is bonding to two oxygens O5 and O6, and other two oxygens generated by symmetry. The less symmetric tetrahedron is bonding with the other four oxygen atoms O1, O2, O3 and O4. The Sc (or RE) ion is coordinated with six oxygens, and it is the smallest coordination found for the RE ions in molybdates. In order to facilitate the understanding of this crystal structure we plotted a view of the γ–phase in Figure 1.3. The arrangement can be observed in this figure, where each tetrahedron is connected with four octahedral through the oxygen atoms and each octahedron is connected with six tetrahedra.

The γ–phase is hydrated at ambient conditions and for this reason we will call it the γ(hydrated)–phase before it loses the water molecules at about 430 K. This implies a certain degree of complexity when one tries to perform studies in the γ–phase at low temperature.

One of the most interesting properties of compounds with γ–phase is that they exhibit negative thermal expansion (Evans et al. 1998). This effect produces the contraction of the material upon heating (or the dilatation of the material upon cooling) and a few materials show this property. There are several important applications for substances with a negative thermal expansion coefficient, in particular, the ZrW_2O_8 family of materials (Zr and W can be replaced with Hf or/and Mo respectively) are used in photonic areas (Wei et al. 2001), in medical applications (Versluis et al. 1996), etc. Tungstates usually exhibit a wider temperature range with negative thermal expansion than molybdates, while molybdates have more negative coefficients (Sumithra et al. 2004). In particular, RE molybdates (RE=Y, Er and Yb) show a linear thermal expansion coefficient as a function of RE cation size. Moreover, as the RE cation size decreases, the thermal expansion coefficient also becomes less negative (Sumithra et al. 2006). In addition, the thermal expansion of $Y_2(MoO_4)_3$ was investigated experimentally from 20 to 450 K by Marinkovic et al. 2009 and theoretically from 0 to 1625 K by Wang et al. 2013. The negative thermal expansion was found experimentally in the whole temperature range, and theoretically in the range from 0 to 1000 K. That means that these compounds have negative thermal expansion over a wide temperature range and encouraging us to keep working on the remaining compounds.

On the other hand, in some isostructural compounds (specifically in tungstates with small trivalent cation) a phase transition to a monoclinic phase with SG $P2_1/a$ was found at 170 K (Evans et al. 2000). This low–temperature structure has a positive thermal expansion coefficient. However, no monoclinic modification for $Y_2(MoO_4)_3$ has been found (Marinkovic et al. 2009), demonstrating that isostructural tungstates and molybdates can have different structural behaviours when they are subjected to temperature changes.

Although, in general, structural flexibility seems to be a key factor for negative thermal ex-

pansion, different mechanisms have been proposed to explain it in different type of compounds. This property is most commonly observed in compounds with flexible M–O–M bridges and it is due to the transverse vibration of the oxygen atoms, making that the M–M distance decreases whereas the M–O distance remains essentially unchanged. These transverse vibrations can occur through coupled librations of the rigid corned sharing polyhedral (tetrahedra and octahedra in case of the γ–phase) called Rigid Unit Modes or RUMs (Giddy et al. 1993). In recent years, questions have been raised regarding whether simple RUMs models are sufficient to explain negative thermal expansion (Ravindran et al. 2003; Tao et al. 2003). Moreover, Marinkovic et al. 2009 found that the polyhedral distortion around the cation A is strongly correlated with the linear negative thermal expansion coefficient of different members of the $A_2M_3O_{12}$ family.

The interest of this phase has grown in the last decade because it possesses a large trivalent ion conductivity (Secco et al. 2002), where the ionic conductivities of the molybdate series become considerably higher in comparison to those of the tungstate series (Imanaka et al. 2000). In particular, $A_2(MO_4)_3$ with A=Sc, Al and M=W, Mo show a conductivity that increases when the temperature increases and a normal decrease when pressure increases. On the other hand, due to the flexibility of $Sc_2(WO_4)_3$ structure, the γ–phase displays a rich variety of behaviours (phase transitions and amorphization) when it undergoes pressure changes (Maczka et al. 2012; Paraguassu et al. 2004). According to what has been said, a comprehensive study of the evolution of the structure with temperature, pressure and ionic radius can help to resolve this controversy.

1.2 Aims

The polymorphism in RE molybdates and their related physical properties are known many years ago. However, the increasing studies in the last two decades for electronic and optical devices makes necessary a revision of the stability and the phase transitions in these compounds. Assuming that small changes in external perturbations (ionic substitution, temperature or

pressure) can modify drastically their crystal structure and, consequently, their physical properties; it is possible to explain, for example, changes in the luminescence of the RE ions and the lifetimes of their electronic emitting levels. Therefore, we aim to increase the available knowledge of these compounds through different characterization techniques: powder diffraction, impedance, optical and Raman spectroscopies, and thermal analysis, adding in some cases *ab initio* total–energy calculations. Each of these characterization techniques has own advantages and we will show that their combination gives detailed information about structural changes occurring in these materials subjected to different temperature and pressure regimes. Thus, we will be able to provide significant insight into the origin of lattice instabilities and structural mechanisms that affect their physical properties.

We will start synthesizing the complete family of compounds. In particular, we will prepare polycrystalline samples with the three crystal structures at ambient conditions: modulated scheelite–type, β'- and γ–phases. We will report about the synthesis conditions to prepare the different polymorphs without mix of phases.

The structural characterization of the polycrystalline samples will be performed using powder diffraction. At ambient conditions, we will identify the crystalline phases and will collect data with enough resolution to refine the crystal structure of the different phases. In order to study the samples at non–ambient conditions, we will apply for beamtime at large facilities. In addition, we will use new tools for the Rietveld method, that can help to explain the structural changes in our compounds due to external perturbations.

Attending to the data collected at ambient conditions, we will perform a preliminary study of the variations produced on the crystal structure of molybdates with different RE ions, i.e. by the chemical pressure effects in these structures, due to the lanthanide contraction. We will be especially interested in those compounds that present several polymorphs.

With respect to the analysis of data at different temperatures, we will infer if the lattice parameters expand or compress normally, their changing rates, and possible phase transitions giving the thermal stability range of each phase. Also, if the atomic parameters are determined,

we will propose the possible structural mechanisms for these variations and the origin of the structural instabilities.

On the other hand, from the data collected in our samples at high pressures, we can infer the properties of the structural compression; we will be able to compare these experimental properties with the theoretical ones. In this case, we will perform calculations from first principles to understand more deeply the changes occurring on the crystal structures and the origin of possible instabilities. Additionally, we will revise if the samples undergo crystalline–crystalline phase transitions, their respective stability ranges and if there is agreement with the theoretical calculations, in order to complete previous works. Moreover, the high–pressure measurements will also allow us the analysis of the loss of long–range order (amorphization) and we will propose, in more detail, the possible mechanisms that explain this process.

In order to complete this study, when the experimental conditions of powder diffraction are not optimal to detect changes on the crystal structure and degree of reversibility, we will draw on other experimental techniques. It is well known that combination of short and long–range probe techniques provides significant insight into the phase transitions and the origin of lattice instabilities. In particular, diffraction data collected under high pressure lose resolution, thus, information obtained by Raman and optical spectroscopies, widely used for this purpose, will be complementary techniques in our research.

As already we have mentioned, the investigation on the crystal–structure dependence with temperature and pressure in the family of RE molybdates, is aimed to better understand their physical properties that is growing interest, due to their optical applications as: scintillators, phosphors, lasers, etc. However, we are more interested in their mechanical, dielectric or electronic properties, that can be explained from the crystal–structure data: ferroelectricity, ferroelasticity and negative thermal expansion. Moreover, we want to identify different types of electric conduction using impedance spectroscopy, and to stablish, for the first time, correlations between the transport mechanisms and the thermal evolution of the crystal structure in these compounds. Moreover, this technique allows to get information about the possible transitions

and structural anomalies, by detecting changes in the permittivity and electrical conductivity.

Finally, we expect that the results derived from this work have important applications for science and technology and to complement previous studies, for use as scientific and technical information in the area of material science.

Chapter 2

Method

This section summarizes the techniques employed in the work presented in this thesis, as well as the methods that we used for the analysis of data that these provided. The more specific aspects about the experimental details are described in the papers attached in chapter 5.

2.1 Solid–state reaction

Solid state reaction consists in the preparation of polycrystalline solids by direct reaction of the starting reactants (powders) at high temperatures for a relatively long heating time (West 2013). In particular, for the synthesis of RE molybdates, the reactants are RE oxide (RE_2O_3) and molybdenum oxide (MoO_3). As the Pr_2O_3 and Tb_2O_3 reactants are highly hygroscopic, $Pr_2(MoO_4)_3$ and $Tb_2(MoO_4)_3$ should require a controlled atmosphere for their synthesis. For that reason, we replaced these oxides for Pr_6O_{11} and Tb_4O_7. The following chemical equation illustrates the general chemical reaction to obtain RE molybdates starting from the oxides:

$$RE_2O_3 + 3\ MoO_3 \rightarrow RE_2(MoO_4)_3$$
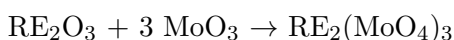
Figure 2.1 shows a schedule of the experimental procedure for the solid–state reaction. In this process, the reactants used in the synthesis should be dried before weighting them to remove any residual. To do that, we pre–heated the MoO_3 and RE_2O_3 powders at 923 and
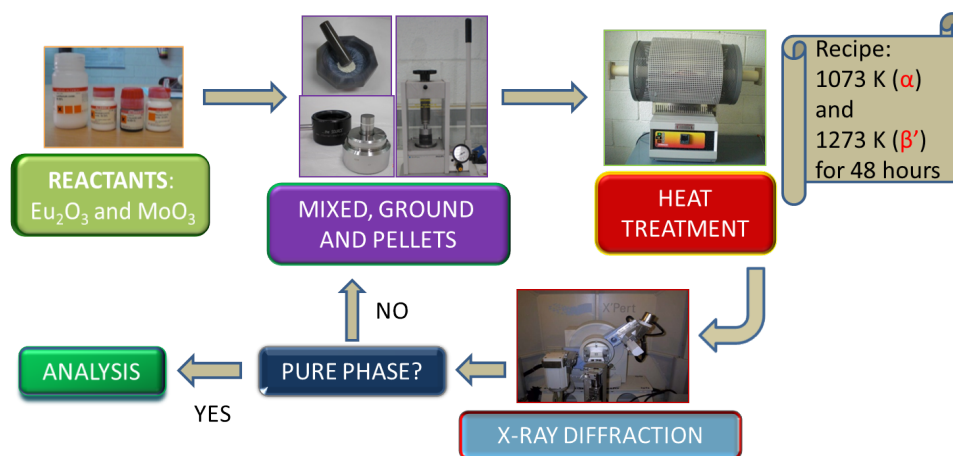
Figure 2.1: Experimental procedure of solid–state reaction. The synthesis of polymorphic $Eu_2(MoO_4)_3$ is given as a example.

1173 K during 10 h, respectively. These pre–heated powders are weighted in stoichiometric amounts, mixed and homogenized with acetone in an agate mortar during half hour in order to maximize the powder surface areas.

The next step for the preparation of RE molybdates is to convert the powders into pellets. In order to do that we use a cylindrical steel die of 13 mm and a hydraulic press to apply pressure up to 5 tn on the sample. The thickness of the pellets should be approximately of 1 mm. The benefits of using pellets are a reduction of the air pores into the sample and an increase in the area of contact between the grains that favours the reaction of the reactants when they are treated thermally to obtain the desired phase.

We checked several thermal treatments for each compound to find the adequate temperature that produces the pure crystalline phase. One example is the case of europium molybdate that can crystallize in the α- and β'–phases, this compound needed to be heated at 1073 and 1273 K for 48 hours to obtain each phase, respectively.

The thermal treatments were performed using a resistance furnace. The pellets were placed inside a platinum crucible into the furnace. We use platinum crucibles because this material

Table 2.1: Thermal treatments applied to synthesize $RE_2(MoO_4)_3$ using the solid–state reaction. The asterisk in β'–$Sm_2(MoO_4)_3$ is used to indicate that the pressure in the hydraulic press was 5 ton. instead of the convectional 2 ton. Note that for $Dy_2(MoO_4)_3$ and $Yb_2(MoO_4)_3$ an intermediate graining is necessary, as well as a second thermal treatment. The values of temperature, stabilization time and the heating/cooling rates for this second thermal treatment are inside brackets in this table.

Compound	Phase	Temperature (K)	Time (h)	Heating rate (K/h)	Cooling rate (K/h)
$La_2(MoO_4)_3$	$La_2(MoO_4)_3$	1073	48	100	100
$Pr_2(MoO_4)_3$	$La_2(MoO_4)_3$	1073	48	100	100
$Nd_2(MoO_4)_3$	$La_2(MoO_4)_3$	1073	48	100	100
$Sm_2(MoO_4)_3$	α	1073	48	100	100
$Eu_2(MoO_4)_3$	α	1073	48	100	100
$Gd_2(MoO_4)_3$	α	1073	48	100	100
$Tb_2(MoO_4)_3$	α	973	48	100	100
$Sm_2(MoO_4)_3$*	β'	1378	12	120	quenching
$Eu_2(MoO_4)_3$	β'	1273	48	100	100
$Gd_2(MoO_4)_3$	β'	1223	48	100	100
$Tb_2(MoO_4)_3$	β'	1223	48	100	100
$Dy_2(MoO_4)_3$	β'	1173 (1273)	48 (12)	100 (120)	100 (360)
$Ho_2(MoO_4)_3$	β'	1173	24	120	120
$Ho_2(MoO_4)_3$	γ	1248	48	120	240
$Er_2(MoO_4)_3$	γ	1323	24	100	100
$Tm_2(MoO_4)_3$	γ	1323	24	100	100
$Yb_2(MoO_4)_3$	γ	1223 (1323)	18 (24)	120 (120)	240 (240)
$Lu_2(MoO_4)_3$	γ	1323	24	100	100
$Y_2(MoO_4)_3$	γ	1323	24	100	100

barely reacts with its environment and it is appropriated to reach high temperatures. The thermal treatments performed to prepare RE molybdates are summarized in Table 2.1.

Finally, we carried out powder X–ray diffraction on a selected thermally–treated pellet to confirm its structural phase and purity. If the sample did not have the phase that we wanted, we repeated the previous process, beginning from the mixing step.

2.2 Powder diffraction

We focused on the powder diffraction method, because our samples are polycrystalline, e.i., solids that are composed of many crystallites randomly orientated. This technique is a crucial tool that is applicable to interdisciplinary studies, with increasing importance and breadth of application as instrumentation, methods, data analysis and modelling.

Diffraction occurs when electromagnetic radiation, with wavelength comparable to atomic spacings, is incident upon a crystalline sample. The waves are scattered in a specular fashion by the atoms in the system, and undergo constructive interference in accordance to Bragg's law, given by the following expression:

$$n\lambda = 2d\sin(\theta) \tag{2.1}$$

where n is an integer, λ is the wavelength of the incident ray, d is the interplanar spacing of parallel lattice planes and θ is the angle between the incident ray and the scattering planes. Figure 2.2 shows the necessary condition for the constructive interference the two electromag-
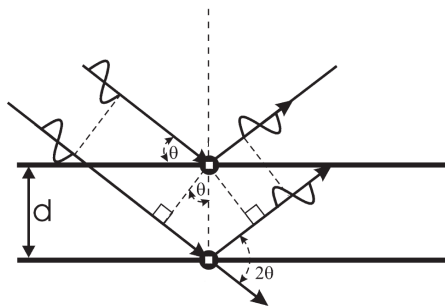

Figure 2.2: Illustration of the geometry used for the simplified derivation of Bragg's law (figure taken from Le Bail et al. 2008).

33

netic waves. This figure deals a simplified solution for diffraction, however in reality, in the case of X–rays, these are not reflected by planes but are scattered by electrons bound to the atoms, and, in general, atoms in one plane will not lie exactly above atoms in the plane below.

Equation 2.1 represents the Bragg equation in direct space. However, in the reciprocal space this equation can be also defined. The reciprocal lattice was invented as convenient representation of the physical of the diffraction by a crystal sample. The points in the reciprocal lattice are related to the vectors defining the crystallographic planes ($\mathbf{a}$, $\mathbf{b}$ and $\mathbf{c}$). There is one point in the reciprocal lattice for each crystallographic plane, hkl. A reciprocal lattice vector $\mathbf{H}_{hkl}$ is the vector from the origin of reciprocal space to the reciprocal lattice point (hkl):

$$\mathbf{H}_{hkl} = h\mathbf{a}^* + k\mathbf{b}^* + l\mathbf{c}^* \qquad h, k, l \in \mathbb{Z} \tag{2.2}$$

where $\mathbf{a}^*$, $\mathbf{b}^*$ and $\mathbf{c}^*$ are vectors defining the reciprocal unit–cell and hkl are the Miller indices. $\mathbf{H}_{hkl}$ is perpendicular to the crystallographic plane hkl and $|\mathbf{H}_{hkl}| = 1/d_{hkl}$, this last expression is a useful variation of the Bragg equation.

In a powder diffraction experiment, a 1–dimensional representation of diffracted intensity as a function of 2θ, diffraction angle, is normally obtained. Thus, the graph of a powder pattern (diffractogram) consists of a sequence of peaks (Bragg reflections) resting on a slowly varying background. These peaks can be characterized by parameters defining their positions (d_{hkl}), intensities (I_{hkl}) and profile (line shape and line width). Powder diffraction techniques are based on the measurement of one or more of these parameters for as many reflections as are required (or can be measured) in a particular application. In the followings subsections we will give more details about these parameters.

Positions (d–spacing)

The principal method for the identification of unknown materials is based on a comparison of experimental data with d–spacings and peak intensities contained in a database. Phase identification and phase diagrams (precise location of phase boundaries) are essentials in our

investigation of RE molybdates. On the other hand, by indexing the peaks it is possible to obtain the cell parameters, although in most our cases these are known; also, we can visualize thermal or pressure compression and expansion by comparing the peaks positions.

Peak intensities I_{hkl}

The total intensity of the scattered X–ray or neutron beam is composed by the coherent scattering, while the part of the incoherent scattering is included on the background. The experimentally measured intensity of coherent scattering is related to cross sections of atoms (actually, clouds of electrons and atomic nuclei) but they are modified by polarization and absorption factors. For chemical elements (O, Mo and RE) belonging to our samples, X–ray absorption edges are not in the range of the energy of the X–ray used. However Sm, Eu and Gd are RE atoms with a substantial neutron absorption cross section for thermal neutrons, thus, samples containing these chemical elements are not recommendable to neutron diffraction experiments.

For X–ray, the scattering from electrons around an atom can be described as the Fourier transform of the electron distribution of each atom and it is known as the scattering factor or form factor $f(Q)$. Scattering factors monotonically increase with the atomic number and fairly strongly on scattering vector (Q). However, neutron scattering is just a point scattering and the observed scattering factor or scattering length (b), for a given element (considering their isotopes) is independent of Q, and the total cross section is given by $\sigma_{coh} = 4\pi\langle b\rangle^2$. Therefore, for X–ray the highest intensity peaks occur at small Q, while for neutron radiation, diffractograms can show strong well defined peaks even at high angles and information about short displacements is not lost. Moreover, b varies erratically with atomic number, and shows considerable variation by isotope. Thus, adjacent elements in the Periodic Table may have very different neutron scattering lengths, that can facilitate their discrimination. In our case, more precise determination of the position of the lighter atoms (oxygen) in presence of the heavier one (molybdenum and rare earths) are better determined by neutron diffraction.

On the other hand, the scattering density $\rho(\mathbf{r})$ for the arrangement of atoms in a crystal,

described as an infinitely repeating motif, can be represented by a Fourier series whose coefficients are known as structure factors. Within the unit–cell, the atoms exhibit own repetition properties as a group of symmetry operations. We can postulate that $\rho(\mathbf{r})$ is localized on the atom centres and assign a scattering factor or scattering length (we will denote both as f_i), then, the corresponding inverse Fourier transform becomes a sum over N atoms positions in the unit–cell

$$F(\mathbf{H}) = \sum_{i=1,\ldots,N} f_i e^{2\pi i(\mathbf{H}\cdot\mathbf{r}_i)} \tag{2.3}$$

The vector $\mathbf{H}$ is the dimensionless indices (hkl) and the vector $\mathbf{r}$ becomes the fractional co-ordinates (xyz) and the sub-index i represents each atom. Then, the diffracted intensity is determined by the interference between the individual scattering centres that make up the crystal structure:

$$I(\mathbf{H}) = F(\mathbf{H})F^*(\mathbf{H}) \tag{2.4}$$

Therefore, from intensities we can obtain information about the crystal structure.

Line shape and line width

In practice, materials contain structural imperfections that give rise to a spread of intensity around each reciprocal–lattice point. There are two categories of structural imperfection that can modify diffraction line profiles by a measurable amount. The first is the finite size of domains over which diffraction is coherent (sub–domains or grain size). In this case the size broadening of the line is constant in the direction d_{hkl}. The second category is based on the fact that a distortion of the crystal arises from microstrain, due to an applied or residual stress, or from a compositional gradient in the sample. For this, the size broadening increases with the order of a reflection. In our case, changes with temperature or pressure contribute normally to this second category.

2.2.1 Data analysis

In order to characterize the powder pattern (position, intensity, line shape and line width) that define each reflection, we have used a model to compare and/or fit the entire observed diffraction pattern. The calculated intensity $y_c(x_i)$ at some point x_i ($2\theta_i$ angle, in our case) is the sum of the contribution from all neighbouring reflections at the positions x_j plus the background at that point $y_b(x_i)$

$$y_c(x_i) = \sum_j I_{cj}\Omega(x_i - x_j) + y_b(x_i) \tag{2.5}$$

where Ω is the function used to model the peaks, normalized to the unit area and multiplied by the area I_{cj} of each reflection j, which is calculated by different ways as we will see in the parts of the Rietveld refinement and profile matching. Finally, the summation over all reflections which contribute to the intensity I_{cj} is performed. The pseudo–Voigt (linear superposition of both Gaussian and Lorentzian functions) approximation of the Voigt function (convolution of Gaussian and Lorentzian functions) is probably the most widely used for modelling the X–ray and neutron Bragg peaks. Owing to the different functional form of instrumental and sample broadening effects as a function of diffraction angle, we normally use a modified function: the Thompson–Cox–Hastings pseudo–Voigt convoluted with axial divergence asymmetry (Finger et al. 1994). With respect to the shape and the width of the profile we refined the special parameter that accounts for the broadening by microstrain. Generally, the instrumental resolution function is provided, which also affects to the profile, but the corresponding parameters are not refined. Following, we will divide on sections the different treatments that we have performed to the diffraction data.

Phase identification

To identify the phase of any compound obtained by solid–state reaction, as we mentioned in section 2.1, we compared the powder pattern with the simulated pattern using the crystal

structure of the known phase. For do that, we use the known cell parameters to calculate the x_j position of each Bragg reflection and its intensity I_{cj} is calculated from equation 2.4, from which a particular intensity $I_{\mathbf{H}}$ depends on the atomic factors and the atomic coordinates, which are known.

Rietveld refinement

When we want to characterize isostructural compounds (some structures of RE molybdates are described in the ICSD database (Bergerhoff et al. 1987)) at non–ambient conditions or changing the RE, we use the Rietveld method (Young 1993) to refine the diffraction patterns. This method uses a least squares approach to refine a theoretical line profile until it matches the measured profile. McCusker et al. 1999 published a guide about how to use the Rietveld method, focusing on experimental aspects of the analysis of powder patterns in a Rietveld refinement and also describes specific features to collect a good diffraction data using different radiation sources. This method calculates the initial peak positions x_j from the cell parameters, which can be refined. In addition, the shift of the instrumental zero is often refined and, in particular cases, it has been also refined the shift of special reflections in the pressure experiments (see paper of the appendix 6.1). It is also possible to calculate the atomic positions and thermal displacements through the intensity of the peaks $I_{c\mathbf{H}}$, i.e. refining the initial positions that are known by comparing observed intensities with those calculated. Thus, the intensity $I_{c\mathbf{H}}$ of a Bragg reflection will be:

$$I_{c\mathbf{H}} = Km_{\mathbf{H}}Lp_{\mathbf{H}}\left|F_{\mathbf{H}}\right|^2 \tag{2.6}$$

Besides the structure factor $F_{\mathbf{H}}$, other parameters related to the sample and experimental geometry affect to the intensity: the scale factor K (which can be refined), the multiplicity of each reflection (hkl) $m_{\mathbf{H}}$ and the Lorentz–polarization factor $Lp_{\mathbf{H}}$. Other effects affecting to the intensity, as the absorption, preferred orientation and extinction were not refined.

Profile matching

The low particle statistic was a clear inconvenient to obtain good intensities, in order to use the crystal structure to model the whole pattern, for instance, in pressure dependent experiments (see papers of section 5.3 and appendix 6.1). It was also not possible to refine the oxygen positions and thermal displacements from X–ray experiments (see paper of section 5.5). In these cases, we used the Le Bail method to obtain the whole pattern decomposition (Le Bail 2005). The free parameters are the same parameters (cell and profile parameters) used in the Rietveld method without prior knowledge of the structure, i.e., the atomic coordinates and the thermal displacements of each atom (isotropic or anisotropic factors). Obviously, other parameters related to the intensity, were not refined. Thus, this method only needs a starting cell and profile parameters (that must be closed to the real parameters). It uses an iterative process to fit the calculated pattern (with sub–index c) to the observed one (with sub–index o) based on a standard least–squares method. Starting to the crudely estimated intensities $I_{c\mathbf{H}}(0)$, the new intensities at cycle $n+1$ are calculated as:

$$I_{c\mathbf{H}}^{n+1} = \sum_i I_{c\mathbf{H}}^n \Omega_{\mathbf{H}}(x_i) \frac{y_0^n(x_i) - y_b^n(x_i)}{y_c^n(x_i) - y_b^n(x_i)} \tag{2.7}$$

Background

Background is often ignored in the analysis of powder diffraction. However, examination of background, especially in the final stages of a profile refinement, is useful. It may reveal features that indicate, for instance, the presence of an amorphous phase or diffuse scattering, pointing the existence of local ordering or clustering in the structure. Background intensity can be estimated by either linear extrapolation between points, where no peaks appear to contribute, or by refining the parameters with empirical polynomials. For modulated background, the Chebyshev polynomials result more robust than the typical Taylor ones. And in some measurements, as for example, those performed under pressure it was only possible to extract points and we

could not obtain information from short- to intermediate–range order. However, in the case of compounds with the property of negative thermal expansion, we could treat the background as though it were from amorphous material, because we have enough resolution by using the Debye scattering equation and the interatomic spacing for first neighbours were calculated (see paper of section 5.6).

Reliability factors

In both least square approaches, Le Bail and Rietveld refinements, parameters defining the model are then refined until the quantity:

$$S = \sum_{i=1}^{N} [y_o(x_i) - y_c(x_i)]^2 \tag{2.8}$$

or a similar expression with an appropriate weighting factor w_i, is a minimum. The summation being over all data points in the diffraction pattern. The quality of the agreement between observed (y_o) and calculated (y_c) profiles in the least squares method is measured by a set of conventional factors:

The profile $R_p = 100 \sum_i |y_{oi} - y_{ci}| / \sum_i |y_{oi}|$,

the weighted profile $R_{wp} = 100[\sum_i |y_{oi} - y_{ci}|^2 / \sum_i w_i |y_{oi}|^2]^{1/2}$,

the Bragg $R_{Bragg} = 100 \sum_k |I_k - I_{ck}| / \sum_k |I_k|$,

the expected $R_{exp} = 100[(N - P + C)/ \sum_i (w_i \times y_{oi}^2)]^{1/2}$,

and the goodness of fit $\chi^2 = (R_{wp}/R_{exp})^2$

where N-P+C is the number of degrees of freedom (N is the total number of points in the pattern less the total number of excluded points, P the number of refined parameters and C the number of strict constraint functions) and w_i is the weights of the observations, calculated as $w_i = 1/\sigma_{oi}$, being σ_{oi} the variance of y_o.

Amplimodes

We have used other version of the Rietveld method, which refines the amplitudes of the atomic displacements with respect to a known structure as fitting parameters instead of the conventional atomic positions. *AMPLIMODES* is the tool that allows to calculate these new parameters (Orobengoa et al. 2009). It is available on the Bilbao Crystallographic Server and it carries out a symmetry–mode analysis. Starting from the experimental structures of the high- and low–symmetry phases, the program determines the global structural distortion that relates both phases. The symmetry modes, compatible with the symmetry break, are then calculated. The program provides the amplitudes of the different symmetry–adapted distortions present in the structure, as well as their corresponding polarization vectors.

The set of structural parameters using the modes description of a distorted phase will be, in general, better adapted for a controlled refinement of the structure or, for instance, for comparative studies between different materials or for *ab initio* calculations. In particular, this analysis has allowed us to study different structural properties of RE molybdates: 1) the driving mechanism of the so-called negative thermal expansion (see paper of section 5.6); 2) The ferroelectric phase with respect the paraelectric one, in terms of two different distortion modes (see paper of section 5.4); and 3) the anomalous behaviour of the thermal evolution for the α-phase by comparing with the more symmetric scheelite phase (see papers of the sections 5.1 and 5.2).

Bond valence

From atomic positions obtained by the Rietveld refinements and theoretical calculations we can calculate bond lengths and angles, as well as polyhedral distortions. In particular, the Bond Valence Model (Brown et al. 1985) was used to study: 1) the temperature dependence of the stability for the structure in modulated scheelite and compounds with negative thermal expansion (see papers of the sections 5.2 and 5.6); and their structures were calculated by the Rietveld refinement; 2) the pressure dependence of the stability for the crystal structure

in modulated scheelite compounds (see paper of the appendix 6.1) and their structures were obtained by *ab initio* calculations; and 3) bond valence sum contour maps to investigate possible paths of ion conduction for modulated scheelite compounds (see paper of section 5.1).

Fullprof program

We chose the suite Fullprof (Rodríguez-Carvajal 1993) set of crystallographic programs (Fullprof, WinPlotr, EdPCR, BondStr, GFourier, FPStudio, etc.) because it is very versatile. It has been used for the Rietveld and Le Bail refinements, to visualize and analysing diffractograms, crystal structures, contour maps; and to calculate geometrical parameters, bond valence sum, etc. Fullprof was the first program to incorporate the refinement of *amplimodes*, taking advantage of the stability of this method to refine crystal structures with a large number of atoms.

2.2.2 Instruments

Powder diffraction techniques have proved to be very useful to characterize $RE_2(MoO_4)_3$ at different conditions of temperature and/or pressure. We have used different types of facilities for conventional X–ray diffraction at the "Servicio Integrado de Difracción de Rayos X (SIDIX)" of University of La Laguna and at the "Centros de Apoyo a la Investigación (CAI)" of University Complutense of Madrid. We have also used larger facilities, as the synchrotron and neutron based sources at Diamond Light Sources (DLS, UK) and at Institut Laue–Langevin (ILL, France), respectively. Thanks to the beamtime granted trough the proposals: 1746, 7758 and 8615 of the beamline *I15* at DLS and 5-24-397 of the beamline *D2B* at ILL. These facilities allowed us to obtain high resolution diffraction patterns of RE molybdates. In the following paragraphs, we will describe the instruments that we have used to collect the diffraction patterns.

We have used two diffractometers at the SIDIX facilities, the PANalytical X'Pert and PANalytical X'Pert Pro (see Figure 2.3). The first one is a conventional diffractometer that collects diffractograms for phase identification and analysis of textures. This diffractometer

Figure 2.3: Photographies of the diffractometers of the SIDIX at the University of La Laguna: PANalytical X'Pert (left) and PANalytical X'Pert Pro (right).

consists in a X–ray radiation generated from a Cu anode supplied with 40 kV and a current of 40 mA. The wavelength of the incident beam is Cu–Kα1,2 after passing through a Ni-β filter. The geometry of the diffractometer is Bragg–Brentano and the diffracted X–rays are detected by reflection. The other diffractometer, the PANalytical X'Pert Pro, allows adjusting their set–up depending on the purpose of the measurement. For instance, we can choose a monochromatic wavelength and to use fixed or variable slits. In our studies, we used a monochromator Si[100] to select only the Cu–Kα1 wavelength (1.54056 Å), a fixed slit and a divergence slit of 1 and 1/2°, respectively. A Xe sealed proportional and X'Celerator detectors were used for each diffractometer, respectively. Measures were collected at different angular range, step size and step time, depending on the detector and the resolution of the experiment (see papers of compendium for more details). We also used other PANalytical X'Pert Pro at the CAI facility, in a similar configuration. In some cases, we used two temperature cameras (Anton Paar HTK-200 and HTK-450) to change the conditions of the sample and collect thermodiffractograms, i.e., to measure in–situ diffractograms of the sample at different temperatures. The range of temperature employed ranged between 150 and 1300 K.

We have also performed several campaigns of powder diffraction measurements. We have

used the *I15* beamline of DLS facility to performed high–pressure powder X–ray diffraction analysis. We used a monochromatic wavelength ($0.485\mathring{A}$ or $0.412\mathring{A}$) and two pressure–transmitting medium: the Dow Corning silicone oil and a 16:3:1 mixture ethanol–methanol–water. We loaded the samples in two different diamond–anvil pressure cells, a Diacell Bragg–Mini and a MiniDac of the University of Paderborn (Germany), both equipped with inconel gaskets. The in–situ pressure was measured using the ruby fluorescence scale (Mao et al. 1978), with the pressure scale recalibrated by Mao et al. 1986. Diffraction data were collected in a pressure range from ambient conditions up to 21 GPa and releasing at selected pressures using a mar345 CCD image plate detector. Exposure time was typically of 5 min. Diffraction patterns were measured at ambient temperature. The angular range did not exceed 30°, because it was conditioned by the pressure cells. Other measurements conditions are given in the papers of section 5.3 and the appendix 6.1.

Neutron diffraction experiment were performed using the neutron powder diffractometer (Debye–Scherrer geometry) at *D2B* beamline of the ILL. We used an incident wavelength of λ=1.5943(1) Å, Ge[335] monochromator, take–off angle 135°, angular range $5° < 2\theta < 165°$ 2θ, without primary collimator and 128 ^{3}He tubes 300 mm in height as the detection system. The sample was placed into an orange top loading cryofurnace installed on the diffractometer and the diffraction patterns were recorded at different temperatures from 150 to 400 K, in a cooling process. Each pattern was collected over 2.5 h. Since these measurements were used to study the hydrated γ–phase, we needed to ensure their total dehydration before measuring it. To do that, we placed the samples about 8 h in a furnace at 423 K inside a vanadium container and, after that, we closed quickly the container. Around three hours were necessary for collecting data of each sample at the selected temperature.

As summary, we first performed powder XRD measurements of RE molybdates at constant temperature changing the pressure. Then, we used neutron diffraction to study the properties of RE molybdates at constant pressure changing the temperature. Measurements of RE molybdates with simultaneous changes of pressure and temperature are not available yet.

2.3   Impedance spectroscopy

Impedance spectroscopy has become an important tool for characterizing the electric properties of materials. It can be used to investigate the dynamics of bound or mobile charge in the bulk or interfacial regions of any kind of solid or liquid material: ionic, semiconducting, mixed electronic–ionic, and even insulators (dielectrics).

The fundamentals of impedance spectroscopy were described by Macdonald et al. 2005. This technique is based on the application of an electrical stimulus (a known voltage V_m) to a sample by means of two electrodes. After that, it is examined the response (the resulting current or voltage) of the sample to the electrical stimulus. A multitude of microscopic processes take place throughout the sample when it is electrically stimulated. They include ionic and dipolar relaxation or atomic and electronic resonances at higher frequencies (see Figure 2.4). In order to use this technique is necessary an impedance bridge. It is a commercial device that can measure several impedance parameters in the frequency range from millihertz to megahertz. For that
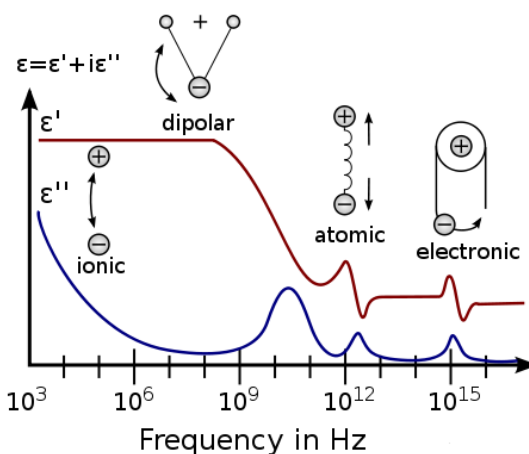

Figure 2.4:   Dielectric permittivity spectrum over a wide range of frequencies. The real (ϵ') and imaginary (ϵ") parts of the complex permittivity are showed, and various processes are depicted: ionic and dipolar relaxation, and atomic and electronic resonances at higher frequencies.

reason, the response of the sample to the sinusoidal voltage is studied at a large interval of frequencies. The impedance bridge is connected to a cell, which can adopt circular cylinder or rectangular parallelepiped shape, and contains two identical electrodes. Such electrodes allow to apply the voltage to the faces of the sample.

The conventional impedance spectroscopy measures the impedance of the cell–sample set by applying a single–frequency voltage to the plane parallel faces of the sample and measuring the phase shift and amplitude of the resulting current at that frequency. We can use either the analogue circuit or the fast Fourier transform (FFT) analysis to characterize the properties of the induced current. The voltage and the current displayed by the sample can be express as:

$$V(t) = V_m sin(\omega t) \tag{2.9}$$

$$I(t) = I_m sin(\omega t + \theta) \tag{2.10}$$

where ω is the angular frequency ($\omega = 2\pi\nu$) and θ is the phase difference between the voltage and the current. The relation between the properties of the sample and its response to the applied periodic voltages or currents is very complex in the time domain. For this reason, we use the Fourier transformation to simplify the mathematical treatment of this analysis.

In the following, we are going to define and relate some physics variables that we will use in our studies. Impedance may be defined by as:

$$Z(\omega) = \frac{F\{V(t)\}}{F\{I(t)\}} \tag{2.11}$$

where $F\{\}$ operator denotes a Fourier transform. The impedance is a complex number of the form $Z(\omega) = Z' + iZ''$, where $i = \sqrt{-1} = exp(i\pi/2)$, and their polar coordinates are

$$Z' = |Z|cos(\theta) \tag{2.12}$$

$$Z'' = |Z|sin(\theta) \tag{2.13}$$

46

with phase angle and modulus

$$\theta = tan^{-1}(Z''/Z') \tag{2.14}$$

$$|Z| = [(Z')^2 + (Z'')^2]^{1/2} \tag{2.15}$$

The conventional impedance spectroscopy measures Z as a function of ν or ω over a wide frequency range. There are several functions that can be defined from the impedance, such as the modulus function ($M = i\omega C_c Z = M' + iM''$) and the dielectric permittivity ($\varepsilon = M^{-1} = Y/i\omega C_c = \varepsilon' - i\varepsilon''$) where Y is the admittance, $C_c = \varepsilon_0 A_c/l$ is the capacitance of the empty measuring cell of electrode area A_c, and electrode separation length l, and ε_0 is the dielectric permittivity of the free space 8.854×10^{-12} F/m.

The measurement and use of the complex ε function is particularly appropriate for dielectric materials, i.e. those with very low conductivity. If we consider a capacitor that has as medium a dielectric material (sample), when we apply an electric field over it, the total density current will be $\overrightarrow{J} = \overrightarrow{\nabla} \times \overrightarrow{H}$, according to the Maxwell equation. Such current has two interactions due to the conduction current and displacement current. Thus, it can express as:

$$\overrightarrow{J} = \overrightarrow{J}_{cond} + \overrightarrow{J}_{desp} = \sigma\overrightarrow{E} + \frac{\partial \overrightarrow{D}}{\partial t} \tag{2.16}$$

where D is the electric displacement and $\overrightarrow{E}$ is the electric field also defined as $\overrightarrow{E}(t) = \overrightarrow{E}_0 exp^{i\omega t}$. Taking account the constitutive relation:

$$\overrightarrow{D}(\omega, t) = \varepsilon^*(\omega)\overrightarrow{E}(\omega, t) \tag{2.17}$$

where $\varepsilon^*(\omega)$ is the conjugate of complex permittivity for a frequency ω, defined as $\varepsilon^*(\omega) = \varepsilon'(\omega) - i\varepsilon''(\omega)$. On the other hand, making use of the complex notation, we can write the complex conductivity as $\sigma = \sigma' + i\sigma''$.

We can rewrite the equation 2.16 as

$$\overrightarrow{J} = \{\sigma' + \omega\varepsilon'' + i\omega\varepsilon'\}\overrightarrow{E} \tag{2.18}$$

At the low frequency range, we assume that σ'' is negligible compared to σ'. In particular, σ'' is null for $\omega = 0$ and σ' is equal to DC conductivity (σ_{dc}). This consideration allows us to define the real part of the total complex conductivity for a given frequency as

$$\sigma'_t(\omega) = \sigma_{dc} + \omega\varepsilon''(\omega) \tag{2.19}$$

and, consequently, the conjugate of the complex dielectric permittivity measured by a impedance bridge can be expressed as

$$\varepsilon^*(\omega) = \varepsilon_\infty + \varepsilon'(\omega) - i\left[\varepsilon''(\omega) + \frac{\sigma_{dc}}{\omega}\right] \tag{2.20}$$

2.3.1 Data analysis

In this work, we are more interested in the frequency and temperature dependence of the electrical conductivity. Our conductivity spectral analysis is based on the Universal Dielectric Response behaviour (Jonscher 1983), as an empirical power law that can describe the frequency and temperature dependence of the dielectric response in a wide range of ionic or semiconductors materials: from glasses to crystals. Particularly, we will fit the real part of the conductivity to the equation:

$$\sigma'(\nu) = \sigma_{dc} + A\nu^s \tag{2.21}$$

where σ_{dc}, A and s are the parameters adjusted at each temperature. The variation of the logarithm of the dc conductivity (σ_{dc}) can be plotted versus 1/T, in order to know if the electrical conduction, in our materials, is a thermally activated process. The activation energy can be calculated from the Arrhenius relation. The parameter s is a fractional exponent with

values between 0 and 1, where any deviation from unity discloses information on the particular type of loss mechanism.

As general rule, for dielectric materials, conductivity at low temperatures is due to impurity defects and mixed states, and the electronic or hole conduction (extrinsic) is more frequency–dependent than the ionic conduction (intrinsic), normally at higher temperatures. However, temperature dependence of the ionic conduction is normally larger. Moreover, a strong dependence on temperature and frequency suggests a polaronic conduction and it is possible to model this dependence. In particular, there is a variety of theoretical approaches that deduce the temperature and frequency dependence of the s exponent from microscopic transport mechanism; involving the classical hopping of a carrier over the potential barrier and the quantum–mechanical tunnelling through the barrier separating two equilibrium positions (Elliott 1987). In figure 2.5 is represented the thermal dependence of the s parameter for different models. Thus, specifically for the overlapping large polaron (OLP) model, the energy barrier (W_H), polaron radius (r_p) and tunnelling distance (R_W) parameters can be obtained from the fit of this model to the experimental curves of s.

On the other hand, the conductivity spectra σ, at different temperatures, can be scaled according to the following equation:

$$\frac{\sigma'}{\sigma_{dc}} = F\left(\frac{\nu}{\nu^\star}\right) \tag{2.22}$$

where $\nu^\star$ can be used as the scaling parameter with the advantage that it is a directly accessible quantity. The dc conductivity has been calculated from the UDR fitting. It is found that the curves for some interval of temperatures collapse on a single master, indicating that the relaxation dynamics of charge carriers is independent of temperature at this region. Typically, for ionic conduction, the concentration of charge carriers is weakly temperature dependent, which in turn arises from the mobility of the ions (Ghosh et al. 2000). Then, it is possible to calculate this concentration, which must be the same for each temperature, and to confirm
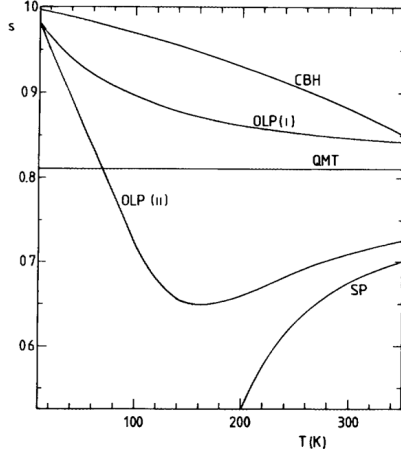
49

Figure 2.5: Temperature dependence of the frequency exponent *s* for different models for ac conduction: correlated barrier hopping (CBH), quantum–mechanical tunnelling (QMT), small polaron (SP) and overlapping large polaron (OLP). For the cases of SP and OLP values of W_H=0.2 and 0.26 eV respectively have been used. For CBH W_M=1.85 eV has been used. In all cases ω_{τ_0}=10^{-9} has been assumed.

that the charge carriers are ions.

2.3.2 Instruments

The impedance spectroscopy measurements were carried out using a Hewlett–Packard 4192A impedance analyser that measures the total impedance of the cell–sample. This equipment uses a frequency range from 5 Hz to 13 MHz and allows to vary the voltage amplitude of the electric stimulus between 5 mV and 1.1 V.

The cell used to examine the dielectric properties of the sample consists of a parallel plate capacitor located at the end of a coaxial line. A diagram of the cell can be seen in Figure 2.6, where all its parts are labelled. In order to determinate the permittivity of the sample, we have to calculate the response of the system to the external voltage at each frequency and the admittance of the cell. To do that, we need to calibrate the instrument connecting different elements at the end of the coaxial line (open end $R = \infty$ Ω, a short cut $R = 0$ Ω and a 50 Ω
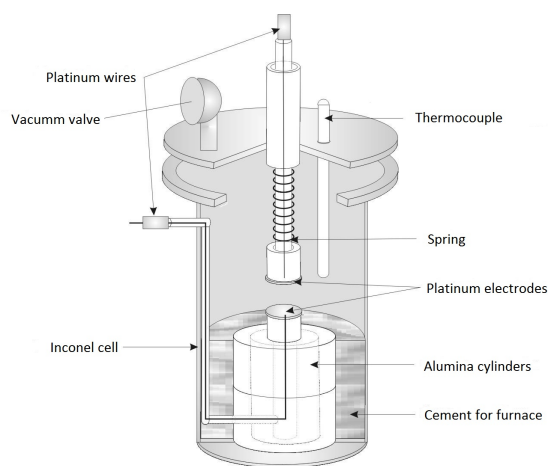
Figure 2.6: Diagram of the cell used in impedance spectroscopy.

resistor). After that, we can calibrate the cell using reference samples. The permittivity of these samples are well known for the whole range of frequencies and temperatures available.

After the instrumental calibration, the next step is the preparation of the sample. In our case, the sample is in form of pellet and its faces should be as flat as possible to ensure the contact between the electrodes and sample. We then cover the two parallel faces of the sample with a platinum paste to improve the contact with the electrodes. This paste needs a specific heat treatment to favour its adhesion to the sample. This heat treatment consists in heating the sample previously covered with platinum paste at 1023 K for 30 min and back to ambient temperature with a high cooling rate (500 K/h approximately). Finally, the cell–sample set was enclosed in a resistance–heated furnace and the temperature was monitored using a thermocouple K–type within an accuracy of ± 0.1 K. Figure 2.7 shows the experimental set–up used. The measurements of the dielectric permittivity were recorded during a heating and cooling cycle over the temperature range from 500 to 900 K, which was dynamically scanned (at a rate of 1.2 K/min) with measurements taken in steps of 5 K. These studies can elucidate information about the mechanisms of transport in the sample and if the conduction current changes with temperature. We also analyse if there is any structural change at the temperature

51
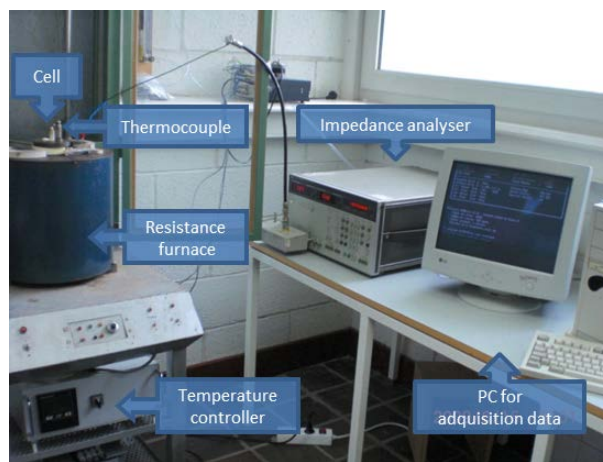
Figure 2.7: Experimental set–up to analyse a sample by impedance spectroscopy at high temperatures.

range studied.

2.4 Optical spectroscopy

The different parts of the electromagnetic spectrum have very different effects upon interaction with matter. Starting with the high frequency (high energy) waves, the matter become transparent and only a small fraction of the radiation is absorbed, but that absorption involves violent ionization events. However, other effects are very important for the study of the matter too, for instance, we have seen how X-rays used for diffraction experiments with wavelength in the approximate range 0.1-5 Å (equivalent to a an energy range of about 125-2.5 keV) are diffracted by crystals (elastic and coherent scattering). As the wave frequencies down into the ultraviolet region until the infrared one, the absorption increases and other different processes happen in the matter. The study of the optical properties of a sample through its interaction with the electromagnetic radiation (light) in this range of frequencies is known as optical spectroscopy.

In Figure 2.8, the sample is illuminated using incident light with intensity I_0. Part of the light will be reflected (I_R), scattered (I_S), absorbed (I_A) and transmitted (I_T). Note that the
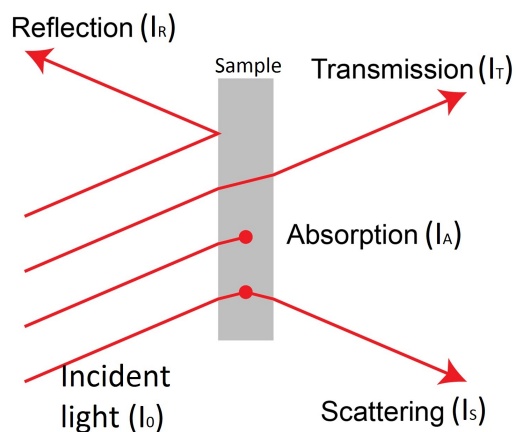
Figure 2.8: Types of processes that appear when the sample is illuminated with a electromagnetic radiation.

transmitted light also can be scattered and refracted. Each one of these processes depends on the composition of the sample and the frequency of the radiation of the incident light. The dependence of these variables is contained on the known factors as transmittance, reflectance and absorbance. However, inelastic scattering, selective absorption and emission (luminescence) can occur too; thus, optical spectroscopy can give information about energy transitions in solids among electron and phonon levels and bandgaps. We have focused on absorption and emission spectroscopies and, separately, on Raman spectroscopy.

2.4.1 Absorption and emission spectroscopies

Absorption spectroscopy studies the absorption of radiation, as a function of frequency or wavelength, due to its interaction with a sample. The sample absorbs energy, i.e., photons, from the radiating field changing the population of its electronic or vibrational levels. The intensity of the absorption varies as a function of frequency, and this variation is obtained in the absorption spectrum, in which it can be observed the absorption bands. On the contrary, emission spectroscopy analyses the light that the sample emits when it is previously excited with

a light source, i.e. the electrons de–excited from the excited levels to the ground state emitting photons, thus producing an emission spectrum with bands (discontinuous spectrum). These bands correspond with the energy difference between two electronic states or vibrational of the atom or molecule. The frequency ranges in which we performed our investigation correspond to the optical range (UV–Vis–NIR).

In particular, we will analyse the absorption and emission spectroscopy of the RE ions. The lanthanide series, associated to the filling of the $4f$ inner shell, covers from the Cerium (Z=58) to Lutetium (Z=71) elements. The neutral lanthanides share the electronic configuration of Xenon (Z=54) plus two or three electrons in the $5d$ and $6s$ shells. Specifically, the f–electrons begin to appear in the ground configuration of the optically active trivalent lanthanide ions (Pappalardo 1978). The optical properties and the energy level diagram of a trivalent lanthanide ion in a solid are ruled by the inter-electronic interaction between the electrons of its incompletely filled inner $4f$ shell and the charge of the host ligands, all distributed in a particular local point symmetry. This information is useful to characterize the energy levels associated to the $4f$ electrons. The absorption peaks will be assigned according to Dieke's diagram (see Figure 2.9). In addition, we will use the dependence of oxygen ions surrounding the RE ions, on the emission spectrum; in order to analyse modifications on the crystal structure that the changes in pressure produce. The Judd–Ofelt theory explains the dependence of the surrounding of the RE ions and the radiative probability (Judd 1962; Ofelt 1962). That means, the emission spectrum varies as a function of the type and numbers of ligands that surround to the RE^{3+} ions forming their first coordination sphere, as well as their distance and bond–angles distributions. Moreover, among the RE ions, Eu^{3+} ion has a relatively simple diagram of levels, which consists in seven ^7F_J (J=0–6) multiplets well separated (around 12000 cm^{-1}) from the ^5D_J (J=0–4) ones and other strongly overlapped excited multiplets above the $^5D_3$ state at around 25000 cm^{-1}. The ground $^7F_0$ level and the lowest emitting $^5D_0$ level are non-degenerated, making easier the identification of the peaks between Stark levels of the multiplets. Thus high–pressure optical spectroscopy have been performed in crystals using the Eu^{3+} ion as local structural probe.
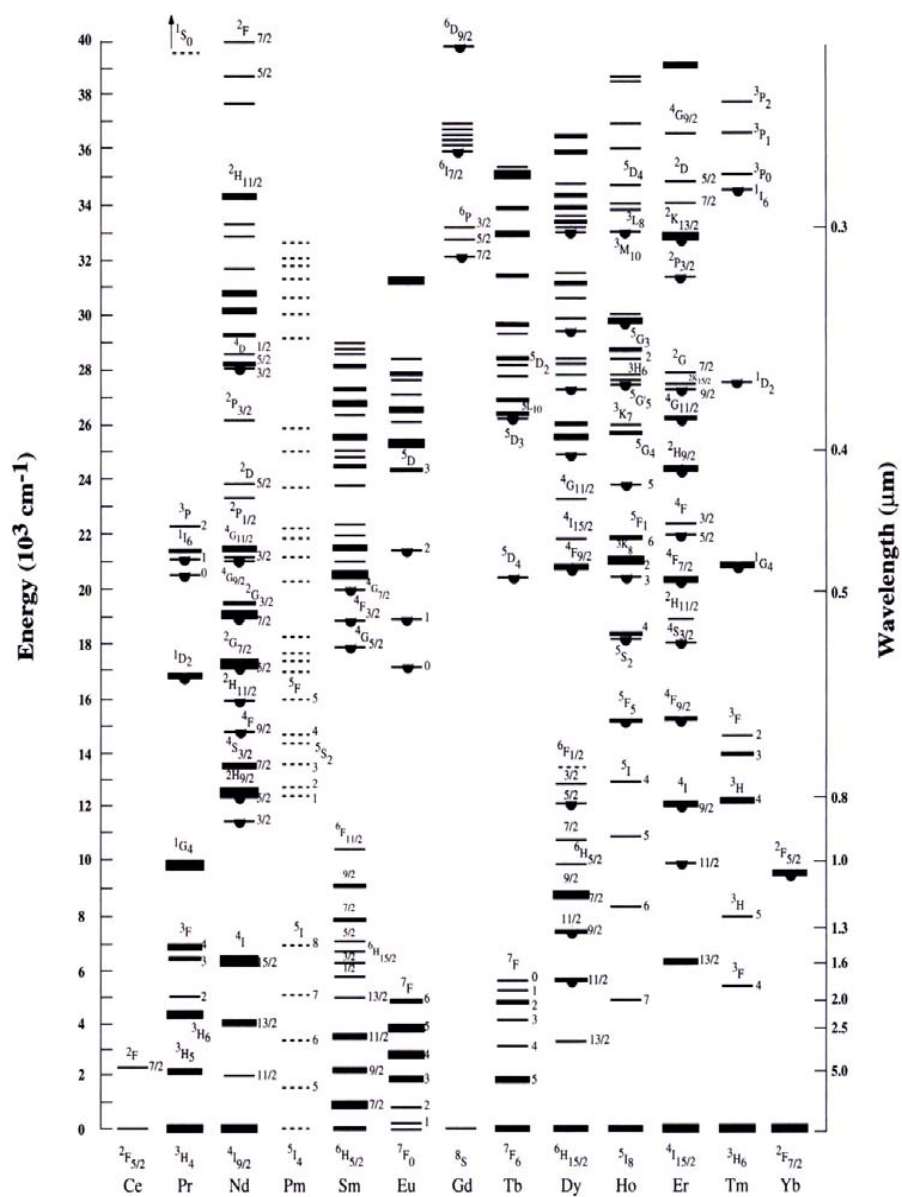
Figure 2.9: Diagram of energy levels of the different trivalent lanthanide ions in LaCl₃ crystal.

Once an absorption process has been taken placed, there are two different mechanisms of returning to the ground state: radiative and non–radiative processes. The radiative, or luminescence, process involves a de–excitation of the lanthanide ions from the excited state back to the ground state by the emission of photons of equal or less energy than those absorbed by the lanthanide ions. Moreover, the energy of the emission must be, as in the absorption case, resonant with the energy of a transition between two energy levels. The non–radiative process occurs when the energy absorbed by the optically active ions is not emitted as radiation of photons but dissipated in the solid. Two different processes may account for this radiationless de–excitation. On one hand, an interaction between the lanthanide ions and the vibrating lattice allows the optically active ion to lose its energy and return to the ground state, i.e. the multiphonon relaxations. On the other hand, if the distances between optically active ions in the solid are short enough and the emission and absorption bands overlap in energy, a very efficient transfer of the energy from the excited lanthanide ions, called donors, to other non–excited lanthanide ions, called acceptors, takes place. In principle, all the excited states of the lanthanide ions can emit photons. However, luminescence from many of these energy levels are only observed at low temperature or in those host matrices with low–phonon energies, due to the strong competition of the efficient non–radiative de–excitation processes.

Instruments

The diffuse reflectance spectrum is equivalent to the absorption spectrum, but without absolute values of intensity. A surface built from a polycrystalline material reflects light diffusely rather than at just one angle as in the case of specular reflection. The spectra were measured using a standard Cary 6000i UV–Vis–NIR spectrophotometer, at the University of Cantabria in Spain. To prepare the measurements, we finely ground the sample in form of pellets using an agate mortar. After that, the powder was placed over a plate and was compacted using a microscope slide (see Figure 2.10). The reference spectrum was collected and subtracted automatically for all measurements. The measurement range selected was from 200 to 1800 nm, with a

Figure 2.10: Cary 6000i UV–Vis–NIR spectrophotometer (left) and the type of plate used in this instrument (right) in order to obtain the diffuse reflectance spectra of a sample.

step of 0.2 nm and averaging time of 0.2 s. All the measurements were performed at ambient conditions.

The emission spectra were recorded with a Spex 75 cm monochromator equipped with Hamamatsu R928 photomultiplier tubes (spectral resolution of 0.1 nm). Room–temperature fluorescence spectra of Eu^{3+} ions in α–$Eu_2(MoO_4)_3$ were obtained by excitation of the sample using a 405 nm laser diode. The experiment was were carried out in a pressure range from 0 to 14.6 GPa (see Figure 2.11), using the same Mini–DAC as in the diffraction experiments, and a mixture of methanol–ethanol–water (16:3:1). Pressures were determined by the ruby
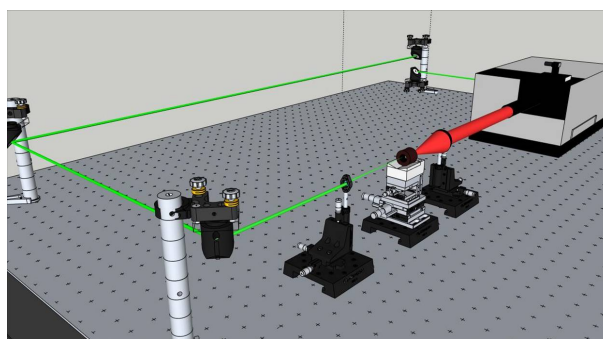

Figure 2.11: Experimental set–up to measure emission spectra at high pressure and ambient temperature.

fluorescence method (Mao et al. 1986).

2.4.2 Raman spectroscopy

As already mentioned, the light can be scattered by the matter. The Raman scattering is an inelastic interaction since the scattered photons have the wavelength shifted to higher or lower wavelengths with respect to the incident photon's wavelength. These shifts in energy (the wavelength is inversely proportional to the energy) give information about the vibrational modes in the system.

The photons with less or more energy provide two parts of the Raman spectrum known as Stokes and anti–Stokes bands, respectively. These bands are characteristic of the sample. The band positions of the Stokes and anti–Stokes scattering patterns are symmetric to the so–called Rayleigh line peak and less intense. The Rayleigh line corresponds to the classical elastic Rayleigh scattering due to the interaction of photons with the harmonically bound electrons. This line is useful to build a relative scale in which the zero wavenumber (in cm^{-1}) correspond to the peak position relative to the Rayleigh scattering. The regions of the scattering spectrum, close to the Rayleigh scattering peak, are referred as Stokes bands (wavenumber with positive relative values) and the anti–Stokes ones (wavenumber negative relative values).

Figure 2.12 displays a schematic energy level diagram of the processes that takes place during Raman and Rayleigh scattering. If we focused on the Stokes bands we can see that they are the results of two transitions, one from a ground vibrational state to a virtual energy level, and the second transition from this virtual energy level to first excited vibrational state. Thus, the scattered photons have less energy than the incident photons. On the case of anti–Stokes bands, the first transition starts on the first exited vibrational state and the second one finishes on the ground vibrational state. Therefore, the scattered photons have more energy than the incident photons. Finally, we can see that the Rayleigh scattering line correspond to the two transitions without change of vibrational state and without change of photon's energy. The probability of the occurrence of a Stokes process is higher than in the case of anti–Stokes
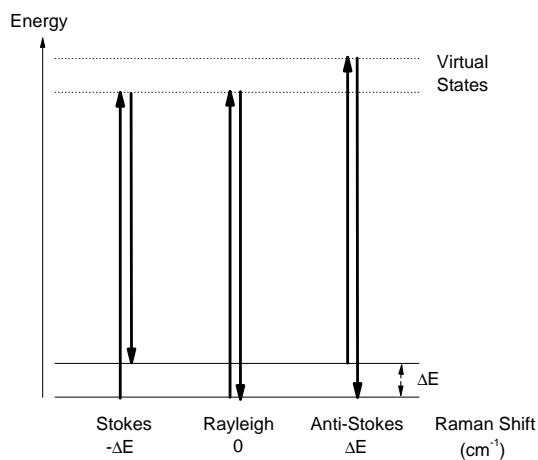
Figure 2.12: Schematic energy level diagram illustrating the processes that occur during Raman and Rayleigh scattering.

because systems are generally initially in the ground state. Consequently, the intensity of the Stokes signals is also generally higher. Therefore, in general, Raman spectroscopy studies focus on Stokes signals.

Raman spectroscopy is a commonly technique employed to study the bonding and structure of amorphous and crystalline systems. In particular, Raman spectroscopy experiments in a diamond anvil cell (DAC) provide an appropriate way to investigate the effect of pressure on the vibrational modes in polycrystalline solids. These vibrational modes produces a single scatter pattern at each pressure. In these pressure experiments, we study how the Raman spectra change, analysing the shift of the peak positions.

Instruments

We performed the Raman spectroscopy analysis at the "Universidad Politécnica de Valencia" and in the Raman Laboratory of the Beamline *I15* at Diamond Light Source (DLS). We performed in the Spanish laboratory high–pressure Raman experiments of powder α–$Eu_2(MoO_4)_3$ samples at ambient temperature. The experiment was carried out in backscattering geometry,
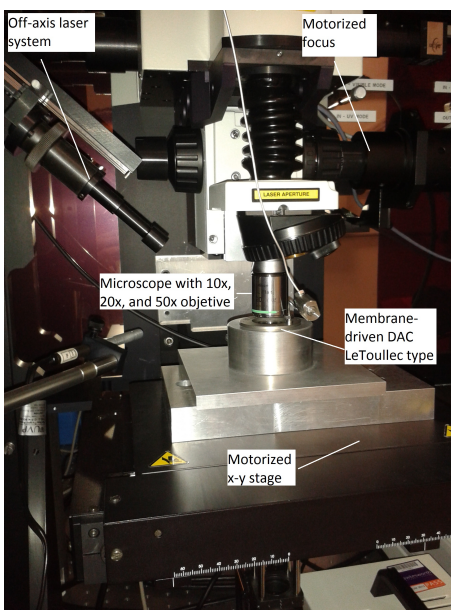
Figure 2.13: Photograph of a standard membrane–driven DAC LeToullec type in the experimental set–up to measure Raman spectra at high pressure.

exciting with a HeNe laser excitation at 633 nm with an incident power of 10 mW and using a HORIBA Jobin Yvon LabRAM HR UV spectrometer in combination with a thermoelectrically cooled multichannel CCD detector with a resolution below 2 cm^{-1}. The beam was focused on the sample using a $50\times$ objective with a beam diameter of approximately 2 μm at the sample. The sample was placed in a membrane–type DAC together with a mixture of methanol–ethanol–water (16:3:1) as pressure–transmitting medium and the pressure was determined by the ruby fluorescence technique using the pressure scale recalibrated by Mao et al. 1986. The diamond culet size was 400 μm and the gasket hole size was 150 μm. The background of the experimental Raman spectra was subtracted and the vibration modes were analysed by fitting the Raman peaks with a Voigt profile.

We then performed at the DLS the Raman spectroscopy measurements of powder samples at ambient temperature. We employed a HORIBA Jobin Yvon LabRAM HR800 Micro–Raman
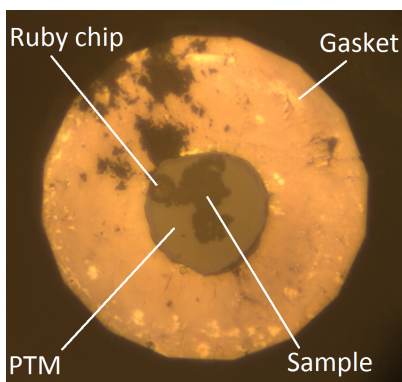
Figure 2.14: Photograph of β'–$Tb_2(MoO_4)_3$ between two diamond anvils in gasketed configuration. The sample, pressure–transmitting medium (PTM), ruby chip and gasket as observed under a microscope by focusing through one diamond anvil.

spectrometer. The experiments were performed in backscattering geometry using the laser excitation at 532 nm with a power of less than 10 mW before the DAC to avoid heating sample. We collected the Raman spectra using a grating of 1200 line/cm, with the frequency range divided in two intervals, one centred at 450 cm^{-1} and the other at 700 cm^{-1}. A total of fourteen samples were measured at ambient pressure. For that purpose, the samples were previously deposited over a microscope slide. From the total number (thirteen) of samples, five of them were chosen to be analysed under high–pressure conditions. We loaded them into two kind of DACs: a standard membrane–driven DAC LeToullec type made by Betsa (see in Figure 2.13) and a mechanical DAC of Syassen–Holzapfel type. Both DACs were equipped with steel gaskets using two type of pressure–transmitting medium: NaCl and a 4:1 mixture of methanol–ethanol. Pressures were determined by the ruby fluorescence method, like in the previous experiment. The diamond culet size was 300 μm and the gasket hole size was 150 μm. Figure 2.14 shows a photograph taken from the camera of the microscope that is used for the Raman spectroscopy measurements. This photograph display the sample loaded in the DAC together with the pressure–transmitting medium and the ruby chip in gasketed configuration.
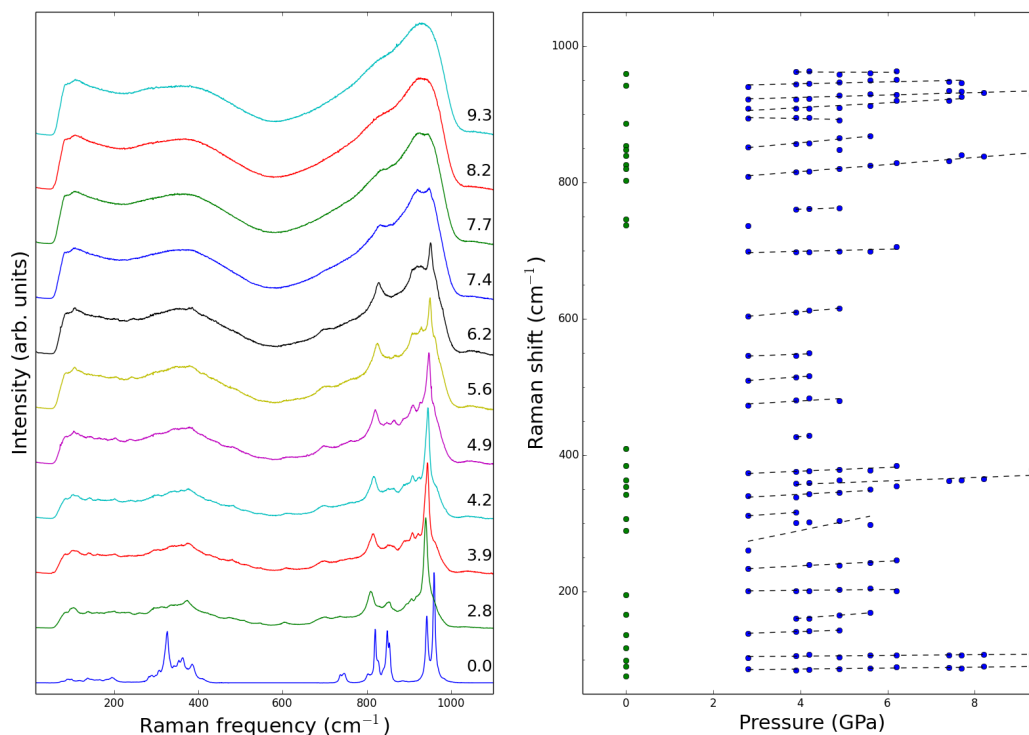
Figure 2.15: Raman spectra (left) and Raman modes (right) of β'–$Tb_2(MoO_4)_3$ during compression from ambient pressure up to 9.3 GPa. Pressure values in GPa units are showed on top of each individual spectre.

In Figure 2.15(left), is showed, for instance, Raman spectra collected at different pressures. In the same figure (right), the corresponding frequencies of their modes, have been extracted by fitting the peaks with a Lorentzian profile. These experimental values of frequencies can be compared with the theoretical ones, obtained by first principle calculations.

2.5 Thermal analysis

The thermal analysis is a group of physical–chemical methods that deal with studying materials and processes in conditions of the temperature programmed changing. These methods are distinguished from other by the specific property that is measured. We are interested in the anal-
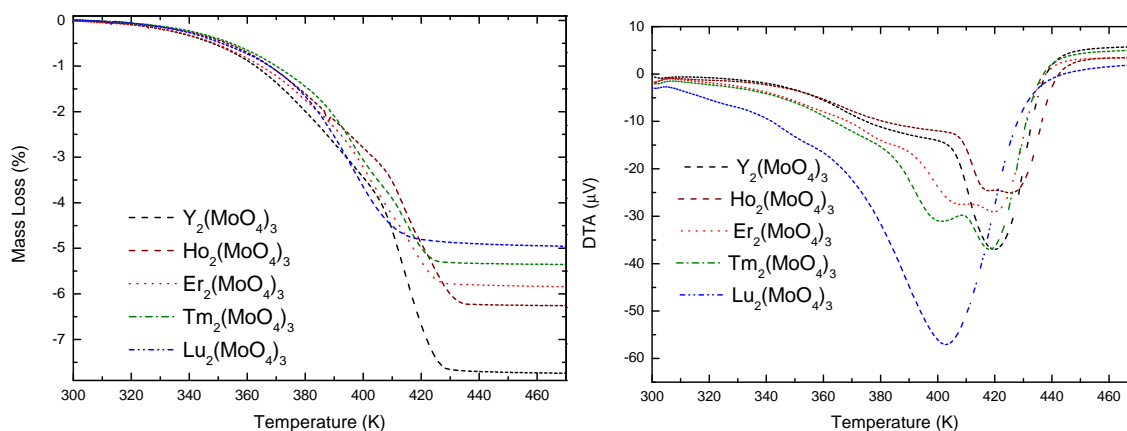
Figure 2.16: TGA (left) and DTA (right) curves for yttrium and RE molybdates. The hydrated molybdates lose the water of hydration from ambient temperature to 430 K.

ysis of the thermal stability of our samples, affected by water loss, crystalline-crystalline phase transitions and melting. For that, we have focused on the simultaneous thermogravimetric–differential thermal analysis (TGA–DTA) and the differential scanning calorimetry (DSC). The use of these techniques must be prior to perform temperature–dependent powder diffraction and dielectric spectroscopy.

TGA is a method in which the mass change of a material are measured, in a controlled atmosphere, as a function of temperature. The first derivatives of TGA is usually plotted to determine points of inflection for more in–depth interpretations. An example of mass changes can be found in Figure 2.16, in which the X–axis represents the different temperatures applied to the sample and the Y–axis mass loss suffered by the sample. In this case, the curves represent the TGA of the γ–hydrated molybdates. These compounds loss waters at 430 K, after this temperature they reach the γ–phase.

Respect to DTA method, it is necessary to use an inert material that will be exposed to the same conditions as the sample of study. They will undergo identical thermal cycles while we record the temperature values of both samples. As they differently react to temperature changes

we will obtain a differential temperature between both samples. If we plot this differential temperature versus the temperature applied to the samples we will have a DTA curve or thermogram. This thermogram can help us to identify the nature of the changes suffered by the sample, either exothermic or endothermic, comparing its behaviour with inert reference. Those changes are represented by peaks in the DTA curve. Thus, those peaks provide information of the transformations that have occurred in the sample, such as glass transitions, crystallization, melting and sublimation. DTA curves are showed in Figure 2.16 (right), in which the X-axis represent the temperature applied and the Y-axis differences of temperatures in microvolts. Two peaks indicate that waters are not removed at the same time for some compounds.

The method of DSC is similar to DTA, because we also need a sample of reference. In this case, we measure the difference in the amount of heat required to increase until the same temperature the sample under study and the sample of reference. Both samples are maintained at nearly the same temperature throughout the experiment. Generally, the temperature program for a DSC analysis is designed in such a way that the sample holder temperature increases linearly as a function of time. The reference sample should have a well–defined heat capacity over the range of temperatures to be scanned. From a DSC experiment we obtain the heat flux versus temperature, thus, this curve can be used to calculate enthalpies of phase transitions.

2.5.1 Instruments

The equipments of TGA–DTA and DSC that we used are placed in the "Servicio de análisis térmico" at SEGAI facility. The TGA and DTA curves were recorded from ambient temperature to 1223 K using a Perkin Elmer Pyris Diamond TGA–DTA balance, under nitrogen gas, with a heating rate of 10 K/min. DSC measurements were carried out in a Perkin–Elmer differential scanning calorimeter Pyris I–DSC from ambient temperature, with two sequential cycles of heating up to 673 K and cooling to 100 K, under nitrogen atmosphere. The heating and cooling rates were 10 K/min.

2.6   *Ab initio* calculations

In last decades the *ab initio* calculations have been developed and improved for the study of matter. In particular, the methods based on the Density Functional Theory (DFT) has demonstrated its usefulness to deal all type of properties, thanks to several approximations that make them computationally possible. In the area of the condensed matter, there is an important branch dedicated to high–pressure studies. The control of this variable allows to understand the role of forces inside of solid, by means of the analysis of the structural changes that take place when the volume of the sample is reduced. This type of changes are reflected on many properties of these systems, which show a interesting behaviour and characteristic to their composition.

First–principles total energy calculations have been performed within the framework of the density–functional theory (DFT) (Hohenberg et al. 1964) using the Vienna *ab initio* simulation package (VASP) (Kresse et al. 1996, 1999). Calculations were carried out with the pseudopotential method and the projector augmented wave (PAW) scheme (Blöchl 1994). Pseudopotentials replace the core electrons but take into account the full nodal character of the all–electron charge density distribution in the core region and make smoothed pseudovalence wave functions which include explicitly in the calculation only the outermost electrons of each atomic species. DFT explains that inside of a solid no all electrons of the atoms has the same contribution with respect to their electronic properties. So, electrons that are in full levels are more ligated to the nucleus, building the core that is not affected by the surrounding chemical environment. On the contrary, the electrons from non–fulfilled external levels are very sensitive to the surrounding and this distribution suffers a large change if the atomic configuration is modified. These external electrons, called valence electrons, provide to solids their characteristic structural properties.

The exchange–correlation energy is a function that only depends on the density of every point of the crystal, that means, that is a function of the local density and changes spatially

65

of continuous form. It is an idealization of the crystal, as well as the possible vibration of the atoms is not taken account. The exchange–correlation energy was taken in the generalized gradient approximation (GGA) with the PBEsol (Perdew et al. 2008) prescription. It is known that standard DFT does not work properly for strongly localized f electrons (Hafner 2008; Pickard et al. 2000). Therefore, we use the GGA + U (U=4 eV) method to account for the strong correlation between the Eu f electrons on the basis of the Dudarev's method (Dudarev et al. 1998). Highly converged results were achieved by extending the set of plane waves up to a kinetic energy cutoff of 520 eV. A dense Monkhorst–Pack grid, of 3×3×2 k–special points, was used to perform integrations along the Brillouin zone (BZ) in order to obtain very well converged energies and forces. The structural configurations were fully relaxed at each volume through the calculation of the forces on the atoms and the components of the stress tensor (Chetty et al. 1989). In the relaxed configurations, the forces on the atoms are less than 0.006 eV/Å and deviations of the stress tensor from a diagonal hydrostatic form are less than 0.1 GPa. It should be noted that, in the DFT formalism, the theoretical pressure P(V) is obtained from the calculated stress (Mujica et al. 2003). Zero point motion and temperature effects were not included in the calculations.

Lattice–dynamics calculations were performed at the zone centre (Γ point) of the BZ using the direct force constant (or supercell) approach (Parlinski 2008). Highly converged results on forces are required for the calculation of the dynamical matrix using this method. The construction of the dynamical matrix at the Γ point of the BZ involves separate calculations of the forces in which a fixed displacement from the equilibrium configuration of the atoms within the primitive cell is considered. The number of such independent displacements in the analysed structures can be reduced taking into account the crystal symmetry (Nye 1957). The diagonalization of the dynamical matrix allows obtaining the frequencies of the Raman modes. Moreover, these calculations identify the symmetry and eigenvectors of the vibrational modes in each structure at the Γ point.

Chapter 3

Results and discussion

In this chapter, we summarize the most important results and the discussion of the work presented in this thesis. We decided to classified these results in three different sections. In the first one, i.e. section 3.1, we show the results of the electrical and structural studies performed in RE molybdates with α–phase at high temperatures. In the following section, section 3.2, we describe the analysis of the α- and β'–phases under high pressure. Finally, in section 3.3, we report a structural analysis of the β'- and γ–phases at different temperatures.

3.1 Electrical and structural studies of the α–phase at high temperature

We have analysed the thermal dependence of the crystal structure and the dielectric properties for the α-phase in $Sm_2(MoO_4)_3$ and $Eu_2(MoO_4)_3$ (see sections 5.1 and 5.2). From theses analyses we have correlated, for the first time, the thermal dependence of the electric properties in these compounds with the thermal evolution of the crystalline structure.

We performed an electric characterization of the α–phase of $Sm_2(MoO_4)_3$ and $Eu_2(MoO_4)_3$ using impedance spectroscopy in the temperature ranges from 500 to 900 K and from 400 to 970 K, respectively. We analysed the real part of the complex conductivity $\sigma'(\nu)$ by fitting it

to the Universal Dielectric Response (Jonscher 1983; León et al. 1997) for each temperature (see section 2.3.1 for more details).

If we focus on the $Sm_2(MoO_4)_3$ compound (the $Eu_2(MoO_4)_3$ sample presents similar results) we detected that $\sigma'(\nu)$ exhibits the UDR from 525 to 905 K (Figure 1b of section 5.2). Then, we obtained the DC conductivity σ_{dc} and the frequency exponent s in that temperature region. The plot of log σ_{dc} versus T^{-1} exhibits an Arrhenius–type temperature dependence (Figure 2 of section 5.2). We observed three expected linear regions with two break temperatures, T_1 and T_2 at 638 and 688 K, related to changes in the conduction mechanisms.

On the other hand, we also studied the structural properties of the α–phase in $Sm_2(MoO_4)_3$ and $Eu_2(MoO_4)_3$ using X–ray diffraction. In order to obtain the cell parameters we refined them using the Le Bail method (Le Bail 2005) (see section 2.2.1 for more details). A first analysis, using thermodiffractometry from 300 to 1000 K, showed that the volume of the cell expands lineally in the whole temperature range, although the lattice parameter a displayed an anomalous temperature dependence (see Figure 3.1(c-d)). The complex behaviour of the parameter a reveals three different regions corresponding to the three conduction regimes. Figure 3.1 shows this correlation from experimental values of $\sigma'(\nu)$ and the thermal dependence of parameter a and even the volume expansion (note that in Figure 3.1 the independent variable is plotted as the temperature inverse). Following, we explain the different types of electric transport mechanisms that we have established in each region.

- The conduction mechanism for the two studied compounds is considered as semiconductor–type at the lower temperature region, from ambient temperature until 600 K, because the real part of the complex conductivity depends strongly of the frequency and the temperature (see Figure 3.1(a-b), the temperature region assigned for the semiconductor–type conduction is coloured in dark blue). The low activation energy, 0.27(3) eV suggests an extrinsic conduction due to impurity centres, donors or acceptors (Gaur et al. 1993). In addition, the anomalous contraction for the parameter a does not favour the volume

68
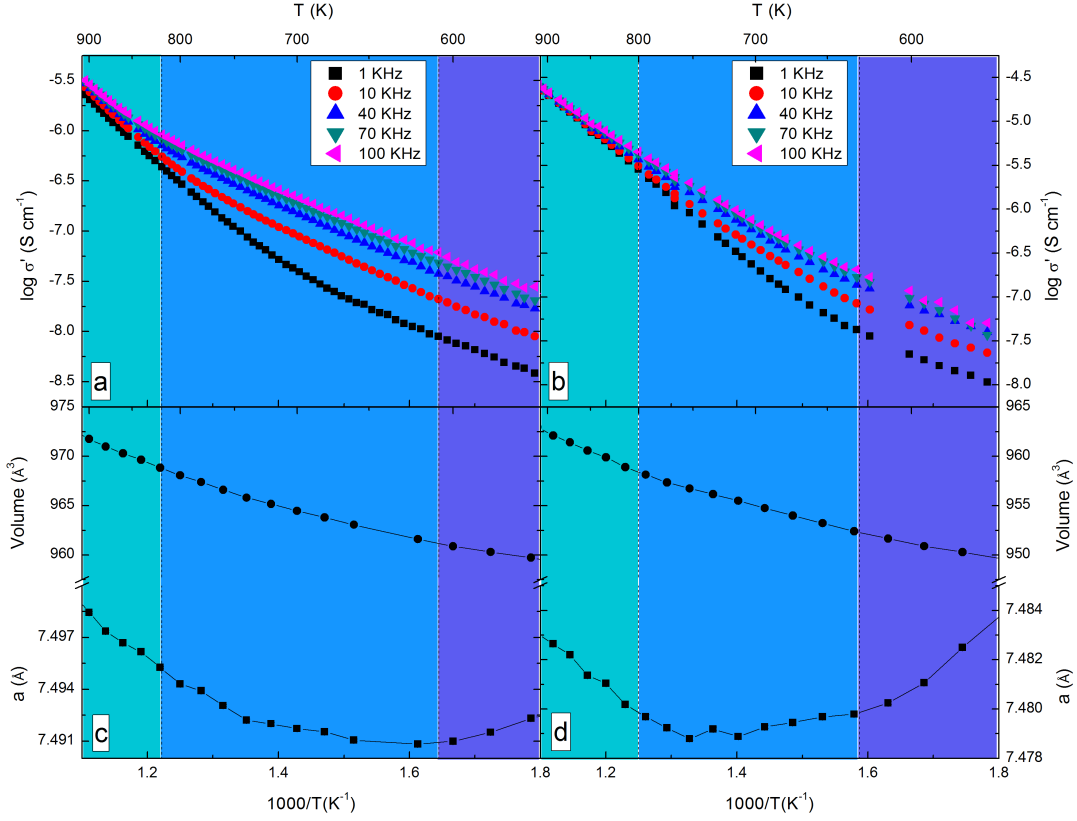
Figure 3.1: Temperature dependence of real part of the complex conductivity (σ') at five frequencies and temperature dependence of lattice parameters a and unit–cell volume for the α–phase in $Sm_2(MoO_4)_3$ (a,c) and $Eu_2(MoO_4)_3$ (b,d). Colours show the temperature regions with different behaviours.

expansion below 600 K and, therefore, the conductivity does not increase significantly with temperature at this region (in dark blue in Figure 3.1).

- At intermediate temperatures, the main conduction mechanism changes to feature a polaronic–type conduct from 600 to 818 K, because the frequency exponent s shows a dependence with the temperature similar to the overlapping large polaron model (Elliott 1987; Ghosh et al. 2000). Thus, the parameter s decreases with increasing temperature

69

until it reaches a minimum at about 750 K and then increases with the rise of temperature (Inset of the figure 2 in section 5.2). One evidence of this possible polaronic behaviour can be observed from Figure 3.1(a-b) in which the conductivity is strongly dependence on the temperature and the frequency; a behaviour that is typical of polaron conduction (Elliott 1987; Gaur et al. 1993). Moreover, the conduction by polarons occurs, approximately, when the lattice parameter a is practically constant (region in medium blue in Figure 3.1), reaching a minimum at 620 K.

- In the last temperature region, the conductivity is less dependent on frequency than the other regions (see Figure 3.1(a-b)). For that reason, we performed a study, typical among ionic conductors, using scaling theories (Dyre et al. 2009; Povolo et al. 1987; Singh et al. 2011). The conductivity spectra were scaled and we found a master curve for these spectra from 810 to 905 K (Figure 3 of section 5.2). This implies that the relaxation dynamics of charge carriers is independent of temperature in this region, thus these compounds exhibit an ionic–type conduction. We have estimated the concentration of the charge carriers from the Nerst–Einstein relation (Howard et al. 1964) for each temperature. The results for this concentration were almost constant, the average value of the concentration of the charge carriers was in the typical range for ionic conductors, in the third temperature region. This means that the temperature dependence of the conductivity arises from the mobility of the ions, rather than the concentration of charge carriers; this is typical for ionic conduction. Finally, the parameter a clearly increases, at 800 K, therefore, the rate of the volume expansion increases with respect to the previous stage, and the transport mechanism, corresponding to the ionic conduction, must be predominant (region in light blue in Figure 3.1).

In order to understand the unusual behaviour of the lattice parameter a, we carried out a diffraction experiment to obtain the crystal structures of both samples at three selected temperatures (450, 650 and 850 K). We calculated the *amplimodes* (Orobengoa et al. 2009)

70

using the scheelite structure $CaMoO_4$ (Hazen et al. 1985) as the high symmetry structure (parent structure) and the α structure as the low symmetry structure (Boulahya et al. 2005; Hartenbach 2008). Then, we applied the symmetry adapted modes method for the Rietveld method (Young 1993), implemented in Fullprof software (Rodríguez-Carvajal 1993), on each diffractogram. Comparing the distortions at different temperatures, we explained the unusual behaviour of the cell parameter a as due to the transversal displacements of the two types of oxygen atoms in the RE–O(1,2)–Mo2 bridges reduce the RE–Mo2 distances, and of the elongation of the tetrahedra around Mo1 in the direction perpendicular to the a axis (Figure 5 of section 5.2).

Finally, we plotted the contour maps of bond–valence sums (González-Platas et al. 1999) for all ions of the cell in order to obtain what ions can support the ionic conduction at high temperatures. We detected that the oxygen ions are connected by paths (with similar valence) at highest temperature, allowing their motion through of the structure when an electric field is applied (Figure 7 of section 5.2). This behaviour suggests that the electrical properties of the sample are well related to the crystal structure, in which the oxygen atoms are the responsible of the more important structural changes and the ionic conduction.

3.2 High–pressure studies of the α- and β'– phases

We analysed the behaviour of the α- and the β'–phases at different pressure conditions, actually in $Eu_2(MoO_4)_3$ (see appendix 6.1) and $Tb_2(MoO_4)_3$ (see section 5.3). We aimed to determine if these two phases undergo structural changes or transitions at high–pressure conditions. A candidate to study the α- and the β'–phases is $Tb_2(MoO_4)_3$ because this compound can crystallizes in both phases. We performed X–ray diffraction from synchrotron radiation and theoretical *ab initio* calculations.

We have simulated the behaviour under pressure of the $La_2(MoO_4)_3$-type, α, β'-, β- and γ–structures for $Tb_2(MoO_4)_3$ by means of *ab initio* calculations (Figure 1 of section 5.3) finding that the α–structure is the most stable one among the ones considered. The β'–structure is a

metastable phase, as it is expected (Brixner et al. 1979). The difference between the energy minimum of both phases is 138 meV pfu and the difference between their volume is 57 Å^3, thus making the α–phase 20% denser than the β'–phase.

From the pressure evolution of the diffractograms (Figure 2b of section 5.3), we can see that the diffraction patterns up to 2 GPa correspond to the β'–phase, and the experimental unit–cell agrees with the theoretical one (Figure 3b of section 5.3). Beyond 2 GPa, the diffraction patterns of the β'–phase start to change, showing more reflections. This change indicates the phase transition from the β'–phase to the so–called δ–phase, which has been detected previously but its crystal structure is unknown. We managed to index the diffraction pattern at 2.81 GPa on the basis of an orthorhombic unit–cell. Then, we refined the diffractograms from 2.81 up to 4.42 GPa. The unit–cell volume of the new phase is almost twice than that of β'–phase, present a low pressures (Figure 3b of section 5.3). Although we did not determine its crystal structure, the unit–cell has been determined for the first time, which can be compatible with point symmetry expected from the results inferred by using fluorescence spectroscopy (Machon et al. 2004). However, other possible phase transitions are not evident from our X–ray diffraction.

After this transformation, if we keep increasing the pressure in the sample, the δ–phase turns to an amorphous state around 6 GPa, in an irreversible process. That means, the sample did not recover a crystalline phase when the pressure was released in the diamond anvil cell.

On the other hand, the α–phase of $Tb_2(MoO_4)_3$ did not undergo any structural phase transition in the pressure range available in our experiment (up to 21 GPa) (Figure 2a of section 5.3). We detected a broadening of the reflections beyond 11.58 GPa that did not allow us to refine the diffractograms obtained after this pressure. This broadening became more important at 21 GPa, indicating that the sample has almost reached the amorphization. A good agreement between experimental and theoretical results was found, i.e., the pressure evolution of the lattice parameters, theoretical and experimental, are very similar.

To fully understand the structural compression and the mechanisms of amorphization in
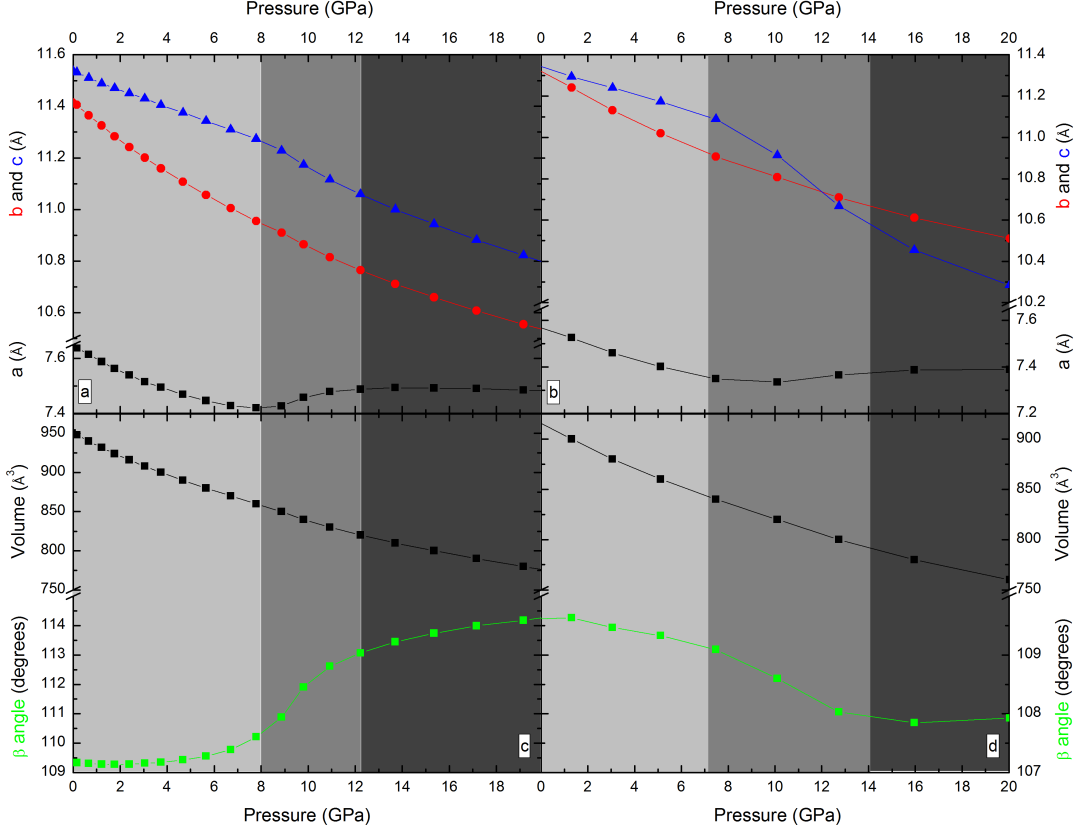
Figure 3.2:   Pressure dependence of the theoretical lattice parameters on the top and the unit–cell volume and beta angle on the bottom for the α–phase in $Eu_2(MoO_4)_3$ (left) and $Tb_2(MoO_4)_3$ (right). Colours show the pressure regions with different stages.

the α–phase, we performed an exhaustive study by powder X–ray diffraction from synchrotron radiation, Raman and optical spectroscopies and *ab initio* calculations in $Eu_2(MoO_4)_3$ under high pressure. We found that the pressure evolution of the diffraction patterns is very similar than that found for $Tb_2(MoO_4)_3$ (Figure 1 of appendix 6.1 and Figure 2a of section 5.3). This means, we did not observe new reflections or extinction of them. However, the unit– cell of α–$Tb_2(MoO_4)_3$ compresses by decreasing the monoclinic β angle while for $Eu_2(MoO_4)_3$ increases (see Figure 3.2). We observed the three frequency regions of Raman modes (external,

bending and stretching modes) for $Eu_2(MoO_4)_3$ which correspond to the original α–phase, and these modes are present in all the pressures measured, without a clear experimental increase or decrease of their number (Figure 8a of section 5.3). Moreover, from luminescence spectra we do not find discontinuities in the spectral parameters such as the number of lines, line shift, line width or line intensity with pressure that could be identified as a strong variation of the Eu^{3+}-O^{2-} bond distances and angles O–Eu–O. Hence, we confirm that a pressure–induced transition to a different crystalline phase does not occur. However, we found certain anomalies that has helped us to understand the mechanisms of the amorphization and to compare with other compounds with α–phase, in particular with $Tb_2(MoO_4)_3$. Attending to these anomalies, we established that the compression process of the α–structure can be described by three stages from results obtained using the different techniques.

- All techniques revealed an isotropic contraction until 8 GPa, i.e. the reflections of the diffraction patterns (Figure 1 of the appendix 6.1), and the peaks of the Raman (Figure 8a of the appendix 6.1) and luminescence spectra (Figures 9 and 10 of the appendix 6.1), only show a slight shift due to the normal contraction of the structure. For α–$Tb_2(MoO_4)_3$ the same isotropic behaviour of Bragg peaks and cell parameters is maintained until 7 GPa (Figure 2a of section 5.3 and Figure 3.2 of this section).

- In contrast, we observed an anisotropic compression between 8 and 12 GPa: a deformation linked to a rotation of the MoO_4 tetrahedra, obtained by theoretical calculations, resulting in a more compact packing of the structure. This distortion can be seen through the pressure dependence of the bond distances and angles (Figures 3 and 4 of the appendix 6.1) and the pictures of the crystal structures (Figures 5 and 6 of the appendix 6.1). This explains the anomalous behaviour of the parameter a and the sudden increasing of the β angle (Figure 3.2). This change in the compression is well correlated to the anomalies in the evolution of the Raman peaks (Figure 8b of the appendix 6.1). These are showed more clearly for the high–frequencies modes (bending and stretching), where the slopes

of pressure dependence change and sometimes become negatives too. This behaviour can be correlated with the beginning of the tetrahedral distortion. Moreover, an increasing of the number Eu^{3+} sites, which translates into stronger crystal–fields, can be predicted by the non–linear broadening of the $^5D_0 \rightarrow {}^7F_0$ emission lines and the non–linear decreasing of the energy red–shifting (Figure 9 of the appendix 6.1). The most abrupt changes in the Eu^{3+} surrounding are also showed through the emission line $^5D_0 \rightarrow {}^7F_1$ where, the two highest energy peaks start to rapidly separate in energy with opposite directions, both increasing the splitting and their *FWHM* until 12 GPa (Figure 11 of the appendix 6.1). For $Tb_2(MoO_4)_3$ it is also possible to distinguish similar anomalies between 7 and 14 GPa.

• The experimental data suggest that the structural transformation to an amorphous state starts after 12 GPa, when the crystal structure rate of compression becomes lower. In the case of X–ray diffraction, we could not continue the refinement beyond 11.6 GPa due to the broadening of the reflections (similar pressure was found for $Tb_2(MoO_4)_3$), then, we do not have experimental information about the unit–cell in this region of pressures, for both compounds. The appearance of the last stage, pressure–induced amorphization, can be confirmed by the broadening of the Raman peaks and finally, with their extinction at 21 GPa (figure 8a of the appendix 6.1). The softening of some experimental modes could confirm this loss of the large–range ordering (figure 8b of the appendix 6.1). From the analysis of the emission lines $^5D_0 \rightarrow {}^7F_J$ (J=0, 1), less changes are observed in the third stage. The red–shift rate decreases with respect to the previous stage. And the singlet levels of the transition $^5D_0 \rightarrow {}^7F_0$ broad abruptly (Figure 9 of the appendix 6.1) resulting in a gradual loss of the large–range ordering. Finally, the theoretical results predicts that the bond valence sum of europium ion becomes too large at 21 GPa, affecting to the balance of the electrical charges and triggering the pressure–induced amorphization.

Finally, when the pressure was released the initial diffraction pattern was recovered, indicating that the changes in the sample are reversible (figure 1 of the appendix 6.1). These

results contrast with the compression of other compounds with the same structure at ambient conditions: α–La$_2$(WO$_4$)$_3$ undergoes two phase transitions before the amorphization and the second transition is irreversible (Sabalisck et al. 2014).

3.3 Structural studies of the β'- and γ–phases at different temperatures

In this section we have summarized the results of the works presented in the sections 5.4, 5.5 and 5.6. In the previous two sections 3.1 and 3.2 we have devoted more time and effort to the study on the α–phase. The work on the other phases has been more introductory; however, we have achieved new results, based on that endeavour to detect any structural changes affecting these molybdates by varying the RE ion or the temperature conditions.

We conducted a preliminary study in RE$_2$(MoO$_4$)$_3$ with RE=Eu–Ho with β'–phase using powder X–ray diffraction at ambient temperature. In Figure 1 of section 5.4 the typical diffractograms of two compounds with β'–phase are shown. The collected data allowed us to refine their ferroelectric–ferroelastic structures (Borchardt et al. 1966), using the symmetry–mode analysis from the paraelectric–paraelastic ones (Jeitschko 1972). We obtained the crystal structure of RE$_2$(MoO$_4$)$_3$, with RE from Eu to Ho, some of them for the first time. A linear correlation was observed between the cell parameters and the RE ionic radius. This dependence on the ionic radius is similar to the pressure dependence generated using the diamond anvil cell, due to the lanthanide contraction that produces the physical effect know as chemical pressure (see Figure 3.3). The distortion from the paraelectric to the ferroelectric structure can be decomposed into three distortion symmetry modes (Perez-Mato et al. 2010): *M2+M4*, *GM1* and *GM3*. Clearly, the global amplitude of the so–called primary mode *M2+M4*, which yields directly the observed symmetry of the ferroelectric phase, is much longer than the amplitude of the polar mode (secondary mode), and moreover, the primary mode is correlated with the RE ionic radius, i.e. longer amplitudes are shown for Eu and Gd molybdates and shorter ones are

76
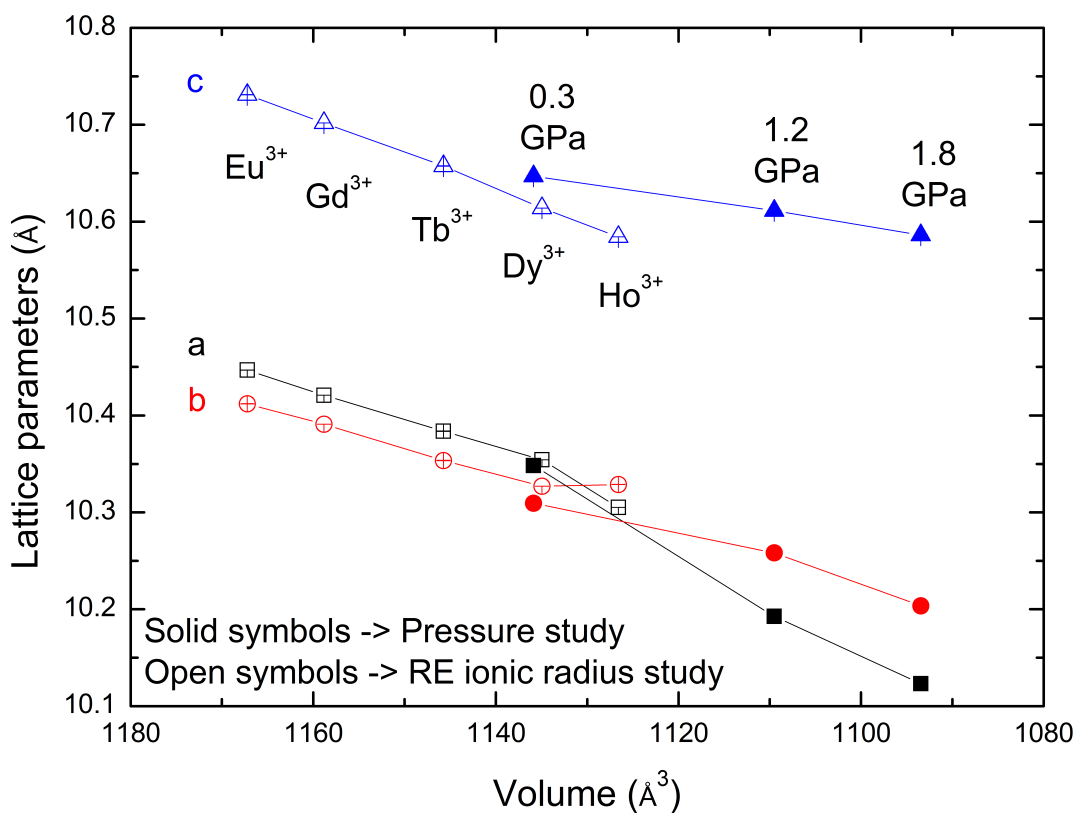
Figure 3.3: Volume dependence of the lattice parameters for β'-$Tb_2(MoO_4)_3$ at different pressure (solid symbols) and for β'-$RE_2(MoO_4)_3$ with different RE ionic radius (open symbols).

shown for Ho and Dy (see Figure 2 of section 5.4). This fact is correlated with the higher Curie temperature for lighter molybdates, revealing RE molybdates with larger ionic radius will need more vibrational energy to reach the transition temperature. Contrary, the amplitude of the polar mode *GM3* (related with the symmetry of the intermediate space group *Cmm2* is not well correlated with the RE ionic radius (see Figure 3 of section 5.4), although more accurate oxygen coordinates must be obtained in order to obtain structural correlations.

When we synthesized RE molybdates using RE ions with smaller cation size, we found only one compound possesses two stable polymorphs with γ- and β'–phases at ambient conditions:

77
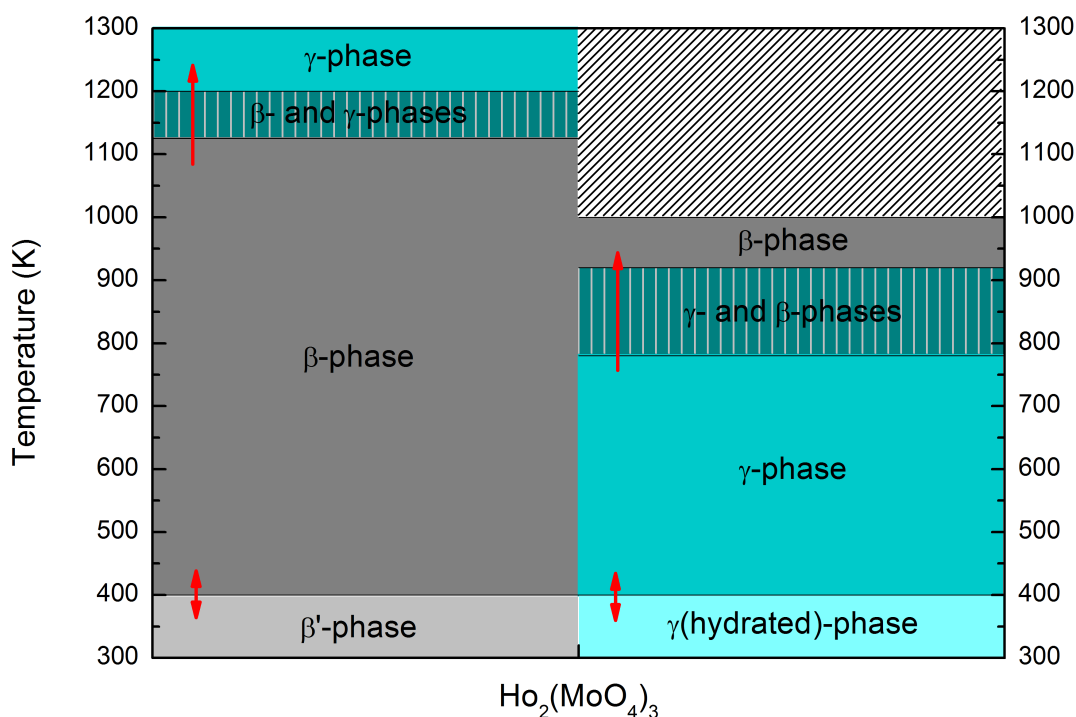
Figure 3.4: Phase diagram for the two phases of $Ho_2(MoO_4)_3$: γ- and β'–phases. The arrows represent the reversibility of the phase transitions and the white patterned area in the graphic is a temperature region without experimental data.

holmium molybdate. However, the yttrium molybdate compound is also expected to have these two structures at ambient conditions (Gates et al. 2007). We performed thermodiffractometry, from 300 to 1300 K, for the two phases of $Ho_2(MoO_4)_3$ to obtain the phase diagram (see Figure 3.4) and the temperature evolution of the cell parameters (see Figure 3 of section 5.5).

We found that the initial β'–phase undergoes a transition to the β–phase at 400 K (reversible process) and then to the γ–phase between 1125 and 1200 K (irreversible process). The β'–β phase transition occurs for isostructural compounds, and it has been widely studied in literature (Jeitschko 1972), but the β–γ phase transition is reported for the first time. Both ferroelectric and paraelectric phases show positive thermal expansion, although their lattice parameter c

decreases when the temperature increases. Meanwhile, the new γ–phase exhibits negative thermal expansion and becomes hydrated at ambient temperature. However, it is interesting to note that between 1125 and 1200 K where both phases coexist, the γ–phase phase does not show a clear negative thermal expansion (see Figure 4 of section 5.5).

In the case of the γ–phase, obtained from the initial hydrated–γ, turns to γ at 400 K (reversible process) (Xiao et al. 2008) and then to the β–phase between 780 and 920 K (irreversible process) (Gates et al. 2007), which undergoes to the β'–phase, as expected, when the temperature decreases (Brixner et al. 1979). The γ–phase exhibits a negative thermal expansion, although its lattice parameter a increases when the temperature increases. Both phases β–phase, first one obtained by heating the β'–phase and second one obtained from the γ–β transition are compared in Figure 3 of section 5.5. The γ–phase exhibits a negative thermal expansion, although its lattice parameter a increases when the temperature increases. We have compared the polymorphs of $Ho_2(MoO_4)_3$ (β' and γ), and despite they show positive and negative thermal expansion, respectively, an anomalous behaviour has been detected during the coexistence of both phases between 775 and 925 K, where the volume of the β'- and γ–phases exhibit negative thermal expansion. These anomalies contrast with the contrary effect observed in the previous experiment between 1125 and 1200 K (see Figure 4 of section 5.5).

Finally, for heavier RE molybdates, with γ–phase, the negative thermal expansion was analysed by X–ray and neutron diffraction, at a temperature range from 150 to 400 K, after the water loss. We performed multi–pattern Rietveld refinements using the symmetry–mode analysis for yttrium, erbium and lutetium molybdates. Regarding other RE molybdates; ytterbium one was reduced during the cooling process by using the Anton Paar TTK camera under vacuum, and the identification of this phase from the X–ray data collection was not possible. For holmium and thulium molybdates the dehydration process, was very quick and both compounds lost crystallinity.

We used the atomic displacements respect to the high–temperature structure as primary parameters in the refinements, instead of using the atomic coordinates. This time, we have

not compared between a more symmetric structure (parent) and a less symmetric one (distorted). In previous works we have compared the scheelite structure with the α–phase and the paraelectric–paraelastic β–phase with the ferroelectric–ferroelastic β'–phase. This approximation helped us to propose a general mechanism for the negative thermal expansion in this family of compounds. Firstly, we calculated the linear thermal expansion coefficient, from refined unit–cell volume, for yttrium, erbium and lutetium molybdates (Figure 2(d) of section 5.6). The absolute value of this coefficient show a proportional dependence with the RE ionic radius, indicating that, the negative thermal expansion is more important in RE molybdates with larger ionic radius.

We examined the amplitude of the displacements and we calculated the corresponding atomic coordinates, at different temperatures, and we organized our study in the following order: 1) We evaluated the tetrahedral and octahedral distortions, as a function of temperature and the RE ionic radius, through calculating of average of bond distances (see Figures 3a, 3b and 3c of section 5.6) and the volume distortion for both polyhedra (see Figure 3d of section 5.6). We did not found an appreciable thermal and ionic–radius dependence of these distances and distortions; 2) We analysed the transverse vibration of binding oxygen atoms and we found the transverse displacements of O1 and O6, with the longest amplitudes, are responsible for the opening observed in the RE–O1–Mo1 and RE–O6–Mo2 bridging angles and the lengthening of the corresponding non–bonded RE...Mo distances, on cooling; 3) As the RE–O–Mo bridges form chained rings along the different axes, resulting in collective displacements of the oxygen atoms, it is possible to explain how the b–axis (especially, through the RE–O1–Mo1 bridges) and the c–axis (through the RE–O6–Mo2 bridges) show negative expansion (see Figure 3.5).

In this work we have refined the same experimental parameters which do not depend on instrument effects for X–Ray and neutrons. As a good result we have managed to refine the same experimental profile parameters for both techniques (U and Y, corresponding to isotropic Gaussian strain and Lorentzian size effects). Moreover, the background of the diffraction patterns was refined using the Debye model for the prominent diffuse scattering observed,
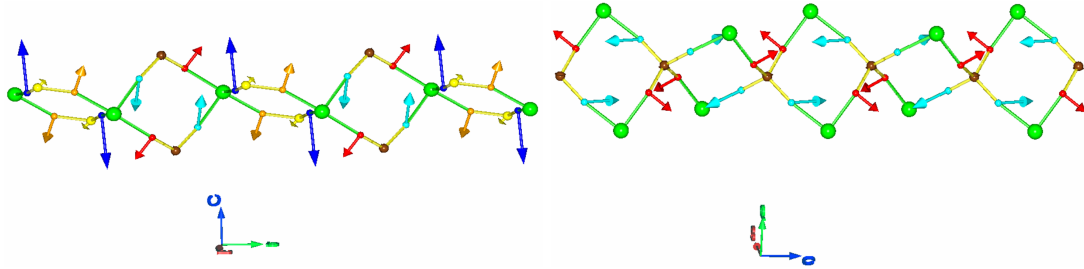
Figure 3.5: Rings formed by RE–O–Mo bridges from the $Er_2(MoO_4)_3$ structure at 150 K where the arrows represent the atomic displacements with respect to the structure at 350 K. Erbium cations are showed in green and molybdenum atoms are in yellow and brown for Mo1 and Mo2, respectively. The oxygen atoms are showed in blue (O1), orange (O2), dark green (O3), magenta (O4), red (O5) and cyan (O6). In the panel left, the collective displacements of the oxygen atoms can explain the elongation of the structure along the b–axis. In the right panel, those oxygens can provide the same effect but along the c–axis.

especially with neutron data (see Figure 1 of section 5.6). Despite samples were dehydrated, we think that the water loss affects to the crystal structure. We have calculated the interatomic distances RE...O, Mo–O, O...O, and RE...Mo from this adjust finding typical values for this structure, however we did not find a clear temperature dependence which help to explain the influence of this static disorder in the negative thermal expansion.

Chapter 4

Conclusions and future perspectives

The most remarkable conclusions of the work presented in this thesis and future perspectives are divided on four parts.

Method

We found that conventional solid–state reaction route is a very appropriate method to obtain polycrystalline RE molybdates with different structural–types. In particular, this method allowed us to prepare four structural–types, they were the $La_2(MoO_4)_3$–type, and the three phases known as: α, β' and γ. A total of nineteen samples of RE molybdates was prepared, including the polymorphs. We have chosen an appropriate combination of characterization techniques that have allowed studying RE molybdates, finding a good agreement between results from several experimental techniques and theoretical calculations.

α–phase

The AC conductivity analysis of RE molybdates with α–phase at high temperature helped to clarify the transport mechanisms in these compounds. In particular, we modelled three transport mechanisms: semiconductor, polaronic and ionic; at three different temperature regions. The polaronic and ionic conductivity were explained, starting from the fit of the Universal Dielectric Response model. On the other hand, we correlated the three tendencies of

the parameter a with each one of the three conduction regions. The unusual dependence of the lattice parameter a could be explained by transversal displacements of two oxygen atoms in the RE–O(1,2)–Mo2 bridges and by the elongation of the tetrahedra around Mo1 in the direction perpendicular to the a axis. At the regime of higher temperatures, oxygen–ion transport was confirmed by plotting contour maps of bond–valence sums. This will lead to perform a deeper analysis of isostructural compounds whose structure have been obtained by neutron diffraction, for example $Tb_2(MoO_4)_3$ and, definitively, to understand how the RE ion affects the electric conductivity at high temperatures for these scheelite–type compounds.

We have also studied the behaviour of the α–phase of $Tb_2(MoO_4)_3$ and $Eu_2(MoO_4)_3$ at high pressure using X–ray diffraction and *ab initio* calculations. For $Eu_2(MoO_4)_3$ this study was completed with Raman spectroscopy and optical spectroscopy. A good agreement between experimental and theoretical results was found. None of the samples showed phase transitions before the amorphization. For that, they constitute interesting examples in which the ambient pressure phase underwent pressure–induced amorphization. A comparison of the results obtained for both compounds establishes that the compression process for α–phase in molybdates can be described by the three stages: an isotropic contraction of the crystal structure up to 7 GPa, an anisotropic compression in the pressure region 7–12 GPa and the begin of the loss of the large–range ordering beyond 12 GPa. Finally, we believe that the amorphization in the α–phase is a consequence of the high distortion of the oxygen–coordination around the both Mo and RE ions, increasing drastically the valence of trivalent ion and changing the balance of the electrical charges to this compound. Then, in these conditions, different environments for the RE ions appear. Currently, we are conducting a structural study of more compounds belong to families of molybdates and tungstates, starting from the same α–phase that would lead us to definitively establish the different ways, depending on ionic radius and type of tetrahedral anion (molybdate or tungstate), for pressure–induced amorphization.

β'–**phase**

We have also performed X–ray diffraction in the β'–phase of $Tb_2(MoO_4)_3$ under high–

pressure conditions. This compound has a phase transition to a δ–phase at 2 GPa and we have proposed a tentative crystallographic cell for this new phase. The cell obtained is orthorhombic. In addition, the axes of the new cell are related to the axes of the β'–cell, with one axis doubled. Moreover, the compound becomes amorphous at 6 GPa, in an irreversible process, indicating that the behaviour of both phases, α and β', under pressure, is markedly different. In view of these results, we will analyse the data collected for different RE molybdates with β'–phase, which undergo the phase transition to δ–phase too. We expect to obtain more structural details of this phase and, after that, we will perform *ab initio* calculations in order to check if the structures proposed are energetically competitive.

On the other hand, the almost complete family of ferroelectric molybdates (β'–phase) was studied by X–ray diffraction at ambient temperature. We obtained the crystal structure for $RE_2(MoO_4)_3$, with RE=Eu, Gd, Tb, Dy and Ho, some of them for the first time. For that, we have analysed the distortion from the paraelectric phase at high temperature (β–phase) to the ferroelectric one. We have confirmed that the primary distortion mode is correlated to the RE ionic radius and, therefore with the Curie temperature. However, we were not able to find a strong correlation between the fitted distortion given by the secondary modes and the RE ionic radius, because the coordinates of the oxygen atoms were not very precise and accurate. We are performing an exhaustive study by neutron diffraction for this ferroelectric family, together with a study of the hysteresis loops.

In addition, the β'–phase of $Ho_2(MoO_4)_3$ was studied from ambient temperature up to 1300 K by thermodiffractometry. We have obtained its phase diagram as a function of temperature and the temperature dependence of the cell parameters. The reversible phase transition was confirmed with the ferroelectric–paraelectric transition of the β' to the β–phase and an irreversible phase transitions β–γ was identified. After that, the new γ–phase exhibits negative thermal expansion and becomes hydrated at ambient temperature.

γ–phase

We performed a similar study to one performed in the β'–phase of $Ho_2(MoO_4)_3$ but this

time in the γ(hydrated)–phase. We found a reversible phase transition that was identified with the dehydration of the γ–phase. At higher temperature an irreversible phase transitions γ–β was identified for the first time. We have compared the polymorphs of $Ho_2(MoO_4)_3$ (β' and γ), and despite they show positive and negative thermal expansion, respectively, an anomalous behaviour has been detected during the coexistence of both phases (in both β–γ and γ–β phase transitions). In future works, we will analyse the neutron diffraction data of both $Ho_2(MoO_4)_3$ polymorphs, which we have already collected, in order to determine the high–temperature structures and to understand the sequence of phase transitions and the origin of instability for these phases in molybdates and tungstates.

Finally, we have performed a comparative study of different isostructural compounds with the γ–phase. We obtained the absolute linear thermal expansion coefficient show a proportional dependence with the cation size of the RE ions, and indicating that, the negative thermal expansion is more important in RE molybdates with larger RE cation size. In general, we have found that the transverse displacements of some oxygen atoms with respect to their positions at higher temperatures, are responsible of the negative thermal expansion. These results have led us to describe the evolution of these displacements in terms of a distortion from a more symmetrical structure (for instance *Im-3m*) given by a symmetry modes analysis. In this way, we will understand why other related structure, such as garnet, nasicon and low–temperature phase of $Al_2(WO_4)_3$ do not experience negative thermal expansion and to relate them with other polymorphic phases (α- and β–phases).

Bibliography

Abe, M., Y. Benino, T. Fujiwara, T. Komatsu, and R. Sato (2005). Writing of nonlinear optical $Sm_2(MoO_4)_3$ crystal lines at the surface of glass by samarium atom heat processing. *J. Appl. Phys.* 97, p. 123516.

Abrahams, S. C. and J. L. Bernstein (1966). Crystal Structure of the Transition–Metal Molybdates and Tungstates. II. Diamagnetic $Sc_2(WO_4)_3$. *J. Chem. Phys.* 45, p. 2745.

Atuchin, V. V., A. S. Aleksandrovsky, O. D. Chimitova, T. A. Gavrilova, A. S. Krylov, M. S. Molokeev, A. S. Oreshonkov, B. G. Bazarov, and J. G. Bazarova (2014). Synthesis and Spectroscopic Properties of Monoclinic α-$Eu_2(MoO_4)_3$. *J. Phys. Chem. C* 118, p. 15404.

Basiev, T. T, A. A Sobol, Y. K. Voronko, and P. G Zverev (2000). Spontaneous Raman spectroscopy of tungstate and molybdate crystals for Raman lasers. *Opt. Mater.* 15, p. 205.

Bergerhoff, G. and I. D. Brown (1987). *Crystallographic Databases*. http://www.fiz-karlsruhe.de/icsd.html.

Birch, F. (1947). Finite Elastic Strain of Cubic Crystals. *Phys. Rev.* 71, p. 809.

Blöchl, P. E. (1994). Projector augmented-wave method. *Phys. Rev. B* 50, p. 17953.

Borchardt, H. J. and P. E. Bierstedt (1966). $Gd_2(MoO_4)_3$: a ferroelectric laser host. *Appl. Phys. Lett.* 8, p. 50.

Boulahya, K., M. Parras, and J. M. González-Calbet (2005). Synthesis, Structural and Magnetic Characterization of a New Scheelite Related Compound: $Eu_2Mo_3O_{12}$. *Eur. J. Inorg. Chem.* 2005, p. 967.

Brenier, A, X Zhang, J Wang, H Zhang, C Tu, J Li, Z Zhu, Y Wang, and Z You (2004). Passive Q-switching of Nd^{3+}:$GdAl_3(BO_3)_4$ crystal. *Opt. Mater.* 26, p. 287.

Brixner, L. H. (1972). π-GMO: Another modification of $Gd_2(MoO_4)_3$. *Mater. Res. Bull.* 7, p. 879.

Brixner, L. H., J. R. Barkley, and W. Jeitschko (1979). *Handbook on the Physics and Chemistry of Rare Earth.* Amsterdam: North-Holland.

Brown, I. D. and D. Altermatt (1985). Bond-valence parameters obtained from a systematic analysis of the Inorganic Crystal Structure Database. *Acta Crystallogr., Sect. B* 41, p. 244.

Bubb, D. M., D. Cohen, and S. B. Qadri (2005). Infrared–to–visible upconversion in thin films of $LaEr(MoO_4)_3$. *Appl. Phys. Lett.* 87, p. 131909.

Cerny, P., H. Jelinkova, T. Basiev, and P. Zverev (2002). Highly efficient picosecond Raman generators based on the $BaWO_4$ crystal in the near infrared, visible, and ultraviolet. *IEEE J. Quantum Electron.* 38, p. 1471.

Chetty, N., A. Muoz, and R. M. Martin (1989). First-principles calculation of the elastic constants of AlAs. *Phys. Rev. B* 40, p. 11934.

Cross, L. E., A. Fouskova, and S. E. Cummins (1968). Gadolinium Molybdate, a New Type of Ferroelectric Crystal. *Phys. Rev. Lett.* 21, p. 812.

Dmitriev, V., V. Sinitsyn, R. Dilanian, D. Machon, A. Kuznetsov, E. Ponyatovsky, G. Lucazeau, and H. P. Weber (2003). In situ pressure-induced solid-state amorphization in $Sm_2(MoO_4)_3$, $Eu_2(MoO_4)_3$ and $Gd_2(MoO_4)_3$ crystals: chemical decomposition scenario. *J. Phys. Chem. Solids* 64, p. 307.

Dudarev, S. L., G. A. Botton, S. Y. Savrasov, C. J. Humphreys, and A. P. Sutton (1998). Electron–energy–loss spectra and the structural stability of nickel oxide: An LSDA+U study. *Phys. Rev. B* 57, p. 1505.

Dyre, J. C., P. Maass, B. Roling, and D. L. Sidebottom (2009). Fundamental questions relating to ion conduction in disordered solids. *Rep. Prog. Phys.* 72, p. 046501.

Elliott, S. R. (1987). A.c. conduction in amorphous chalcogenide and pnictide semiconductors. *Adv. Phys.* 36, p. 135.

Errandonea, D. and F. J. Manjón (2008). Pressure effects on the structural and electronic properties of ABX_4 scintillating crystals. *Prog. Mater. Sci.* 53, p. 711.

Evans, J. S. O., T. A. Mary, and A. W. Sleight (1998). Negative Thermal Expansion in $Sc_2(MoO_4)_3$. *J. Solid State Chem.* 137, p. 148.

Evans, J. S. O. and T. A Mary (2000). Structural phase transitions and negative thermal expansion in $Sc_2(MoO_4)_3$. *Int. J. Inorg. Mater.* 2, p. 143.

Finger, L. W., D. E. Cox, and A. P. Jephcoat (1994). A correction for powder diffraction peak asymmetry due to axial divergence. *J. Appl. Crystallogr.* 27, p. 892.

Gai, S., C. Li, P. Yang, and J. Lin (2014). Recent Progress in Rare Earth Micro/Nanocrystals: Soft Chemical Synthesis, Luminescent Properties, and Biomedical Applications. *Chem. Rev.* 114, p. 2343.

Gates, S. D. and C. Lind (2007). Polymorphism in yttrium molybdate $Y_2Mo_3O_{12}$. *J. Solid State Chem.* 180, p. 3510.

Gaur, K., M. Singh, and H. B. Lal (1993). Electrical transport in light rare–earth molybdates. *J. Mater. Sci.* 28, p. 3816.

Ghosh, A. and A. Pan (2000). Scaling of the Conductivity Spectra in Ionic Glasses: Dependence on the Structure. *Phys. Rev. Lett.* 84, p. 2188.

Giddy, A. P., M. T. Dove, G. S. Pawley, and V. Heine (1993). The determination of rigid-unit modes as potential soft modes for displacive phase transitions in framework crystal structures. *Acta Crystallogr., Sect. A* 49, p. 697.

Globus, M., B. Grinyov, and J. K. Kim (2005). *Inorganic Scintillators for Modern and Traditional Applications*. Kharkov: Institute for Single Crystals.

González-Platas, J., C. González-Silgo, and C. Ruiz-Pérez (1999). *VALMAP* 2.0: contour maps using the bond-valence-sum method. *J. Appl. Crystallogr.* 32, p. 341.

Guo, C., T. Chen, L. Luan, W. Zhang, and D. Huang (2008). Luminescent properties of $R_2(MoO_4)_3$:Eu^{3+} (R=La, Y, Gd) phosphors prepared by solgel process. *J. Phys. Chem. Solids* 69, p. 1905.

Hafner, J. (2008). Ab-initio simulations of materials using VASP: Density-functional theory and beyond. *J. Comput. Chem.* 29, p. 2044.

Hartenbach, I. (2008). Die Kristallstruktur von Samarium-Sesquimolybdat $Sm_2(MoO_4)_3$. *Zeitschrift fr anorganische und allgemeine Chemie* 634, p. 2044.

Hazen, R. M., L. W. Finger, and J. W. E. Mariathasan (1985). High-pressure crystal chemistry of scheelite-type tungstates and molybdates. *J. Phys. Chem. Solids* 46, p. 253.

Hitchcock, F. R. M. (1895). The tungstates and molybdates of the rare earths. *J. Am. Chem. Soc.* 17, p. 520.

Hohenberg, P. and W. Kohn (1964). Inhomogeneous Electron Gas. *Phys. Rev.* 136, B864.

Howard, R. E. and A. B. Lidiard (1964). Matter transport in solids. *Rep. Prog. Phys.* 27, p. 161.

Imanaka, N., T. Ueda, Y. Okazaki, S. Tamura, and G.-y. Adachi (2000). Trivalent ion conduction in molybdates having $Sc_2(WO_4)_3$-type structure. *Chem. Mater.* 12, p. 1910.

Jayaraman, A, S. K. Sharma, Z. Wang, S. Y. Wang, L. C. Ming, and M. H. Manghnani (1993). Pressure-induced amorphization of $Tb_2(MoO_4)_3$: A high pressure Raman and X–Ray diffraction study. *J. Phys. Chem. Solids* 54, p. 827.

Jayaraman, A., S. K. Sharma, Z. Wang, and S. Y. Wang (1997). Pressure-induced amorphization in the α-phase of $Nd_2(MoO_4)_3$ and $Tb_2(MoO_4)_3$. *Solid State Commun.* 101, p. 237.

Jeitschko, W. (1972). A comprehensive X–ray study of the ferroelectric-ferroelastic and paraelectric-paraelastic phases of $Gd_2(MoO_4)_3$. *Acta Crystallogr., Sect. B* 28, p. 60.

Jonscher, A. K. (1983). *Dielectric Relaxation in Solids.* London: Chelsea Dielectrics Press.

Judd, B. R. (1962). Optical absorption intensities of rare–earth ions. *Phys. Rev.* 127, p. 750.

Kaminskii, A., A. Butashin, H.-J. Eichler, D Grebe, R Macdonald, K Ueda, H Nishioka, W Odajima, M Tateno, J. Song, M Musha, S. Bagaev, and A. Pavlyuk (1997). Orthorhombic ferroelectric and ferroelastic $Gd_2(MoO_4)_3$ crystal – a new many-purposed nonlinear and

optical material: efficient multiple stimulated Raman scattering and CW and tunable second harmonic generation. *Opt. Mater.* 7, p. 59.

Keve, E. T. (1971). Ferroelectric ferroelastic paramagnetic β-$Gd_2(MoO_4)_3$ crystal structure of the transition–metal molybdates and tungstates. VI. *J. Chem. Phys.* 54, p. 3185.

Kojima, S. and T. Nakamura (1978). Electro-optical properties of gadolinium molybdate. *Phys. Rev. B* 18, p. 453.

Kresse, G. and J. Furthmüller (1996). Efficient iterative schemes for *ab initio* total-energy calculations using a plane-wave basis set. *Phys. Rev. B* 54, p. 11169.

Kresse, G. and D. Joubert (1999). From ultrasoft pseudopotentials to the projector augmented-wave method. *Phys. Rev. B* 59, p. 1758.

Lavín, V., T. Tröster, U. R. Rodríguez-Mendoza, I. R. Martín, and V. D. Rodríguez (2002). Spectroscopic monitoring of the Eu^{3+} ion local structure in the pressure induced amorphization of $EuZrF_7$ polycrystal. *High Pressure Res.* 22, p. 111.

Le Bacq, O., D. Machon, D. Testemale, and A. Pasturel (2011). Pressure-induced amorphization mechanism in $Eu_2(MoO_4)_3$. *Phys. Rev. B* 83, p. 214101.

Le Bail, A. (2005). Whole powder pattern decomposition methods and applications: A retrospection. *Powder Diffr.* 20, p. 316.

Le Bail, A., I. Madsen, L. M. D. Cranswick, J. K. Cockcroft, P. Norby, A. D. Zuev, A. Fitch, J. Rodriguez-Carvajal, C. Giacovazzo, R. B. Von Dreele, P. Scardi, N. C. Popa, R. Allmann, L. A. Solovyov, B. Hinrichsen, U. Schwarz, A. Altomare, A. Moliterni, R. Caliandro, R. Rizzi, N. V. Y. Scarlett, and M. Jansen (2008). *Powder Diffraction. Theory and Practice.* Ed. by R. E. Dinnebier and S. J. L. Billinge. The Royal Society of Chemistry, p001.

León, C., M. L. Lucía, and J. Santamaría (1997). Correlated ion hopping in single-crystal yttria-stabilized zirconia. *Phys. Rev. B* 55, p. 882.

Logvinovich, D, A Arakcheeva, P Pattison, S Eliseeva, P Tomes, I Marozau, and G Chapuis (2010). Crystal structure and optical and magnetic properties of $Pr_2(MoO_4)_3$. *Inorg Chem.* 49, p. 1587.

Lucazeau, G, P Bouvier, A Pasturel, O. L. Bacq, and T Pagnier (2009). High-Pressure Study of $Gd_2(MoO_4)_3$ by Raman Scattering and Ab Initio Calculations. *Acta Phys. Pol., A* 116, p. 1.

Lucazeau, G., O. Le Bacq, A. Pasturel, P. Bouvier, and T. Pagnier (2011). High-pressure polarized Raman spectra of $Gd_2(MoO_4)_3$: phase transitions and amorphization. *J. Raman Spectrosc.* 42, p. 452.

Macdonald, J. R. and W. B. Johnson (2005). "Fundamentals of Impedance Spectroscopy". In: *Impedance Spectroscopy*. John Wiley & Sons, Inc., p. 1.

Machon, D, V. Dmitriev, V. Sinitsyn, and G Lucazeau (2004). $Eu_2(MoO_4)_3$ single crystal at high pressure: Structural phase transitions and amorphization probed by fluorescence spectroscopy. *Phys. Rev. B* 70, p. 1.

Maczka, M., A. S. Filho, W. Paraguassu, P. Freire, J. M. Filho, and J. Hanuza (2012). Pressure-induced structural phase transitions and amorphization in selected molybdates and tungstates. *Prog. Mater. Sci.* 57, p. 1335.

Mao, H. K., P. M. Bell, J. W. Shaner, and D. J. Steinberg (1978). Specific volume measurements of Cu, Mo, Pd, and Ag and calibration of the ruby R1 fluorescence pressure gauge from 0.06 to 1 Mbar. *J. Appl. Phys.* 49, p. 3276.

Mao, H. K., J. Xu, and P. M. Bell (1986). Calibration of the ruby pressure gauge to 800 kbar under quasi-hydrostatic conditions. *J. Geophys. Res.: Solid Earth* 91, p. 4673.

Marinkovic, B. A., M. Ari, R. R. de Avillez, F. Rizzo, F. F. Ferreira, K. J. Miller, M. B. Johnson, and M. A. White (2009). Correlation between AO_6 polyhedral distortion and negative thermal expansion in orthorhombic $Y_2Mo_3O_{12}$ and related materials. *Chem. Mater.* 21, p. 2886.

Mason, J. (1990). Lanthanide probes in life, chemical and earth sciences: Theory and practice. Jean-Claude G. Bünzli and Gregory R. Choppin (Eds). Elsevier, Amsterdam, 1989, pp. 432, 87, ISBN 0-444-88199-9. *Magn. Reson. Chem.* 28, p. 737.

McCusker, L. B., R. B. Von Dreele, D. E. Cox, D. Louër, and P. Scardi (1999). Rietveld refinement guidelines. *J. Appl. Crystallogr.* 32, p. 36.

Mujica, A., A. Rubio, A. Muñoz, and R. J. Needs (2003). High-pressure phases of group–IV, III–V, and II–VI compounds. *Rev. Mod. Phys.* 75, p. 863.

Neeraj, S, N Kijima, and A. Cheetham (2004). Novel red phosphors for solid-state lighting: the system $NaM(WO_4)_{2-x}(MoO4)_x$:Eu^{3+} (M=Gd, Y, Bi). *Chem. Phys. Lett.* 387, p. 2.

Nye, J. F. (1957). *Physical properties of crystals. Their representation by Tensor and Matrices.* Oxford University Press.

Ofelt, G. S. (1962). Intensities of crystal spectra of rare–earth ions. *J. Chem. Phys.* 37, p. 511.

— (1963). Structure of the f^6 configuration with application to rare–earth ions. *J. Chem. Phys.* 38, p. 2171.

Orobengoa, D., C. Capillas, M. I. Aroyo, and J. M. Perez-Mato (2009). *AMPLIMODES*: symmetry-mode analysis on the Bilbao Crystallographic Server. *J. Appl. Crystallogr.* 42, p. 820.

Pang, L.-X., G.-B. Sun, and D. Zhou (2011). $Ln_2Mo_3O_{12}$ (Ln = La, Nd): A novel group of low loss microwave dielectric ceramics with low sintering temperature. *Mater. Lett.* 65, p. 164.

Pappalardo, R. (1978). Spectroscopy and Luminescence of Lanthanides and Actinides. In: *Luminescence of Inorganic Solids*. Ed. by B. Di Bartolo, V. Godberg, and D. Pacheco. Springer US, p. 175.

Paraguassu, W., M. Maczka, A. G. Souza Filho, P. T. C. Freire, J. Mendes Filho, F. E. A. Melo, L. Macalik, L. Gerward, J. Staun Olsen, A. Waskowska, and J. Hanuza (2004). Pressure-induced structural transformations in the molybdate $Sc_2(MoO_4)_3$. *Phys. Rev. B* 69, p. 094111.

Parlinski, K. (2008). *software PHONON*. http://wolf.ifj.edu.pl/phonon/.

Pask, H. and J. Piper (2000). Diode–pumped $LiIO_3$ intracavity Raman lasers. *IEEE J. Quantum Electron.* 36, p. 949.

Paski, E. F. and M. W. Blades (1988). Analysis of inorganic powders by time-wavelength resolved luminescence spectroscopy. *Anal. Chem.* 60, p. 1224.

Perdew, J. P., A. Ruzsinszky, G. I. Csonka, O. A. Vydrov, G. E. Scuseria, L. A. Constantin, X. Zhou, and K. Burke (2008). Restoring the density-gradient expansion for exchange in solids and surfaces. *Phys. Rev. Lett.* 100, p. 136406.

Perez-Mato, J. M., D. Orobengoa, and M. I. Aroyo (2010). Mode crystallography of distorted structures. *Acta Crystallogr., Sect. A* 66, p. 558.

Pickard, C. J., B. Winkler, R. K. Chen, M. C. Payne, M. H. Lee, J. S. Lin, J. A. White, V. Milman, and D. Vanderbilt (2000). Structural properties of lanthanide and actinide compounds within the plane wave pseudopotential approach. *Phys. Rev. Lett.* 85, p. 5122.

Ponomarev, B. K. (2002). Magneto–electrical properties of rare earth molybdates. *Ferroelectrics* 280, p. 95.

Povolo, F. and M. Fontelos (1987). Time-temperature superposition principle and scaling behaviour. *J. Mater. Sci.* 22, p. 1530.

Ravindran, T. R., A. K. Arora, and T. A. Mary (2003). Anharmonicity and negative thermal expansion in zirconium tungstate. *Phys. Rev. B* 67, p. 064301.

Rodríguez-Carvajal, J. (1993). Recent advances in magnetic structure determination by neutron Powder Diffraction. *Physica B* 192, p. 55.

Röntgen, W. C. (1896). On a new kind of rays. *Science* 3, p. 227.

Sabalisck, N. P., J. López-Solano, C. Guzmán-Afonso, D. Santamaría-Pérez, C. González-Silgo, A. Mujica, A. Muñoz, P. Rodríguez-Hernández, S. Radescu, X. Vendrell, L. Mestres, J. A. Sans, and F. J. Manjón (2014). Effect of pressure on $La_2(WO_4)_3$ with a modulated scheelite-type structure. *Phys. Rev. B* 89, p. 174112.

Secco, R. A., H Liu, N Imanaka, and G Adachi (2002). Anomalous ionic conductivity of $Sc_2(WO_4)_3$ mediated by structural changes at high pressures and temperatures. *J. Phys.: Condens. Matter* 14, p. 11285.

Bibliography

Sharma, N., K. M. Shaju, G. V. Subba Rao, B. V. R. Chowdari, Z. L. Dong, and T. J. White (2004). Carbon-Coated Nanophase $CaMoO_4$ as Anode Material for Li Ion Batteries. *Chem. Mater.* 16, p. 504.

Shionoya, S., W. M. Yen, and H. Yamamoto (2006). *Phosphor Handbook.* The CRC Press laser and optical science and technology series. Taylor & Francis.

Singh, P., Raghvendra, O. Parkash, and D. Kumar (2011). Scaling of low-temperature conductivity spectra of $BaSn_{1-x}Nb_xO_3$ ($x \leq 0.100$): Temperature and compositional-independent conductivity. *Phys. Rev. B* 84, p. 174306.

Sumithra, S. and A. M. Umarji (2004). Role of crystal structure on the thermal expansion of $Ln_2W_3O_{12}$ (Ln=La, Nd, Dy, Y, Er and Yb). *Solid State Sci.* 6, p. 1313.

— (2006). Negative thermal expansion in rare earth molybdates. *Solid State Sci.* 8, p. 1453.

Suzuki, F., T. Honma, and T. Komatsu (2014). Unique crystal growth with crystal axis rotation in multi-ferroic β'-$(Sm,Gd)_2(MoO_4)_3$ narrow lines patterned by lasers in glass. *J. Phys. Chem. Solids* 75, p. 954.

Svensson, C., S. C. Abrahams, and J. L. Bernstein (1979). Ferroelectric–ferroelastic $Tb_2(MoO_4)_3$: Room temperature crystal structure of the transition-metal molybdates. VII. *J. Chem. Phys.* 71, p. 5191.

Takai, S., K. Sugiura, and T. Esaka (1999). Ionic conduction properties of $Pb_{1x}M_xWO^{4+}$ (M = Pr, Tb). *Mater. Res. Bull.* 34, p. 193.

Tao, J. and A. Sleight (2003). The role of rigid unit modes in negative thermal expansion. *J. Solid State Chem.* 173, p. 442.

Templeton, D. H. and A. Zalkin (1963). Crystal structure of europium tungstate. *Acta Crystallogr.* 16, p. 762.

Toledano, J. C. and P. Toledano (1987). *The Landau Theory of Phase Transtions.* Singapore: World Scientific.

Tripathi, A. K. and H. B. Lal (1980). Electrical Transport in Rare–Earth Molybdates: $Gd_2(MoO_4)_3$ and $Tb_2(MoO_4)_3$. *J. Phys. Soc. Jpn.* 49, p. 1896.

Versluis, A., W. H. Douglas, and R. L. Sakaguchi (1996). Thermal expansion coefficient of dental composites measured with strain gauges. *Dent. Mater.* 12, p. 290.

Volkov, V., C. Cascales, A. Kling, and C. Zaldo (2005). Growth, structure, and evaluation of laser properties of $LiYb(MoO_4)_2$ single crystal. *Chem. Mater.* 17, p. 291.

Wang, L., F. Wang, P.-F. Yuan, Q. Sun, E.-J. Liang, Y. Jia, and Z.-X. Guo (2013). Negative thermal expansion correlated with polyhedral movements and distortions in orthorhombic $Y_2Mo_3O_{12}$. *Mater. Res. Bull.* 48, p. 2724.

Wei, Z., Y. Yu, H. Xing, Z. Zhuo, Y. Wu, L. Zhang, W. Zheng, and Y. Zhang (2001). Fabrication of chirped fiber grating with adjustable chirp and fixed central wavelength. *IEEE Photonics Technol. Lett.* 13, p. 821.

West, A. (2013). *Solid State Chemistry and its Applications*. United Kingdom: John Wiley & Sons.

Xiao, X. L., Y. Z. Cheng, J. Peng, M. M. Wu, D. F. Chen, Z. B. Hu, R. Kiyanagi, J. S. Fieramosca, S. Short, and J. Jorgensen (2008). Thermal expansion properties of $A_2(MO_4)_3$ (A=Ho and Tm; M=W and Mo). *Solid State Sci.* 10, p. 321.

Yen, W. M., S. Shionoya, and H. Yamamoto (2007). *Phosphor Handbook*. New York: CRC Press.

Yi, G., B. Sun, F. Yang, D. Chen, Y. Zhou, and J. Cheng (2002). Synthesis and characterization of high–efficiency nanocrystal up-conversion phosphors: ytterbium and erbium codoped lanthanum molybdate. *Chem. Mater.* 14, p. 2910.

Young, R. A. (1993). *The Rietveld Method*. Oxford: Oxford Science Publications.

Zalkin, A. and D. H. Templeton (1964). X–ray diffraction refinement of the calcium tungstate structure. *J. Chem. Phys.* 40, p. 501.

Chapter 5

Published Papers

The different papers that constitute the work presented in this thesis on the modality of *"Compendium of Publications"* are included in this chapter in the following order:

1. Electrical transport and anomalous structural behavior of α–$Eu_2(MoO_4)_3$ at high temperature.

2. Structural anomalies related to changes in the conduction mechanisms of α–$Sm_2(MoO_4)_3$.

3. Pressure evolution of two polymorphs of $Tb_2(MoO_4)_3$.

4. Crystal structure and non–linear properties of $A_2(MoO_4)_3$ (A=Eu, Gd, Tb, Dy and Ho)

5. Polymorphism in $Ho_2(MoO_4)_3$.

6. Structural investigation of the negative thermal expansion in yttrium and rare earth molybdates.
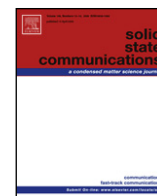
Electrical transport and anomalous structural behavior of α-Eu$_2$(MoO$_4$)$_3$ at high temperature

C. Guzmán-Afonso [a], M.E. Torres [a,*], C. González-Silgo [b], N. Sabalisck [a], J. González-Platas [b,c], E. Matesanz [d], A. Mujica [b]

[a] *Dpto. Física Básica, Universidad de La Laguna, Tenerife, Spain*
[b] *Dpto. de Física Fundamental II, Universidad de La Laguna, Tenerife, Spain*
[c] *Servicio Integrado de Difracción de Rayos X, Universidad de La Laguna, Tenerife, Spain*
[d] *C.A.I. Difracción de Rayos X, Universidad Complutense de Madrid, Spain*

ARTICLE INFO

ABSTRACT

The study of XRD patterns of α-Eu$_2$(MoO$_4$)$_3$ modulated scheelite reveals an anomalous behavior of its lattice parameter a in the range of temperatures from 473 to 973 K. We have analyzed the real part of the complex conductivity in the frequency range from 0.1 to 10,000 kHz and the temperature range from 550 to 900 K, and found that it follows a universal dielectric response. Detailed analysis of the temperature dependence of the adjusted parameters within this model shows that, in a temperature range, the dominant mechanism of electrical transport is due to the overlapping of large polarons. Rietveld refinements were performed using symmetry adapted modes at 523, 723 and 923 K in order to study the thermal dependence of the distortion from the scheelite structure and to interpret the structural effects that favor the formation of polarons.

1. Introduction

Rare-earth (RE) molybdates, RE$_2$(MoO$_4$)$_3$, crystallize in a variety of structures depending upon the method used in their preparation and the value of the RE ionic radius. Light RE molybdates (RE = La–Eu) can occur in differently ordered scheelite-type (CaWO$_4$) structures, where one-third of the calcium substituted by the RE forms vacancies. In particular, the α phase of Eu$_2$(MoO$_4$)$_3$ is monoclinic [1,2] with space group $C2/c$ and $Z = 4$. The strong anisotropy and lanthanide impurity acceptance of scheelite molybdates have promoted their use as efficient laser hosts and Raman shifters [3]. On the other hand, electrical transport studies on polycrystalline La–Eu molybdates in the temperature range 450–1200 K, using electrical conductivity and Seebeck coefficient measurements, have shown different linear regions with temperature breaks occurring due to a change in the conduction mechanisms [4]. In Ref. [4], the authors propose that, since the calculated values for mobility in these compounds are an order of magnitude smaller than those expected from the normal energy band model, the charge carriers in these bands become polarons. For high temperature, the conduction can be intrinsic with large polarons of

intermediate coupling as the main charge carriers. A similar high temperature study in Gd$_2$(MoO$_4$)$_3$ and Tb$_2$(MoO$_4$)$_3$ [5] confirmed the localization of the 4f electrons, so their contribution to electrical conduction can only be through the low mobility of small polarons. It would be interesting to clarify the formation of polarons and how this can produce a deformation of the crystal lattice.

In this article, we present a high temperature study of the electrical conductivity and its correlation with the crystal structure of α-Eu$_2$(MoO$_4$)$_3$. Several different theories have been previously used to obtain such a behavior from the microscopic transport properties including hopping or tunneling of the charge carriers through an energy barrier separating different localized states [6–9]. In these models, each mechanism leads to a different frequency and temperature dependence of the real part of the complex conductivity, which can be given by the universal dielectric response [10,11].

2. Experiment

Europium molybdate was prepared by conventional solid-state synthesis. MoO$_3$ and Eu$_2$O$_3$ powders (Aldrich, 99.99%) were preheated, respectively, at 923 and 1173 K for 10 h before use. These preheated powders were weighed in stoichiometric amounts, mixed and homogenized in an agate mortar. The resulting powder was then pressed into pellets and finally sintered in air atmosphere

---

* Corresponding author.
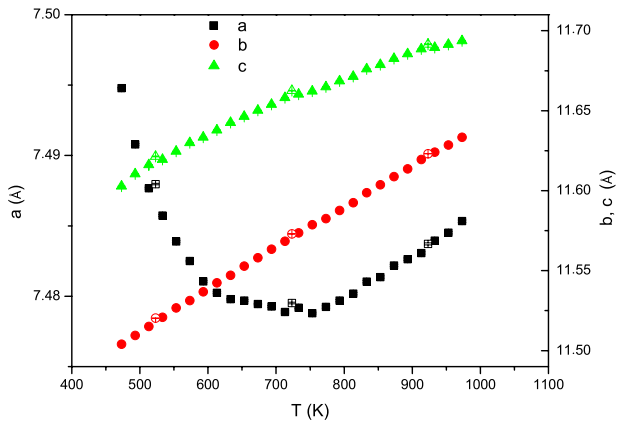 *E-mail address:* metorres@ull.es (M.E. Torres).

Fig. 1. Temperature dependence of the lattice parameters of α-Eu$_2$(MoO$_4$)$_3$. Solid symbols correspond to our first experiment and open symbols to our second experiment. Standard deviations are smaller than the respective symbols on the graphic.

Fig. 2. Projection of a layer structure in a plane perpendicular to the b axis, at 523 (left), 723 (right) and 923 K (bottom). The arrows indicate the amplitudes of the modes, which have been magnified for clarity. (For interpretation of the references to colour in this figure legend, the reader is referred to the web version of this article.)

at 1073 K for 48 h in a platinum crucible. The structural phase of the sample was confirmed by X-ray diffraction. In the first experiment, powder diffraction data were collected in a PANalytical X'Pert PRO diffractometer (Bragg–Brentano mode) with an X'Celerator detector using CuKα radiation from 473 to 973 K. The angular range $10° < 2\theta < 80°$ was scanned at a step size of 0.0167° and 50 s step time. Divergence and anti-scatter slits were set at 0.5° and 1°, respectively and the detector was used in scanning mode with an active length of 2.12°. Only a secondary 0.02 rad Soller slit was used. In the second experiment, the slow scan for Rietveld analysis was measured at three selected temperatures (523, 723 and 923 K). This time three scans for each temperature stage were collected in the range $10° < 2\theta < 120°$ and with a step time of 100 s. Conductivity measurements were carried out using a Hewlett-Packard 4192 A impedance analyzer which was controlled by a computer. Measurements were recorded during a heating and cooling cycle, in the frequency range 10^2–10^7 Hz with an applied voltage of 0.7 V_{pp}, over the temperature range 400–970 K. The samples were in the form of pellets with surfaces coated with platinum paste, 13 mm in diameter and 1–1.5 mm in thickness.

3. Results and discussion

Taking as the starting point, the structural parameters [2] of α-Eu$_2$(MoO$_4$)$_3$, we performed a profile matching to the diffractograms of the first experiment using the program FullProf [12]. We used a given instrumental resolution function to model the profile of our equipment and took, as fitting parameters, those related to microstrains and grain size. The instrument zero, the background and cell parameters were refined also. Fig. 1 shows the temperature dependence of the lattice parameters. With increasing temperature, the b and c lattice parameters expand monotonously over the entire range of temperatures. The a parameter, however, experiences a rapid contraction until 600 K. From 600 to 800 K, this parameter remains constant, within experimental error, and finally expands from 800 K to a higher temperature. Monoclinic angle, β, and volume behave monotonically, decreasing and increasing, respectively. The observed behavior of the a parameter, unusually anomalous, led us to conduct a more in-depth structural study, using the diffractograms of the second experiment.

In this work, we have applied a new alternative method for treating distorted structures by means of symmetry-mode analysis, performed using the program AMPLIMODES, developed in the Bilbao Crystallographic Server [13], and the Rietveld [14] refinement of the amplitudes of such symmetry modes, instead

of dealing with the atomic coordinates using the FullProf program [12]. The AMPLIMODES program gives the atomic coordinates of the more symmetric parent structure (scheelite, CaMoO$_4$) on the basis of the less symmetric and distorted structure (α-Eu$_2$(MoO$_4$)$_3$), supplying the crystallographic cell, the space group and the transformation matrix as input data. Moreover, this program determines the global structural distortion that relates both phases and the symmetry modes (amplitudes and polarization vectors) compatible with the symmetry break. Then, the amplitudes of such a collective mode were refined using FullProf. They can be initially zero, because we have the same parent structure, but it is transformed in the low symmetry space group basis. Afterward, we can refine the amplitude associated to both atoms and vacancies and also the occupation factors. Next, new atomic coordinates, including the vacancies, are calculated by FullProf, summing the distortion vectors to the initial ones. In order to calculate these distortions, the lattice parameters of the scheelite structure (CaMoO$_4$) [15] have been transformed to the cell lattice parameters corresponding to the Eu$_2$(MoO$_4$)$_3$ structure [2] by the matrix:

$$\begin{bmatrix} -1 & 0 & 2 \\ 1 & 0 & 1 \\ 0 & 1 & 0 \end{bmatrix} + \begin{bmatrix} 1/2 \\ 0 \\ 1/2 \end{bmatrix}. \tag{1}$$

The final structures are not very different from α-Eu$_2$(MoO$_4$)$_3$ [2] but we have observed an anomalous behavior of one of the three symmetry modes in which the distortion can be decomposed with respect to the parent scheelite structure. Fig. 2 shows this distortion (with respect to the scheelite structure) as vectors (colored arrows) for each oxygen: O1 (black), and other oxygen atoms (red). Heavier atoms Eu (green), Eu vacancy (white), Mo1 (dark brown) and Mo2 (light brown) do not show displacements.

There is a clear difference between the direction of the displacement of the oxygen O1 at 523 K with respect to both displacements at 723 and 923 K; however other oxygen displacements are similar. Then it should be possible to explain how the a axis pass from a negative to a positive expansion through the transverse displacements of O1 which is responsible for the changes in the Eu–O1–Mo1 bridging angle and the shortening (or lengthening) of the corresponding non-bonded Eu–Mo distance. Then, this structural effect could induce the formation of polarons [16] in this range of temperatures.

Table 1 shows the final structural parameters of α-Eu$_2$(MoO$_4$)$_3$ with space group $C2/c$, at three temperatures corresponding to

Table 1
Lattice parameters, fractional atomic coordinates and B factors of α-Eu$_2$(MoO$_4$)$_3$, with space group $C2/c$, at 523, 723 and 923 K corresponding to the three conducting regimes.

(Å)	523 K			723 K			923 K		
	x/a	y/b	z/c	x/a	y/b	z/c	x/a	y/b	z/c
Eu1	0.1696 (14)	0.62500	0.0902 (9)	0.1600 (4)	0.6265 (6)	0.0900 (4)	0.1598 (4)	0.6266 (7)	0.0902 (4)
Mo1	0.1507 (13)	0.1135 (7)	0.0678 (9)	0.1530 (16)	0.1128 (8)	0.0702 (10)	0.1547 (19)	0.1126 (9)	0.0706 (12)
Mo2	0.00000	0.3745 (11)	0.25000	0.00000	0.3736 (11)	0.25000	0.00000	0.3734 (13)	0.25000
O1	0.970 (4)	0.0451 (14)	0.095 (2)	0.969 (6)	0.047 (3)	0.089 (3)	0.952 (6)	0.040 (3)	0.084 (4)
O2	0.829 (4)	0.552 (2)	0.027 (2)	0.840 (4)	0.573 (3)	0.005 (3)	0.837 (5)	0.565 (3)	0.008 (3)
O3	0.739 (5)	0.2801 (14)	0.676 (3)	0.783 (6)	0.277 (3)	0.725 (4)	0.787 (6)	0.282 (3)	0.729 (4)
O4	0.317 (5)	0.7801 (14)	0.121 (3)	0.335 (6)	0.772 (3)	0.122 (4)	0.341 (6)	0.779 (3)	0.123 (3)
O5	0.874 (4)	0.462 (2)	0.270 (2)	0.879 (4)	0.456 (3)	0.276 (3)	0.874 (5)	0.460 (3)	0.281 (3)
O6	0.561 (5)	0.7199 (14)	0.954 (3)	0.629 (6)	0.709 (3)	1.011 (4)	0.635 (6)	0.704 (3)	1.020 (3)

	a (Å)	b (Å)	c (Å)	β (°)		R_B (%)	R_{exp} (%)	R_{wp} (%)	χ^2
523 K	7.48805 (4)	11.52048 (7)	11.6217 (2)	108.797 (3)		7.20	6.35	11.6	3.34
723 K	7.47959 (5)	11.57323 (9)	11.6627 (2)	108.698 (3)		7.64	7.03	12.5	3.24
923 K	7.48380 (6)	11.62335 (10)	11.6916 (2)	108.657 (3)		8.47	7.73	13.7	3.03

B (Å^2)	Eu1	Mo1	Mo2	O1	O2	O3	O4	O5	O6
523 K	0.68 (15)	0.4 (2)	0.9 (2)	1.3 (4)	1.3 (4)	1.3(4)	1.3 (4)	1.3 (4)	1.3 (4)
723 K	1.62 (18)	0.45 (18)	0.5 (2)	1.8 (5)	1.8 (5)	1.8 (5)	1.8 (5)	1.8 (5)	1.8 (5)
923 K	1.75 (20)	0.8 (2)	0.9 (3)	1.2 (6)	1.2 (6)	1.2 (6)	1.2 (6)	1.2 (6)	1.2 (6)
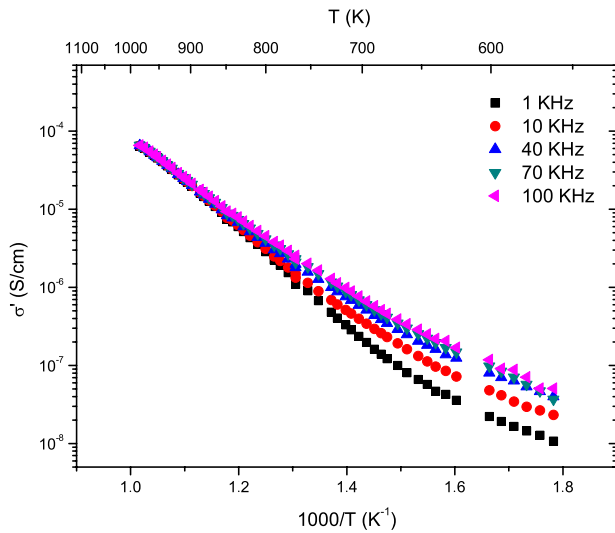
Fig. 3. Temperature dependence of σ' at five different frequencies, measured during the cooling cycle.

Fig. 4. Frequency dependence of the real part of the complex conductivity at several temperatures, measured during the cooling cycles. The solid lines are best fits to Eq. (3).

the three conducting regimes. The large values of R_B indicate that although the model is good, the statistics are not enough. For example, it is difficult to solve the possible thermal disorder in the oxygen atoms. We are performing a more exhaustive structural analysis in order to improve the structural correlation with the transport mechanisms which are described, for the first time, in this family of compounds.

The measured conductivity (σ') of α-Eu$_2$(MoO$_4$)$_3$ as a function of the inverse of temperature is shown in Fig. 3 for five different frequencies. It can be noticed from this figure that the conductivity is frequency-dependent in the temperature range below 623 K, while at higher temperatures it becomes strongly temperature-dependent and less frequency dependent, a behavior that is typical of polaron conduction [17,18]. At higher temperatures, the conductivity for all frequencies almost coincides with σ_{dc}. A similar behavior is expected for ionic conduction.

Considering the results shown in Fig. 3 and in order to investigate a possible polaron mechanism, we decided to study the conductivity in the temperature interval from 623 to 900 K. It has been previously shown [10] that for many amorphous and crystalline systems the real part of the complex conductivity $\sigma'(\nu)$

follows the so-called universal dielectric response behavior, that can be expressed as:

$$\sigma'(\nu) = \sigma_{dc} + A\nu^s \tag{2}$$

where, σ_{dc} is the dc conductivity, A is a temperature dependent constant, ν is the measuring frequency and the frequency exponent s is less than or equal to one. A slightly different version of the above equation is:

$$\sigma'(\nu) = \sigma_{dc}\left[1 + \cos\left(\frac{s\pi}{2}\right)\left(\frac{\nu}{\nu_p}\right)^s\right]. \tag{3}$$

Here, ν_p, the so-called crossover frequency, is the frequency where the slope change in the real part of complex conductivity occurs. In these models [11], each mechanism leads to a different frequency and temperature dependence for the conductivity and s exponent. The conductivity of the α-phase of Eu$_2$(MoO$_4$)$_3$ (σ') measured as a function of the frequency at various temperatures (623–834 K) is shown in Fig. 4. Solid lines in Fig. 4 show the typical fit obtained with Eq. (3), from which the temperature dependence of σ_{dc} and s can be obtained.

The variation of the dc conductivity, plotted as $\ln \sigma_{dc}$ versus $1000/T$, is shown in Fig. 5. It can be seen from this plot that there
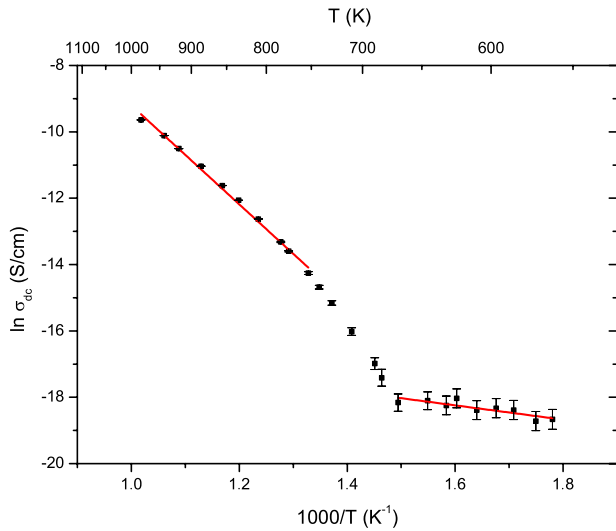
Fig. 5. Temperature dependence of the *dc* conductivity obtained from data corresponding to the cooling cycle. Error bars show the standard deviations. The solid lines are linear fittings in appropriate temperature intervals.

Fig. 6. Calculated temperature dependence of the frequency exponent *s* obtained from data recorded during the cooling cycle. Error bars show the standard deviations. The solid curve is a fit to the overlapping large polaron model [Eq. (5)].

are three regions with different conduction mechanisms. This type of temperature dependence of the *dc* conductivity indicates that the electrical conduction in these materials is a thermally-activated process, which can be explained using the Arrhenius relation:

$$\sigma_{dc} = \sigma_0 \exp\left(-\frac{E_a}{2k_BT}\right) \tag{4}$$

where σ_0 is a pre-exponential factor, E_a is the activation energy, and k_B is the Boltzmann constant. The values of the activation energy, calculated from the slope of the Arrhenius plot by fitting the experimental data to Eq. (4), are 0.34 ± 0.03 eV and 2.55 ± 0.3 eV for the lower temperature (below 700 K) and higher temperature regions, respectively.

The temperature dependence of the frequency exponent *s* is shown in Fig. 6. It can be seen that *s* decreases with increasing temperature up to a certain temperature, exhibiting a minimum at about 700 K. Such a behavior is predicted by the overlapping large polaron model (OLP) [8]:

$$s = 1 - \frac{8\alpha R_\omega + 6W_{H0}r_p/R_\omega k_BT}{[2\alpha R_\omega + W_{H0}r_p/R_\omega k_BT]^2} \tag{5}$$

where, W_{H0} and r_p are the energy barrier and polaron radius, respectively, and R_ω is the tunneling distance at a frequency $\omega = 2\pi\nu$, given by:

$$R_\omega = \frac{1}{4\alpha}\left[\ln\left(\frac{1}{\omega\tau_0}\right) - \frac{W_{H0}}{k_BT}\right]$$

$$+ \left\{\left[\ln\left(\frac{1}{\omega\tau_0}\right) - \frac{W_{H0}}{k_BT}\right]^2 + \frac{8\alpha r_p W_{H0}}{k_BT}\right\}^{1/2}. \tag{6}$$

The position of the minimum of the *s*–*T* curve matches that of the minimum of the lattice parameter *a*; see Fig. 1. Thus, the contraction of the *a* parameter can influence the formation of polarons. The fit with Eq. (5) is also depicted in Fig. 6. The calculated fitting parameters were $\ln\left(\frac{1}{\omega\tau_0}\right) = 42.58 \pm 2.13$, $W_{H0} = 2.62 \pm 0.13$ eV, $r_p = 0.57 \pm 0.03$ Å and $\alpha = 0.25 \pm 0.01$ Å^{-1}. The value of the factor $\ln\left(\frac{1}{\omega\tau_0}\right)$ is in the typical order of magnitude for the overlapping large polaron model [9]. The order of magnitude of the radius of the polaron is more typical of small polarons, which may be because, in our experiment, the temperatures are quite high compared with other studies. Temperature is an important
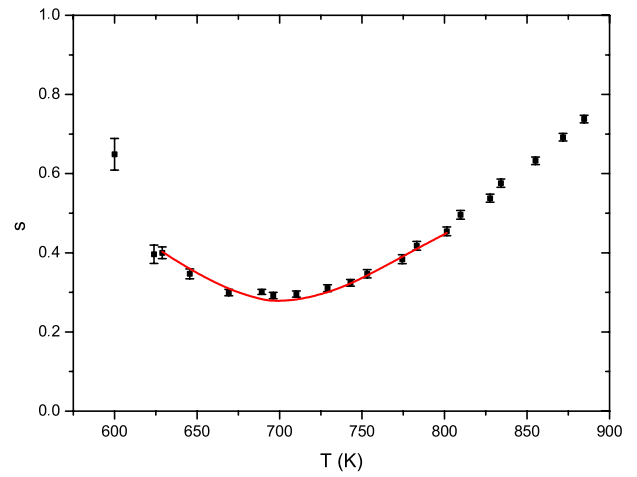
factor since as the temperature increases the thermal motion is greater and the ability to polarize the ions locally in the network is reduced. Although the model of Eq. (5) has been developed for large polarons, it is also valid for smaller radii [19]. On the other hand, the calculated energy barrier W_{H0} is high compared with other studies [20]; so we infer that at high temperatures the energy required to display this behavior is much greater. This energy is approximately the difference of the activation energy in the Arrhenius behavioral adjustment. From the calculated value of α and taking into account the *ac* conductivity in the overlapping large polaron model [9,8], given as follows,

$$\sigma'(\nu) = \frac{\pi^5}{6}e^2(k_BT)^2 N_f^2 \frac{\nu R_\omega^4}{2\alpha k_BT + W_{H0}r_p/R_\omega^2}, \tag{7}$$

we obtain a value of the density of states at the Fermi level $N_f \sim 10^{22}$ eV^{-1}cm^{-3}, which is a reasonable value for this parameter.

4. Conclusion

This work provides a detailed study of the transport properties of the scheelite-like α-Eu$_2$(MoO$_4$)$_3$ compound as a function of the temperature (550–900 K) and the frequency (0.1–10,000 kHz). The main result is that the conduction mechanism has been established using the overlapping large polaron model, after the interpretation of the fitting parameters according to this model, in the intermediate range from 630 to 800 K. Furthermore, we have found a clear correlation between the changes of the three conducting regimes, with an anomalous thermal dependence of the cell parameter *a*. Finally, we suggest that the different transversal displacements of one type of oxygen in Eu–O–Mo bridges can help to explain the no thermal dependence of the *a* parameter during the intermediate regimen and, therefore, this can be associated to the polaronic transport, but a more detailed structural study is necessary.

Appendix. Supplementary data

Supplementary material related to this article can be found online at doi:10.1016/j.ssc.2011.08.009.

References

[1] L.G. Sillen, A. Nylander, Ark. Kem. 17A (1943) 1.
[2] K. Boulahya, M. Parras, J.M. González-Calbet, Eur. J. Inorg. Chem. 5 (2005) 967.
[3] J.A. Dharmadhikari, A.K. Dharmadhikari, G.R. Kumar, Appl. Phys. Lett. 83 (2003) 2527.
[4] K. Gaur, M. Singh, H.B. Lal, J. Mat. Sci. 28 (1993) 3816.
[5] A.K. Tripathi, H.B. Lal, J. Phys. Soc. Japan 49 (1980) 1896.
[6] N.F. Mott, Adv. Phys. 50 (2001) 865.
[7] I.G. Austin, N.F. Mott, Adv. Phys. 50 (2001) 757.
[8] S.R. Elliott, Adv. Phys. 36 (1987) 135.
[9] A.R. Long, Adv. Phys. 31 (1982) 553.
[10] A.K. Jonscher, Dielectric Relaxation in Solids, Chelsea Dielectrics Press, London, 1983.
[11] C. León, M.L. Lucía, J. Santamaría, Phys. Rev. B 55 (1997) 882.
[12] J. Rodríguez-Carvajal, Physica B 192 (1993) 55.
[13] D. Orobengoa, C. Capillas, M.I. Aroyo, J.M. Perez-Mato, J. Appl. Cryst. A 42 (2009) 820.
[14] R.A. Young, The Rietveld Method, Oxford University Press, New York, 1993.
[15] International Tables for X-Ray Crystallography, vol. III, Kynoch Press, Birmingham, 1962.
[16] K.C. Kao, Dielectric Phenomena in Solids, Academic Press, San Diego, 2004.
[17] A. Levstik, C. Filipič, V. Bobnar, I. Levstik, D. Hadži, Phys. Rev. B 74 (2006) 153104.
[18] A. Levstik, C. Filipic, V. Bobnar, S. Drnovsek, J. Holc, Z. Trontelj, Z. Jaglicic, Solid State Commun. 150 (2010) 1249.
[19] M.P.J. van Staveren, H.B. Brom, L.J. de Jongh, Phys. Rep. 208 (1991) 1.
[20] S. Bhattacharya, A. Ghosh, Phys. Rev. B 68 (2003) 224202.

Structural anomalies related to changes in the conduction mechanisms of α-Sm$_2$(MoO$_4$)$_3$

C Guzmán-Afonso[1], C González-Silgo[2], M E Torres[3], E Matesanz[4] and A Mujica[2]

[1] Departamento de Física Fundamental y Experimental, Electrónica y Sistemas, Universidad de La Laguna, E-38206 S/C Tenerife, Spain
[2] Departamento de Física Fundamental II and MALTA Consolider Team, Universidad de La Laguna, E-38206 S/C Tenerife, Spain
[3] Departamento de Física Básica, Universidad de La Laguna, E-38206 S/C Tenerife, Spain
[4] C A I Difracción de Rayos X, Universidad Complutense de Madrid, E-28040 Madrid, Spain

E-mail: mcguzman@ull.es

Abstract

Polycrystalline samples of α-phase samarium molybdate were prepared by solid-state synthesis and used for x-ray diffraction (from 300 to 1000 K) and dielectric spectroscopy (from 500 to 900 K and from 10^2 to 10^6 Hz). The electrical conductivity follows the universal dielectric response, and three different regimes of conduction (with semiconductor, polaronic, and ionic characteristics) were ascribed. The polaronic mechanism in the range from 600 to 810 K was probed using the overlapping large polaron model. Above 810 K, the application of scaling laws suggests an ionic conductivity. The thermal dependence of the lattice parameter a shows three different trends in correspondence with the three conduction regimes observed. An analysis using adapted symmetry modes facilitated the Rietveld refinement and the study of the thermal dependence of the distortion arising from the oxygen displacements. We suggest that the transversal displacements of oxygen atoms in Sm–O–Mo bridges joined to the elongation of tetrahedra can help to explain this anomalous behavior. From the calculated bond-valence contour maps, new sites for the oxygen atoms, at higher temperatures, were detected which favor oxygen motion and would then be related to the ionic conduction. This correlation has been compared and extended to α-Eu$_2$(MoO$_4$)$_3$.

(Some figures may appear in colour only in the online journal)

1. Introduction

Tungstates and molybdates, ABX$_4$ compounds with scheelite-type structure, are technologically important materials with applications as phosphors [1], detectors of ionizing radiation [2, 3], efficient laser hosts [4], and Raman shifters [5]. In recent years, scheelite-type oxides (PbWO$_4$) have been found to exhibit a high oxide-ion conduction in intermediate temperature ranges [6]. Furthermore, in the last few years there has arisen renewed interest in scheelite-type compounds and their evolution under pressure [7], a kind

of study which is fast becoming an important subject on its own because pressure can provide valuable insight into the structural, electronic, and transport properties of these materials.

Rare earth (RE) tritungstates and trimolybdates RE$_2$(MO$_4$)$_3$ (with M = W or Mo) adopt different crystalline structures depending on both the rare earth cation and the method of synthesis. Light rare earth molybdates and tungstates crystallize in the scheelite-type structure of CaWO$_4$ with one third of the positions occupied by calcium being vacant. One can distinguish three different arrangements

depending on the ordering of the vacancies. The crystal structures of $RE_2(MoO_4)_3$ (with RE = La, Ce, Pr, Nd) are monoclinic with space group $C2/c$ and $Z = 12$ [8]. Another different crystal structure has been found for $Bi_2(MoO_4)_3$, with space group $P2_1/c$ and $Z = 4$ [9] while lighter tritungstates $RE_2(WO_4)_3$ (with RE = La–Dy) have space group $C2/c$ but $Z = 4$ [10]. In particular, α-$Eu_2(MoO_4)_3$ and α-$Sm_2(MoO_4)_3$ belong to this last group [11, 12]. The so-called β'-phases of the rare earth trimolybdates are not of the scheelite-type family and their structural and dielectric properties have been well studied on account of their ferroelectric properties [13, 14]. On the other hand, the heavier tritungstates and trimolybdates (RE = Ho–Lu), with the same structure as that of γ-$Sc_2(WO_4)_3$ [15], exhibit negative thermal expansion [16]. These materials are also well known for their trivalent cation conductivity [17]. However, few works have been published dealing with the conductivity of the α-phase of rare earth tritungstates and trimolybdates in comparison with those for the β' and γ phases and for other ABX_4 compounds.

Electric transport studies of rare earth molybdates (from La to Eu) have shown the existence of different linear regions with break temperatures associated to a change in the conduction mechanism [18]. By using dc conductivity and Seebeck coefficient measurements, Gaur *et al* [18] proposed, without a more exhaustive study, that the conduction can be intrinsic with large polarons of intermediate coupling as the main charge carriers. We have recently reported a dielectric spectroscopy study of α-$Eu_2(MoO_4)_3$ using the overlapping large polaron model [19] to explain the mechanism of charge carriers in this compound at temperatures from 630 to 800 K, which we found correlated with an anomaly in its thermal expansion detected when analyzing the thermal dependence of the crystal structure within this range of temperatures [20]. In the present work, we extend the study of the transport and structural properties to the isostructural compound α-$Sm_2(MoO_4)_3$, which allows a comparison with europium molybdate, reaching a more general description of the transport properties in this family of compounds and their correlation with thermal expansion. We are especially interested in possible ionic transport mechanisms at high temperatures for these type of materials and for that purpose we have also added a new study, typical among ionic conductors, using scaling theories [21] and bond-valence contour maps [22].

2. Experimental details

Depending on the method of preparation, rare earth trimolybdates can be obtained in either the α or β' forms [23]. In particular, our α-$Sm_2(MoO_4)_3$ samples were prepared by conventional solid-state synthesis. MoO_3 and Sm_2O_3 powder (Aldrich, 99.99%) were pre-heated at 923 K and 1173 K, respectively, for 10 h before use. These pre-heated powders were weighed in stoichiometric amounts, mixed and homogenized in an agate mortar. The resulting powder was pressed (3 tn) into cylindrical pellets 13 mm in diameter and 1 mm in thickness, approximately, and finally synthesized

in air atmosphere at 1123 K for 48 h in a platinum crucible. The α-phase was confirmed by x-ray diffraction to be without impurities. The conductivity measurements were carried out using a computer-controlled Hewlett–Packard 4192 impedance analyzer. One pellet was selected (with the given dimensions) and their parallel surfaces were coated with platinum paste. The pellet sample was then placed into the cell, which consists of a parallel plate capacitor located at the end of a coaxial line. This cell was enclosed in a resistance-heated furnace and the temperature was monitored using a thermocouple within an accuracy of ± 0.1 K. Measurements of the dielectric permittivity were recorded during a heating and cooling cycle, in the frequency range from 10^2 to 10^6 Hz with an applied voltage of 0.7 Vpp, over the temperature range from 500 to 900 K, which was dynamically scanned (at a rate of 1.2 K min^{-1}) with measurements taken in steps of 5 K. The complex permittivity was obtained from the dielectric spectroscopy measurements and was divided into a real and imaginary part. The imaginary part was used to obtain the real part of the complex conductivity (σ'). Data for the dependence of σ' on frequency (ν, in Hz) were scanned at each temperature. Two diffraction runs, at different temperatures, were performed using powder samples from the remaining pellets. In both runs, the powder diffraction data were collected in a PANalytical X'Pert PRO diffractometer (Bragg–Brentano mode) with an X'Celerator detector using Cu Kα radiation and a Ni β-filter. All measurements were carried out during a heating process under still air atmosphere, using an Anton Paar HTK-2000 camera. The first experimental setting permitted us to obtain the cell parameters from 300 to 1000 K of the whole-pattern fits [24]. The angular range $5° < 2\theta < 80°$ was scanned at a step size of 0.017° and 100 s step time. Divergence and anti-scatter slits were set at 0.5° and 0.5°, respectively, and the detector was used in scanning mode with an active length of 2.12°. 0.02 rad incident and diffracted Soller slits were used. A second experimental setting was used, at three selected temperatures (450, 650, and 850 K) for obtaining better counting statistics and increasing the magnitude of the scattering vector Q in order to perform Rietveld refinements [25]. With respect to the first run, only the range of scans and step time were changed to $10° < 2\theta < 120°$ and 300 s, respectively.

3. Results and discussion

3.1. Transport properties

All the results shown here correspond to data obtained during cooling cycles. (Data collected in heating cycles yield essentially the same results.) Figure 1(a) shows a plot of the experimental $\log \sigma'$ versus inverse temperature at five selected frequencies. The conductivity is strongly temperature and frequency dependent up to high temperatures over 800 K where its dependence on frequency becomes less pronounced. A similar behavior was previously found by us in $Eu_2(MoO_4)_3$ [20], with the change occurring around 750 K. The frequency dependence of σ' is shown in figure 1(b), where it is possible to detect a cross frequency dividing at
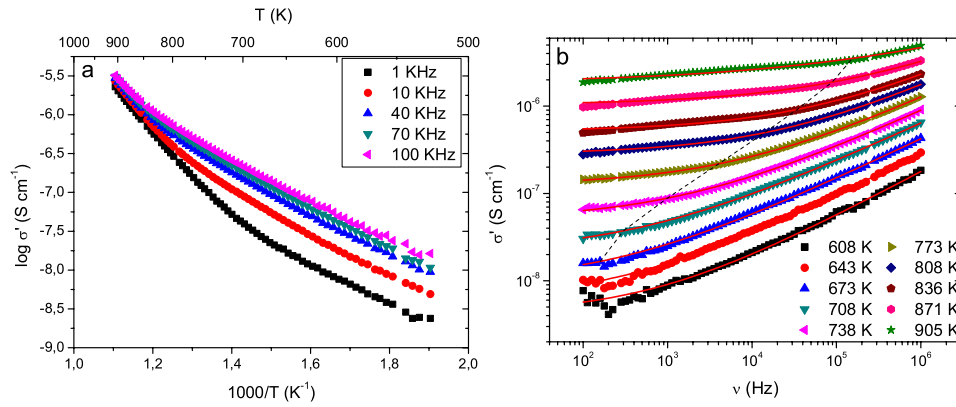
Figure 1. (a) Temperature dependence of σ' at five frequencies and (b) frequency dependence of σ' at several temperatures for α-$Sm_2(MoO_4)_3$. The solid lines are the fits to equation (2). The dashed line in (b) indicates the crossover frequency at each temperature.

least two slopes, for each temperature. Considering the results shown in figures 1(a) and (b) and in order to investigate possible different types of conductivity mechanisms, we decided to study the conductivity in the temperature interval from 525 to 905 K and the frequency interval from 10^2 to 10^6 Hz. The conductivity spectra analysis is based on the Universal Dielectric Response (UDR) behavior as an empirical power law to describe the frequency dependence of the dielectric response in a wide range of disordered materials, including ionic glasses, nonstoichiometric crystals, polycrystalline and amorphous semiconductors, organic acids, and ionic or electronic conducting polymers [26–28]. In particular, the real part of the conductivity spectra $\sigma'(\nu)$ tends towards the dc conductivity as the frequency decreases and shows a dispersive regime where the conductivity strongly increases with the frequency. Jonscher [29] proposed to describe the frequency dependence of the ac conductivity by an equation of the type:

$$\sigma'(\nu) = \sigma_{dc} + A\nu^s \qquad (1)$$

where σ_{dc} is the dc conductivity, A is a temperature-dependent parameter and s is a fractional exponent with values between 0 and 1, depending on many body interactions among charge carriers. A slightly different version of the above equation is:

$$\sigma'(\nu) = \sigma_{dc}\left[1 + \cos\left(\frac{s\pi}{2}\right)\left(\frac{\nu}{\nu_p}\right)^s\right] \qquad (2)$$

where the crossover frequency ν_p and the term $\cos(\frac{s\pi}{2})$ are introduced [30]. This last factor affects the calculated value for the crossover frequency which determines the frequency of the slope change, dividing the behavior of $\sigma'(\nu)$ in the mentioned two regions which are detected in figure 1(b), where we also represent by solid lines the fitting of these experimental values using equation (2). From these fittings we obtained the temperature dependence of σ_{dc}, s, and ν_p. We could use equation (2) until 905 K. Above this temperature the value of ν_p was very close to the measured frequency limit (10^6 Hz) and the fitting was worse.

The dc conductivity and the crossover frequency obtained from the fitted curves exhibit an Arrhenius-type temperature

dependence:

$$\sigma_{dc} = \sigma_0 \exp\left(-\frac{E_a}{2k_BT}\right). \qquad (3)$$

This dependence enables us to know if the electrical conduction in these materials is a thermally activated process at a range of temperatures, where σ_0 is a pre-exponential factor, E_a is the activation energy, and k_B is the Boltzmann constant. The variation of the dc conductivity, plotted as $\ln\sigma_{dc}$ versus $1000/T$, is shown in figure 2. As can be seen, there are three regions with different activation energies, which agrees with the study of Guzmán-Afonso *et al* [20]. Equation (3) was fitted within each of the three different temperature intervals 533–638 K, 638–688 K, and 688–899 K, respectively. The values obtained for the activation energy E_a calculated from the different slopes in figure 2 were: 0.27 ± 0.03 eV, 1.3 ± 0.1 eV, and 2.6 ± 0.3 eV for the low, intermediate, and high temperature regions, respectively. These values are slightly smaller than those previously obtained in europium molybdate [20] but the ratio between the two activation energies of both compounds is the same as the ratio reported in Gaur *et al* [18] using other experimental techniques.

Three thermally activated processes can be distinguished in figure 2. In the first region, the conductivity is very low and it is difficult to perform an exhaustive study by dielectric spectroscopy alone. It is known that tungstates and molybdates with the tetragonal scheelite structure (SG $I4_1/a$) are wide bandgap semiconductors [31]. This type of compound exhibits very narrow and highly correlated 4f bands and the participation of 4f electrons in conduction is unlikely [32]. It seems, however, likely that the electrons in 5d bands, thermally excited from the 4f or 5p bands, and the holes left are responsible for the electrical conduction. However, an additional contribution has been detected by other techniques (Hall and Seebeck effects [33]) which might be due to impurity defects and mixed states. For instance, in this region the low activation energy is twice the typical ionization energy of the ionized impurity centers (donors or acceptors) [32] and this mechanism is responsible for the observed value of the Hall coefficient. We are presently investigating, by dielectric
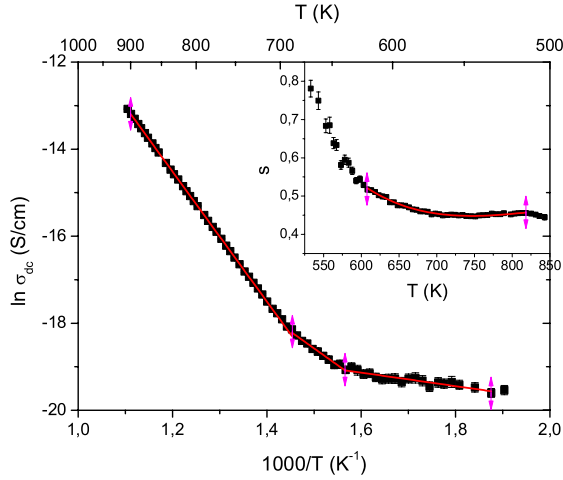
Figure 2. Temperature dependence of the dc conductivity for α-$Sm_2(MoO_4)_3$. The solid lines are linear fittings in appropriate temperature intervals (delimited by marks). The inset shows the calculated temperature dependence of the frequency exponent s obtained from the data and the solid curve is the fit to the overlapping large polaron model (equations (7) and (8)).

spectroscopy and other dc conductivity techniques, several members of the trimolybdates family with different crystal structures at low temperatures.

With respect to the second region, a strong dependence on temperature and frequency suggests a polaron behavior [18, 19]. The inset to figure 2 shows the temperature dependence of the frequency exponent s. Any deviation of the value of s from unity discloses information on the particular type of loss mechanism involved [26]. There is a variety of theoretical approaches that deduce the temperature and even frequency dependence of s from the microscopic transport mechanisms, involving the classical hopping of a carrier over the potential barrier separating two energetically favorable sites and quantum-mechanical tunneling through the barrier separating two equilibrium positions [19]. In this region we have compared different models with our experimental findings: correlated barrier hopping (CBH), quantum-mechanical tunneling (QMT), small polaron (SP) and overlapping large polaron (OLP) [19, 34]. In figure 2 it can be seen that s decreases with increasing temperature until it reaches a minimum at 750 K and then increases with the rise of temperature. According to the QMT model defined by equation (4), s is temperature independent but frequency dependent and thus this model is unable to explain the experimental results presented in figure 2. The CBH model given by equation (5), where W_M is the effective barrier height, is not applicable in this region, because s decreases gradually with increasing temperature. In the small polaron model described by equation (6), where W_H is the polaron hopping energy, s is temperature dependent, but increases with increasing temperature, in contrast to figure 2. In the overlapping large polaron (OLP) model, characterized by equations (7) and (8), the exponent s is both temperature and frequency dependent; s initially decreases with increasing temperature, it reaches a minimum at a particular temperature

and then increases with the rise of temperature. This behavior is in good agreement with the results shown in figure 2. Originally this model was developed for the tunneling of overlapping large polarons, but it was later argued that it is in fact applicable to small polarons as well [35].

$$s = 1 - \frac{4}{\ln(\frac{1}{\omega\tau_0})} \tag{4}$$

$$s = 1 - \frac{6k_BT}{W_M + k_BT\ln(\omega\tau_0)} \tag{5}$$

$$s = 1 - \frac{4}{\ln(\frac{1}{\omega\tau_0}) - \frac{W_H}{k_BT}} \tag{6}$$

$$s = 1 - \frac{8\alpha R_\omega + 6W_{H0}r_p/R_\omega k_BT}{[2\alpha R_\omega + W_{H0}r_p/R_\omega k_BT]^2} \tag{7}$$

$$R_\omega = \frac{1}{4\alpha}\left[\ln\left(\frac{1}{\omega\tau_0}\right) - \frac{W_{H0}}{k_BT}\right]$$
$$+ \left\{\left[\ln\left(\frac{1}{\omega\tau_0}\right) - \frac{W_{H0}}{k_BT}\right]^2 + \frac{8\alpha r_p W_{H0}}{k_BT}\right\}^{1/2}. \tag{8}$$

In equations (7) and (8), W_{H0} denotes the energy barrier, r_p is the polaron radius, R_ω is the tunneling distance, and α is the wavefunction decay constant. The fitting to this model in the range of temperatures from 608 to 818 K is depicted by a solid line in the inset of figure 2. The calculated fitting parameters were: $\ln(1/\omega\tau_0) = 18.9 \pm 0.2$, $W_{H0} = 1.01 \pm 0.06$ eV, $r_p = 1.6 \pm 0.2$ Å and $\alpha = 0.39 \pm 0.07$ Å^{-1}. The value of the factor $\ln(1/\omega\tau_0)$ is within the typical order of magnitude for the OLP model [36]. The characteristic relaxation time τ_0 is 6×10^{-13} s at an intermediate frequency of 10^4 Hz. The value obtained for the polaron radius r_p is adequate within the OLP model [19]. On this occasion, we obtained a larger value than the polaron radius previously calculated for europium molybdate, but it is very similar to the one obtained for $EuWO_4$ in the range $680 < T(K) < 725$ (which the authors of [32] calculated by assuming the number of sites per unit volume). Moreover, the calculated energy barrier W_{H0} is smaller than that obtained for europium molybdate (2.62 eV), and this may be related to the activation energy which is smaller too, as we discussed earlier. In $EuWO_4$, the authors of [32] assumed a region $500 < T(K) < 680$ in which the conduction is by large polarons with an activation energy of 1.51 eV higher than the energy of 0.346 eV observed in the small polaron region. We cannot distinguish these two regions in our compounds, as they could be mixed in the present case. Although in $Sm_2(MoO_4)_3$ the polaron radius and the calculated energy barrier W_{H0} are smaller and higher, respectively, than typical values obtained in other studies [35], we consider the model of equations (7) and (8) developed for large polarons as essentially valid in this case. The differences observed between the calculated values of r_p and W_{H0} of $Sm_2(MoO_4)_3$ and $Eu_2(MoO_4)_3$ come from the fitting of s at higher temperatures for europium molybdate (values of $Sm_2(MoO_4)_3$ are better for the OLP model). Temperature is an important factor since as temperature increases the thermal motion is greater and the ability to

polarize the ions locally in the network is reduced, then r_p diminishes and W_{H0} can increase [20].

In order to study the third region, where the conductivity is less dependent on frequency, and to make a comparison with the other two regions and with previous results on europium molybdate, the conductivity spectra at different temperatures of $Sm_2(MoO_4)_3$ and $Eu_2(MoO_4)_3$ were scaled. The conductivity spectra, at different temperatures, can lead to a single master curve, indicating that the conduction mechanism does not depend on temperature. This fact is known as a time–temperature superposition principle (TTSP) [37] and it can be expressed by the following scaling law [38]:

$$\frac{\sigma'}{\sigma_{dc}} = F\left(\frac{\nu}{\nu^\star}\right) \tag{9}$$

where $\nu^\star$ is the characteristic frequency or scaling frequency used to scale the conductivity spectra. The scaling method consists in choosing a function depending on frequency, temperature, dc conductivity, concentration of mobile charge carriers, etc, for the frequency axis. In the past few years, different scaling models have been proposed [37, 39]. We have used the same scaling method as the authors of [37, 40] for their ionic compounds (glasses, crystals):

$$\frac{\sigma'}{\sigma_{dc}} = F\left(\frac{\nu}{\sigma_{dc}T}\right) \tag{10}$$

where the factor $\sigma_{dc}T$ was used as the scaling parameter with the advantage that it is a directly accessible quantity instead of an arbitrarily determined parameter $\nu^\star$. Figure 3 shows the scaling of the conductivity at high temperatures for both compounds. We see that the conductivity collapses on a single curve above 809 K for $Eu_2(MoO_4)_3$. For $Sm_2(MoO_4)_3$ this temperature boundary is less clear, though the collapse appears to occur at around the same value. From figure 3 it can be seen that data at 750 K for both compounds do not scale properly in the single master curve, a fact that is again more clearly seen in the case of $Eu_2(MoO_4)_3$ due to more abrupt changes in the conductivity between different regions (see [20]). This implies that the relaxation dynamics of charge carriers is independent of temperature in this region, which is better defined for $Eu_2(MoO_4)_3$. Typically, for ionic conduction, the concentration of charge carriers is weakly temperature dependent and the temperature dependence of the conductivity arises from the mobility of the ions [39]. Then, using the Nernst–Einstein relation [41]:

$$\sigma_{dc} = \frac{n_c e^2 \gamma \lambda^2 H_R \nu_H}{k_B T} \tag{11}$$

must result in a constant concentration of mobile charge carriers in this region. In equation (11), the parameter n_c is the concentration of mobile charge carriers, e is the electronic charge, λ is the hopping distance, γ is a geometrical factor for ion hopping ($\gamma = 1/6$ for isotropic materials), H_R is the Haven ratio which indicates the degree of correlation between the successive hops, and ν_H is the hopping frequency of mobile ions. We have estimated n_c from equation (11), assuming that the crossover frequency is equal to the hopping
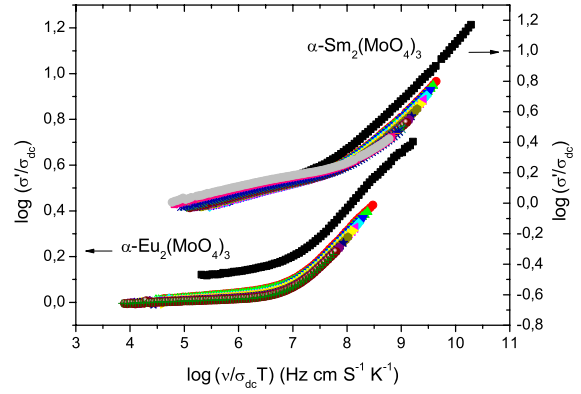
Figure 3. Master plot of the conductivity spectra of α-$Sm_2(MoO_4)_3$ and α-$Eu_2(MoO_4)_3$ in the temperature ranges from 810–905 K and 809–886 K, respectively. The data at 750 K are also shown, as a black square symbol, for both compounds.

frequency of the hopping ions, which has been widely used in previous works [39, 42–44], so that σ_{dc} and ν_p are obtained from equation (2). Moreover we used the mean values of R_ω and s, as λ and H_R respectively, because their definitions are very similar. The result for the concentration of charge carriers was about 2.9×10^{22} and 1.4×10^{22}, almost constant in this region for $Sm_2(MoO_4)_3$ and $Eu_2(MoO_4)_3$, respectively, suggesting only a weak temperature dependence of the concentration of charge carriers. Other ionic conductors with scheelite-type structure have been studied and show a similar behavior and conductivity values at high temperatures [45].

3.2. Structural characterization

In order to obtain the thermal dependence of the crystallographic cell parameters we analyzed the diffraction patterns in our first run for each temperature from 300 to 1000 K. We obtained the scale factor, instrument zero, cell parameters, microstrain and domain size (given by U and Y, parameters from the profile function), and the background coefficients from powder diffraction data by iterating full pattern profile fittings, with the Le Bail algorithm [24], using the FullProf program [46]. We started with the crystallographic cell of α-$Sm_2(MoO_4)_3$ [12], the instrumental resolution function (Thomson–Cox–Hastings pseudo-Voight with axial divergence asymmetry [47]), which was defined for our diffractometer, with the background modeled by a Chebyshev polynomial with eight coefficients. In total, 16 different parameters were refined.

Figure 4 shows the temperature dependence of the lattice parameters obtained from the first run (solid symbols). With increasing temperature, the lattice parameters b and c expand monotonously over the entire range of temperatures. The parameter a, however, undergoes a contraction until 600 K. From 600 to 700 K this parameter remains constant and finally increases beyond 700 K. The monoclinic angle β decreases and the volume increases. Thus, we can distinguish three different regions, depending on the behavior of the parameter a, according to those observed in the Arrhenius
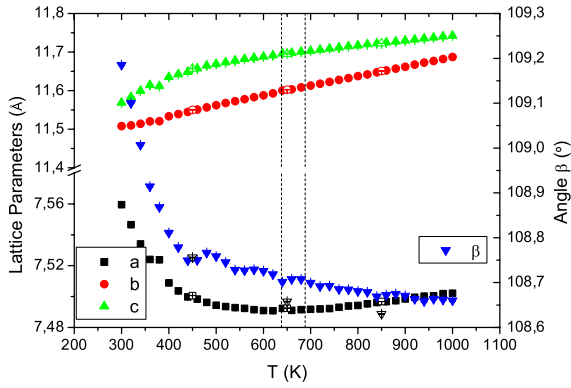
Figure 4. Temperature dependence of the lattice parameters for α-Sm$_2$(MoO$_4$)$_3$. The solid symbols are the profile matching and the open symbols the Rietveld refinement.

plot of figure 2. The anomalous contraction of the parameter *a* below 600 K corresponds to the semiconductor behavior. The conduction by polarons occurs, approximately, when *a* is practically constant. When the parameter *a* clearly increases (at 800 K), the transport mechanism corresponds to ionic conduction. Similar thermal dependences of cell parameters were obtained for α-Eu$_2$(MoO$_4$)$_3$ [20]. In that case the parameter *a* remains constant at higher temperatures than in samarium molybdate. The minimum value of the parameter *a* occurs at 753 K while for samarium molybdate it occurs at 620 K. This shift upwards in temperatures for europium molybdate is also observed in its dc conductivity behavior. It thus appears that both the thermal dependence of the cell parameter and the electrical conductivity are correlated.

The observed behavior of the parameter *a*, anomalous and clearly correlated with the changes in the conduction mechanism, led us to conduct a more in-depth structural study using the diffractograms obtained during the second run in which the counting statistics and the angular range were increased. These diffraction patterns were used to apply a new alternative method for treating distorted structures by means of symmetry-mode analysis, performed using the AMPLIMODES program, in the Bilbao Crystallographic Server [48], and the Rietveld [25] refinement of the amplitudes of such symmetry modes, instead of dealing with the atomic coordinates using the FullProf program [46]. This method is especially useful for treating structures with a great number of atomic positions which are free parameters where their displacements are correlated through the analysis of modes [49]. The AMPLIMODES program gives the atomic coordinates of the more symmetric parent structure on the basis of the less symmetric and distorted structure, supplying the crystallographic cell, the space group, and the transformation matrix as input data.

We assumed that, at very high temperature, rare earth tritungstates and trimolybdates, with distorted scheelite structures, undergo a transition to a more disordered phase with tetragonal scheelite-type structure CaMoO$_4$ [50, 51]. The crystal structure, in all the ranges of temperatures studied, is the monoclinic α-phase of the rare earth tritungstates

and trimolybdates, where one third of the calcium atoms substituted by RE form vacancies. The program determines the global structural distortion that relates both phases and the symmetry modes (amplitudes and polarization vectors) compatible with the symmetry break. In order to calculate these distortions, the lattice parameters of the scheelite structure were transformed to the cell parameters corresponding to the α-Sm$_2$(MoO$_4$)$_3$ structure [12] using the transformation matrix:

$$\begin{bmatrix} -1 & 0 & 2 \\ 1 & 0 & 1 \\ 0 & 1 & 0 \end{bmatrix} + \begin{bmatrix} 1/2 \\ 0 \\ 0 \end{bmatrix}. \tag{12}$$

Then, the amplitudes of such a collective mode were refined using FullProf. We started from the less distorted structure at 850 K and the amplitudes were initially zero, i.e. with the same parent structure in the basis of the space group with lower symmetry. The refined amplitudes obtained at 850 K were used as the starting point for the analysis at 650 K, and the results of this analysis were in turn used for the analysis at 450 K. It must be taken into account that the amplitudes associated with both atoms and vacancies (with the occupation factors fixed to zero) were refined too. After the refinement, new atomic coordinates were calculated using FullProf, summing up the distortion vectors to the initial ones. Also, scale, cell parameters, size domains, microstrain, and background coefficients were refined by the Rietveld method, using the same profile function and polynomial as in previous runs, at the same time as the amplitudes of the symmetry modes.

The final structures were not very different from that of the α-phase [12] but we have observed a thermal dependence of the symmetry modes in which the distortion can be decomposed with respect to the scheelite structure. From the symmetry-mode analysis, the distortion was decomposed in three symmetry modes, given by the irreducible representations: *GM*1+, *GM*2+, and *DT*2. The oxygen atom displacements are larger than those of the heavier atoms and, in general, the behavior of different distortion components (oxygen displacements given in terms of symmetry modes) are similar to those observed in Eu$_2$(MoO$_4$)$_3$ [20]. The *GM*1+ mode, at the center of the Brillouin zone, keeps the parent symmetry and decreases from 0.31 to 0 Å when the temperature increases from 450 to 850 K. The mode of symmetry *DT*2 is associated to the point Δ(1/3, 1/3, 0) and triples the tetragonal scheelite cell. This distortion decreases slightly from 1.10 to 0.94 Å when the temperature increases. The *GM*1+ and *DT*2 symmetry modes show a normal behavior, whereas the ferroelastic *GM*2+ mode at the center of the Brillouin zone breaks the tetragonal symmetry to monoclinic and increases slightly from 0.25 to 0.42 Å when the temperature increases. This distortion could be correlated with anomalous behavior in the monoclinic angle β.

In figure 5 the structures of α-Sm$_2$(MoO$_4$)$_3$ at 300, 450, 650, and 850 K are shown. Heavier atoms and their polyhedra are differently colored. In the four panels of figure 5 it is possible to see, qualitatively, the relative change of the
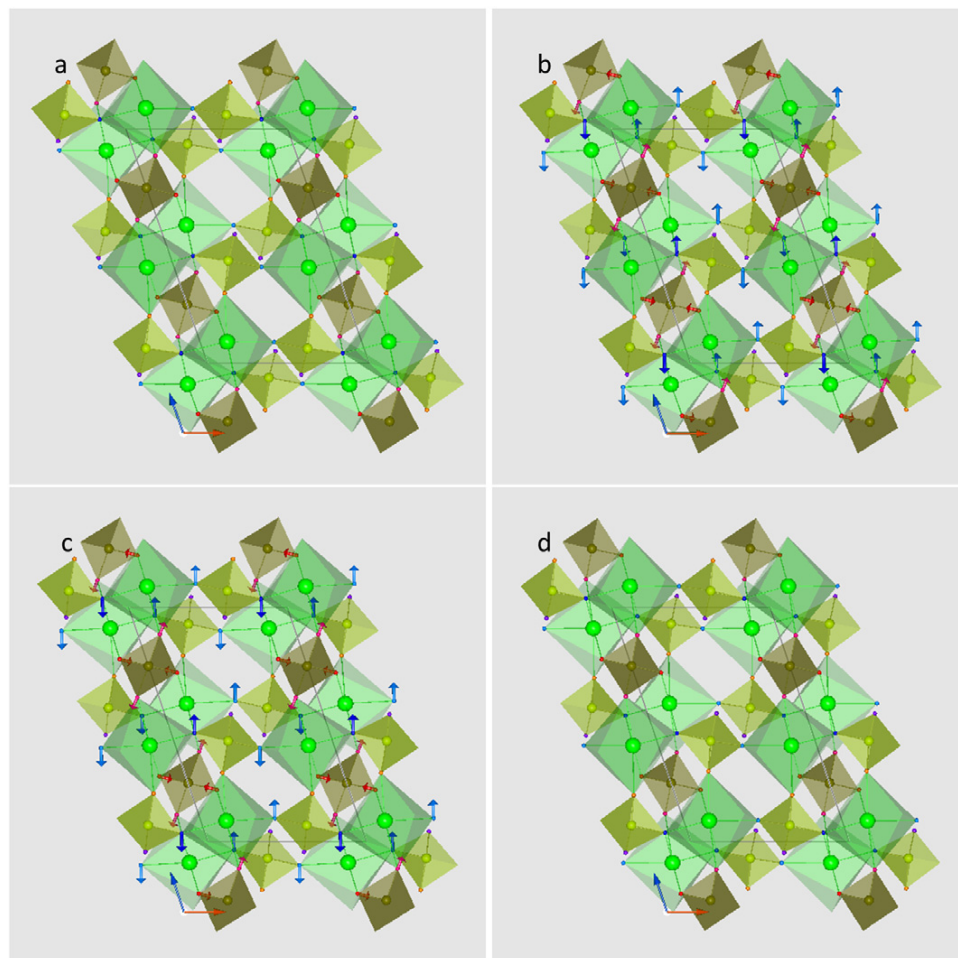
Figure 5. Projection of a layer of α-Sm$_2$(MoO$_4$)$_3$ in a plane perpendicular to the *b* axis, at (a) 300 K, (b) 450 K, (c) 650 K, and (d) 850 K. The arrows indicate the oxygen displacements involving transversal modes and elongation of tetrahedra perpendicular to the *a* axis at intermediate temperatures. Each ion is represented by a different color: Sm (green), Mo1 (brown), Mo2 (yellow), O1 (dark blue), O2 (light blue), O3 (violet), O4 (red), O5 (orange), and O6 (pink).

distortion with increasing temperature. The more symmetric tetrahedron around Mo1 shows an elongation perpendicular to the *a* axis at intermediate temperatures. Note that this tetrahedron is not connected to Sm atoms through oxygen bridges in the *a* direction. There is also a short displacement of the oxygen atoms O1 and O2 perpendicular to the *a* direction which in turn results in a change of the Sm–O(1, 2)–Mo2 bridging angles and the shortening of the Sm–Mo2 distances, a typical observation for transversal modes in compounds with negative expansion [52]. The shortening of the distance between Sm and Mo along the *a* axis is related to the negative expansion of this cell parameter. A novel and detailed explanation using this type of analysis for yttrium and other rare earth molybdates can be found in [16], including accurate coordinates for the oxygen atoms and comparison of the distortions at several temperatures.

Table 1 shows the final refined structural parameters of α-Sm$_2$(MoO$_4$)$_3$ at three temperatures, corresponding to the three different conduction regimes. We presented a similar table for Eu$_2$(MoO$_4$)$_3$ in [20]. In the current study,

the R_B factor is smaller than in α-Eu$_2$(MoO$_4$)$_3$, indicating that the oxygen positions are better calculated and that the previous analysis has been improved. This observed structural effect could induce the formation of polarons in this range of temperatures and produce the change in conduction mechanisms from semiconductor to insulator. Similar behaviors, involving structural and conductivity anomalies, have been described in recent works [53–56].

Analysis of the conductivity spectra of samarium and europium molybdates at high temperatures evidence an ionic conduction mechanism, but we cannot distinguish the type of charge carrier. Several studies show that oxide-ion conductors have a similar behavior at high temperature and where the anion concentration is also similar to our estimation of carriers concentration. However, trivalent cationic conduction is described for tritungstates and trimolybdates with formula A$_2$(MO$_4$)$_3$, where A is a trivalent metal or rare earth with smaller ionic radius [17]. We have carried out the bond-valence sum calculations in order to check that the structures obtained at different temperatures are chemically valid and

Table 1. Lattice parameters, fractional atomic coordinates, and *B* factors of α-$Sm_2(MoO_4)_3$, with space group $C2/c$, at 450 K, 650 K, and 850 K, corresponding respectively to the three conduction regimes.

(Å)	450 K			650 K			850 K		
	x/a	*y/b*	*z/c*	*x/a*	*y/b*	*z/c*	*x/a*	*y/b*	*z/c*
Sm1	0.331(1)	0.6238(5)	0.9098(7)	0.3393(2)	0.625 00	0.9107(2)	0.3338(8)	0.625 00	0.9095(5)
Mo1	0.653(1)	0.8818(6)	0.0686(7)	0.658(1)	0.8783(4)	0.0701(6)	0.655(1)	0.8800(3)	0.0702(7)
Mo2	0.500 00	0.3723(9)	0.750 00	0.500 00	0.3684(8)	0.750 00	0.500 00	0.3651(6)	0.750 00
O1	0.146(2)	0.047(1)	0.965(1)	0.148(2)	0.0459(4)	0.964(1)	0.156(2)	0.0498(7)	0.970(1)
O2	0.027(2)	0.5451(4)	0.898(2)	0.027(2)	0.5459(4)	0.900(2)	0.028(2)	0.5498(7)	0.885(1)
O3	0.923(3)	0.279(1)	0.548(2)	0.916(3)	0.2820(7)	0.543(2)	0.877(3)	0.275(1)	0.552(2)
O4	0.164(2)	0.957(1)	0.724(1)	0.167(2)	0.9541(4)	0.721(1)	0.160(2)	0.9502(7)	0.714(1)
O5	0.754(3)	0.701(1)	0.802(1)	0.739(3)	0.699(1)	0.794(1)	0.788(3)	0.703(1)	0.8010(5)
O6	0.143(3)	0.210(1)	0.385(2)	0.138(3)	0.2180(7)	0.384(2)	0.159(3)	0.207(1)	0.803(1)

	a (Å)	*b* (Å)	*c* (Å)	β (deg)		R_B (%)	R_{exp} (%)	R_{wp} (%)	χ^2
450 K	7.500 67(2)	11.549 88(4)	11.657 3(1)	108.756(1)		5.94	8.77	13.7	2.49
650 K	7.492 49(2)	11.602 18(4)	11.695 46(7)	108.6575(9)		6.66	9.58	14.0	2.20
850 K	7.496 80(2)	11.650 78(4)	11.722 60(9)	108.630(1)		6.53	10.34	14.3	1.98

B (Å^2)	Sm1	Mo1	Mo2	O1	O2	O3	O4	O5	O6
450 K	0.88(8)	0.6(1)	0.8(1)	1.5(2)	1.5(2)	1.5(2)	1.5(2)	1.5(2)	1.5(2)
650 K	1.09(8)	0.9(1)	0.7(1)	2.3(2)	2.3(2)	2.3(2)	2.3(2)	2.3(2)	2.3(2)
850 K	1.6(1)	1.1(1)	1.1(1)	3.1(2)	3.1(2)	3.1(2)	3.1(2)	3.1(2)	3.1(2)

also to represent bond-valence contour maps [57, 58]. Bond-valence isosurfaces can help visualize the migration pathways of the mobile ions in solid electrolytes, provided that the ion transport from one equilibrium site to the next one follows pathways along which the valence mismatch $\nabla V = |V - V_{ideal}|$ remains as small as possible. We have started with the structural data of table 1 and we have used the Bond-Str program, implemented in the FullProf Suite [46]. The aim of this program is to calculate the sum of bond valences that a particular atom (ion conductor) has if it is placed at any arbitrary point in the crystal. By moving this atom through different positions, its valence-sum contour map or bond-valence isosurfaces can be displayed [22].

Figure 6 shows the temperature dependence of the calculated valences for the samarium Sm1, vacancies of samarium Sm2, molybdenum, and oxygen ions. The sum of bond valence around the Sm ions decreases when the temperature increases (although at intermediate temperatures it remains rather stable) which is a normal behavior due to the volume expansion. The sum of bond valence around the vacancies is slightly greater at intermediate temperatures, so a hole diminution is expected. The thermal dependence of Mo valences at intermediate temperatures is anomalous and can be due to the distortions of the tetrahedra at such temperatures. These results are correlated with the structural anomalies in the cell parameter *a* as described previously, and the values obtained are quite reasonable, taking into account the limited resolution of our experiment regarding the position of the oxygen atoms. (Previous results for europium molybdate are, however, less good in this respect [20].) We have calculated bond-valence maps for all atom types of our structure in order to obtain qualitative results which support the conduction mechanism proposed by the ac conductivity analysis at high temperatures. Accurate oxygen positions are not necessary to plot contours maps, for which all that is needed are accurate
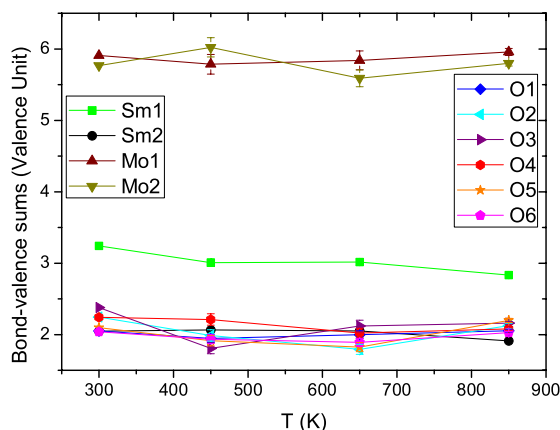
Figure 6. Calculated valences for Sm^{3+}, Mo^{6+}, and O^{2-} in α-$Sm_2(MoO_4)_3$, as a function of temperature.

atomic positions for Sm1, Mo1, and Mo2 in both compounds. In figure 7, we have detected new possible sites for the oxygen atoms at higher temperatures in $Sm_2(MoO_4)_3$ and $Eu_2(MoO_4)_3$ (see selected regions in this figure) which would favor their motion when an electric field is applied (in the regime of ionic transport). Contour bond-valence maps of Mo and Sm cations do not show any acceptable pathways.

4. Conclusions

This work provides a detailed study by dielectric spectroscopy of the transport properties of scheelite-like α-$Sm_2(MoO_4)_3$ as a function of temperature (500–900 K) and frequency (10^2–10^6 Hz). We have found a clear correlation between the existence of three conducting regimes, semiconductor, polaronic, ionic (obtained from the universal dielectric response
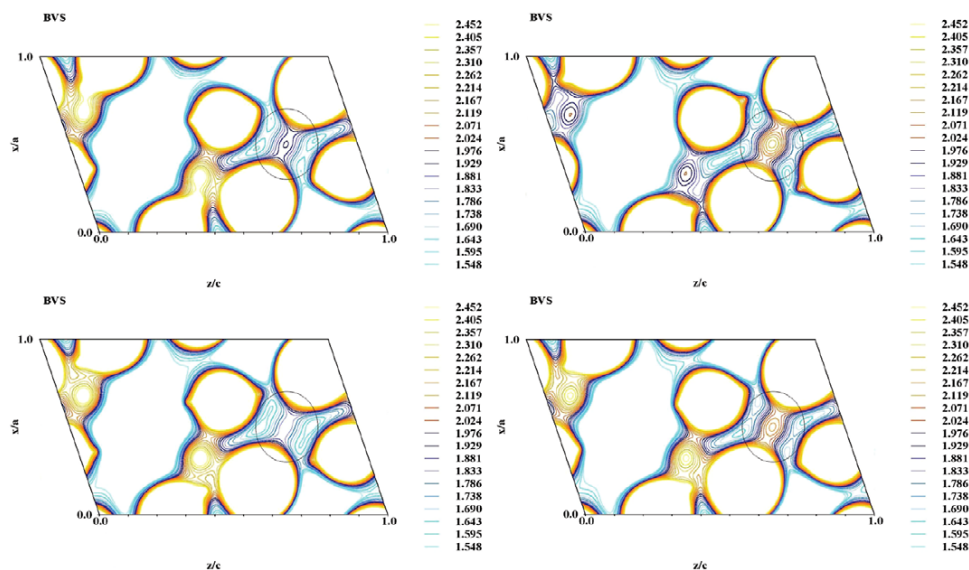
Figure 7. Bond-valence sum contour maps for O^{2-}. Upper panels are for α-$Sm_2(MoO_4)_3$ at 450 K (left) and 850 K (right). Bottom panels are for α-$Eu_2(MoO_4)_3$ at 523 K (left) and 923 K (right).

behavior [29]), and an anomalous thermal dependence of the lattice parameter *a* (obtained by x-ray diffraction) from 300 to 1000 K. We suggest that the different transversal displacements of two types of oxygen atoms in Sm–O(1, 2)–Mo2 bridges joined to the elongation of the tetrahedra around Mo1, in the same direction perpendicular to the *a* axis, help to explain the thermal dependence of the cell parameter, at the three regimes. For that, we refined three crystal structures at 450, 650, and 850 K and we performed an adapted symmetry-mode analysis [48] for a better visualization of the distortions due to the oxygen displacements. At an intermediate range, where the parameter *a* does not depend on temperature, we assumed polaronic transport, which was corroborated with the overlapping large polaron model [19]. At the regime of higher temperatures, possible oxygen-ion transport was confirmed by studying the frequency-dependent conducting spectra, at different temperatures, using a scaling law [37, 40], and by plotting contour maps of bond-valence sums [22] from the crystal structures, determined at different temperatures. Results were compared and extended to other isostructural compound α-$Eu_2(MoO_4)_3$, giving more consistency to our assumptions. The study of electrical conductivity in scheelite-type compounds is of growing interest [6] and our work provides new results on compounds which have been so far very little studied. In addition, we have provided a comprehensive data analysis, in which measurements obtained with conventional techniques were combined with several universal models and different modern tools of analysis, opening up new insights.

Acknowledgments

References

[1] Yen W M, Shionoya S and Yamamoto H 2007 *Phosphor Handbook* (New York: CRC)
[2] Globus M, Grinyov B and Kim J K 2005 *Inorganic Scintillators for Modern and Traditional Applications* (Kharkov: Institute for Single Crystals)
[3] Nagornaya L L *et al* 2009 *IEEE Trans. Nucl. Sci.* **56** 2513
[4] Kvapil J 1981 *J. Appl. Crystallogr.* **14** 355
[5] Brenier A, Zhang X, Wang J, Zhang H, Tu C, Li J, Zhu Z, Wang Y and You Z 2004 *Opt. Mater.* **26** 287
[6] Huang H, Feng X, Zhu W, Zhang Y, Wen T L and Tang T B 2003 *J. Phys.: Condens. Matter* **15** 5689
[7] Sen A, Chaplot S L and Mittal R 2003 *Phys. Rev.* B **68** 134105
[8] Jeitschko W 1973 *Acta Crystallogr.* B **29** 2074
[9] van den Elzen A F and Rieck G D 1973 *Acta Crystallogr.* B **29** 2433
[10] Templeton D H and Zalkin A 1963 *Acta Crystallogr.* **16** 762
[11] Boulahya K, Parras M and González-Calbet J M 2005 *Eur. J. Inorg. Chem.* **2005** 967
[12] Hartenbach I 2008 *Z. Anorg. Allg. Chem.* **634** 2044
[13] Keve E T, Abrahams S C and Bernstein J L 1971 *J. Chem. Phys.* **54** 3185
[14] Ponomarev B K 2002 *Ferroelectrics* **280** 95
[15] Abrahams S C and Bernstein J L 1966 *J. Chem. Phys.* **45** 2745
[16] Guzmán-Afonso C, González-Silgo C, González-Platas J, Torres M E, Lozano-Gorrín A D, Sabalisck N, Sánchez-Fajardo V, Campo J and Rodríguez-Carvajal J 2011 *J. Phys.: Condens. Matter* **23** 325402
[17] Secco R A, Liu H, Imanaka N and Adachi G 2002 *J. Phys.: Condens. Matter* **14** 11285
[18] Gaur K, Singh M and Lal H B 1993 *J. Mater. Sci.* **28** 3816
[19] Elliott S R 1987 *Adv. Phys.* **36** 135

[20] Guzmán-Afonso C, Torres M E, González-Silgo C, Sabalisck N, González-Platas J, Matesanz E and Mujica A 2011 *Solid State Commun.* **151** 1654
[21] Povolo F and Fontelos M 1987 *J. Mater. Sci.* **22** 1530
[22] González-Platas J, González-Silgo C and Ruiz-Pérez C 1999 *J. Appl. Crystallogr.* **32** 341
[23] Brixner L H, Barkley J R and Jeitschko W 1979 *Handbook on the Physics and Chemistry of Rare Earth* (Amsterdam: North-Holland)
[24] Le Bail A 2005 *Powder Diffract.* **20** 316
[25] Young R A 1993 *The Rietveld Method* (Oxford: Oxford Science)
[26] Jonscher A K 1977 *Nature* **267** 673
[27] Ngai K L, Jonscher A K and White C T 1979 *Nature* **277** 185
[28] Dissado L A and Hill R M 1979 *Nature* **279** 685
[29] Jonscher A K 1983 *Dielectric Relaxation in Solids* (London: Chelsea Dielectrics)
[30] León C, Lucía M L and Santamaría J 1997 *Phys. Rev.* B **55** 882
[31] Errandonea D and Manjón F J 2008 *Prog. Mater. Sci.* **53** 711
[32] Lal H B, Dar N and Kumar A 1974 *J. Phys. C: Solid State Phys.* **7** 4335
[33] Wang L M, Sou U C, Yang H C, Chang L J, Cheng C M, Tsuei K D, Su Y, Wolf T and Adelmann P 2011 *Phys. Rev.* B **83** 134506
[34] Ghosh A 1990 *Phys. Rev.* B **41** 1479
[35] van Staveren M P J, Brom H B and de Jongh L J 1991 *Phys. Rep.* **208** 1
[36] Long A R 1982 *Adv. Phys.* **31** 553
[37] Dyre J C, Maass P, Roling B and Sidebottom D L 2009 *Rep. Prog. Phys.* **72** 046501
[38] Singh P, Raghvendra , Parkash O and Kumar D 2011 *Phys. Rev.* B **84** 174306
[39] Ghosh A and Pan A 2000 *Phys. Rev. Lett.* **84** 2188
[40] Kumar M M and Ye Z G 2005 *Phys. Rev.* B **72** 024104
[41] Howard R E and Lidiard A B 1964 *Rep. Prog. Phys.* **27** 161
[42] Hairetdinov E F, Uvarov N F, Patel H K and Martin S W 1994 *Phys. Rev.* B **50** 13259
[43] Bhattacharya S and Ghosh A 2006 *Phys. Rev.* B **74** 184308
[44] Ahmad M M, Yamane Y and Yamada K 2009 *J. Appl. Phys.* **106** 074106
[45] Esaka T 2000 *Solid State Ion.* **136–137** 1
[46] Rodríguez-Carvajal J 1993 *Physica* B **192** 55
[47] Thompson P, Cox D E and Hastings J B 1987 *J. Appl. Crystallogr.* **20** 79
[48] Orobengoa D, Capillas C, Aroyo M I and Perez-Mato J M 2009 *J. Appl. Crystallogr.* **42** 820
[49] Perez-Mato J M, Orobengoa D, Aroyo M I and Elcoro L 2010 *J. Phys.: Conf. Ser.* **226** 012011
[50] Hazen R M, Finger L W and Mariathasan J W E 1985 *J. Phys. Chem. Solids* **46** 253
[51] Nassau K, Shiever J W and Keve E T 1971 *J. Solid State Chem.* **3** 411
[52] White G K 1993 *Contemp. Phys.* **34** 193
[53] Pellicer-Porres J, Martínez-García D, Segura A, Rodríguez-Hernández P, Muñoz A, Chervin J C, Garro N and Kim D 2006 *Phys. Rev.* B **74** 184301
[54] Bueno P R, Tararan R, Parra R, Joanni E, Ramírez M A, Ribeiro W C, Longo E and Varela J A 2009 *J. Phys. D: Appl. Phys.* **42** 055404
[55] Schefer J, Schaniel D, Pomjakushin V, Stuhr U, Petříček V, Woike T, Wöhlecke M and Imlau M 2006 *Phys. Rev.* B **74** 134103
[56] Chernyshov D, Rozenberg G, Greenberg E, Pomyakushina E and Dmitriev V 2009 *Phys. Rev. Lett.* **103** 125501
[57] Adams S and Swenson J 2002 *Solid State Ion.* **154–155** 151
[58] Adams S and Swenson J 2005 *J. Phys.: Condens. Matter* **17** S87

113

Pressure evolution of two polymorphs of Tb$_2$(MoO$_4$)$_3$[†]

C. Guzmán-Afonso[a*], J. López-Solano[b,c], C. González-Silgo[b], S.F. León-Luis[a], E. Matesanz[d] and A. Mujica[b]

[a]*Dpto. Física Fundamental y Experimental, Electrónica y Sistemas, Facultad de Física, Universidad de La Laguna, Tenerife, Spain;* [b]*Dpto. Física Fundamental II, and Instituto de Materiales y Nanotecnología, Facultad de Física, Universidad de La Laguna, Tenerife, Spain;* [c]*Izaña Atmospheric Research Center, Agencia Estatal de Meteorología, Tenerife, Spain;* [d]*C.A.I. Difracción de Rayos X, Facultad de C. C. Químicas, Universidad Complutense de Madrid, Madrid, Spain*

We have studied the high pressure behavior of the α and β'-phases of Tb$_2$(MoO$_4$)$_3$ using a combination of powder X-ray diffraction and *ab initio* calculations. The α-Tb$_2$(MoO$_4$)$_3$ phase did not undergo any structural phase transition in the pressure range from 0 up to the maximum experimental pressure of 21 GPa. We observed line broadening of the diffraction patterns at pressures above 7 GPa, which may be due to non-hydrostatic conditions. The complete amorphization of the sample was not reached in the pressure range studied, as expected from previous Raman studies. The behavior under pressure of the β'-Tb$_2$(MoO$_4$)$_3$ phase is similar to that of other rare-earths trimolybdates with the same structure at room temperature. A phase transition was observed at 2 GPa. The new phase, which can be identified as the δ-phase, has never been completely characterized by diffraction studies. A tentative indexation has been performed and good refined cell parameters were obtained. We detect indications of amorphization of the δ-Tb$_2$(MoO$_4$)$_3$ phase at 5 GPa.

Keywords: X-ray diffraction; *ab initio* calculations; rare-earth molybdates; structural transitions

1. Introduction

Depending on the rare-earth (RE) ion, tri-molybdates of the RE$_2$(MoO$_4$)$_3$ family are known to crystallize under normal conditions in four different crystal structures, which in turn can undergo temperature- and pressure-driven structural phase transitions.[1,2] Molybdates with RE = La–Nd feature the La$_2$(MoO$_4$)$_3$-type phase which is a modulated scheelite-type structure.[3] Those with RE = Sm–Tb crystallize in the α-phase, first described in Eu$_2$(WO$_4$)$_3$, and which is also a modulated scheelite-type structure but with a different ordering of vacancies and RE cations.[4] Molybdates with RE = Sm–Ho have the β'-phase, which has been thoroughly described for the ferroelectric Gd$_2$(MoO$_4$)$_3$ compound, and which features a high temperature transition to the paraelectric β-phase.[5] Finally, molybdates in the RE = Ho–Lu range crystallize in the γ-phase, a well-known structure with negative thermal expansion.[6] Besides featuring a profusion

---

of crystal structures, this family of compounds is interesting for its technological applications, ranging from scintillators to Raman shifters and second-harmonic generators.[2]

The focus of this study is the structural behavior of $Tb_2(MoO_4)_3$ under pressure. At room conditions, two stable polymorphs of this compound can be synthesized: the α and β'-phases.[4,5] The α-phase has a monoclinic structure with space group *C2/c* whereas the β'-phase is orthorhombic with space group *Pba2*. Under compression, previous fluorescence, Raman spectroscopy, and X-ray diffraction (XRD) studies on molybdates with the β'-phase (Sm, Eu, Gd, and Tb trimolybdates) have found different phase transitions, including one at around 2.5 GPa to a structural phase which has not been completely characterized.[7–10] On the other hand, a study on $Eu_2(MoO_4)_3$ showed that pressure-induced amorphization (PIA) was reached at 6.5 and 19.5 GPa for the β' and α-phases, respectively. The Raman bands of these two high pressure samples showed a similar behavior beyond the onset of the amorphization, indicating that the final situation of both polymorphs is the same.[11] In the following sections, we present results of our combined XRD and *ab initio* study.

2. *Ab initio* calculations

We have simulated the behavior under pressure of the β', α, γ, and $La_2(MoO_4)_3$-type structures by means of *ab initio* calculations. These calculations were carried out using the VASP code, which works within the framework of the density functional theory using pseudo-potentials and plane-waves basis sets.[12,13] With regard to the pseudo-potentials, we have worked within the projector-augmented waves method,[14,15] with the PBESol generalized gradient approximation for the exchange and correlation energy.[16] To ensure a total-energy convergence of 1 meV per formula unit (pfu), we used plane-waves basis sets with an energy cutoff of 520 eV together with dense Monkhorst-Pack grids [17] appropriate for each structure. At each volume considered, a full optimization of the atomic positions and lattice parameters, constrained to the symmetry compatible with the initial space group and set of Wyckoff positions, was performed. In the final optimized configurations, atomic forces were required to be smaller than $0.005 \, eV/Å^3$, and the stress tensor was required to be diagonal with differences between its components of less than 0.1 GPa.

In Figure 1, we have plotted the energy vs. volume curves of the four structures considered in our theoretical study. According to our calculations, the α-phase structure is the most stable one among the ones considered. The β' structure is a possible metastable phase. The difference between the energy minimum of both phases is 138 meV pfu and the difference between their volumes is $57 \, Å^3$ pfu, thus making the α-phase 20% denser than the β'-phase. The position of the γ-phase in Figure 1 clearly shows that this phase is not stable under normal conditions. Although the $La_2(MoO_4)_3$-type structure is only slightly higher in energy than the α-phase, and can thus be viewed as energetically competitive, a phase transition from the α-phase to this phase would involve a complete re-ordering of cations and vacancies, which would make such transition quite unlikely.[3]

3. Synthesis

Both phases of $Tb_2(MoO_4)_3$ were prepared by the conventional solid-state ceramic method. High purity chemical reagents Tb_4O_7 and MoO_3 (Aldrich, 99.999%) were mixed in stoichiometric amounts and homogenized in an agate mortar. The resulting powder was pressed (3 tn) into cylindrical pellets 13 mm in diameter and 1 mm in thickness, in order to improve the chemical
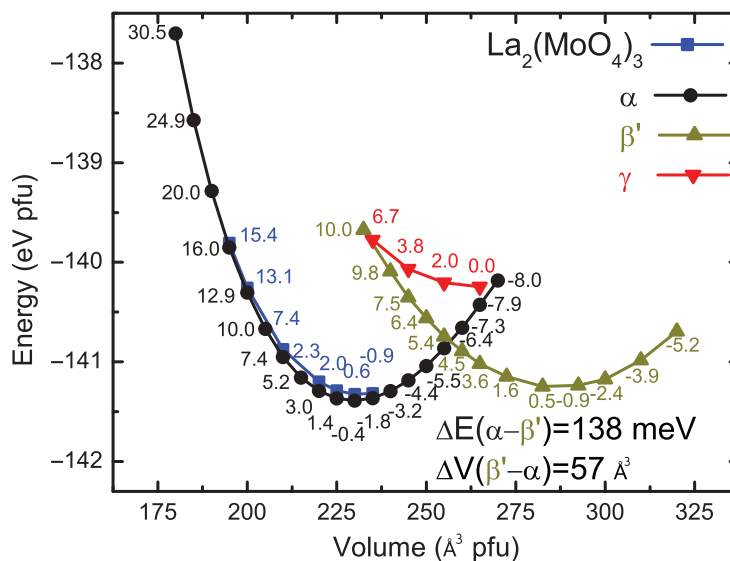
Figure 1. *Ab initio* energy-volume curves of the β', α, γ, and $La_2(MoO_4)_3$-type structures. The numbers next to each symbol indicate the calculated pressure (in GPa) for the corresponding volume and structure.

reaction in the furnace. Samples were synthesized at 973 K to obtain the α-phase and at 1223 K to obtain the β'-phase. Both thermal treatments needed 48 hours under air atmosphere. In order to check the purity of the sample, XRD patterns were measured at room conditions by continuous scanning with a step of 1 °/min, using a PANalytical X'Pert PRO diffractometer (Bragg-Brentano mode) with a primary monochromator of Ge (111) and an X'Celerator detector, using Cu $K_{\alpha 1}$ radiation (40 kV and 30 mA) in the angular range $10° < 2\theta < 80°$.

4. Powder XRD at high pressure

We performed powder XRD at high pressures at the *I15* beamline of Diamond Light Source. Because the experiments were performed on different dates, different wavelengths were employed for the α and β'-phases: 0.485 and 0.412 Å, respectively. We do not expect this to affect our results. The pressure-transmitting medium was ethanol–methanol–water in the proportion 16:3:1. We loaded the samples in two different diamond-anvil pressure cells, a Diacell Bragg-Mini and a MiniDac of the University of Paderborn, both equipped with inconel gaskets. The in situ pressure was measured using the ruby fluorescence scale. The data were collected using a mar345 image plate detector placed at 520 and 500 mm from the α and β'-phase samples, respectively. All the patterns were measured at room temperature. The observed intensities were integrated as a function of 2θ to get conventional one-dimensional diffraction profiles. The FIT2D software [18] was used for the preliminary reduction of the data. We obtained the cell parameters from the powder diffraction data by iterating full pattern profile fittings with the Le Bail algorithm,[19] using the FullProf software [20] and starting from the crystallographic cell obtained from our *ab initio* study.

5. Results and discussion

Figure 2(a) shows the diffraction patterns of the α-phase from ambient pressure up to 21 GPa, the maximum pressure allowed by our experimental setup. As it can be observed, we obtain good fits up to 7 GPa. Above this pressure, we start to see a broadening of the reflections. The
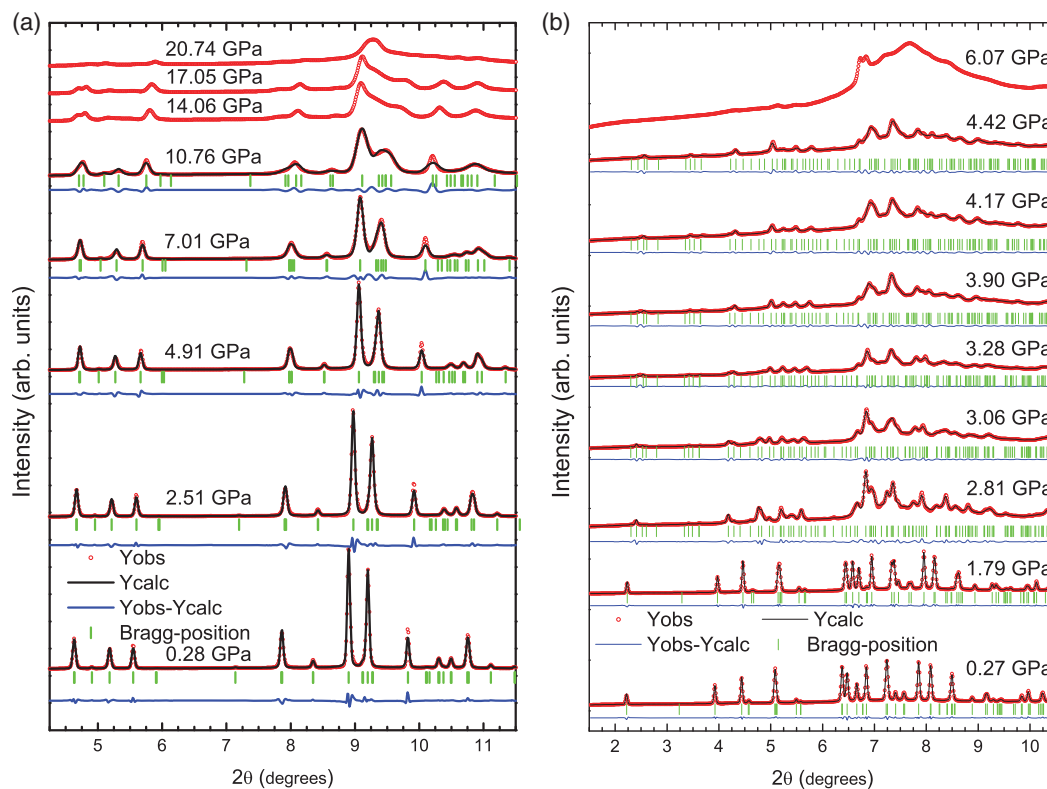
Figure 2. Diffraction patterns of $Tb_2(MoO_4)_3$ at selected pressures. The experimental results (open circles) are shown together with the calculated patterns (black) and residuals (blue). The ticks indicate the positions of Bragg reflections.

refinements converged up to 11.58 GPa, the broadening of the reflections not allowing us to continue the refinement beyond this pressure. However, we have not observed important changes nor a complete amorphization up to 21 GPa. Moreover, we did not observe indications of any phase transition in this pressure range, and the structure was fully recovered upon releasing the pressure. Several authors have performed Raman spectroscopy in molybdates with the α-phase and they also did not observe any phase transition, whereas amorphization was reached at rather high pressures: 21.2 GPa for $Eu_2(MoO_4)_3$,[11] 15.5 GPa for $Nd_2(MoO_4)_3$, and 25 GPa for $Tb_2(MoO_4)_3$.[21] Our results are thus in agreement with these previous works.

Figure 3 shows the evolution of experimental and theoretical lattice parameters and volume with pressure of the α-phase. This is, to our knowledge, the first time that the structural evolution under pressure of this material is studied by either XRD or *ab initio* calculations. A good agreement on an unusual compression behavior of the lattice parameters is observed up to 7 GPa, when the experimental results start to worsen due to the gradual loss of hydrostatic conditions in the sample, and hence the experimental and theoretical results start to deviate from each other. Also note that in this figure, the lattice parameter *a* was plotted using a different scale than *b* and *c* scale.

Figure 2(b) shows the diffraction patterns of the β'-phase at different pressures, together with the corresponding fitted profiles and Bragg positions. We can see that the diffraction patterns up to 2 GPa correspond to the β'-phase and that beyond 5 GPa the amorphization region has been reached. Beyond 2 GPa the diffraction patterns undergo a pronounced change. New reflections appear and some previous reflections disappear (or they are considerably shifted). These changes likely indicate the formation of a new phase that we believe could be the so-called δ-phase. This latter phase has been previously observed by other authors in Sm, Eu, Gd, and Tb
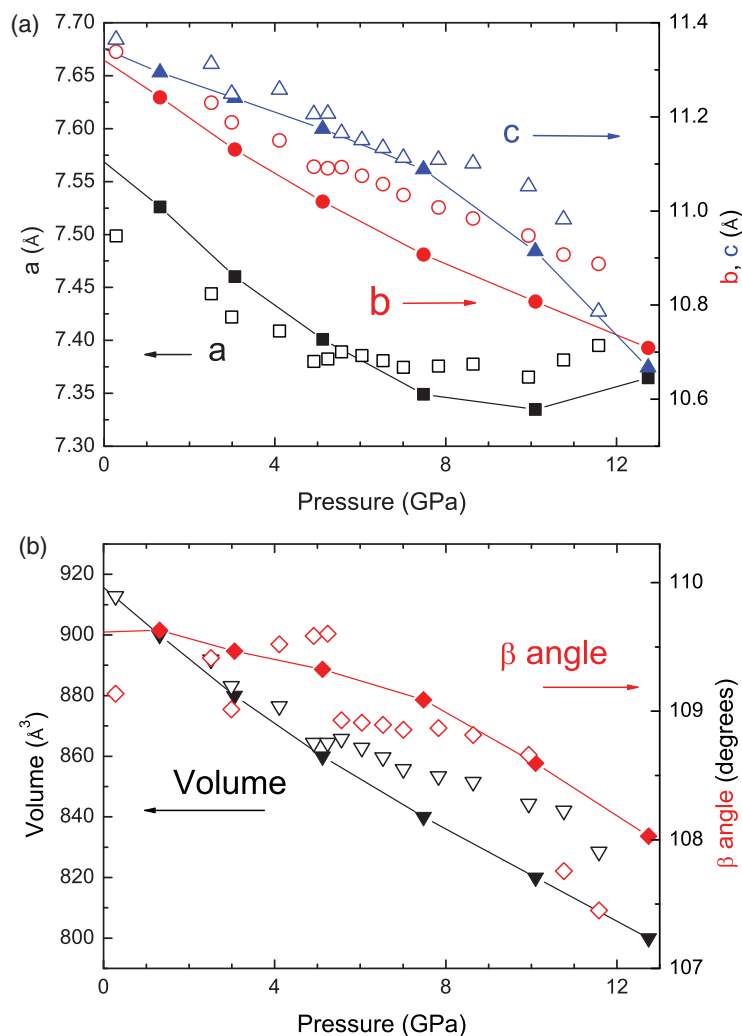
Figure 3.   Dependence with pressure of the lattice parameters (upper panel) and unit cell volume and beta angle (bottom panel) of α-Tb$_2$(MoO$_4$)$_3$. Theoretical and experimental data are represented by solid and empty symbols, respectively. The data for the *a, b,* and *c* cell parameters are represented by black squares, red circles, and blue triangles, respectively; the unit cell volume is represented by black triangles and the β angle by red diamonds. The different sets of theoretical data have been joined by solid lines as a guide to the eye. Note the different scale used for the representation of the *a* parameter with respect to that used for the *b* and *c* parameters.

molybdates,[7–10] but, so far, has not been properly characterized by XRD studies. We indexed the diffraction pattern at 2.81 GPa on the basis of an orthorhombic unit cell with lattice parameters $a = 19.655$ Å, $b = 10.234$ Å, $c = 9.362$ Å (ordered with an arbitrary criterion, $a > b > c$). We then refined the cell parameters with the Le Bail algorithm [19] from patterns above 2 GPa. In this way, we obtained good fits for all the patterns up to 4.42 GPa. As shown in Figure 4, there is a good agreement between the experimental and theoretical cell parameters of the β'-phase. We have also included the lattice parameters of the δ-phase in Figure 4. Note that both the values of the *a* cell parameter and the volume of the δ-phase are shown divided by two, as both magnitudes are almost twice than those in the low-pressure β'-phase. Figure 4 shows a large discontinuity in the unit cell volume at the transition pressure, which suggests that the phase transition undergone by the β'-phase must imply important structural changes. These changes are also evident in the Raman profiles in the range from 0.1 and 3.5 GPa reported by Jayaraman et al.[10] We must stress, however, that we have not been able to completely characterize the new δ-phase.
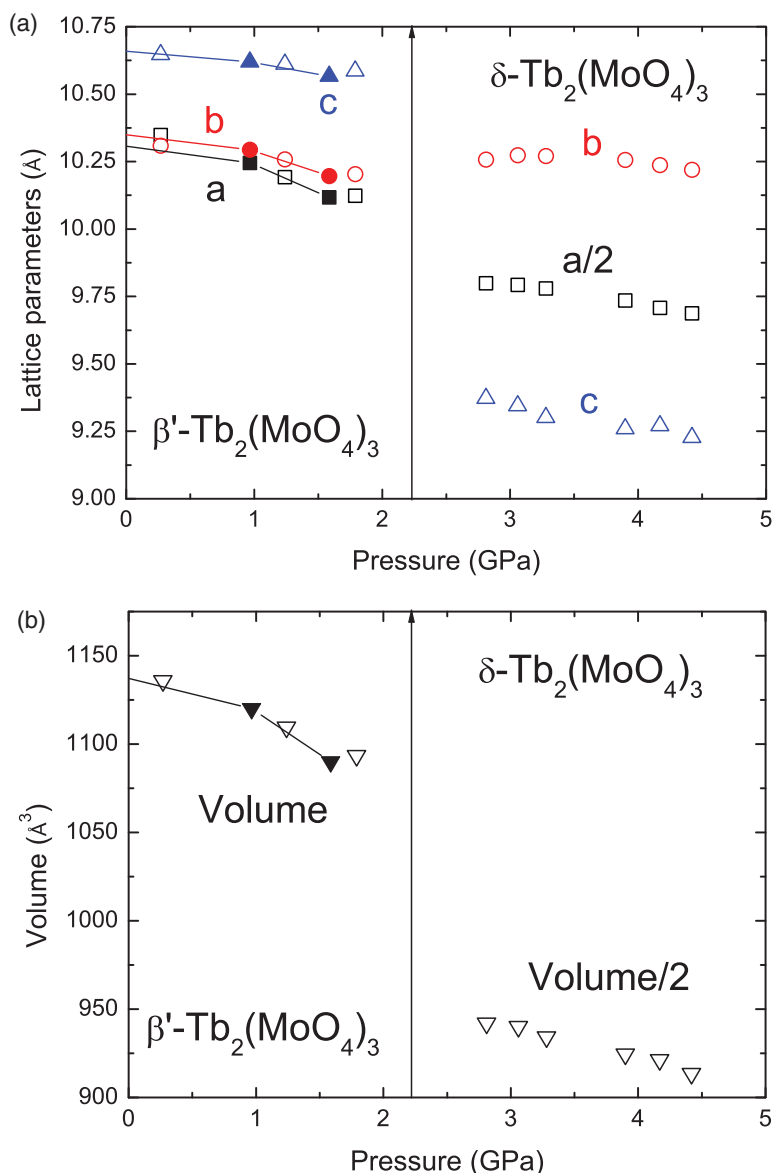
Figure 4. Same as Figure 3, for the β'-Tb$_2$(MoO$_4$)$_3$ and δ-Tb$_2$(MoO$_4$)$_3$ phases. Note that the values of both the a parameter and the unit cell volume of the δ-phase are shown divided by two.

6. Conclusions

In this work, we have described the pressure dependence of the crystal structure of the α and β' polymorphs of Tb$_2$(MoO$_4$)$_3$, using powder XRD data refined by the Le Bail method and theoretical data provided by *ab initio* total-energy calculations on several structural phases. The behavior of both the α and β'-phases is markedly different, as expected. A good agreement between experimental and theoretical results is found, and thus allows a full characterization of the compression of the α-phase up to the possible loss of hydrosticity. In order to understand the complete evolution of the crystal structure of the α-phase, without a clear indication of phase transition, and the mechanisms of the PIA, it would be convenient to reach the amorphization region in several RE molybdates, which in turn would probably entail the use of a different pressure-transmitting medium so as to maintain hydrostatic conditions at these elevated pressures. The compression mechanisms of the β'-phase can also be described up to the phase transition.

However, after the phase transition, we were unable to fully characterize the possible new δ-phase. We are working in a complete characterization of this new phase for several RE molybdates using various theoretical methods, including *ab initio* random search with symmetry information provided by the diffractograms. The poor data quality prevents a Rietveld refinement, but from the extracted intensities, and using different metrics ($c' = 2c$ or $a' = 2a$) and space groups, it is possible to propose structure using simulated annealing (as implemented in the FullProf program) and check them with *ab initio* calculations.

Acknowledgements

References

[1] Brixner LH, Barkley JR, Jeitschko W. Handbook on the physics and chemistry of rare earths. Amsterdam: North-Holland; 1979.

[2] Maczka M, Souza Filho AG, Paraguassu W, Freire PTC, Mendes Filho J, Hanuza J. Pressure-induced structural phase transitions and amorphization in selected molybdates and tungstates. Prog Mater Sci. 2012;57(7):1335–1381.

[3] Jeitschko W. Crystal structure of $La_2(MoO_4)_3$, a new ordered defect Scheelite type. Acta Crystallogr Sect B. 1973;29(10):2074–2081.

[4] Templeton DH, Zalkin A. Crystal structure of europium tungstate. Acta Crystallogr. 1963;16(8):762–766.

[5] Jeitschko W. A comprehensive X-ray study of the ferroelectric–ferroelastic and paraelectric–paraelastic phases of $Gd_2(MoO_4)_3$. Acta Crystallogr Sect B. 1972;28(1):60–76.

[6] Abrahams SC, Bernstein JL. Crystal structure of the transition-metal molybdates and tungstates. II. diamagnetic $Sc_2(WO_4)_3$. J Chem Phys. 1966;45(8):2745–2752.

[7] Dmitriev V, Sinitsyn V, Dilanian R, Machon D, Kuznetsov A, Ponyatovsky E, Lucazeau G, Weber HP. In situ pressure-induced solid-state amorphization in $Sm_2(MoO_4)_3$, $Eu_2(MoO_4)_3$ and $Gd_2(MoO_4)_3$ crystals: chemical decomposition scenario. J Phys Chem Solids. 2003;64(2):307–312.

[8] Machon D, Dmitriev VP, Sinitsyn VV, Lucazeau G. $Eu_2(MoO_4)_3$ single crystal at high pressure: structural phase transitions and amorphization probed by fluorescence spectroscopy. Phys Rev B. 2004;70:094117.

[9] Lucazeau G, Le Bacq O, Pasturel A, Bouvier P, Pagnier T. High-pressure polarized Raman spectra of $Gd_2(MoO_4)_3$: phase transitions and amorphization. J Raman Spectrosc. 2011;42(3):452–460.

[10] Jayaraman A, Sharma SK, Wang Z, Wang SY, Ming LC, Manghnani MH. Pressure-induced amorphization of $Tb_2(MoO_4)_3$: a high pressure Raman and X-ray diffraction study. J Phys Chem Solids. 1993;54(7):827–833.

[11] Le Bacq O, Machon D, Testemale D, Pasturel A. Pressure-induced amorphization mechanism in $Eu_2(MoO_4)_3$. Phys Rev B. 2011;83:214101.

[12] Kresse G, Hafner J. *Ab initio* molecular dynamics for liquid metals. Phys Rev B. 1993;47:558–561.

[13] Kresse G, Furthmüller J. Efficient iterative schemes for *ab initio* total-energy calculations using a plane-wave basis set. Phys Rev B. 1996;54:11169–11186.

[14] Kresse G, Joubert D. From ultrasoft pseudopotentials to the projector augmented-wave method. Phys Rev B. 1999;59:1758–1775.

[15] Blöchl PE. Projector augmented-wave method. Phys Rev B. 1994;50:17953–17979.

[16] Perdew JP, Ruzsinszky A, Csonka GI, Vydrov OA, Scuseria GE, Constantin LA, Zhou X, Burke K. Restoring the density-gradient expansion for exchange in solids and surfaces. Phys Rev Lett. 2008;100:136406.

[17] Monkhorst HJ, Pack JD. Special points for Brillouin-zone integrations. Phys Rev B. 1976;13:5188–5192.

[18] Hammersley AP, Svensson SO, Hanfland M, Fitch AN, Hausermann D. Two-dimensional detector software: from real detector to idealised image or two-theta scan. High Pressure Res. 1996;14(4–6):235–248.

[19] Le Bail A. Whole powder pattern decomposition methods and applications: a retrospection. Powder Diffr. 2005;20:316–326.

[20] Rodríguez-Carvajal J. Recent advances in magnetic structure determination by neutron powder diffraction. Physica B. 1993;192(1–2):55–69.

[21] Jayaraman A, Sharma SK, Wang Z, Wang SY. Pressure-induced amorphization in the α-phase of $Nd_2(MoO_4)_3$ and $Tb_2(MoO_4)_3$. Solid State Commun. 1997;101(4):237–241.

Crystal structure and non-linear properties of $A_2(MoO_4)_3$ (A $=$ Eu, Gd, Tb, Dy and Ho)

C. Guzmán-Afonso [a,b], C. González-Silgo [a], M.E. Torres [b,*], N. Sabalisck [b], A.D. Lozano-Gorrín [a,c], J. González-Platas [a,c], E. Matesanz [d]

[a] Departamento de Física Fundamental II. Universidad de La Laguna, Spain
[b] Departamento de Física Básica, Universidad de La Laguna, Spain
[c] Servicio Integrado de Difracción de Rayos X, Universidad de La Laguna, Tenerife, Spain
[d] C.A.I. Difracción de Rayos X, Universidad Complutense de Madrid, Spain

ARTICLE INFO

ABSTRACT

Ferroelectric–ferroelastic rare earth (RE) molybdates $RE_2(MoO_4)_3$ have been prepared by the conventional solid-state synthesis and X-ray powder diffraction has been collected using two diffractometers PANalytical X'Pert Pro at room temperature. The crystal structures have been calculated by Rietveld refinement, using a new symmetry modes procedure in order to evaluate the correlation between the distortions, with respect to the paraelectric–paraelastic structure, with the ionic radii. Although the coordinates of the oxygen atoms are not very precise and accurate, we have observed different behavior of the ferroelastic–ferroelectric order parameter.

© 2011 Elsevier B.V. All rights reserved.

1. Introduction

Sm–Ho molybdates show the typical β'-$Gd_2(MoO_4)_3$ ferroelectric–ferroelastic structure (the crystal structure of Gd and Tb molybdates are in ICSD [1]). In particular $Gd_2(MoO_4)_3$ has attracted attention since it has shown to be an efficient frequency doubling medium for laser diode pumping [2]. Recently an interesting compound of this family ($LaEr(MoO_4)_3$) has been investigated for infrared to visible up-conversion [3]. Also, it is of great interest to synthesize crystallized glasses consisting of ferroelectric materials [4]. A sound knowledge of the optical properties of $RE_2(MoO_4)_3$ crystals, it is of fundamental importance for the application of these materials. Previous investigations of second order susceptibility suggest that the major part of non-linear optical properties of these types of compound is due to the orientation of the MoO_4 tetrahedral and the hyper-polarizability of the Mo—O bonds [5]. However, other authors found that the major contribution to the non-linear properties of rare earth molybdates come from the REO_7 groups [6]. Unfortunately only little experimental data on the optical susceptibility of the discussed crystals are available so far, and structural data of Sm, Eu, Dy and Ho molybdates are not given in the ICSD. In this work we apply a new alternative way of treating distorted structures using a symmetry modes analysis [7,8] which gives us an input file to perform with FullProf [9] the Rietveld refinement of the amplitudes of such modes, instead of the atomic positions. This new procedure will let us discuss the different distorted structures of the molybdates family from a new point of view.

2. Experimental

2.1. Synthesis

Eu–Ho molybdates were prepared by conventional solid-state synthesis. MoO_3 and Eu_2O_3 powders (Aldrich, 99.99%) were pre-heated, respectively, at 923 and 1173 K for 10 h before use. These preheated powders were weighed in stoichiometric amounts, mixed, and homogenized in an agate mortar. The resulting powder was then pressed into pellets and finally sintered in air atmosphere at 1273 K for Eu, Dy and Ho, and at 1223 K for Gd and Tb molybdates for 48 h in platinum crucibles.

2.2. X-ray diffraction

The experiments were conducted at two X-ray diffraction facilities: 1) SIDIX, at the University of La Laguna and 2) C.A.I., at the Complutense University of Madrid. Powder diffraction data for Rietveld refinement were collected in two different PANalytical X'Pert PRO diffractometers (Bragg–Brentano mode) with a X'Celerator detector using $CuK\alpha_1$ radiation ($\lambda = 1.5405(1)$ Å) in the SIDIX laboratory and using $CuK\alpha$ radiation, in the C.A.I. laboratory. The angular range 5°, 10°<2θ<100°, 120°, by continuous scanning with step size of 0.02° (approximately) and different total step time (100–

* Corresponding author.
E-mail address: metorres@ull.es (M.E. Torres).

300 s). Divergence and incident anti-scatter slits were set at 0.25° and 0.5° (C.A.I) and 0.5° and 1° (SIDIX). Diffracted anti-scatter slit was set at 0.25° (C.A.I). A secondary 0.02 rad Soller slit was used in SIDIX and incident and diffracted 0.02 rad Soller slit were used in C.A.I. The detector was used in scanning mode with an active length of 2.14° (SIDIX) and 2.12° (C.A.I.).

3. Results and discussion

Rietveld refinements were performed using the program FullProf [9]. The experimental profiles were modeled using a Thompson–Cox–Hasting pseudo-Voigt profile shape function, with two adjustable parameters (U and Y, corresponding to isotropic Gaussian strain and Lorentzian size effects); fixed values (U_{ins}, V_{ins}, W_{ins}, X_{ins} and Y_{ins}) were used for the instrumental resolution parameters, as well as the peak asymmetry (S/D and S/L). The background was modeled by a polynomial function with more than six coefficients and less than twelve. With respect to the crystal structure, we have not refined the atomic coordinates. We have obtained the ferroelectric structures, analyzing the distortion from the paraelectric phase by the structure refinement in terms of symmetry adapted modes. Given the high (paraelectric–paraelastic) and the low (ferroelectric–ferroelastic) symmetry structures, AMPLIMODES [7] relates them on the basis of symmetry-adapted modes, and calculates the amplitudes and the polarization vectors of the distortion modes, of different symmetry, frozen in the structure. Once the decomposition of the proposed structure (in our case it was β-Gd$_2$ (MoO$_4$)$_3$) is done, the new free parameters (the amplitudes of collective modes) are more adequate, for a controlled refinement of the structure, than the atom positions. Then, the program FullProf refines the amplitudes of such symmetry modes and the asymmetric unit coordinates of the ferroelectric–ferroelastic phase will be calculated from the paralectric–paraelastic phase plus the distortion in terms of the amplitudes and the polarization vectors of the symmetry modes. Results of the refinement are shown in Fig. 1 and Table 1.

The results of the refinements are different depending on the resolution of the diffractogram and depending on possible mixed phase. The β′-Eu$_2$(MoO$_4$)$_3$ and β′-Ho$_2$(MoO$_4$)$_3$, with worst results, are mixed with the α-Eu$_2$(MoO$_4$)$_3$ and γ-Ho$_2$(MoO$_4$)$_3$ phases, respectively because both generate a very modulated background: α-Eu$_2$ (MoO$_4$)$_3$ has a short range ordering and γ-Ho$_2$(MoO$_4$)$_3$ is hydrated. For the refinement of Tb$_2$(MoO$_4$)$_3$ structure a very low resolution pattern was used. The correlation of cell parameters with the ionic radii is perfectly linear and it was expected, but this has never been shown from data obtained by Rietveld refinement. The standard deviations of the atomic coordinates are quite good (they are around $\pm 8 \cdot 10^{-4}$ for heavier atoms and $\pm 5 \cdot 10^{-3}$ for lighter atoms), if we take into account that oxygen atoms positions are difficult to calculate by X-ray powder diffraction.

Tb and Gd molybdates structures are known [10,11] and the coupling of ferroic properties is structure dependent and can be expressed, since each atom (x_1, y_1, z_1) is related to another atom at the same class (x_2, y_2, z_2), as:

$$(x_1, y_1, z_1) = (^1/_2 - y_2, x_2, 1 - z_2) + \Delta \qquad (1)$$

where Δ is a displacement vector.

Very recently Perez-Mato et al. [8] have performed a symmetry mode description of the Pba2 structure of Gd$_2$(MoO$_4$)$_2$ using AMPLIMODES. The total displacement vector Δ can decompose in three distortion modes. A primary one corresponds to the irrep M2 +M4 (irreducible representation) associated with the point M (1/2, 1/2, 0) at the border of the Brillouin zone. A secondary polar mode, at the center of the Brillouin zone with symmetry, is given by irrep GM3. Finally, other secondary mode given by irrep GM1 keeps the parent symmetry. In Table 1 we have shown similar results for a similar
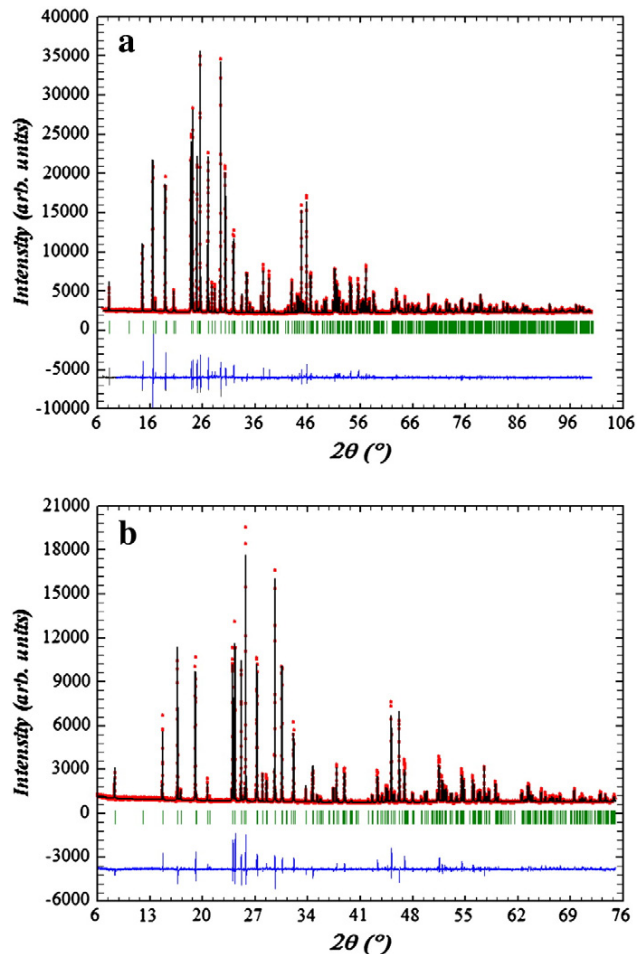
Fig. 1. Examples of the powder diffraction patterns collected for: a) Gd$_2$(MoO$_4$)$_3$ and b) Dy$_2$(MoO$_4$)$_3$. Observed data (+) are shown along with the pattern (solid line) calculated from Rietveld analysis and differences (lower trace). Bars indicate the Bragg positions.

analysis in the complete family of the ferroic rare earth molybdates. Again, the primary distortion mode is dominant for all compounds (always more than twice), although, due to the less precise and accurate oxygen coordinates, distortions are longer.

Also, the global amplitude of irrep M2 + M4, in general, increases as the ionic radii increases, according with the Curie temperatures [12] and the average of the non-linear optical coefficients [6], and, as it can be seen in Fig. 2, the arrows, which represent this distortion for each atom, are in similar direction. Note that the refinements of the

Table 1
Conventional reliability factors of the Rietveld refinement with all non-excluded points and global amplitude of different irreducible representation.

	Eu$_2$(MoO$_4$)$_3$	Gd$_2$(MoO$_4$)$_3$	Tb$_2$(MoO$_4$)$_3$	Dy$_2$(MoO$_4$)$_3$	Ho$_2$(MoO$_4$)$_3$
R_{wp}(%)	18.8	16.2	19.3	17.3	13.9
χ^2	3.2	5.48	2.83	3.95	15.4
R_B(%)	8.10	5.82	6.78	8.1	5.18
GM1[Å]	0.43(6)	0.85(3)	0.91(6)	0.58(4)	0.39(3)
GM3[Å]	1.40(11)	0.67(7)	0.62(9)	0.50(9)	0.78(6)
M2 + M4[Å]	2.21(11)	2.13(7)	2.55(18)	1.56(11)	1.63(5)
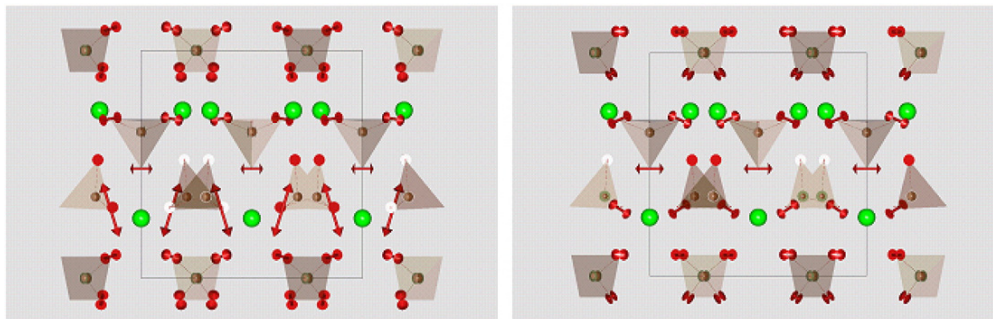
Fig. 2. b-axis view of the paraelectric structures of $Gd_2(MoO_4)_3$ (left) and $Ho_2(MoO_4)_3$ (right) showing the M2 + M4 primary mode by arrows. Arrows were magnified for clarity reasons.
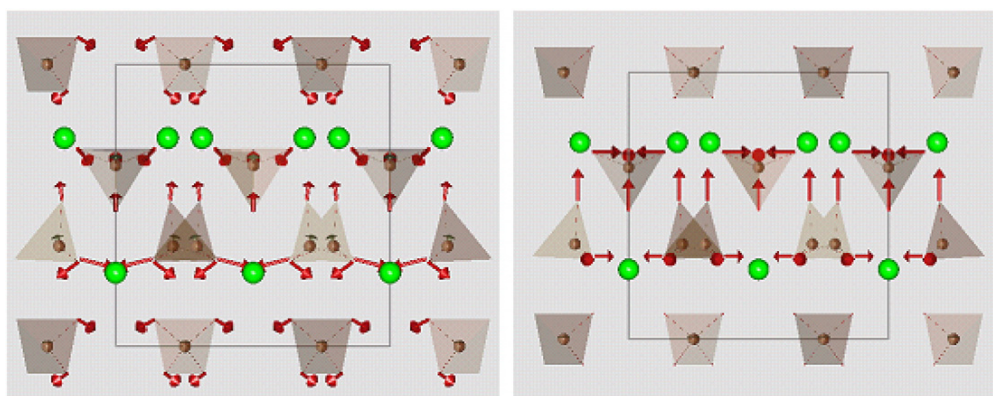
Fig. 3. b-axis view of the paraelectric structures of $Eu_2(MoO_4)_3$ (left) and $Dy_2(MoO_4)_3$ (right) showing the GM3 polar mode by arrows. Arrows were magnified for clarity reasons.

$Tb_2(MoO_4)_3$ and $Ho_2(MoO_4)_3$ structures are not very good. However the maximum atomic displacement in the distortions (calculated from single crystal data) is of the order of 0.4 for $Gd_2(MoO4)_3$ [10] while for $Tb_2(MoO_4)_3$ is 0.7 Å [11] without correlation of the ionic radii. Clearly, the global amplitude of the primary mode, which yields directly the observed symmetry, is much longer than the amplitude of the polar mode. In addition this amplitude is also rather well correlated with the difference of the cell parameters a–b, carrying the most important role in the phase transition. On the other side, we didn't find similar correlation in the global amplitude of irrep GM3, which is responsible of the spontaneous polarization and the spontaneous strain in the Pba2 phase. Moreover, as we can see in Fig. 3, the arrows which represent the distortion of each atom have very different directions.

4. Conclusion

More accurate crystal structures are necessary to correlate the spontaneous polarization and strain with the ionic radii of the rare earth in this ferroelectric molybdates family. However, with our results we have observed how the primary distortion mode is correlated with the ionic radii and with the difference of the cell parameters a–b, so that molybdates with atoms with larger ionic radius will need more vibrational energy to reach the transition temperature. Neutron powder diffraction of terbium, dysprosium, holmium molybdate and $LaEr(MoO_4)_3$ is in progress, at different temperatures around T_c, to determine the role of the primary distortion mode and the order parameters (secondary distortion modes) in the paraelectric–ferroelectric transition. AMPLIMODES program also will be very suitable for studying these distortions as a function of temperature, as it has been done for different ionic radii.

References

[1] Inorganic Crystal Structure Database (ICSD). Version 2010/1. Fachinformations-zentrum Karlsruhe, Germany, 2010.
[2] Nishioka H, Odajima W, Tateno M, Ueda K, Kaminskii AA, Butashin AV, et al. Femtosecond continuously tunable second harmonic generation over the entire-visible range in orthorhombic acentric $Gd_2(MoO_4)_3$ crystals. Appl Phys Lett 1997;70:1366–8.
[3] Tsukada Y, Honma T, Komatsu T. Self-organized periodic domain structure for second harmonic generations in ferroelastic β'-(Sm,Gd)$_2$(MoO$_4$)$_3$ crystal lines on glass surfaces (vol 94, art no 041915, 2009). Appl Phys Lett 2009;94: 059901–059901-3.
[4] Abe M, Benino Y, Fujiwara T, Komatsu T, Sato R. Writing of nonlinear optical Sm_2 $(MoO_4)_3$ crystal lines at the surface of glass by samarium atom heat processing. J Appl Phys 2005;97:123516–7.
[5] Bonneville R, Auzel F. Linear and nonlinear susceptibilities of rare earth ferroic molybdates. J Chem Phys 1977;67:4597–602.
[6] Xue D, Betzler K, Hesse H, Lammers D. Linear and nonlinear optical susceptibilities of orthorhombic rare earth molybdates $RE_2(MoO_4)_3$. J Phys Chem Solids 2002;63: 359–61.
[7] Orobengoa D, Capillas C, Aroyo MI, Perez-Mato JM. AMPLIMODES: symmetry-mode analysis on the Bilbao Crystallographic Server. J Appl Crystallogr 2009;42: 820–33.
[8] Perez-Mato JM, Orobengoa D, Aroyo MI. Mode crystallography of distorted structures. Acta Crystallogr A 2010;66:558–90.

[9] Rodriguez-Carvajal J. FULLPROF. Program for Rietveld analysis of X-ray and neutron powder diffraction patterns. France: Laboratoire Léon Brillouin (CEA-CNRS); 1993.

[10] Jeitschko W. A comprehensive x-ray study of ferroelectric–ferroelastic and paraelectric–paraelastic phases of $Gd_2(MoO_4)_3$. Acta Crystallogr B 1972;28:60–76.

[11] Abrahams SC, Bernstein JL, Lissalde F, Nassau K. Thermal expansivity and spontaneous strain temperature dependence in $Tb_2(MoO_4)_3$. J Appl Crystallogr 1978;11:699–700.

[12] Tomaszewski PE. Structural phase transitions in crystals I. database. Phase Transit B 1992;38:127–220.

Polymorphism in Ho$_2$(MoO$_4$)$_3$

C. González-Silgo,[1,a] C. Guzmán-Afonso,[2] V. M. Sánchez-Fajardo,[3] S. Acosta-Gutiérrez,[1] A. Sánchez-Soares,[1] M. E. Torres,[3] N. Sabalisck,[3] E. Matesanz,[4] and J. Rodríguez-Carvajal[5]

[1]*Dpto. Física Fundamental II, Universidad de La Laguna, Avda. Astrofísico Fco. Sánchez, s/n, 38206 La Laguna, Tenerife, Spain*
[2]*Dpto. Física Fundamental y Experimental, Electrónica y Sistemas, Universidad de La Laguna, Avda. Astrofísico Fco. Sánchez, s/n, 38206 La Laguna, Tenerife, Spain*
[3]*Dpto. Física Básica, Universidad de La Laguna, Avda. Astrofísico Fco. Sánchez, s/n, 38206 La Laguna, Tenerife, Spain*
[4]*C.A.I. Difracción de Rayos X, Universidad Complutense de Madrid, 28040 Madrid, Spain*
[5]*Institut Laue-Langevin, 6 rue Jules Horowitz, BP 156, 38042 Grenoble Cedex 9, France*

[a]Electronic mail: csilgo@ull.es

Two polymorphs of Holmium molybdate, known as β'-phase and γ-phase, were prepared by solid state reaction with different thermal treatments. These polycrystalline samples have been studied for the first time by X-ray thermodiffractometry from room temperature up to 1300 K. We found that the initial β'-phase undergoes a transition to a-β-phase and then to a γ-phase. The γ (hydrated)-phase, turns to the γ (dehydrated)-phase and then to the β-phase. Each sequence involves a reversible and an irreversible phase transition for Ho$_2$(MoO$_4$)$_3$. Both polymorphs have remarkable physical properties like nonlinear optics, ferroelectricity and negative thermal expansion. We have calculated the linear expansion coefficients of both phases. We have obtained a positive coefficient for the β'-phase and a negative one for the γ-phase. Moreover, we have made a comparison of the obtained coefficients with previous results for other rare earth molybdates.

Key words: powder diffraction, phase transition, polymorphism

I. INTRODUCTION

All the known structures of molybdates at room temperature, with general composition noted as RE$_2$(MoO$_4$)$_3$ (RE=rare earth) and depending on the ionic radius, belong to four structure types: La$_2$(MoO$_4$)$_3$ (Jeitschko, 1973), Eu$_2$(WO$_4$)$_3$ (Templeton and Zalkin, 1963), β'-

$Gd_2(MoO_4)_3$ (Jeitschko, 1972) and $Sc_2(WO_4)_3$ (Abrahams and Bernstein, 1966). Rare earth molybdates with intermediate ionic radii show the β'-$Gd_2(MoO_4)_3$ ferroelectric-ferroelastic phase. The $Gd_2(MoO_4)_3$, with *Pba*2 space group attracts attention since it has shown to be an efficient frequency doubling medium for laser diode pumping (Kojima and Nakamura, 1978). The corresponding paraelectric-paraelastic phase (β) belongs to the P-42$_1m$ space group and arises after a phase transition at about 450 K. The heavier molybdates with the $Sc_2(WO_4)_3$ structure type have a *Pbcn* space group; this structure is known as γ-phase and exhibits negative thermal expansion (NTE) (Guzmán-Afonso *et al.*, 2011). A possible ferroelastic phase (γ'-phase), with positive thermal expansion, is expected at very low temperatures but it has only been found in some isostructural compounds (Evans and Mary, 2000).

Holmium trimolybdate belongs to the family of rare earth trimolybdates, with two stable phases at room temperature: γ (hydrated) and β'. The coexistence of these two phases has only been studied in $Y_2(MoO_4)_3$ at room temperature (Gates and Lind). In this work we will study the sequence of reversible and irreversible phase transitions of the two $Ho_2(MoO_4)_3$ phases that appear while increasing the temperature.

II. EXPERIMENTAL

A. Synthesis

Polycrystalline holmium trimolybdates were prepared by conventional solid-state synthesis (Kim *et al.*, 1991). We have obtained the initial β' and γ (hydrated) phases by using different thermal treatments: 1173 K for 24 h and 1250 K for 48 h, respectively. We will name them with their "initial phase" in the following X-ray experiments discussion.

B. X-ray diffraction

X-ray thermodiffractometry was performed using a PANalytical X'Pert PRO diffractometer with Bragg-Brentano geometry and Cu $K\,\alpha$ radiation (45 KV and 40 mA). An

X'Celerator detector was employed to collect XRD data over the 2θ angular range from 5° to 80° with a step size of 0.017° and a counting time of 50 and 100 s/step for the γ and β' phases, respectively. The samples were measured at different temperature ranges: from 300 K to 1000 K (in steps of 25 K) for the initial γ-Ho$_2$(MoO$_4$)$_3$ phase; and from 300 K to 1300 K (in steps of 20 K) for the initial β'-Ho$_2$(MoO$_4$)$_3$ phase. Measurements were carried out during a heating process under a still air atmosphere using an Anton Paar HTK 2000 camera.

III. RESULTS AND DISCUSSION

We have plotted the diffraction patterns measured for each sample using the 2D Contour tool of the FullProf software (Rodríguez-Carvajal, 1993). Figure 1 shows the sequence of phase transitions for Ho$_2$(MoO$_4$)$_3$ in the studied temperature range. We found that the initial β'-phase undergoes a transition to the β-phase (reversible process) and then to the γ-phase (irreversible process), which becomes hydrated at room temperature. For the other polymorph, the initial hydrated γ-phase turns to γ-phase (reversible process) and then to the β-phase (irreversible process), which changes to the β'-phase at room temperature.

The first transition of the (initially) β'-Ho$_2$(MoO$_4$)$_3$ sample occurs at 400 K and the second transition between 1125 and 1200 K. For the (initially) γ (hydrated)-Ho$_2$(MoO$_4$)$_3$ sample, the first transition takes place around 400 K and the second one between 780 and 920 K. The second transition of each sample occurs within a temperature interval in which the β and γ phases coexist. It can be seen that the transformation from the γ-Ho$_2$(MoO$_4$)$_3$ to the β-Ho$_2$(MoO$_4$)$_3$ is slower than the reverse process.
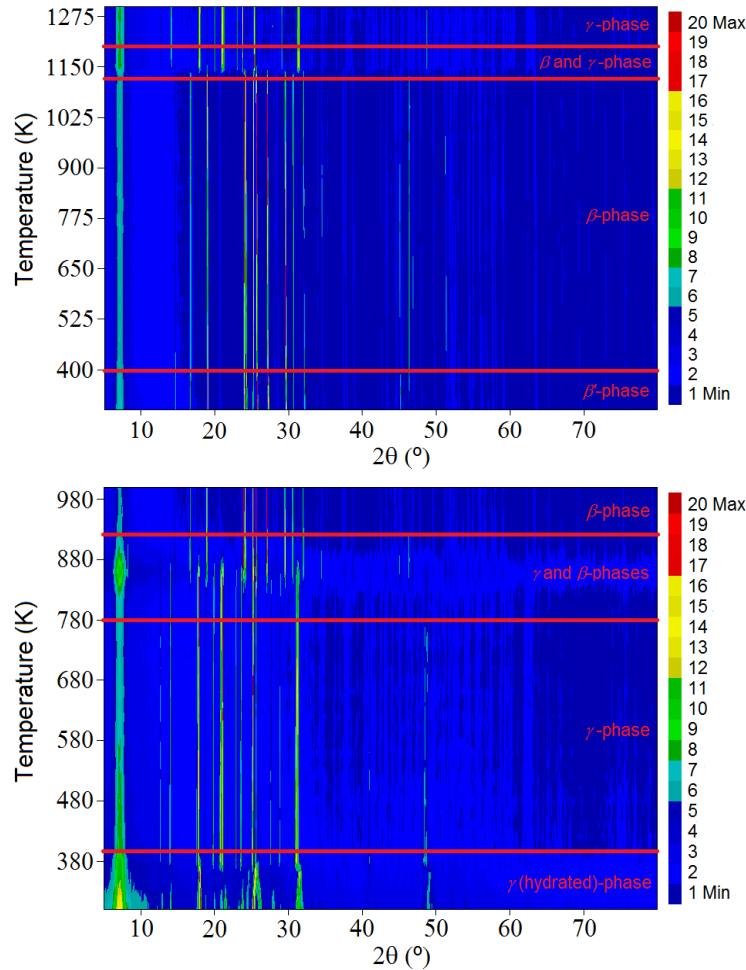
Figure 1. 2D contour plot of the X-ray diffraction patterns for the initial *β'*-phase (up) and for the *γ* (hydrated)-phase (down). Each pattern has been normalized to the highest peak. The red lines divide the temperature range into regions with different structural phases.

In order to obtain the thermal dependence of the crystallographic cell parameters, we have analyzed the X-ray diffraction patterns. We have obtained the scale factor, instrument zero, cell parameters, microstrain and domain size (given by U and Y parameters from the Thompson-Cox-Hasting pseudo-Voigt profile shape function) and the background coefficients (modeled by a Chebyshev polynomial) from powder diffraction data by iterating full pattern profile fittings [with the Le Bail (2005) algorithm] using the FullProf software (Rodríguez-Carvajal, 1993). We have used the sequential mode to perform the profile matching of all diffractograms. This method is useful when the processing of a large number of diffraction patterns that have been collected during a single experiment as function of an external parameter is desired, and the changes between two consecutive patterns are very small. The results of the refinements provided the reliability factors, χ^2, R_B, and R_{wp}, varying from 1.5 to 2.4, 0.7 to 1.8% and from 0.3

to 2.3%, respectively. The patterns from 300 to 400 K for γ (hydrated)-$Ho_2(MoO_4)_3$ were not fitted. Figure 2 shows two examples of obtained profile matching using the described procedure in this work. Both diffraction patterns belong to the initial samples, phases β' and γ (hydrated), measured after heating to 1000 K and had already transformed into the β-phase. The diffractograms are very similar, so that the Bragg positions appear at the same angles and the relative intensities are equal. We were not able to compare the γ-phase, since we did not heat the initial γ-phase beyond 1200 K, where we would expect a β-γ phase transition, according to the synthesis conditions and the phase relationships of the $RE_2(MoO_4)_3$-type rare earth molybdates, given by Brixner *et al.*, (1979). The γ-β phase transition was not described by the mentioned authors.
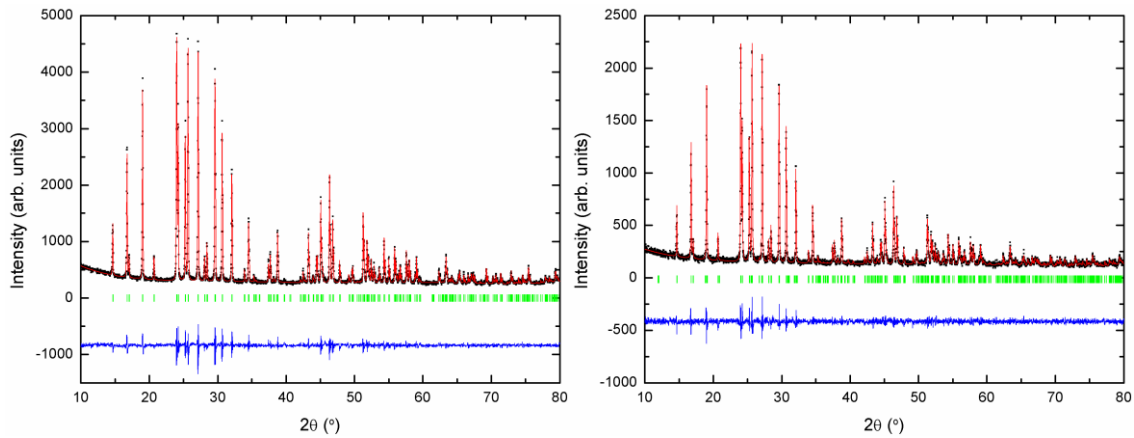
Figure 2. Profile matching for the initial *β'*-phase sample (left) and for the initial *γ* (hydrated)-phase sample (right) at 1000 K. Both patterns were indexed with the *β*-phase. The dotted line indicates observed intensities, and the profile fit is shown by a red line. The difference between observed and calculated intensities is plotted with a blue line, and the vertical bars represent the expected positions of diffraction peaks.
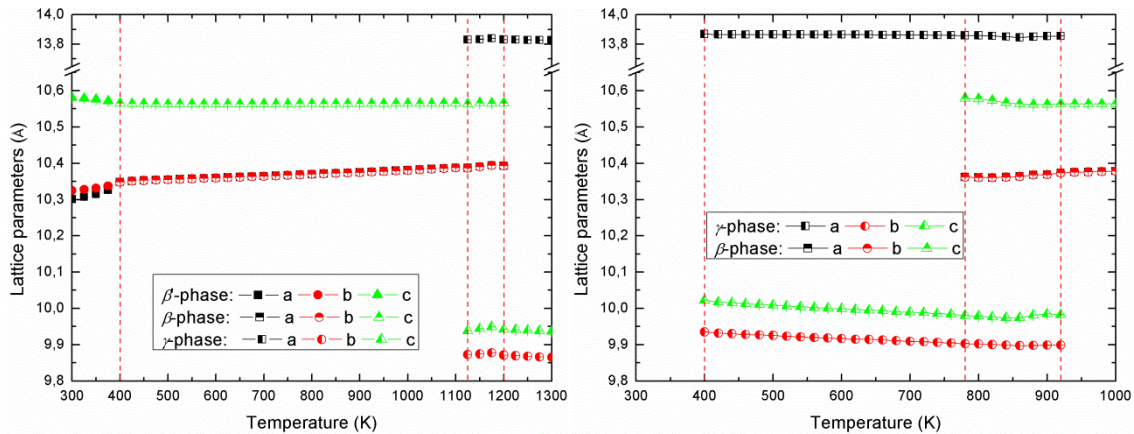
Figure 3. Temperature dependence of the lattice parameters for the initial *β'*- $Ho_2(MoO_4)_3$ (left) and for the *γ*-$Ho_2(MoO_4)_3$ (right). The red dashed lines divide the temperature range into regions with different structural phases.

Figure 3 shows the variation of the unit-cell structural parameters for the initial samples: β' and γ-Ho$_2$(MoO$_4$)$_3$. On the left figure we have the lattice parameters of the initial β'-phase and their thermal dependence. For this sample, the **a** and **b** parameters increase when the temperature increases and become equal at completion of the transformation into the β phase. The **c** parameter decreases until the transformation into the β phase, and then it continues decreasing more slowly until it reaches the γ phase, when all the cell parameters decrease. The thermal dependence of cell parameters for the sample with an initial γ-phase can be seen in figure 3 (right). At first all the cell parameters decrease with increasing temperature; when the phase transition to the β phase has been completed, the **a** and **b** parameters increase slightly with temperature, while the **c** parameter remains constant. During the coexistence of both phases there is an anomalous behavior: the slopes of the thermal dependence of the cell parameters change.

Figure 4 shows the thermal dependence of volume for both samples. The more dense β'-phase expands when the temperature increases, but it shows an anomalous behavior during the coexistence of phases. The behavior around the ferroelectric-paraelectric phase transition is similar to other molybdates: LaEr(MoO$_4$)$_3$, Tb$_2$(MoO$_4$)$_3$ and Dy$_2$(MoO$_4$)$_3$, which we have studied from 225 to 375 K (González-Silgo *et. al.*, 2011). The obtained coefficient for for β'-Ho$_2$(MoO$_4$)$_3$ was 1.02×10^{-5} K^{-1}, in this temperature interval. At higher temperatures, we have observed a similar dependence to other trimolybdates (González-Silgo *et. al.*, 2011). On the other hand, we have found that the less dense sample γ (dehydrated)-Ho$_2$(MoO$_4$)$_3$ exhibits negative thermal expansion from 400 to 780 K, after water loss, as it is observed with other similar molybdates (Guzmán-Afonso *et al.*, 2011) and from 1125 K to melting. We have calculated the linear thermal expansion coefficient α_L (negative value) until 780K for γ-Ho$_2$(MoO$_4$)$_3$, and we have confirmed that α_L is less negative when the ionic radius decreases (Guzmán-Afonso *et al.*, 2011). The calculated value was -6.25×10^{-6} K^{-1}; thus, it shows the largest negative linear expansion coefficient for this family of compounds. When both phases coexist, the behavior is anomalous and it is correlated with the β phase. During the β-γ phase transition, their volume increases just before the disappearance of the phase β; whereas during the γ-β phase transition, the volume of both phases decrease and its thermal dependence turns positive before the disappearance of the phase γ. After this, the volume of the β phase increases normally.
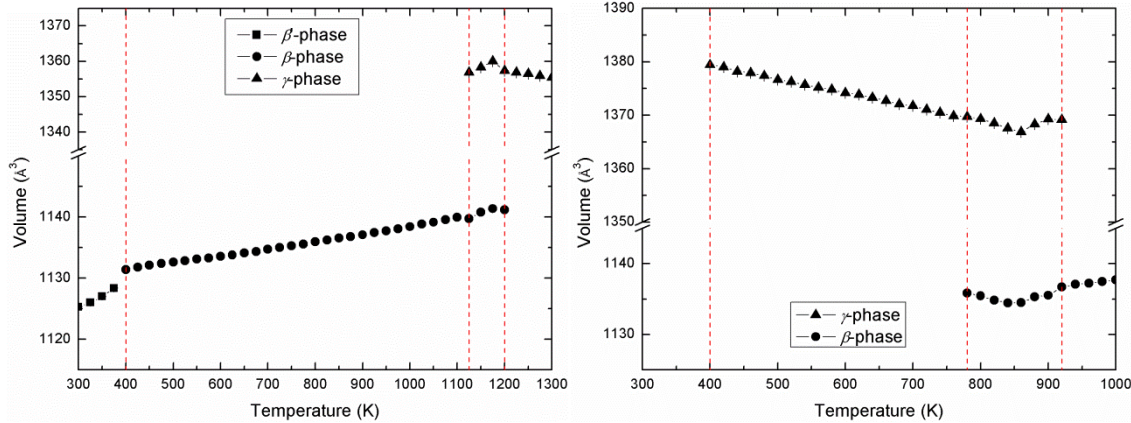
Figure 4. Temperature dependence of volume for the initial *β'*-phase sample (left) and for the *γ*-phase sample (right). The red dashed lines divide the temperature range into regions with different structural phases.

IV. CONCLUSION

Holmium molybdate can crystallize in two different phases (*β'* and *γ)* and their structural parameters are known at room temperature. We have described the evolution of both phases with the temperature. We have obtained a different phase diagram depending on the starting phase. We have analyzed the evolution of the lattice parameters and the volume of both samples. Two reversible phase transitions: *β'-β* and *γ (*hydrated) - *γ* (dehydrated) and two irreversible phase transitions *β-γ* and *γ-β* (with the latter exhibiting phase coexistence) have been detected for each starting sample. The *β'-β* phase transition is similar to other studied compounds*:* when the ionic radius decreases, the positive linear expansion coefficient is positive, although the **c** parameter decreases when the temperature increases (González-Silgo *et. al.*, 2011). Negative thermal expansion has been found for the *γ*-phase, and the negative linear expansion coefficient decreases when the ionic radius decreases, as observed for similar compounds (Guzmán-Afonso *et al.*, 2011). However, an anomalous behavior has been detected during the coexistence of phases. This last result could help us understand the negative expansion. Therefore we need to study the crystal structure of both phases during the irreversible phase transition. The ILL research proposal number 57431 has been accepted to perform a neutron diffraction experiment in the D2B beamline at high temperature, starting from the *γ* phases of $Ho_2(MoO_4)_3$, $Ho_2(WO_4)_3$, $Tm_2(MoO_4)_3$ and $Tm_2(WO_4)_3$.

ACKNOWLEDGMENTS

Abrahams, S. C. and Bernstein, J. L. (**1966**). "Crystal Structure of the Transition-Metal Molybdates and Tungstates. II. Diamagnetic $Sc_2(WO_4)_3$," J. Chem. Phys. **45**, 2745-2752.

Brixner, L. H., Barkley, J. R. and Jeitschko, W. (**1979**). *Handbook on the Physics and Chemistry of Rare Earth* (Amsterdam: North-Holland).

Evans, J. S. O and Mary, T. A. (**2000**). "Structural phase transitions and negative thermal expansion in $Sc_2(MoO_4)_3$," Int. J. Inorg. Mater. **2**, 143-151.

Gates, S. D. and Lind, C. (**2007**). "Polymorphism in yttrium molybdate $Y_2Mo_3O_{12}$," J. Solid State Chem. **180**, 3510-3514.

González Silgo, C., Torres, M. E., Guzmán-Afonso, C., Sabalisck, N., Lozano-Gorrín, A. D., González-Platas, J., Matesanz, E., Rodríguez-Carvajal. J. (2011). Crystal structure and non-linear properties of A2(MoO4)3 (Report Proposal 5-23-626). Grenoble, France: Institut Laue-Langevin user portal. https://club.ill.fr/cv/servlet/ReportFind

Guzmán-Afonso, C., González-Silgo, C., González-Platas, J., Torres, M. E., Lozano-Gorrín, A. D., Sabalisck, N., Sánchez-Fajardo, V., Campo, J. and Rodríguez-Carvajal, J. (**2011**). "Structural investigation of the negative thermal expansion in yttrium and rare earth molybdates," J. Phys.: Condens. Matter **23**, 325402 (9pp).

Jeitschko, W. (**1973**). "Crystal structure of $La_2(MoO_4)_3$, a new ordered defect Scheelite type," Acta Crystallogr., Sect. B: Struct. Crystallogr. Cryst. Chem. **29**, 2074-2081.

Jeitschko, W. (**1972**). "A Comprehensive X-ray Study of the Ferroelectric-Ferroelastic and Paraeleetric-Paraelastic Phases of $Gd_2(MoO_4)_3$," Acta Crystallogr., Sect. B: Struct. Crystallogr. Cryst. Chem. **28**, 60-76.

Kim, S., Lee, G.S., Shrout, T.R. and Venkataramani, S. (**1991**). "Fabrication of fine-grain piezoelectric ceramics using reactive calcination," J. Mater. Sci. **26**, 4411-4415.

Kojima, S. and Nakamura, T. (**1978**). "Electro-optical properties of gadolinium molybdate," Phys. Rev. B **18**, 453-458.

Le Bail, A. (**2005**). "Whole powder pattern decomposition methods and applications: A retrospection," Powder Diffr. **20**, 316-326.

Rodríguez-Carvajal, J. (**1993**). "Recent advances in magnetic structure determination by neutron powder diffraction," Physica B **192**, 55-69.

Templeton, D. H. and Zalkin, A. (**1963**). "Crystal structure of europium tungstate," Acta Crystallogr. **16**, 762-766.

Structural investigation of the negative thermal expansion in yttrium and rare earth molybdates

**Candelaria Guzmán-Afonso[1], Cristina González-Silgo[2],
Javier González-Platas[2,3], Manuel Eulalio Torres[1],
Antonio Diego Lozano-Gorrín[3], Nanci Sabalisck[1],
Víctor Sánchez-Fajardo[1], Javier Campo[4] and
Juan Rodríguez-Carvajal[5]**

[1] Departamento de Física Básica, Universidad de La Laguna, Tenerife, Spain
[2] Departamento de Física Fundamental II, Universidad de La Laguna, Tenerife, Spain
[3] Servicio Integrado de Difracción de Rayos X, Universidad de La Laguna, Tenerife, Spain
[4] Instituto de Ciencia de Materiales de Aragón, CSIC–Universidad de Zaragoza, Spain
[5] Institut Laue–Langevin, Grenoble, France

E-mail: csilgo@ull.es

Abstract
The $Sc_2(WO_4)_3$-type phase ($Pbcn$) of $Y_2(MoO_4)_3$, $Er_2(MoO_4)_3$ and $Lu_2(MoO_4)_3$ has been prepared by the conventional solid-state synthesis with preheated oxides and the negative thermal expansion (NTE) has been investigated along with an exhaustive structural study, after water loss. Their crystal structures have been refined using the neutron and x-ray powder diffraction data of dehydrated samples from 150 to 400 K. The multi-pattern Rietveld method, using atomic displacements with respect to a known structure as parameters to refine, has been applied to facilitate the interpretation of the NTE behavior. Polyhedral distortions, transverse vibrations of $A \cdots O$–Mo (A = Y and rare earths) binding oxygen atoms, non-bonded distances $A \cdots Mo$ and atomic displacements from the high temperature structure, have been evaluated as a function of the temperature and the ionic radii.

S Online supplementary data available from stacks.iop.org/JPhysCM/23/325402/mmedia

(Some figures in this article are in colour only in the electronic version)

1. Introduction

Most materials exhibit an expansion upon heating. However, a few are known to contract, i.e. show a negative thermal expansive (NTE) in a particular temperature range. Several solids have been identified with NTE behavior: ZrW_2O_8, ZrV_2O_7, $Sc_2W_3O_{12}$ and other related families (having corner linked octahedral and tetrahedral frameworks), zeolites and zeolite-like materials ($AlPO_4$ and NASICON), as well as carbon nanotubes and metal organic frameworks [1, 2]. Cubic zirconium tungstate (ZrW_2O_8) is the best known example of large isotropic negative expansion persisting over a wide temperature range [3–5]. There are a number of important potential applications for substances with a negative coefficient

of thermal expansion, where the overall expansion coefficient of a body can be precisely tailored to a specific positive, negative or even zero value. In particular, the ZrW_2O_8 family of materials (Zr and W can be replaced with Hf or/and Mo, respectively) are used in the electronic or/and photonic areas [6, 7], in medical applications [8], etc.

In the last decade, a significant amount of research into tungstates and molybdates belonging to the $A_2(MO_4)_3$ family, where A is a trivalent ion ranging from Al to Dy and M is W^{6+} or Mo^{6+}, has been carried out. This increased interest of the scientific community can be attributed to the discovery that various compounds in this family display NTE [9]. Moreover, the $Sc_2(WO_4)_3$-type structure with flexible frameworks, relatively low densities and the presence of lattice modes that

becomes softer on volume reduction predispose these materials to a rich behavior upon the application of pressure [10]. On the other hand, the quasi-two-dimensional layered structures are suitable for trivalent ion conduction [11]. These materials can crystallize in an orthorhombic phase (with $Sc_2(WO_4)_3$-type structure, *Pbcn*) [12] or in a monoclinic phase (with $Al_2(WO_4)_3$ or $Fe_2(MoO_4)_3$-type structure, $P2_1/a$) [13, 14]. Some of them undergo a ferroelastic phase transition between both phases [15] but only the orthorhombic compounds have NTE. In general, tungstates exhibit NTE in a wider range of temperature while molybdates have more negative coefficients and the NTE property increases with the ionic radius of the trivalent cation [16]. In particular, molybdates with formula $A_2(MoO_4)_3$ show a very intense NTE above 450 K, when A = Y, Ho–Lu [17]; because they are hygroscopic, no detailed structural investigation into these rare earth molybdates at low temperatures is currently available in the literature. The ICSD (Inorganic Crystal Structure Database) does not contain solved structures of molybdates from dysprosium to lutetium and only the structure of yttrium molybdate is described [18]. The study of the structural behavior of these compounds upon application of pressure, as well as the study of their ionic conduction and other properties, can contribute to a better understanding of the NTE. Specifically, it is not yet clear whether the NTE behavior of rare earth molybdates could be possible at room or lower temperatures for completely dehydrated samples.

Although, in general, structural flexibility seems to be a key factor for NTE, different mechanisms have been proposed to explain this feature in different type of compounds. The origin of NTE can be explained in terms of phonons that have a negative Grüneisen parameter γ [19]: 'an increasing in volume increases tension in the bonds; the restoring force for transverse motion is thus enhanced, raising the frequency and so contributing negatively to this parameter'. The NTE in oxides is most commonly observed in crystals and glasses with strong M–O–M bridges and is then due to the transverse vibration of the oxygen atoms. For some of these structures there are many modes of low frequency having strongly negative γ. In a transverse vibration of the bridging oxygen in a M–O–M bond (where M is usually a metal), the M–M distance decreases whereas the M–O distance remains essentially unchanged. Large amplitude transverse vibrations of the oxygen atoms can occur through coupled oscillations of the rigid corner sharing polyhedra forming the structure (RUMs or rigid unit modes [20]). In this context, there are, essentially, two competing active components in NTE: the thermal expansion of atom pairs has a positive contribution (longitudinal modes), whereas rotations of rigid units (transverse vibrational modes and libration) have a negative contribution. In recent years, questions have been raised regarding whether simple RUMs models are sufficient to explain NTE. Ravindran *et al* [21] and Tao and Sleight [22] cite several examples where NTE exists regardless of RUMs. For the $A_2Mo_3O_{12}$ family it seems that polyhedral distortion plays the main role in this behavior [23]. Very recently, Marinkovic *et al* [24] analyzed the dehydrated orthorhombic phase of $Y_2(MoO_4)_3$ and found that the polyhedral distortion is strongly correlated with the linear NTE coefficient of different members of the $A_2M_3O_{12}$ family.

In the following sections we show the structural and thermal behavior, in the 150–400 K temperature range, for three dehydrated samples: $Y_2(MoO_4)_3$, $Er_2(MoO_4)_3$ and $Lu_2(MoO_4)_3$. We present the results of combined neutron and x-ray Rietveld refinements in order to obtain the maximum information on the mechanisms involved in NTE, in this temperature range. In order to investigate the above-mentioned mechanisms we apply a structural refinement in which the atomic displacements are used as fundamental primary free parameters instead of traditional position atom coordinates.

2. Experimental methods

2.1. Synthesis

Yttrium and rare earth molybdates have been prepared by conventional solid-state synthesis. A_2O_3 (A = Y and rare earth) and MoO_3 powder (both, Aldrich, 99.99%) were preheated, respectively, at 1173 and 923 K for 10 h before use. These preheated powders were weighed in stoichiometric amounts, mixed and homogenized in an agate mortar. The resulting powder was then pressed into pellets and finally sintered in air atmosphere at 1323 K for 24 h in platinum crucibles. X-ray powder diffraction data confirmed the absence of impurities in the above samples that were, however, very hydrated at room temperature. In order to confirm the stability of all compounds, both TG–DTA (thermogravimetric/differential thermal analysis) and DSC (differential scanning calorimetry) analysis were performed.

2.2. X-ray and neutron diffraction

Powder diffraction data for Rietveld refinement were collected in a PANalytical X'Pert PRO diffractometer (Bragg–Brentano mode) with a X'Celerator detector using the Cu Kα_1 radiation ($\lambda = 1.5405(1)$ Å), in the angular range $10° < 2\theta < 100°$, by continuous scanning with a step size of $0.02°$ and total step time of 200 s. Divergence, anti-scatter slits were set at $0.5°$, $1°$ respectively and the detector was used in scanning mode with an active length of $2.14°$. Only a secondary 0.02 rad Soller slit was used. The sample was pressed into a holder of dimensions 14×10 mm^2. Measurements at different temperatures were carried out during a cooling process using an Anton Paar TTK 450 camera from 400 to 150 K under vacuum (5×10^{-4} mbar) assuring totally dehydrated samples; and the final scan was performed with the addition of three cycles in order to check any change in the sample during the experimental process. The cooling rate was 10 K min^{-1} leaving 5 min between measurements to stabilize the temperature in the sample. The experiments were conducted at the x-ray diffraction facility (SIDIX) at the University of La Laguna.

The neutron powder diffractometer D2B (Debye–Scherrer geometry) of the Institut Laue–Langevin (Grenoble, France) was used for data collection with an incident wavelength $\lambda = 1.5943(1)$ Å, Ge[335] monochromator, take-off angle $135°$, angular range $5° < 2\theta < 165°$, without primary collimator and 128 ^{3}He tubes 300 mm in height as the detection system. A complete diffraction pattern was obtained with 100 steps of $0.025°$ in 2θ; however eight consecutive scans

of 100 steps each were added for increasing the statistics of the final diffraction pattern. To ensure their total dehydration, all samples were placed in a furnace at 423 K for about 8 h inside the vanadium container and closed before introducing it into the cryofurnace installed on the D2B diffractometer. The diffraction patterns were recorded at different temperatures from 400 to 150 K. Each pattern was collected over 2.5 h. Two kinds of patterns were extracted from the raw data, one corresponding to a binning of the central equatorial zone of the detector for which the resolution is higher, and another integrating the whole detector for which the counting statistics are better despite a worse resolution.

Temperature calibration from the minimum up to the maximum operating temperature of each instrument is frequently performed by employing similar NIST phase transformation temperature standards assuring an error less than ± 3 K. Moreover, a visual inspection of neutron and x-ray patterns in the Q space shows very similar peak positions for each sample and temperature, and similar shifts between different temperatures, so joined refinements were justified.

2.3. Structure refinements

Multi-pattern Rietveld refinements were performed using the program FullProf [25] on two different neutron diffraction datasets and one set of x-ray diffraction data with 0.4:0.4:0.2 as weight factors. The starting structural model was the orthorhombic structure of $Y_2(MoO_4)_3$ at 403 K [18] with space group *Pbcn*, then atomic parameters of the three samples at 400 K were refined by the classical approach. For refinement at lower temperatures a new approach was used. The experimental profiles were always (classical and new) modeled using a Thompson–Cox–Hastings pseudo-Voigt profile shape function [26], with two adjustable parameters (U and Y, corresponding to isotropic Gaussian strain and Lorentzian size effects); fixed values (U_{ins}, V_{ins}, W_{ins}, X_{ins} and Y_{ins}) were used for the instrumental resolution parameters, as well as the peak asymmetry (S/D and S/L). A prominent modulated diffuse scattering was observed, despite samples being dehydrated. The background was modeled via the Debye equation [27] plus a polynomial of degree 3. The wavelength of both neutron diffraction patterns was refined at a first stage of refinements of each compound at 400 K maintaining fixed the cell obtained by the corresponding x-ray pattern. The refined wavelength was very similar and was fixed to $\lambda = 1.592\,16$ Å for all compounds at all temperatures.

A more direct way to study these compounds (to analyze possible transverse modes as a more important mechanism) is the refinement of atomic displacements instead of atomic coordinates. The program FullProf [25] can refine these displacements from a known structure with the same space group and a similar unit cell. We started from the structure of the three molybdates at 400 K which was refined using the classical approach. Then, the remaining structures, at lower temperatures, were obtained by refining shifts of the atomic coordinates with respect to the structure at 400 K. The shifts of the different atom coordinates with respect to the high temperature structure were initially zero. We provide

details of how to perform the refinements in the supporting information (available at stacks.iop.org/JPhysCM/23/325402/mmedia). The use of this approach with respect to the classical refinement has the advantage of directly obtaining the displacement of atom positions that can be easily visualized with the program FpStudio [28]. It is also possible to reduce the number of degrees of freedom of structural parameters when these shifts are close to zero, to restrain and/or to constrain them and to use parametric Rietveld refinement where the displacements can depend on 'non-crystallographic' values such as temperature, etc.

3. Results and discussion

3.1. Refinement of the crystal structure

DSC curves of yttrium and rare earth molybdates do not show anomalies after water loss in two cycles of warming and cooling (from 100 to 650 K), as in previous studies [17]. Then, the results presented in this work correspond to experiments in dehydrated samples of $Lu_2(MoO_4)_3$ at 400, 303, 250, 225, 200 K and $Er_2(MoO_4)_3$ and $Y_2(MoO_4)_3$ at 400, 350, 300, 250, 200, 150 K, i.e. performed in an interval of temperature where the stability is guaranteed. All the samples were measured by both neutron and x-ray diffraction to determine the crystalline structure with maximum reliability. It is well known that neutron diffraction provides better structural information on light atoms than x-ray diffraction, especially when light atoms are accompanied by heavy atoms as is the case in these samples. An example of diffraction patterns refined with the Rietveld method is shown in figure 1 for the $Lu_2(MoO_4)_3$ compound. From the background refinement given by a Debye-like function plus a polynomial function (figure 1) for the three patterns, we have calculated four good values of interatomic distances and the average values were: 2.17(3), 2.99(2), 3.85(5), 4.90(6) Å for $A \cdots O$, $O \cdots O$, $Y \cdots Mo$ and $Mo \cdots Mo$, respectively. We did not find a clear temperature dependence of the atomic separations extracted from the Debye function. To study the instantaneous structure we need very high resolution data ($Q > 20$ Å) by using atomic pair distribution function (PDF) analysis [29].

The results of the refinements are consistent with similar studies of molybdates and tungstates by neutron diffraction. Reliability factors R_{wp} and χ^2 for neutron patterns vary from 8.84 to 13.7% and from 1.86 to 4.32, respectively, without any correlation with temperature or type of compound and are very similar to those obtained for $Sc_2(WO_4)_3$ [9] with 7.62% and 2.287 as averaged values and $Y_2(WO_4)_3$ [30] with 9.26% and 1.77 at room temperature for R_{wp} and χ^2 measured under similar conditions. $R(F^2)$ ranging between 3.87 and 2.37% for 2557 reflections while that obtained by TOF (time of flight) data of the monoclinic phase of scandium molybdate was 3.56% for 3153 reflections [31].

X-ray profile reliability factors were compared with those of the synchrotron results [24, 31]. They are not significantly worse, if it is taken into account that our results correspond to a multi-pattern refinement in which neutron data were given a higher weight. Erbium and yttrium molybdate refinement showed worse reliability factors,
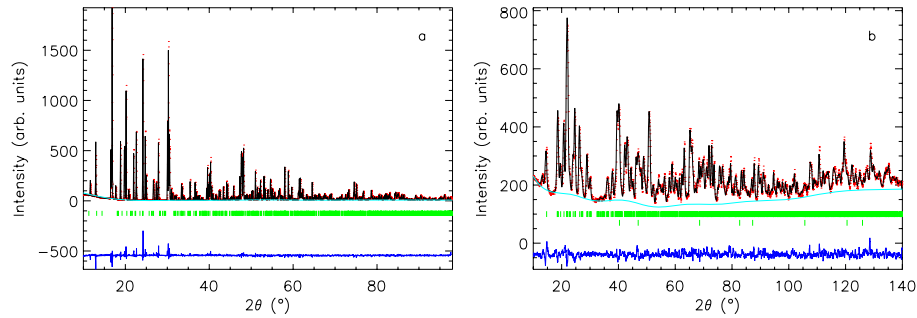
Figure 1. Examples of powder diffraction patterns collected for $Lu_2(MoO_4)_3$ at 200 K: (a) on a PANalytical X'Pert Pro diffractometer and (b) on a D2B powder diffractometer integrating the entire detector. Observed data (red dots) are shown along with the pattern (black line) calculated from Rietveld analysis and difference/s.u. (blue line) and green bars indicate the Bragg positions. The second group of reflections corresponds to the aluminum cryofurnace. Also, the background calculated from the Debye model is shown in the figures (turquoise line).
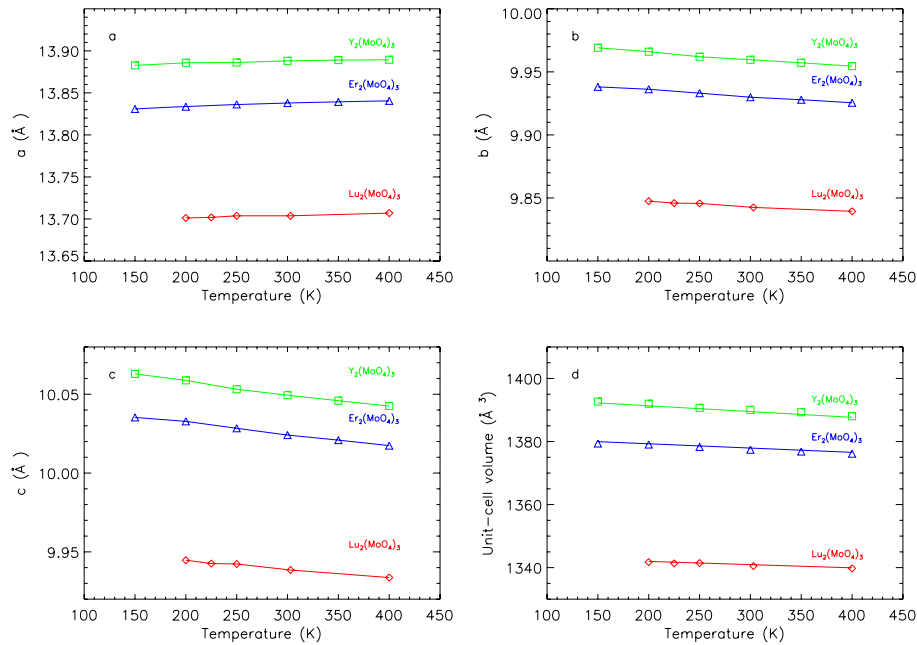
Figure 2. (a)–(c) Variation of lattice parameters and (d) volume as a function of temperature for $Y_2(MoO_4)_3$, $Er_2(MoO_4)_3$ and $Lu_2(MoO_4)_3$. Standard deviations are smaller than respective symbols on the graphs. Panel (d) indicates experimental values as spots and a solid line for linear fitting.

probably due to a weaker collected global intensity. Standard deviations of cell parameters were lower than those obtained for tungstates [9, 30] and $Y_2(MoO_4)_3$ [24] but similar to $Sc_2(MoO_4)_3$ ([31] also obtained by multi-pattern refinement). The final Rietveld reliability factors for the refined diffraction patterns for all compounds and temperatures are provided in the supporting information (available at stacks.iop.org/JPhysCM/23/325402/mmedia).

The variation with temperature of the unit cell parameters and volume of the samples is shown in figure 2. The behavior is the same for all compounds, the *b* and *c* axes decrease with increasing temperature while the *a*-axis increases insignificantly when the temperature increases. The present results in fact agree with results of Marinkovic *et al* [24] as both show the *a*-axis to be invariant with the temperature.

The variation of volume (figure 2(d)) is close to linear and we have calculated the linear expansion coefficient $\alpha_L (= \alpha_V/3)$ obtaining -4.38×10^{-6}, -3.27×10^{-6} and -2.52×10^{-6} K^{-1} for $Y_2(MoO_4)_3$, $Er_2(MoO_4)_3$ and $Lu_2(MoO_4)_3$, respectively, and differs from other results, almost half of the values obtained by Marinkovic *et al* [24] and [16] probably due to the temperature range and the number of observations used in the fit procedure. From these results it can be stated that dehydrated rare earth molybdates show NTE behavior in the range 150 to 400 K as occurs with yttrium molybdate [24] and, in our case, a correlation was found between the ionic radii and NTE coefficients, also observed by other authors (for instance in Barrera *et al* [19] and Sumithra and Umarji [17]).

The structure of all compounds, at different temperatures, was obtained by refining the displacements of atomic
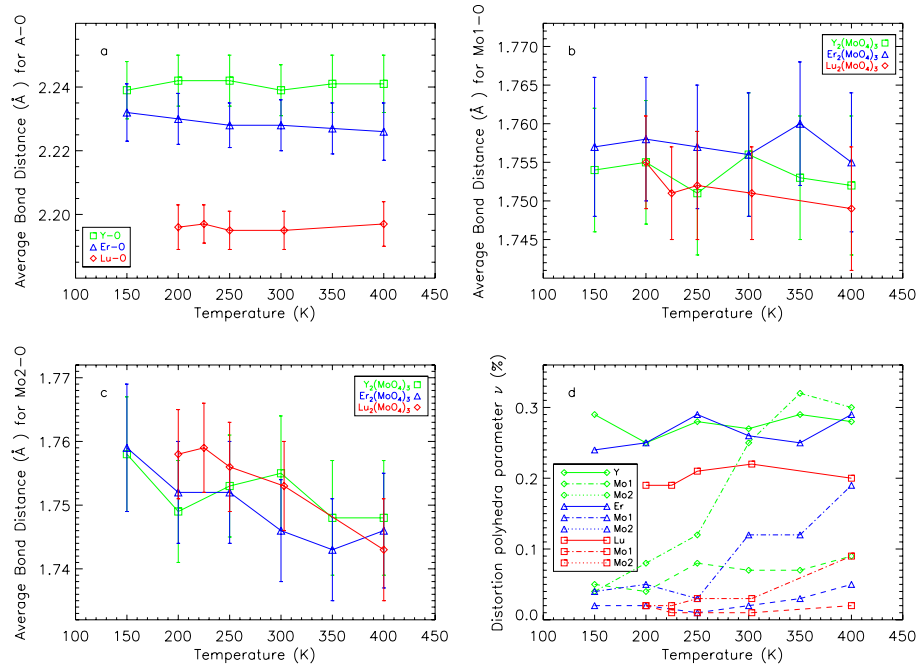
Figure 3. Average bond distance for (a) A–O, (b) Mo1–O, (c) Mo2–O and (d) polyhedral volume distortion for octahedral and tetrahedral groups as a function of temperature in $Y_2(MoO_4)_3$, $Er_2(MoO_4)_3$ and $Lu_2(MoO_4)_3$.

coordinates from the high temperature structure, in turn obtained at 400 K, using a conventional multi-pattern Rietveld refinement (see supporting information available at stacks. iop.org/JPhysCM/23/325402/mmedia). The precision of our fractional atomic coordinates is similar to those available from Evans and Mary [31], Forster and Sleight [32] and Marinkovic *et al* [24]. Refined structures are formed by corner linked AO_6 octahedral and MoO_4 tetrahedral frameworks and it is generally assumed that these polyhedra are inherently distorted and bridging distances and angles are the basic structural features for NTE, in this type of compound [23]. The following sections are dedicated to the study both aspects.

3.2. Analysis of coordination polyhedra

We have not found significant changes in A–O (figure 3(a)) coordination bonds during heating. This is indeed the case for other tungstates [9, 30]. However, we found a contraction of the Mo–O distances when the temperature rises (figures 3(b) and (c)). This is in agreement with other studies that established that W–O and Mo–O bond lengths undergo a reduction during heating [9, 24] because correlated oscillations can lead to this apparent decrease in bond distances [33]. These results are to be expected considering that Mo–O bonds are stronger (having practically zero expansion, especially in the more symmetric tetrahedron) than A–O (having typical linear positive expansion). In consequence, if vibrational transverse modes exist, a contraction and slight changes in tetrahedral and octahedral volumes must be observed.

Concerning the internal angles of octahedral and tetrahedral groups, we found no appreciable thermal and ionic radii dependence (see supporting information available

at stacks.iop.org/JPhysCM/23/325402/mmedia). Maximum and minimum values in O–A–O angles were 95.3°–85.1° for $Y_2(MoO_4)_3$, 95.3°–85.6° for $Er_2(MoO_4)_3$ and 94.4°–86.5° for $Lu_2(MoO_4)_3$. The maximum observed angular differences were 2.4° for O1–Y1–O5, 1.8° for O1–Er1–O2 and 1.6° for O3–Lu1–O4. The maximum variations in O–Mo1–O were 1.6°, 1.9° and 0.9° for $Y_2(MoO_4)_3$, $Er_2(MoO_4)_3$ and $Lu_2(MoO_4)_3$, respectively, and 2.7°, 1.7° and 1.6° for O–Mo2–O angles in the same sequence as before.

Bond valence sums (BVSs) have been calculated (figure 4), using the Bond_Str program belonging to the FullProf Suite. Mo atoms are, in general, over bonded but only Mo2 reduces its calculated valence, using the BVS [34], when the temperature decreases. In accordance with the above discussion, this effect presumably contributes to a slight decrease in the tetrahedron volume with increasing temperature. Although rare earths are over bonded, especially in the case of yttrium, there is no noticeable change in their calculated valence and coordination bonds during heating, this is also the case for other tungstates [9, 30].

We have compared our results with the recent conclusions obtained by Marinkovic *et al* [24] for the case of yttrium: (1) polyhedral distortion, calculated by using the volume distortion parameter $\nu(\%)$ proposed by Makovicky and Balic-Zunic [35], is strongly correlated with the linear coefficient of the thermal expansion (α_l) of different members of the $A_2M_3O_{12}$ family. (2) The distortions of the AO_6 and MoO_4 polyhedra increase slightly with increasing temperature.

Figure 3(d) shows the variation with temperature of the volume distortion parameter calculated using the program Bond_Str [36]. As expected, we observed that the distortion parameters of the octahedral groups AO_6 are larger than those
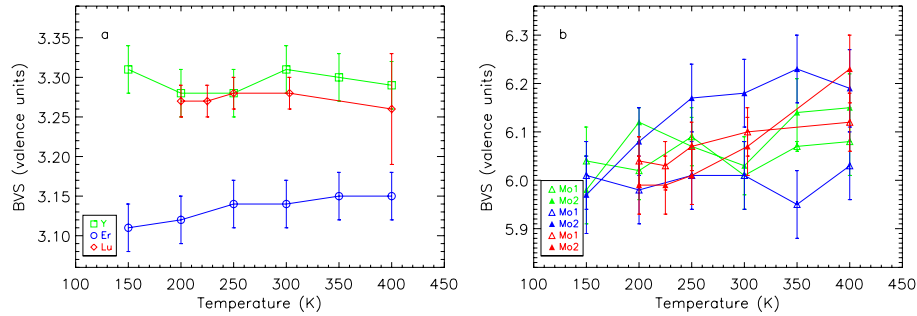
Figure 4. Calculated valences for Y^{3+} ($\square$), Er^{3+} ($\bigcirc$), Lu^{3+} ($\lozenge$) and Mo^{6+} ($\triangle$ for Mo1, $\blacktriangle$ for Mo2) as a function of temperature for $Y_2(MoO_4)_3$ (green lines), $Er_2(MoO_4)_3$ (blue lines) and $Lu_2(MoO_4)_3$ (red lines) compounds.
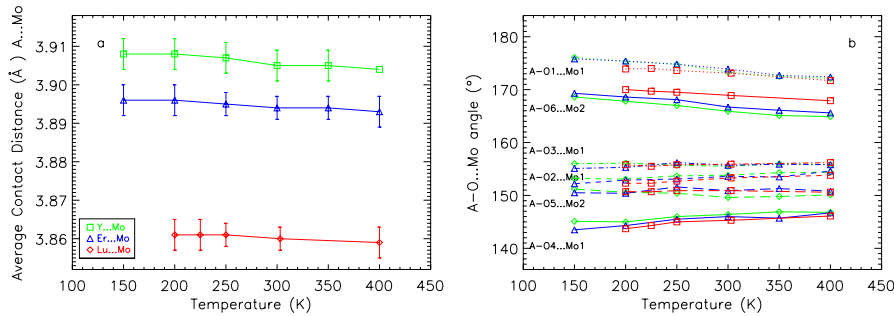
Figure 5. (a) Average contact $A \cdots Mo$ distance and (b) A–O–Mo bridging angles (error bars are comparable with respective symbols on the graph) as a function of temperature for $Y_2(MoO_4)_3$ (green), $Er_2(MoO_4)_3$ (blue) and $Lu_2(MoO_4)_3$ (red).

of the tetrahedral groups MoO_4. The values of $\nu(\%)$ for YO_6 and ErO_6 are similar, whereas this value is lower for LuO_6. The values of $\nu(\%)$ for $Mo1O_4$ in $Er_2(MoO_4)_3$ and $Lu_2(MoO_4)_3$ are similar, whereas this value is greater for $Y_2(MoO_4)_3$. However, the distortion parameters of $Mo2O_4$ tetrahedra are clearly correlated with the ionic radii of cation A and with the linear thermal expansion coefficient α_1. On the other hand, the distortion of octahedral AO_6 groups and tetrahedral $Mo1O_4$ groups are independent of temperature ($0.2 < \nu(\%) < 0.3$ and less than 0.1, respectively) in our smaller range of temperature, whereas the tetrahedral $Mo2O_4$ groups become more distorted with increasing temperature. The differences found in the $\nu(\%)$ parameters with respect to the results of Marinkovic *et al* [24] are due to geometric calculations based on different structural data. The reliability $\nu(\%)$ parameters depend strongly on the correct structural information. It is well known that, for this type of compound, and using only x-ray diffraction, the oxygen positions are less reliable due to their lower x-ray scattering cross section with respect to the heavier metal atoms. Definitively, our results are in agreement with the general statement that by increasing polyhedral size, e.g. replacing the polyhedron central A-cation with a larger cation, its ability to distort increases (more flexibility), hence increasing the NTE effect [23].

3.3. Transversal modes by oxygen displacements

If the oxygen–cation bonds of polyhedra are maintained (except for $Mo2O_4$ in which the distance Mo2–O slightly increases and becomes more distorted when the temperature

decreases), relative displacements between second neighbors must occur (between oxygen anions and between cations). As expected [37] and seen in figure 5, $A \cdots Mo$ distances generally contract on heating. When O4 is involved the distance increases for the three compounds (see supporting information available at stacks.iop.org/JPhysCM/23/325402/mmedia). However, only A–O1–Mo1 and A–O6–Mo2 bridging angles clearly contract on heating (being always the longest), for all compounds. This result is also observed in scandium molybdate [31] and tungstate [9]. Moreover A–O4–Mo2 expands on heating (it is always the shortest), for all compounds, in accord with the corresponding $A \cdots Mo$ expansion. The changes in $A \cdots Mo$ distances and A–O–Mo bridging angles, due to traversal movement of oxygen atoms appear to be at the origin of the NTE, in this type of compound.

Figures 6(a)–(c) show the refined oxygen displacements, on cooling, for AO_6 and the two MoO_4 polyhedra. This picture is automatically obtained with the program FullProf Studio [28] included in the FullProf Suite, after the Rietveld refinement of the shifts of the atomic coordinates with respect to the higher temperature structure. A conventional refinement does not generate an output file (*.fst) suitable for display with FpStudio and showing arrows. For reasons of clarity, the arrows were magnified on figures 6(a)–(c), 7 and 8 and their direction indicates the oxygen displacement on cooling (the values of the amplitudes, in Å, are provided in the supporting information available at stacks.iop.org/JPhysCM/23/325402/mmedia). With the exception of O3, the remaining oxygen atoms have detectable amplitudes (>0.05 Å) when compared
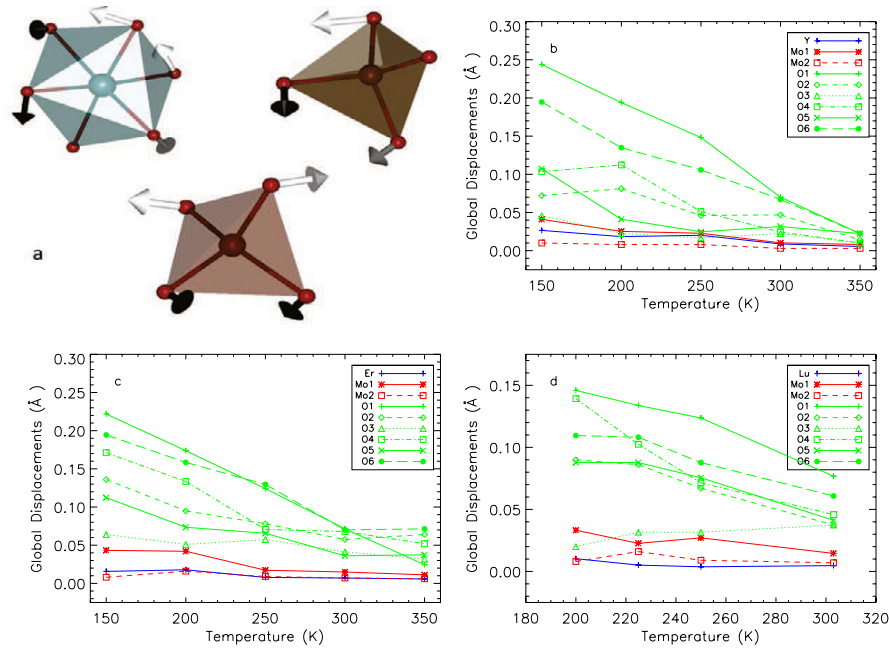
Figure 6. (a) Isolated polyhedra: AO_6 (left), $Mo1O_4$ (right) and $Mo2O_4$ (bottom) in which the atom displacements are represented using arrows in order to obtain an intuitive picture of what happens on cooling. The thermal dependence of these displacements of each atom in Å with respect to the structure at 400 K, are shown for (b) $Y_2(MoO_4)_3$ (c) $Er_2(MoO_4)_3$ and (d) $Lu_2(MoO_4)_3$.
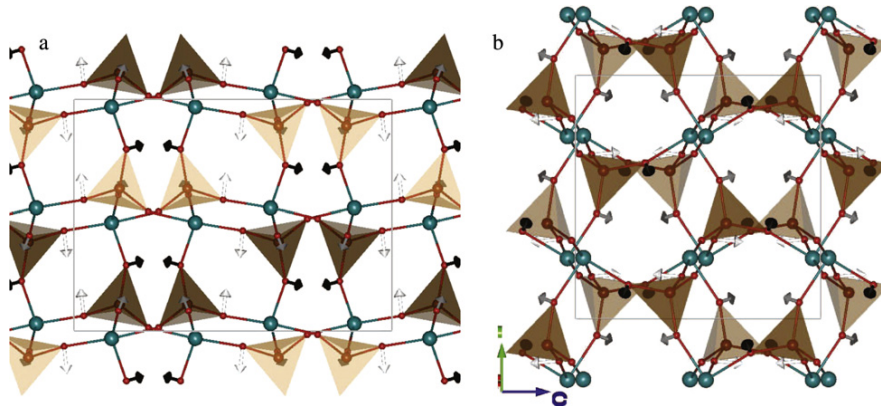
Figure 7. Structure of A_2MoO_4 without the $Mo2O_4$ tetrahedra and drawing the oxygen displacements with respect to the HT structure. (a) *b*-axis view and (b) *a*-axis view. The white arrow is the displacement of O1, the gray arrow is the displacement of O2 and the black arrow is the displacement of O4. Note that the displacement of O3 is negligible in the graph, such that no arrow is associated with this atom.

with typical thermal displacements. From a graphical point of view, it is difficult to assign rigid movements to polyhedra as the oxygen atoms seem to be shifted randomly. This may explain why the refinements, using rigid body constraints were not sufficiently good for our compounds, leading us to query whether the presence of RUMs plays a key role in the NTE mechanism. Tao and Sleight [22] did not find RUMs in their analysis of $A_2(MO_4)_3$ structures either.

In figures 6(d)–(f), the thermal dependence of the displacements (arrows) from the structure at 400 K for each atom in Å can be observed (which are obtained by refining the shifts of the atomic coordinates). In general, the displacements of O1, O6 and O4 increase more steeply with temperature. Also, these displacements are longer in $Y_2(MoO_4)_3$ and

shorter in $Lu_2(Mo_4)_3$. It is important to note here that displacements of O4 are always shorter than those of O1 and the displacements of O6 are longer than those of O5 (we compare oxygen atoms in different tetrahedra). At this point, our discussion will be focused on the study (figures 7 and 8) of the dependence, on cooling, of the changes in cell dimensions with respect to changes in non-bonding A · · · Mo distances and their angles, through the bridging oxygen displacements shown in figures 6(d)–(f).

3.4. Visualization of the structural mechanisms

In figure 7 it can be seen that the amplitude of the displacement of O1 and its direction are in agreement with the bridging
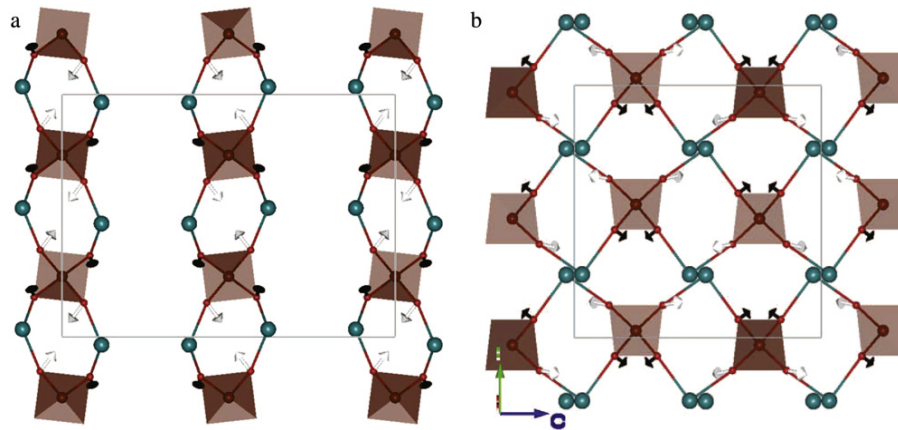
Figure 8. Structure of A_2MoO_4 without the $Mo1O_4$ tetrahedron and drawing the oxygen displacements with respect to the *HT* structure. (a) *b*-axis view and (b) *a*-axis view. The black arrow is the displacement of O5 and the white arrow is the displacement of O6.

angle opening. Contrarily, the direction of the displacement obtained for O4 and O2 is consistent with the bridging angle closing. This is consistent with the thermal dependence of A–O–Mo angles shown in figure 5. In particular, from figure 7(a), rings involving O1 (black arrow) and O4 (white arrow) are connected along the *c*-axis through Mo1–O2–A bridges (O2 with a gray arrow), but two consecutive rings are not connected along the *a*-direction. Although, on cooling, an opening of the A–O1–Mo1 angle and a lengthening of its corresponding non-bonding distance A $\cdots$ Mo1 (given by a displacement of the atom O1) are visible, there is no cooperative effect to expand the *a*-parameter, which can be slightly shortened by typical longitudinal modes. In the same figure, a slight closing of the A–O4–Mo1 angle and shortening of the non-bonding distance A $\cdots$ Mo1 (given by the displacement of the atom O4), without cooperative effect, must not be sufficient for a contraction (instead of an expansion) of the *c*-parameter. From figure 7(b), rings involving O1 and O2 are connected through O3 (without arrow) along the *b*-axis. The lengthening of the A–O1–Mo1 bridge exceeds any possible slight shortening of the A–O2–Mo1 bridge (given by the smaller displacement of the atom O2), producing, on cooling, a global expansion of the *b*-parameter. Rings involving O1 and O3 are connected, through O4, along the *c*-axis. Using a similar argument, the stronger opening of the A–O1–Mo1 angle than the slight closing of the A–O4–Mo1 angle may result in a net contraction of the *c*-parameter. The contribution of oxygen bridges, involving $Mo1O_4$ tetrahedra, does not seem to determine the expansion of the *c*-parameter on cooling.

On the other hand, in figure 8 it can be seen that the displacement of the atom O6 is significantly longer than that of O5 and its direction is consistent with the bridging angle increment observed in figure 5. In figure 8(a) particularly we can clearly see that the two type A–O6–Mo2 bridges and the two type A–O5–Mo2 bridges make rings along the *c*-axis, connecting the two more symmetric $Mo2O_4$ tetrahedra, containing O5 (black arrow) and O6 (white arrow) in the corners. Since such rings are not connected along the *a*-direction there is no cooperative effect of transversal modes to

expand the *a*-parameter. The increasing of the first bridging angle and its non-bonded distance, on cooling (given by the displacement of the atom O6), contributes decisively to the expansion of the *c*-parameter as compared with the previous mechanism involving the A–O1–Mo1 and A–O4–Mo1 bridges. However, the expansion in the *b*-direction is more difficult to explain because, as seen in figure 8(b), the rings involving O5 and O6 atoms are not connected in this direction and the lengthening of the non-bonding distance A $\cdots$ Mo2 would not reach a cooperative effect. However, the nearly plane square rings parallel to the *bc* plane show a clear expansion with a more important component along the *b*-direction. This fact, together with the mechanism described above, which involves the A–O1–Mo1 bridge, leads us to explain the *b*-parameter expansion on cooling. Finally, we want to comment that, in the above discussion, we have described how *b* and *c* axes show negative expansion and how the *a*-axis does not show a negative expansion, although we have not delved into the origin of these transversal movements. In general, the different arrangement of harder MoO_4 tetrahedra than AO_6 octahedra along the three axes explains the anisotropic axial thermal expansion; this is a well know phenomenon in simple molybdates, which affects both thermal expansion and compressibility [38, 39].

4. Conclusions

The thermal behavior of the orthorhombic (*Pbcn*) crystal structure of $Y_2(MoO_4)_3$, $Er_2(MoO_4)_3$ and $Lu_2(MoO_4)_3$ has been investigated by multi-pattern Rietveld refinement from neutron and x-ray data. We have found that, similarly to yttrium molybdate [24], other rare earth molybdates exhibit negative thermal expansion from 150 to 400 K, after water loss. The absolute values of the linear thermal expansion coefficients decrease with the A^{3+} ionic radius. The obtained results are $\alpha_L = -4.38 \times 10^{-6}$, -3.27×10^{-6} and -2.52×10^{-6} K^{-1} for $Y_2(MoO_4)_3$, $Er_2(MoO_4)_3$ and $Lu_2(MoO_4)_3$, respectively. The differences found in the coefficients when compared with literature data in similar compounds are certainly due to the

temperature range selected in the fitting procedure. However, we have obtained the same unit cell behavior for all dehydrated compounds: the *b* and *c* axes decrease on heating from 150 to 450 K.

Due to the precise oxygen positions by neutrons, we have been able to determine accurately the behavior of bridging angles, their corresponding, non-bonded distances and the distortion of the more symmetric tetrahedron. In general, A$\cdots$Mo distances expand on cooling, as is expected for NTE, although only the angles A–O1–Mo1 and A–O6–Mo expand significantly. This is the basic structural feature that provokes NTE. Moreover, the most symmetric tetrahedron distorts and expands on cooling in order to diminish the BVS around Mo2. This is the other possible contributing mechanism to NTE in this family of compounds.

The use of atom displacements with respect to the high temperature structure as primary parameters in the refinements, instead of atom positions, has helped us to propose a reasonable mechanism for the NTE behavior in the present compounds. This mechanism is not usually explained in such detail because it is not usual practice to represent differences between coordinates, at different temperatures, instead of distances and bond angles, distortions of polyhedra and other geometric calculations. The displacements of each atom from the structure at higher temperature are correlated to the thermal expansion coefficients. In particular, we have found that the transverse displacements of O1 and O6, with the longest amplitudes, are responsible for the opening observed in A–O1–Mo1 and A–O6–Mo2 bridging angles and the lengthening of the corresponding non-bonded A$\cdots$Mo distances on cooling. As the A–O–Mo bridges form chained rings along the different axes, resulting in collective displacements of the oxygen atoms, it is possible to explain how the *b* (through A–O1–Mo1 bridges) and *c* (through A–O6–Mo2 bridges) axes show negative expansion and how the *a*-axis does not show a negative expansion, without considering rigid motions of the involved polyhedra. The refinement of atom displacements from a known structure, used for first time in this work, offers an exciting prospect for researchers to study crystal structures that are distorted by temperature, pressure, or changes in their composition.

Acknowledgments

References

[1] Kwon Y K, Berber S and Tománek D 2004 *Phys. Rev. Lett.* **92** 015901
[2] Wu Y, Kobayashi A, Halder G J, Peterson V K, Chapman K W, Lock N, Southon P D and Kepert C J 2008 *Angew. Chem. Int. Edn Engl.* **47** 8929
[3] Evans J S O, Mary T A, Vogt T, Subramanian M A and Sleight A W 1996 *Chem. Mater.* **8** 2809
[4] Evans J S O, Jorgensen J D, Short S, David W I F, Ibberson R M and Sleight A W 1999 *Phys. Rev.* B **60** 14643
[5] Evans J S O, David W I F and Sleight A W 1999 *Acta Crystallogr.* B **55** 333
[6] Holzer H and Dunand D 1997 Processing, structure and thermal expansion of metal matrix composites containing zirconium tungstenate *4th Int. Conf. on Composite Engineering (Hawaii)*
[7] Wei Z, Yu Y, Xing H, Zhuo Z, Wu Y, Zhang L, Zheng W and Zhang Y 2001 *IEEE Photon. Technol. Lett.* **13** 821
[8] Versluis A, Douglas W H and Sakaguchi R L 1996 *Dent. Mater.* **12** 290
[9] Evans J S O, Mary T A and Sleight A W 1998 *J. Solid State Chem.* **137** 148
[10] Varga T, Wilkinson A P, Lind C, Bassett W A and Zha C-S 2005 *J. Phys.: Condens. Matter* **17** 4271
[11] Imanaka N, Ueda T, Okazaki Y, Tamura S and Adachi G 2000 *Chem. Mater.* **12** 1910
[12] Abrahams S C and Bernstein J L 1966 *J. Chem. Phys.* **45** 2745
[13] Hanuza J, Maczka M, Hermanowicz K, Andruszkiewicz M, Pietraszko A, Strek W and Deren P 1993 *J. Solid State Chem.* **105** 49
[14] Chen H Y 1979 *Mater. Res. Bull.* **14** 1583
[15] Sleight A W and Brixner L H 1973 *J. Solid State Chem.* **7** 172
[16] Sumithra S and Umarji A M 2004 *Solid State Sci.* **6** 1313
[17] Sumithra S and Umarji A M 2006 *Solid State Sci.* **8** 1453
[18] Marinkovic B A, Jardim P M, de Avillez R R and Rizzo F 2005 *Solid State Sci.* **7** 1377
[19] Barrera G D, Bruno J A O, Barron T H K and Allan N L 2005 *J. Phys.: Condens. Matter* **17** R217
[20] Giddy A P, Dove M T, Pawley G S and Heine V 1993 *Acta Crystallogr.* A **49** 697
[21] Ravindran T R, Arora A K and Mary T A 2003 *Phys. Rev.* B **67** 064301
[22] Tao J Z and Sleight A W 2003 *J. Solid State Chem.* **173** 442
[23] Miller W, Smith C, Mackenzie D and Evans K 2009 *J. Mater. Sci.* **44** 5441
[24] Marinkovic B A, Ari M, de Avillez R R, Rizzo F, Ferreira F F, Miller K J, Johnson M B and White M A 2009 *Chem. Mater.* **21** 2886
[25] Rodríguez-Carvajal J 1993 *Physica* B **192** 55
[26] Thompson P, Cox D E and Hastings J B 1987 *J. Appl. Crystallogr.* **20** 79
[27] Young R A 1993 *The Rietveld Method* (Oxford: Oxford Science Publications)
[28] Chapon L C and Rodríguez-Carvajal J 2008 FullProf Studio (version 2.0 August 2008) www.ill.eu/sites/fullprof/
[29] Farrow C L, Juhas P, Liu J W, Bryndin D, Boin E S, Bloch J, Proffen Th and Billinge S J L 2007 *J. Phys.: Condens. Matter* **19** 335219
[30] Woodcock D A, Lightfoot P and Ritter C 2000 *J. Solid State Chem.* **149** 92
[31] Evans J S O and Mary T A 2000 *Int. J. Inorg. Mater.* **2** 143
[32] Forster P M and Sleight A W 1999 *Int. J. Inorg. Mater.* **1** 123
[33] Cruickshank D W J 1956 *Acta Crystallogr.* **9** 754
[34] Brown I D and Altermatt D 1985 *Acta Crystallogr.* B **41** 244
[35] Makovicky E and Balic-Zunic T 1998 *Acta Crystallogr.* B **6** 766
[36] Rodríguez-Carvajal J 2010 Bond_Str (version May-2010) www.ill.eu/sites/fullprof/
[37] Xiao X L, Cheng Y Z, Peng J, Wu M M, Chen D F, Hu Z B, Kiyanagi R, Fieramosca J S, Short S and Jorgensen J 2008 *Solid State Sci.* **10** 321
[38] Errandonea D, Kumarb R S, Mac X and Tuc C 2008 *J. Solid State Chem.* **181** 355
[39] Errandonea D, Santamaría-Pérez D, Achary S N, Tyagi A K, Gall P and Gougeon P 2011 *J. Appl. Phys.* **109** 043510

Chapter 6

Appendices

In this chapter, we include a paper that has been submitted to a scientific journal and this paper is under revision. The title of this paper is "Experimental and theoretical study of α–$Eu_2(MoO_4)_3$ under compression". We decided include it in the manuscript because this work strongly complement the previous titled "Pressure evolution of two polymorphs of $Tb_2(MoO_4)_3$". We also add the supplementary material of the paper "Structural investigation of the negative thermal expansion in yttrium and rare earth molybdates". Moreover, we include a short section about some thermodynamic relations that we used during this work.

Experimental and theoretical study of α-$\mathbf{Eu_2(MoO_4)_3}$ under compression

C. Guzmán-Afonso,[1, a)] S. F. León-Luis,[1, 2, 3] J. A. Sans,[3, 4] C. González-Silgo,[1, 2, 3] P. Rodríguez-Hernández,[1, 2, 3] S. Radescu,[1, 2, 3] A. Muñoz,[1, 2, 3] J. López-Solano,[1, 2, 5] D. Errandonea,[3, 6] F. J. Manjón,[3, 4] U. R. Rodríguez-Mendoza,[1, 2, 3] and V. Lavín[1, 3, 7]

[1)] Departamento de Física, Universidad de La Laguna, 38200 La Laguna, Tenerife, Spain
[2)] Instituto de Materiales y Nanotecnología, Universidad de La Laguna
[3)] MALTA Consolider Team
[4)] Instituto de Diseño para la Fabricación y Producción Automatizada, Universidad Politécnica de Valencia, 46022 Valencia, Spain.
[5)] Izaña Atmospheric Research Center, Agencia Estatal de Meteorología, Tenerife, Spain
[6)] Departamento de Física Aplicada, 46100 Burjassot, Valencia, Spain
[7)] Instituto de Estudios Avanzados en Atómica, Molecular y Fotónica, Universidad de La Laguna

The compression process in the α-phase of europium trimolybdate was revised employing several experimental techniques. X-ray diffraction using synchrotron radiation, Raman scattering and optical spectroscopy experiments were performed up to a maximum pressure of 21 GPa. In addition, the crystal structure and Raman mode frequencies have been studied by means of first-principles density functional based methods. Results suggest that the compression process of α-$Eu_2(MoO_4)_3$ can be described by three stages. Below 8 GPa, the α-phase suffers an isotropic contraction of the crystal structure. Between 8 and 12 GPa, the compound undergoes an anisotropic compression due to distortion and rotation of the MoO_4 tetrahedra. This behavior is confirmed by the unusual pressure dependence of the a parameter and the β angle of the unit cell, and it is also correlated to the anomalies in the evolution of the Raman peaks and the non-linear broadening of the $^5D_0 \rightarrow {^7F_0}$ emission line. At pressures above 12 GPa, a clear decrease of the red-shifting and an increase in the linewidth of the peak corresponding to the $^5D_0 \rightarrow {^7F_0}$ transition suggest that the amorphization process starts. Finally, the sample reaches the amorphization at 21 GPa without any occurrence of a crystalline-crystalline phase transition in the whole range of pressure.

I. INTRODUCTION

Trimolybdates and tritungstates with chemical formula $RE_2(MO_4)_3$ (RE=rare earth; M=Mo, W) are a large group of important materials from both the fundamental and technological points of view. They include several polymorphic materials which are mainly used as scintillators in high energy physics,[1] outer space and medical diagnostic devices. They are also good phosphors due to the fluorescence of the majority of the RE ions.[2] Crystals containing Eu^{3+} ions are of particular interest because these ions produce the efficient red photoluminescence necessary for the creation of white-light emitting diodes.[3]

For rare earths with intermediate ionic radii, the two structural phases of these families of compounds at ambient conditions are the α-phase,[4] with space group $C2/c$ and modulated scheelite-type structure, and the β'-phase,[5] with space group $Pba2$ and which only occurs for trimolybdates.[6] On the one hand, compounds crystallizing in the α-phase possess a strong anisotropy and a good lanthanide impurity acceptance, which favors

its use as efficient laser hosts and Raman shifters.[7] On the other hand, compounds crystallizing in the β'-phase show piezoelectric, ferroelectric, ferroelastic and nonlinear properties, as well as second harmonic generation, which can be potentially used as efficient self-frequency-doubling crystals and memory materials,[8] among other applications. In particular, europium trimolybdate can adopt either phase, depending on the crystallization conditions.

Note that other polymorphs are also possible in these families of compounds: trimolybdates with lighter RE ions can crystallize in other modulated scheelite-type structure, known as $La_2(MoO_4)_3$.[9] Both tritungstates and trimolybdates having heavier RE ions crystallize in the γ-$Sc_2(WO_4)_3$ structure which displays negative thermal expansion, and abnormal thermal and pressure dependence of ionic conductivity.[10,11] This rich polymorphism makes these compounds good prototypes to understand concepts related to the physics of pressure-induced phase transitions and amorphization processes.

The monoclinic α-phase with space group $C2/c$ and $Z=4$ is one type of modulated scheelite-type structure ($CaWO_4$-like), with 2/3 of the calcium ions substituted by RE ions and 1/3 by vacancies. A description of these modulated structures, emphasizing the different ordering of vacancies, is given by Jeitschko[9]. The crystal struc-

a) mcguzman@ull.es

ture of the α-phase features two different Mo (or W) surroundings. On the one hand, Mo1 forms symmetric tetrahedra near the vacancy sites and it is placed at the *4e* Wyckoff site. On the other hand, Mo2 forms more distorted tetrahedra at the general *8f* Wyckoff site. RE atoms are also in general positions surrounded by eight oxygen atoms. The stoichiometric vacancies introduce a differentiating effect with respect to simple and double molybdates (or tungstates), which should change the compressibility of these compounds.

Several studies have been performed to investigate the compression of α- and β'-phases in trimolybdates. These studies have revealed that the pressure-induced amorphization (PIA) in β'-phase compounds is irreversible and occurs at lower pressures (roughly 4 GPa).[12–14] Furthermore, before the PIA is reached, a phase transition to a δ-phase may take place.[15] On the other hand, Raman scattering measurements have evidenced that α-phase compounds, like $Nd_2(MoO_4)_3$ and $Tb_2(MoO_4)_3$, undergo a partially reversible PIA at 13 and 18 GPa, respectively.[16] Curiously, PIA in both α- and β'-phases has been explained as a spatial self-organization of the oxygen clouds around the Mo and RE subnetworks.[17,18] According to the literature, RE trimolybdates with the α-phase undergo PIA without crystalline-crystalline transitions, although some anomalies are found around 12 GPa.[18] This lack of transitions has resulted in these compounds being less studied than the ones with the β'- and γ-phases, which feature many phase transitions. Very recently, we have studied the compression of a tritungstate with α-phase, $La_2(WO_4)_3$, which undergoes two phase transitions prior to PIA.[19]

In this work, we will focus on the study of the compression of a trimolybdate with α-phase, $Eu_2(MoO_4)_3$, at room temperature in order to reach a better understanding of the PIA mechanisms in tritungstates and trimolybdates with α-phase. X-ray diffraction using synchrotron radiation, Raman scattering and optical spectroscopy experiments were performed in polycrystalline samples. Our results have been compared to those of a very recent work where α-$Eu_2(MoO_4)_3$ has been characterized at ambient conditions with these three techniques.[20] In addition, *ab initio* calculations were carried out to complement our experimental results and to help in the analysis of experimental data. The combination of all these methods allows us to provide a more comprehensive and complete picture of the structural (at long and short range order) and of vibrational behavior at high pressure of the α-phase in trimolybdates. We will show that α-$Eu_2(MoO_4)_3$ undergoes PIA without any intermediate structural phase transition, what allows following pressure-induced structural changes until amorphization. Our results strongly complement previous results of Raman and XAS studies combined with numerical simulations in $Eu_2(MoO_4)_3$ by Le Bacq *et al.*[17], mainly focused on its β'-phase.

II. EXPERIMENTAL AND THEORETICAL DETAILS

The sample of α-$Eu_2(MoO_4)_3$ was prepared by conventional solid-state synthesis (see Ref. 21 for more details). The polycrystalline powder was measured at room temperature by two X-ray diffractometers. On the one hand, we employed a synchrotron radiation source (λ=0.485 Å) equipped with a MAR345 CCD detector at the *Beamline I15* of the Diamond Light Source. On the other hand, we used a conventional SuperNova diffractometer, ($K\alpha$ molybdenum radiation) equipped a 135-mm Atlas CCD detector at the "Servicio Integrado de Difracción de Rayos X (SIDIX)" of University of La Laguna. Pressures reached in the synchrotron experiment, up to 14.6 GPa, were generated with a MiniDac-type diamond anvil cell (DAC; with aperture angle of 40° and designed at the University of Paderborn in Germany) using Dow Corning silicone oil as pressure-transmitting medium. The diamond culet size was 400 μm and the chamber size was 300 μm in diameter and 50 μm thickness. Pressures reached in the conventional experiment, up to 5.3 GPa, were generated with a Diacell Bragg-Mini DAC (with aperture angle of 85°) using a mix of methanol-ethanol-water 16:3:1 as pressure-transmitting medium. The diamond culet size was 500 μm and the chamber size was 200 μm in diameter and 100 μm thickness. In both experiments, the in-situ pressure was measured using the ruby fluorescence technique,[22] with the pressure scale recalibrated by Mao, Xu, and Bell[23] and the observed intensities were integrated as a function of the 2θ angle using the Fit2D software,[24] in order to give 1D-diffraction patterns. The 1D-diffraction patterns were refined by iterating full pattern profile fittings with the Le Bail method,[25] using the FullProf software[26] and starting from the crystallographic cell obtained in Ref. 20. The background was modeled by a linear interpolation between points. Besides, the lattice parameters, the half-width parameter, related to the Gaussian broadening of the peaks due to isotropic microstrains, was also refined. Above 4.7 GPa, anisotropic broadening and shifts of some reflections, were detected systematically (only in the data measured in the synchrotron experiment) and they were refined too.

Raman scattering measurements of powder α-$Eu_2(MoO_4)_3$ samples at room temperature were performed in backscattering geometry, exciting with a HeNe laser at 632.8 nm with an incident power of 10 mW and using a HORIBA Jobin Yvon LabRAM HR UV spectrometer in combination with a thermoelectrically cooled multichannel CCD detector with a resolution below 2 cm^{-1}. The background of the experimental Raman spectra was subtracted and vibrational modes were analyzed by fitting the Raman peaks with a Voigt profile. The beam was focused on the sample using a 50× objective with a beam diameter of approximately 2 μm at the sample. For high-pressure Raman measurements, the sample was placed in a membrane-type DAC. The diamond culet size was 400 μm and the gasket hole size was

150 μm. A mixture of methanol-ethanol-water (16:3:1) was used in this case as a pressure-transmitting medium and the pressure was measured using the same method we used in the diffraction experiment.

Room-temperature fluorescence spectra of Eu^{3+} ions in α-$Eu_2(MoO_4)_3$ were excited with a 405 nm laser diode and recorded with a Spex 75 cm monochromator equipped with Hamamatsu R928 photomultiplier tubes (spectral resolution of 0.1 nm). High-pressure measurements were carried out at room temperature in a pressure range from 0 to 14.6 GPa, using the same Mini-DAC as in the diffraction experiments, and a mixture of methanol-ethanol-water (16:3:1). Pressures were determined by the ruby fluorescence method, as in the previous experiments.

First-principles total-energy calculations were performed within the framework of the density-functional theory (DFT)[27] using the Vienna *ab initio* simulation package (VASP).[28,29] Calculations were carried out with the pseudopotential method and the projector augmented wave (PAW) scheme.[30] Pseudopotentials replace core electrons but take into account the full nodal character of the all-electron charge density distribution in the core region and produce smoothed pseudovalence wave functions which include explicitly in the calculation only the outermost electrons of each atomic species (2s and 2p electrons of O; 4p, 5s, and 4d electrons of Mo; and 5s, 5p, 4f, and 6s of Eu). The exchange-correlation energy was taken in the generalized gradient approximation (GGA) with the PBEsol[31] prescription. It is known that standard DFT does not work properly for strongly localized f electrons.[32,33] Therefore, we use the GGA+U (U=4 eV) method to account for the strong correlation between the Eu f electrons on the basis of Dudarev's method.[34] Highly converged results were achieved by extending the set of plane waves up to a kinetic energy cutoff of 520 eV. A dense Monkhorst-Pack grid of $3\times3\times2$ k-special points was used to perform integrations along the Brillouin zone (BZ) in order to obtain very well converged energies and forces. The structural configurations were fully relaxed at each volume through the calculation of the forces on atoms and the components of the stress tensor.[35] In the relaxed configurations, the forces on the atoms are less than 0.006 eV/Å and deviations of the stress tensor from a diagonal hydrostatic form are less than 0.1 GPa. It should be noted that, in the DFT formalism, the theoretical pressure P(V) is obtained from the calculated stress.[36] Zero point motion and temperature effects were not included in the calculations.

Lattice-dynamics calculations were performed at the zone center (Γ point) of the BZ using the direct force constant (or supercell) approach.[37] Highly converged results on forces are required for the calculation of the dynamical matrix using this method. The construction of the dynamical matrix at the Γ point of the BZ involves separate calculations of the forces in which a fixed displacement from the equilibrium configuration of the atoms within the primitive cell is considered. The number of such inde-
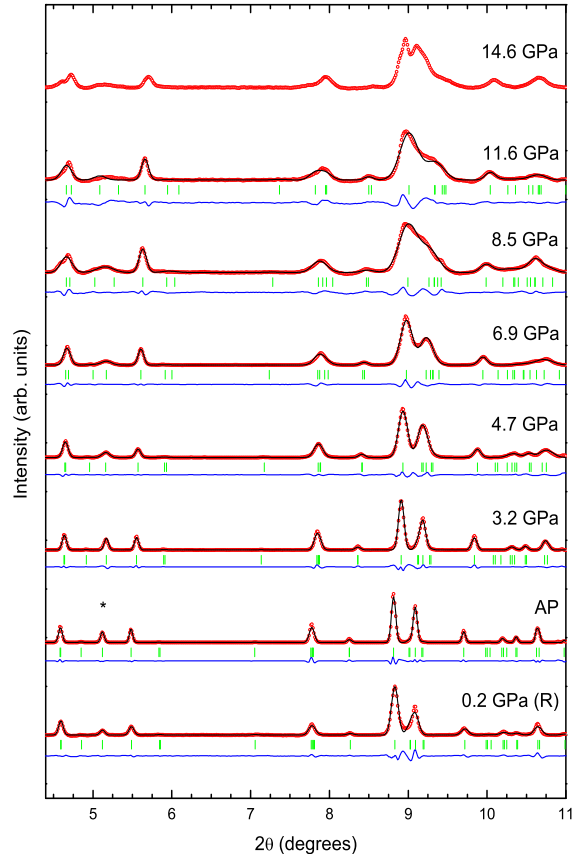
Figure 1. Diffraction patterns of α-$Eu_2(MoO_4)_3$ at selected pressures only for the synchrotron experiment. Experimental results (open circles) are shown together with the calculated patterns (red lines) and residuals (blue lines). The ticks indicate the positions of Bragg reflections. Pressures are indicated in the figure, and the patterns labeled with the initials AP and R were collected at ambient pressure and at 0.2 GPa after pressure release, respectively.

pendent displacements in the analyzed structures can be reduced by taking into account the crystal symmetry.[38] The diagonalization of the dynamical matrix allows obtaining the frequencies of the Raman modes. Moreover, these calculations allow for the identification of the symmetry and eigenvectors of the vibrational modes in each structure at the Γ point.

III. RESULTS AND DISCUSSION

A. Pressure dependence of the lattice parameters

Fig. 1 shows a selection of XRD patterns of $Eu_2(MoO_4)_3$ up to 14.6 GPa. The background has been subtracted and the diffraction patterns have been normalized in order to improve their visualization. All re-
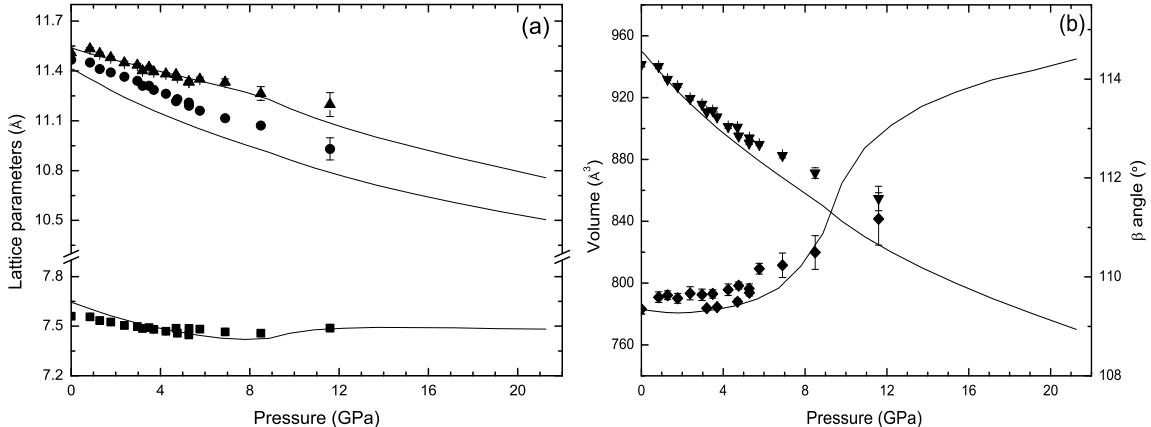
Figure 2. Pressure dependence of experimental (solid symbols, data calculated from sinchrotron and conventional radiation source) and theoretical (black lines) lattice parameters for α-Eu$_2$(MoO$_4$)$_3$. The left panel shows the a (■), b (●), and c (▲) lattice parameters. The right panel shows the volume (▼) and the β angle (♦). Lines are a guide to the eye and error bars represent the standard deviations. Experimental lattice parameters were calculated using data from both synchrotron (up to 14.6 GPa) and conventional (up to 5.3 GPa) experiments.

flections of the initial diffractogram at ambient pressure (AP; 1 atm) correspond to the expected ones for α-Eu$_2$(MoO$_4$)$_3$, i.e. we did not observe any reflections from impurities. The most notable feature of these diffractograms is that the widths of some reflections start to increase above 4.7 GPa. For instance, this effect is clearly visible for the reflection with Miller indices (0 0 2) located at 5.1^o (see the asterisk in Fig. 1). In addition, some of these reflections show a systematic shift to lower angles with increasing pressure. Both effects can be due to an excessive number of crystal grains loaded in the DAC, so that the grains are subjected to a non-hydrostatic stresses from grain-to-grain contacts. This would result in a non-uniform strain within a grain (microstrain) or/and over larger distances (macrostrain), producing the peak broadening and shifting, respectively. In spite of this possible non-hydrostatic condition of the sample, we did not observe any phase transition in the whole pressure range of the synchrotron experiment. This result is in agreement with our own (see section III C) and previous Raman studies.[17] The same behavior has been found in isostructural α-Tb$_2$(MoO$_4$)$_3$ pressurized up to 20.74 GPa.[15] Based on the results of these two isostructural compounds, we expect the same behavior for all RE trimolybdates with α-phase, i.e. the sequence of trimolybdates with RE from samarium to dysprosium.

The bottom diffractogram of Fig. 1, marked with an R and corresponding to the release from high pressure, is similar to the diffractogram measured at AP, although the peaks are slightly wider. This broadening can be due to the non-hydrostatic stresses that remain in the sample after release of pressure. Overall, it can be concluded that the compression of the cell is almost a reversible process.

In order to obtain more information about the behavior of α-Eu$_2$(MoO$_4$)$_3$ under pressure, we refined all diffractograms collected up to 11.6 GPa, and also the one obtained after decompression. These refinements are displayed as black lines in Fig. 1. The refinements were not performed at pressure larger than 11.6 GPa due to the broadening of the reflections. The experimental pressure dependence of the lattice parameters, the monoclinic β angle, and the volume were obtained from these refinements. The pressure evolution of these five parameters are plotted in Fig. 2, together with the theoretical lattice parameters calculated by *ab initio* methods. Note that a reasonable agreement is found between experimental data from sinchrotron and conventional radiation source. Moreover, the theoretical data reproduce the experimental behavior of the lattice parameters. When pressure increases, b and c lattice parameters decrease monotonously, whereas a parameter suffers a contraction up to 8 GPa. After that pressure, its value increases smoothly, remaining constant after 12 GPa according to the *ab initio* calculations. The monoclinic angle β increases with pressure, suffering an abrupt increment on its slope above 8 GPa and up to 12 GPa. Although the compression behavior of the a parameter is remarkably different than that of the other parameters, the volume decreases monotonically. This unusual dependence with pressure of the a parameter is similar to that found in α-Tb$_2$(MoO$_4$)$_3$, although in this latter compound the monoclinic angle decreases with increasing pressure.[15]

We have fitted the calculated data up to 12.2 GPa with a third order Birch-Murnaghan equation of state (EOS), obtaining a V_0=950.6(6) Å^3, B_0=63(1) GPa and B'_0=3.7(2). We also used the previous equation to fit the experimental data up to 11.6 GPa, obtaining V_0=941.41(6) Å^3, B_0=88(4) GPa and B'_0=6(1). Thus, the pressure evolution of the experimental volume shows a larger bulk modulus than the one inferred from the theoretical data, so that the sample is not as compressible as the theoretical data predict. We believe that

this difference could be probably related to the excessive number of crystal grains loaded into the chamber, causing the mentioned anisotropic stress on the sample and decreasing the compressibility of the crystal structure as Errandonea, Muñoz, and Gonzalez-Platas[39] explain. The difference found between the theoretical and experimental bulk modulus can also be due to the influence of the pressure-transmitting medium.[40] In particular in scheelite-type compounds it is well known that the use of a pressure-transmitting medium different than Ne or He tends to underestimate the compressibility (overestimate bulk modulus).[41,42] On the other hand, the difference between theoretical and experimental volume is most likely related to the usual overestimation of the equilibrium volume (which leads to an underestimation of the bulk modulus) produced by the GGA exchange-correlation approximation.[36] It is interesting to note that the bulk modulus of $Eu_2(MoO_4)_3$ is similar to that obtained for the scheelite-type $EuMoO_4$ (B_0=71(6) GPa) under similar experimental conditions.[43] This is due to the similitude between both structures and the fact that in both compounds the Mo–O bonds are less compressible than the Eu–O ones, which thus account for most of the crystal compression. We have also calculated the bulk modulus for α-$Tb_2(MoO_4)_3$ using the data provided in Ref. 15. The obtained values are 76(1) and 81(9) GPa for the theoretical and experimental bulk modulus, respectively, and both are quite close to the present experimental result.

In summary, we can distinguish three compression regions: one extending from AP up to 8 GPa, another from 8 GPa up to 12 GPa, and a third one for pressures above 12 GPa. Between 8 and 12 GPa, some abrupt changes are observed, but they do not result in a phase transition. From our own and previous Raman experiments,[16,17] and theoretical calculations,[15] a lowering of symmetry is indeed not expected. In the next section we focus on the study of the compression of the α-crystal structure calculated from *ab initio* methods in order to explain the unusual behavior of the lattice parameters in the already-mentioned three pressure regions.

B. Structural compression

Based upon calculations we will now try to deepen in the understanding of the structural mechanisms that cause the anomalies observed before PIA. We have calculated bond distances and angles using the theoretical atomic coordinates. We have also studied the bond valence sum[44] for the cations and the distortion of the EuO_8 polyhedra by compression. Bond distances around the Mo1–O, Mo2–O, and Eu–O ions are plotted in Fig. 3. Note that we have assigned atoms using the same criterion as in Ref. 45, i.e. the more symmetric $Mo1O_4$ tetrahedron is formed by the oxygen atoms O1 and O2, and the corresponding two oxygens, whose positions are generated by a symmetry C_2 axis. The less symmetric

$Mo2O_4$ tetrahedron is coordinated by the oxygen atoms O3, O4, O5 and O6. As shown in Fig. 3(a), at pressures above 8 GPa Mo1–O1 and Mo2–O(4,5) bond distances increase unusually. Moreover, at higher pressures, other oxygen atoms come closer to the Mo1 and Mo2 ones, resulting in new bond distances smaller than 2.5 Å for both tetrahedra (these bonds are not shown in Fig. 3(a)). However, the europium coordination polyhedron involves eight oxygen atoms from positions O1 to O6 during all the range of pressures. The most notable feature shown in Fig. 3 is that the Eu–O bond distances are more compressible than the Mo–O bond distances. Note that the most abrupt and anomalous changes in both types of bond distances take place between 8 and 12 GPa.

The unusual expansion of Mo–O bond distances must be related to the pressure dependence of bond angles. In Fig. 4 we have plotted the pressure dependence of selected angles. As we can see in Fig. 4(a), at lower pressures the dispersion from the tetrahedral angle (about 109°) of the O–Mo2–O angles is related to the larger distortion of the $Mo2O_4$ tetrahedron with respect to the more symmetric $Mo1O_4$ one. However, this situation changes at higher pressures, with the O–Mo1–O angles showing the largest dispersion above 12 GPa. Overall, the changes of tendency in the angles also happen between 8 and 12 GPa, as it is also observed for the cell parameters. In order to correlate the pressure dependence of the polyhedral bond distances and angles with the evolution of lattice parameters under pressure, we have also plotted in Fig. 4(b) the angles of the oxygen bridges Eu–O–Mo which connect all the crystal structure. We will discuss these curves together with Figs. 5 and 6, where different views of the crystal structure of the α-phase are drawn. Note that in these figures, we have plotted the atomic coordinates at four selected pressures, *viz.*, 0, 7.8, 12.2 and 17.2 GPa. In Fig. 5 we can see that both MoO tetrahedra rotate anticlockwise along the b-axis and slightly deform as pressure increases. Fig. 5 clearly shows that, at 12.2 and 17.2 GPa, the tetrahedra are more aligned along the a axis (colored in red in Fig. 5), forming a more compact crystal packing. We can go even further in our description of the pressure effect on the α-phase, and explain the decrease of the a parameter as a result of the rotation and deformation of the MoO tetrahedra, up to a pressure when the alignment along the a-axis is reached. After this, the a parameter increases up to a pressure where it becomes constant.

The β-angle increases following the anticlockwise rotation of the MoO_4 tetrahedra. This increase is also observed in $La_2(WO_4)_3$[19] up to the first pressure-induced phase transition, while in $Tb_2(MoO_4)_3$ the opposite behavior is observed,[15] with tetrahedra undergoing a clockwise rotation in the pressure range from 7.5 to 12.7 GPa. Moreover, the evolution of all the oxygen-bridge angles (see Fig. 4) helps to explain the rotation and deformation of both tetrahedra and therefore the unusual compression of the cell parameters. The more drastic contraction occurs for the angles Eu–O1–Mo1, Eu–O3–Mo2 and Eu–
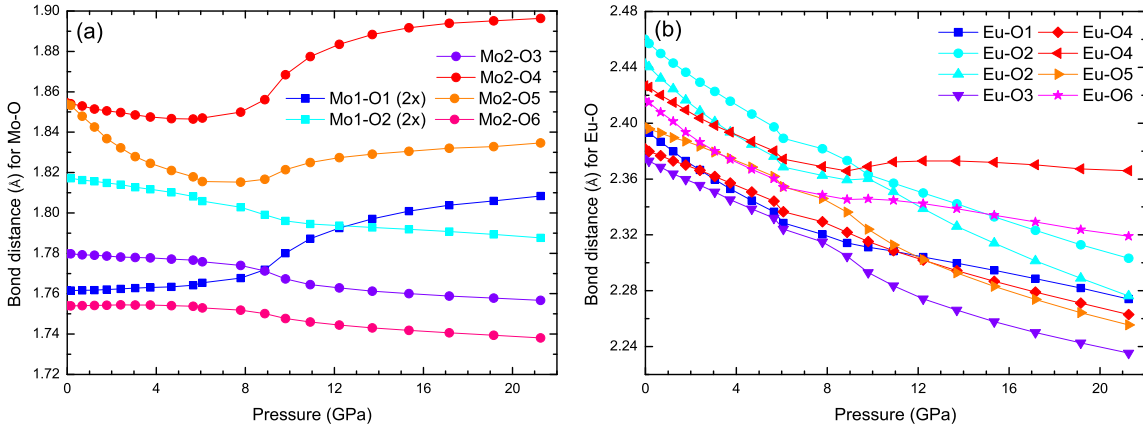
Figure 3. Bond lengths for (a) Mo–O and (b) Eu–O as a function of pressure for α–Eu$_2$(MoO$_4$)$_3$.
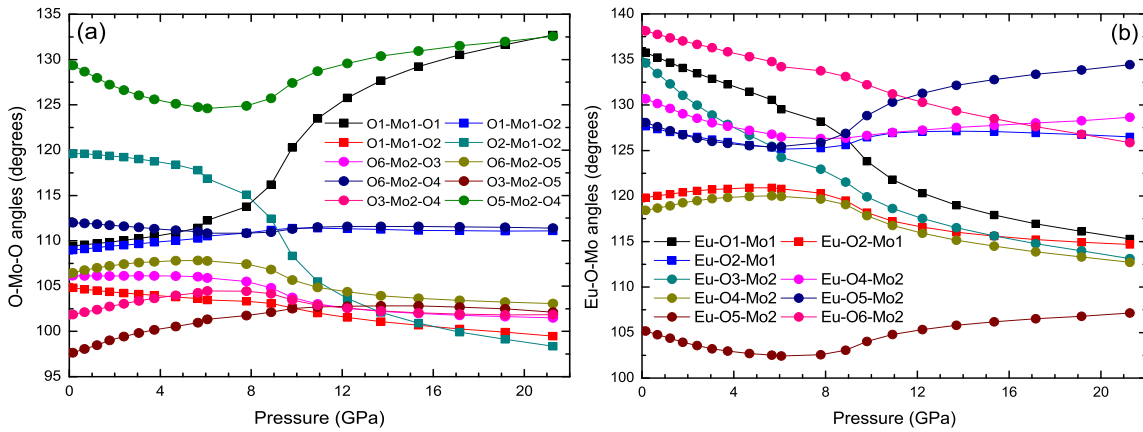
Figure 4. (a) O–Mo–O and (b) Eu–O–Mo bridging angles as a function of pressure for α-Eu$_2$(MoO$_4$)$_3$.

O6–Mo2. The changes in these bridges must be thus the major reason for the alignment of both tetrahedra. This is best shown in Fig. 6, where it can be observed the alignment of the O1 atoms along the a-axis, and of the O3 and O6 oxygens along the c-axis (colored in green in Fig. 6). Furthermore, note that the experimental results from X-ray diffraction show that the broadening of the patterns is almost recovered at ambient pressure, as it also happens in other trimolybdates with α-phase.[16,17] This may be the result of the reversibility of the rotations and deformations of the MoO$_4$ groups described above. Note that this is not the case of La$_2$(WO$_4$)$_3$ and probably other light RE tritungstates with the α-phase, where vacancies and RE atoms are disordered and the structure is not recovered at ambient conditions.[19]

As pressure further increases, the next change on this compound would be PIA at about 21 GPa, according to Raman results of Ref. 17 and our own results (see section III C). In order to determine the causes of PIA, we have calculated the bond valence sums of Eu and Mo ions at different pressures using the program Bond_Str.[26,44]

We have plotted the difference between the bond valence sums for cations and their corresponding oxidation number in Fig. 7. We have observed that this value increases for Eu ion in the whole range of pressures. However, the behavior for the Mo ions is markedly different, with a change of tendency (turnaround) in the pressure dependence at 10 GPa. These values decrease at lower pressure, allowing a compensation between the increase of the valence in the Eu ion and the decrease of the valences in the Mo ions. At higher pressures, all bond valence sums increase and this may have an effect on the structural stability. We also show the polyhedral distortion of EuO$_8$ in the inset of Fig. 7. This distortion has an abrupt change at about 10 GPa, increasing very fast at higher pressures. Our results show that the surroundings of the molybdenum and europium ions play an important role in the compression and amorphization of the sample. For this reason we have carried out a study of the Raman scattering on α-Eu$_2$(MoO$_4$)$_3$, and also of the luminescence of the Eu ion under pressure. We devote the next sections to present the results of these studies.
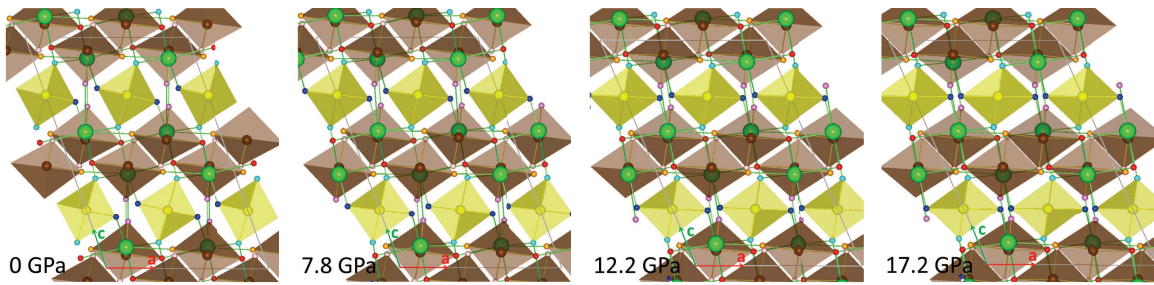
Figure 5. View along the b-axis of the α-Eu$_2$(MoO$_4$)$_3$ structure at four selected pressures. Europium cations are shown in green. Molybdenum atoms and their coordination tetrahedra are yellow for Mo1, and brown for Mo2. The oxygen atoms are shown in dark blue (O1), cyan (O2), violet (O3), red (O4), orange (O5) and pink (O6).
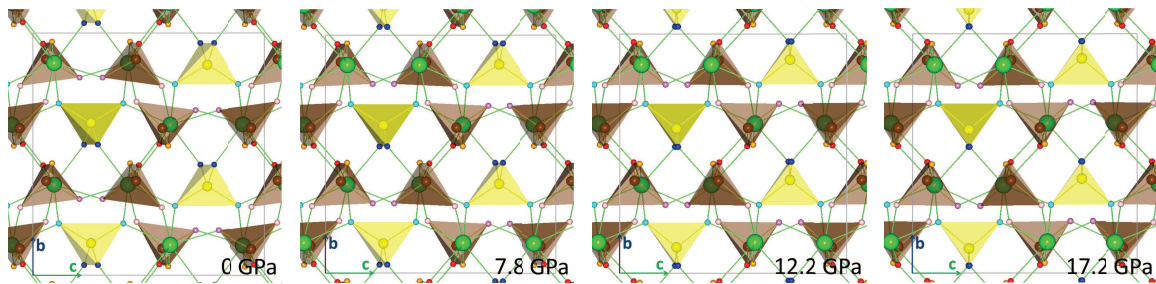
Figure 6. Same as Fig. 5 but showing a view along the a-axis.
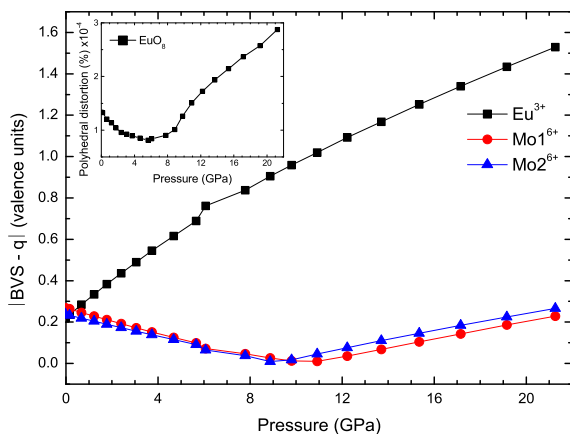
Figure 7. Pressure evolution of the difference between bond valence sums and the oxidation number for the Eu^{3+}, Mo1^{6+} and Mo2^{6+} ions. Inset shows the polyhedral distortion for EuO$_8$ at different pressures.

C. Vibrational properties

The monoclinic structure of α-Eu$_2$(MoO$_4$)$_3$ at AP has 102 normal vibrational modes at the center of the Brillouin zone:[46]

$$\Gamma: 25A_g(R) + 24A_u(IR) + 26B_g(R) + 24B_u(IR) + A_u$$
$$+ 2B_u$$

Since the structure is centrosymmetric, vibrational modes are either Raman (R) or infrared (IR) active. There are 51 Raman-active modes and 48 IR-active modes, plus one A_u and 2 B_u acoustic modes. Fig. 8(a) shows the Raman spectra obtained during compression of the α-Eu$_2$(MoO$_4$)$_3$ phase up to 21 GPa. Raman scattering spectra show a large number of Raman modes at low pressures. This is in agreement with the theoretical modes of the α-phase, and the analysis performed in Ref. 20 (see in Table I). These modes are grouped in three regions, corresponding to the external (or lattice) modes (0–200 cm^{-1}), bending modes of MO$_4$ tetrahedra (200–500 cm^{-1}), and stretching modes of MoO$_4$ tetrahedra (700–1000 cm^{-1}) with a very noticeable energy gap between the two latter groups. This phonon gap between bending and stretching modes is similar to that occurring in scheelite-type molybdates and tungstates.[47,48] Note that two fluorescence bands of the Eu^{3+} ion at 511 and 634 cm^{-1} are inside this energy gap, and thus are located at a range where they will have a small effect on the detection of Raman peaks close to them. These kind of peaks were also detected by Dmitriev et $al.$[13].

Besides the expected upshift of the Raman peaks with increasing pressure, we did not observed abrupt changes in the Raman spectra up to 8.3 GPa. This is in agreement with previous results for the α-phase of Nd$_2$(MoO$_4$)$_3$, Tb$_2$(MoO$_4$)$_3$, and Eu$_2$(MoO$_4$)$_3$.[16,17] Above 8.3 GPa, a
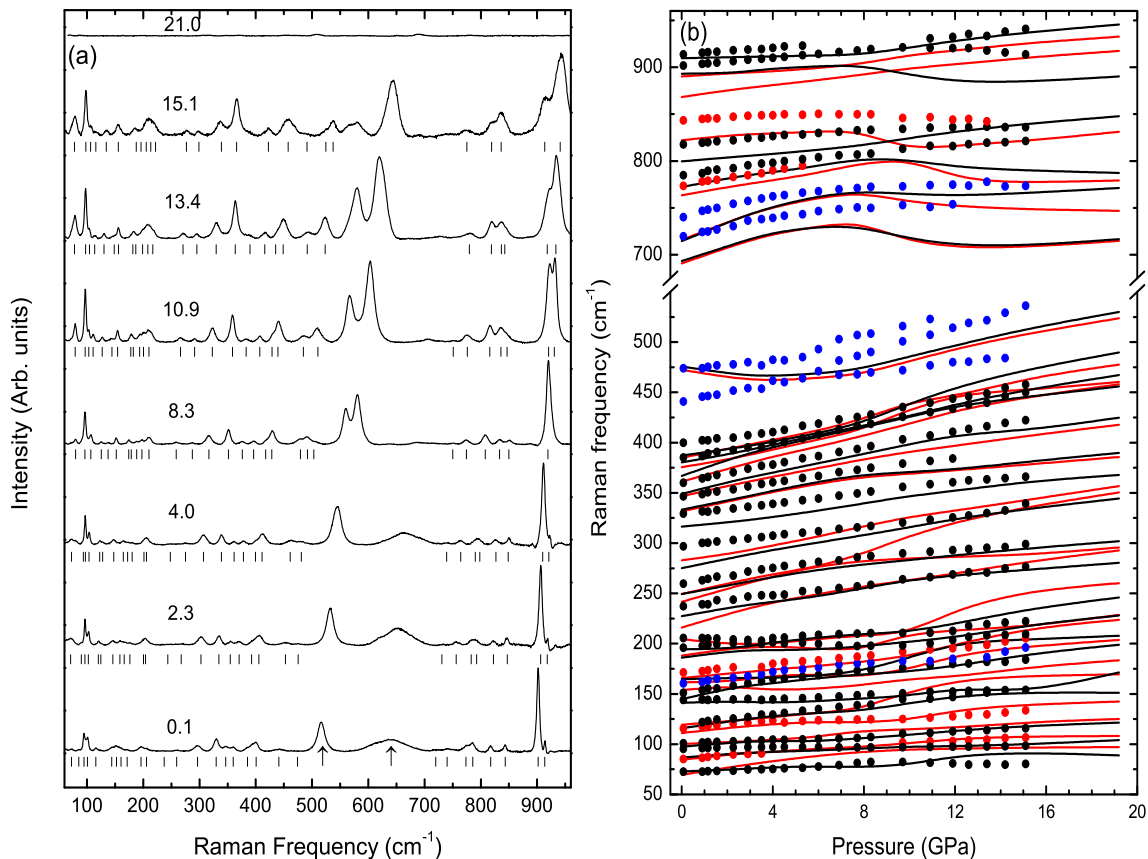
Figure 8. (a) Selection of Raman spectra and (b) pressure dependence of the Raman mode frequencies in α-Eu$_2$(MoO$_4$)$_3$ under pressure according to our experiments (circles) and theoretical calculations (lines). Next to each spectrum we give the pressure (in GPa) measured using the ruby fluorescence method. Ticks indicate the peak positions. The arrows denote Eu^{3+} fluorescence bands. Different colors have been used for distinguishing the symmetry of the Raman modes: black for Ag, red for Bg and blue for modes without assigned symmetry or second order modes.

slight splitting of the high-frequency modes was observed, suggesting a minor structural change. This splitting was also observed in Ref. 17, but not in the other aforementioned studies, in which pressure was increased in larger steps.[16] Moreover, we have observed the onset of PIA above 21 GPa, as in Ref. 17. This amorphization pressure is higher than that of Nd$_2$(MoO$_4$)$_3$ (13 GPa) and Tb$_2$(MoO$_4$)$_3$ (18 GPa).[16] This seems to suggest that a clear correlation between the amorphization pressure and the RE ionic radii cannot be established. However, we must note that the Raman spectrum of Nd$_2$(MoO$_4$)$_3$ in Ref. 16 likely corresponds to a La$_2$(MoO$_4$)$_3$-type structure, which is also a modulated scheelite-type structure, but it is not isostructural to the α-phase.

Fig. 8(b) shows the pressure dependence of the experimental Raman mode frequencies on upstroke to 20 GPa (full symbols) which are compared with the theoretical results (solid lines). Up to 8.3 GPa, most of the Raman peaks of the α-phase exhibit a monotonic shift of frequency which is consistent with the general contraction of the unit-cell parameters shown by our X-ray diffrac-

tion measurements. Overall, in this range of pressures, the experimental Raman modes are in reasonable agreement with the ones obtained in our calculations, without a clear experimental increase or decrease of the number of Raman modes.

The three frequency regions corresponding to the original α-phase are present in all the pressures measured, with similar pressure dependence and experimental-theoretical correspondence. However, some anomalies, more clearly seen in the theoretical calculations, can be discussed on the basis of the observed and calculated compression of the crystal structure. Several stretching modes soften (exhibit a negative pressure coefficients) between 8 and 12 GPa. This behavior can be observed experimentally at least in the second highest frequency mode above 10.9 GPa and it can be correlated with the unusual behavior of the a parameter, and the beginning of the distortion of the tetrahedra. This trend changes above 12 GPa, coinciding with the alignment of the tetrahedra along the a-axis and the consequent small compression of the a parameter. With respect to the bending-

Table I. Theoretical and experimental Raman-active mode frequencies (ω_0, in cm^{-1}) and pressure coefficients ($\partial\omega/\partial p$, in cm^{-1}/GPa) in α-Eu$_2$(MoO$_4$)$_3$ at lower pressures (<3 GPa).

Sym.	ω_0 (the.)	$\partial\omega/\partial p$ (the.)	ω_0 (exp.)	$\partial\omega/\partial p$ (exp.)	ω_0 (exp.)[a]
Bg^1	69.6	3.2	-	-	52.6
Ag^1	73.0	0.9	72.6	0.8	59.2
Bg^2	84.6	1.8	85.2	1.8	85.0
Ag^2	86.7	1.2	95.2	0.7	84.0
Ag^3	97.5	1.3	101	0.8	93.8
Bg^3	100	1.0	-	-	95.2
Bg^4	111	2.3	116	2.0	101.2
Ag^4	116	2.9	121	2.5	98.2
Bg^5	119	2.2	-	-	115.4
Ag^5	141	0.1	144	0.4	144.0
Ag^6	145	3.5	151	3.0	151.3
Bg^6	154	0.2	-	-	119.1
Bg^7	161	1.1	161[b]	2.8	158
Ag^7	165	0.8	161[b]	2.8	158
Bg^8	166	2.0	171	2.4	170.7
Ag^8	186	2.4	196	2.1	195.9
Bg^9	188	2.4	-	-	205.4
Ag^9	194	0.6	-	-	-
Bg^{10}	204	-1.3	206	-0.3	237.7
Bg^{11}	216	6.3	-	-	261.3
Ag^{10}	227	3.7	237	3.3	237.7
Bg^{12}	242	6.3	-	-	261.3
Ag^{11}	249	4.3	260	3.8	-
Bg^{13}	249	5.0	-	-	-
Ag^{12}	275	4.3	297	2.9	296.9
Bg^{14}	283	3.9	-	-	296.9
Ag^{13}	316	2.6	330	2.3	-
Bg^{15}	332	4.6	-	-	329.1
Ag^{14}	333	4.7	347	3.4	338.7
Bg^{16}	347	4.7	-	-	359.7
Ag^{15}	349	5.1	360	4.8	347.3
Bg^{17}	361	5.9	-	-	363.4
Ag^{16}	367	6.6	-	-	383.4
Bg^{18}	375	4.6	-	-	392.1
Ag^{17}	380	4.5	385	3.6	400.5
Bg^{19}	385	4.5	-	-	418.8
Ag^{18}	387	3.7	400	2.4	418.8
Bg^{20}	473	-2.8	441[c]	4.6	478.7
Ag^{19}	476	-2.7	474[c]	2.2	478.7
Bg^{21}	691	7.9	719[b]	5.5	720.9
Ag^{20}	693	7.7	719[b]	5.5	739.7
Ag^{21}	714	9.5	741[b]	5.7	773.6
Bg^{22}	716	8.8	741[b]	5.7	785.1
Bg^{23}	763	4.1	774	3.9	816.8
Ag^{22}	772	4.2	785	3.5	816.8
Ag^{23}	800	2.0	817	2.2	842.5
Bg^{24}	822	2.0	843	1.8	842.5
Bg^{25}	868	3.3	-	-	913.8
Bg^{26}	890	1.4	-	-	913.8
Ag^{24}	893	1.5	902	2.1	901.4
Ag^{25}	910	0.5	913	1.7	-

[a] Ref. 20

[b] These modes could be either of Ag or of Bg modes.

[c] These modes could be second order modes.

modes region, a slight change of the slope is observed between 8 and 12 GPa, and again it can be related to the start of the tetrahedral distortion. As regards the region of the external modes, this is the most difficult region to analyze since there are a lot of Raman modes whose frequencies overlap. Several Raman modes change

their pressure coefficients near 8 GPa; however, this feature is barely detected in our experiments. The analysis is even more difficult at pressures beyond 12 GPa because the broadening of peaks gives rise to their overlapping. This likely related to the development of the PIA.

As already commented, the Raman spectrum of Eu$_2$(MoO$_4$)$_3$ can be divided into three regions, correlate well with the pressure coefficients observed for the Raman-active modes in those regions (see Table I). Below 200 cm^{-1} Raman-active modes have the smallest pressure coefficients (below 3.5 cm^{-1}/GPa). Between 200 and 500 cm^{-1} Raman modes have pressure coefficients between 2.6 and 6.6 cm^{-1}/GPa. Finally, the pressure coefficients of the stretching modes vary from 0.5 to 9.5 cm^{-1}/GPa. This behavior is similar to that found in scheelite-type molybdates and tungstates.[48,49] Furthermore, when analyzing the pressure dependence of the Raman-active modes of Eu$_2$(MoO$_4$)$_3$, it can be observed that many Raman-active modes in trimolybdates are grouped into Ag and Bg pairs with similar frequencies (and in many cases) similar behavior with increasing pressure. Most of these pairs are related to Eg modes of the parent scheelite structure.[48,49] In particular, the two bending modes with largest frequency (around 470 cm^{-1} according to our calculations) and the four stretching modes with lowest frequency (around 700 cm^{-1} according to our calculations) derive from the Eg modes of the scheelite structure. Furthermore, these pair modes in trimolybdates are weakly observed in Raman scattering as the Eg modes of the scheelite structure in molybdates.

In order to understand better the similarities between Raman-active modes in the scheelite structure of molybdates and the distorted scheelite structure of trimolybdates we will focus in the high frequency modes corresponding to Mo–O stretching modes of the MoO$_4$ tetrahedra. In trimolybdates there are twelve Raman-active modes (6Ag + 6Bg) while in scheelite-type PbMoO$_4$[49] there are four Raman-active modes (Ag+Bg+Eg) because Eg mode is doubly degenerated. In summary, there are three times more modes in trimolybdates than in molybdates with scheelite-related structure. According to our experimental and theoretical results, the pressure coefficients of the Raman-active Mo–O stretching modes in trimolybdates and molybdates decrease on increasing frequency. In PbMoO$_4$, ν_3(Eg^5), ν_3(Bg^5) and ν_1(Ag^3) modes have theoretical pressure coefficients of 1.7, 0.5 and -0.7 cm^{-1}/Pa, respectively.[49] Similarly for our theoretical results, the average pressure coefficients of the four stretching modes with lowest, middle and highest frequencies are 8.5, 3.1 and 1.7 cm^{-1}/GPa, respectively. The average pressure coefficients in trimolybdates are larger than those in molybdates, suggesting that the force of Mo–O stretching bonds is more affected by the compression in trimolybdates than molybdates.
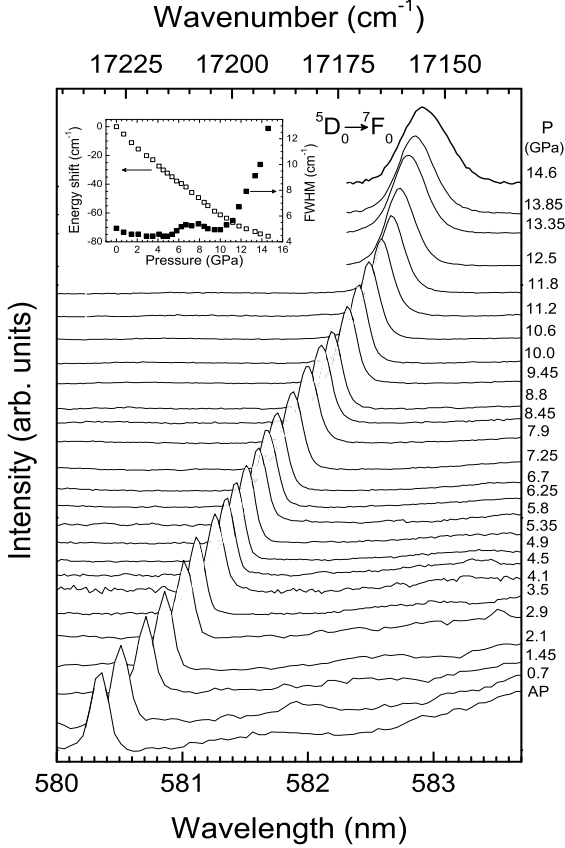
Figure 9. Emission spectra to the $^5D_0 \rightarrow ^7F_0$ transition of α-Eu$_2$(MoO$_4$)$_3$ at different pressures. Inset shows the peak position and the FWHM for this transition.

D. Eu^{3+} surrounding

To improve our experimental knowledge of the pressure dependence for the coordination polyhedra, we have taken the advantage of the relatively simple diagram of Eu^{3+} ion levels and the high dependence of its luminescence on its surrounding. The electronic energy levels scheme of the Eu^{3+} ion in solids consists of seven ^7F_J (J=0–6) multiplets well separated (around 12000 cm^{-1}) from the ^5D_J (J=0–4) ones, plus other strongly overlapped excited multiplets above the $^5D_3$ state at around 25000 cm^{-1}. The ground $^7F_0$ level and the lowest emitting $^5D_0$ level are non-degenerated, making easier the identification of the peaks between Stark levels of the multiplets. Several high pressure optical studies have thus been performed in crystals using the Eu^{3+} ion as local structural probe, and in particular the PIA has been demonstrated by optical spectroscopy in Eu(OH)$_3$,[50] EuZrF$_7$,[51,52] and β'-Eu$_2$(MoO$_4$)$_3$.[53]

In the case of the α-Eu$_2$(MoO$_4$)$_3$ structure, the Eu^{3+} ions are expected to predominantly enter into a site surrounded by eight oxygen ligands with C_1 local point sym-

metry, which causes a complete breakdown of the degeneracy of the electronic levels of the free-Eu^{3+} ion into (2J+1) Stark levels.[54,55] According to group theory, the Eu^{3+} ions at a C_1 site give rise to a number of Stark levels equal to 2J+1=1, 3, 5, 7, 9 with angular momentum J=0, 1, 2, 3, 4, respectively. The absorption and emission bands show a structure of peaks due to the splitting of the ^7F_J (J=1–4) levels induced by the crystal-field. Thus, if the $^7F_0$ or the $^5D_0$ levels are involved in the optical transitions, the peak energies can be used to obtain a complete identification of the number and energy positions of the ^7F_J Stark components in the α-Eu$_2$(MoO$_4$)$_3$ crystal. In this way, intra-configurational $4f^6$–$4f^6$ transitions of the Eu^{3+} ions have been identified comparing the peak energies with the free Eu^{3+} ion energy level diagram.[54]

In our experiments at AP, the emission spectrum has been obtained exciting at 395 nm (25316 cm^{-1}) in resonance with the $^7F_0 \rightarrow ^5L_6$ transition. This spectrum shows different structured bands corresponding to the $^5D_0 \rightarrow ^7F_J$ (J=0–4) transitions that are very close to those presented in Ref. 20. The absence of emission starting from the ^5D_J (J=1–3) levels is due to the high-energy phonons found in the molybdate matrix, i.e. when the Eu^{3+} ions are excited to any level above the $^5D_0$ one, there is a fast non-radiative multiphonon relaxation to this level. From the $^5D_0$ level, the Eu^{3+} ions decay radiatively, since the large energy difference to the $^7F_6$ level prevents the possibility of multiphonon relaxation. Thus, its quantum emission efficiency is close to the unity. Different peaks corresponding to the $^5D_0 \rightarrow ^7F_J$ (J=0–4) transitions can be identified in the emission spectra. The $^5D_0 \rightarrow ^7F_0$ transition gives a single narrow peak at 580.3 nm (see Fig. 9), indicating that all the Eu^{3+} ions occupy exactly the same local surrounding in the α-Eu$_2$(MoO$_4$)$_3$ structure at AP, despite the lack of symmetry of their surroundings. Moreover, no other peaks belonging to sites of a different structural phase are found. The $^5D_0 \rightarrow ^7F_1$ (585–605 nm) transition shows magnetic-dipole character and is allowed by all the selection rules independently of the composition of the host matrix.[56–58] The existence of three overlapped peaks for this transition is the first indication of the low symmetry of the Eu^{3+} surroundings in the trimolybdate crystal.[55] The $^5D_0 \rightarrow ^7F_2$ (608–635 nm) and the $^5D_0 \rightarrow ^7F_4$ (685–720 nm) transitions are electric-dipole in nature and are forced by the odd CF Hamiltonian. It is worth noting that the $^5D_0 \rightarrow ^7F_0$ and the $^5D_0 \rightarrow ^7F_3$ (640–675 nm) transitions are strictly forbidden in the frame of the intermediate scheme of the Judd-Ofelt theory,[59,60] and their low intensities are explained by the J-mixing effect,[61,62] that mixes the wave functions of the $^7F_0$ ground level with those of the $^7F_2$ multiplets.

To obtain more information about the effect of the volume compression on the local surroundings of the Eu^{3+} ions, the present study has been limited to the analysis of the luminescence spectra associated with the $^5D_0 \rightarrow ^7F_0$ transition, which is expected to show higher sensitivity

to changes in the Eu^{3+}–O^{2-} bond length and angles. As pointed out by Machon *et al.*[53], the literature data show that the down-shift of the $^5D_0$ lowest emitting level with pressure is much faster than for the ^7F_J multiplets, whose Stark levels vary non-uniformly in energy, giving rise to an overall red-shift of the luminescence with pressure. Note that, within the range of pressures from ambient conditions up to 14.6 GPa, there are no discontinuities in spectral parameters such as the number of lines, evolution of the frequencies, or intensity with pressure. Thus, in our experiments there are not strong variations of the Eu^{3+}–O^{2-} bond distances or angles and, hence, we do not observe any pressure-induced transition to a different crystalline phase. Discontinuities were not observed in the emission of Eu^{3+} doped α-$Gd_2(MoO_4)_3$ up to 25 GPa.[63] However, for the β'-$Eu_2(MoO_4)_3$, some discontinuities have been found by Machon *et al.*[53] when describing the structural phase transitions and PIA.

The effects of pressure on the $^5D_0 \rightarrow ^7F_0$ transition have been addressed by measuring in detail the emission between these singlet (non-degenerated) levels from AP up to 14.6 GPa (see Fig. 9). Antic-Fidancev, Lemaître-Blaise, and Caro[64] clearly show that the $^5D_0$ state of Eu^{3+} has little or no correlation with parameters such as bond length and coordination number. However, the use of the variations of the energy of the $^5D_0 \rightarrow ^7F_0$ transition to assess the overall Eu^{3+}–O^{2-} bond covalency is reasonable in the case of the α-$Eu_2(MoO_4)_3$ crystals, since both the nature of the ligands and the local structure are expected to vary gradually with pressure. On the other side, the comparison of the variations of the full width at half maximum (FWHM) of this peak at high pressure with respect to the value at AP can be used as a fingerprint of the initial stages of an increase of the number Eu^{3+} sites in the crystal, and hence, the beginning of the amorphization.

Taking into account the values obtained for the red-shift and the FWHM of the $^5D_0 \rightarrow ^7F_0$ peak plotted in the inset of Fig. 9, three different pressure stages, or regimes, can be clearly observed.

1. The first stage, from ambient pressure to 8 GPa, can be divided in two sub-stages with minor changes: I) from ambient to around 4.5–4.9 GPa the emission shows a single and narrow peak that shift to the red, i.e. to lower energies, with a quasi-linear rate of approximately -6.5 cm^{-1}/GPa (0.22 nm/GPa), while the FWHM slightly decreases ($\sim$ 0.6 cm^{-1}); and I') from 4.9 to 8 GPa, with an inflection point for both the red-shift, which decreases to -5.5 cm^{-1}/GPa (0.18 nm/GPa), and the FWHM. The two sub-stages (I and I') of pressure give more or less the same results, with really slight variations of the red-shift rate and the peak width, indicating that only minor Eu^{3+} site symmetry structural changes take place between AP and 8 GPa, accompanied by an overall increase of the Eu^{3+}–O^{2-} bond covalency.

2. In the second stage from 8 up to 12 GPa, the red-shifting and the broadening of the FWHM are clearly non-linear. The FWHM reaches similar values at the measured extreme pressures of this stage (7.9 and 11.8 GPa). Both effects can only be ascribed to an amorphization of the α-$Eu_2(MoO_4)_3$ crystals. With increasing pressure, the broadening increases and simultaneously a broad shoulder appears at the high-energy side of the $^5D_0 \rightarrow ^7F_0$ peak. These effects are associated to the generation of different surroundings for the Eu^{3+} ions in stronger crystal-field environments as a result of the compression and further distortions of the original Eu-ligand bond distances and angles of the local surrounding at AP, which we call the "original" Eu^{3+} site. While a similar red-shifting rate is expected for this "original" Eu^{3+} site, pressure generates new distorted sites for the Eu^{3+} ions, especially with stronger crystal-field strengths, and whose $^5D_0 \rightarrow ^7F_0$ energies are blue-shifted by the J-mixing interaction.[58,65] The proximity of the $^7F_1$ and $^7F_2$ multiplets compared to the energy separation between the $^5D_0$ and the $^5D_2$ multiplets have suggested to Nishimura and Kushida[61] that the inhomogeneous broadening of the $^5D_0 \rightarrow ^7F_0$ peak is mainly due to the downward energy shift of the $^7F_0$ level induced by the J-mixing. These results indicate an increase in the fluctuation of the local structures and crystal-field strengths due to differences in the Eu-ligand bond distances and angles that results in a large variety of surroundings and a broadening of the $^5D_0 \rightarrow ^7F_0$ peak, which becomes a band, but without significant shift. In this scenario, within the henceforth second stage of pressures between 8 and 12 GPa, these new stronger crystal-field sites would start to be created. At around 10.5 GPa there is an inflection point in the pressure dependence of several bond lengths, angles and lattice parameters. This produces abrupt structural changes which may lead to the amorphization.

3. Finally, starting from 12 GPa, the evolution of the structural parameters becomes more monotonous under pressure and the PIA begins.

The three pressure stages, or regimes, found analyzing the $^5D_0 \rightarrow ^7F_0$ emission can be correlated with the results obtained for the $^5D_0 \rightarrow ^7F_1$ transition. However, the pressure dependence of the $^5D_0 \rightarrow ^7F_2$ transition is less clear to interpret (the $^5D_0 \rightarrow ^7F_2$ transition is not shown in this work). Fig. 10 shows the $^5D_0 \rightarrow ^7F_1$ transition as a function of pressure. Since the $^5D_0$ levels are a singlet, the positions of the $^7F_1$ Stark levels with respect to the $^7F_0$ ground level are collected and plotted as a function of pressure in Fig. 11. Three different pressure stages can be observed when the positions of the three peaks of the $^5D_0 \rightarrow ^7F_1$ transition are analyzed. The first stage is subdivided in two stages with minor
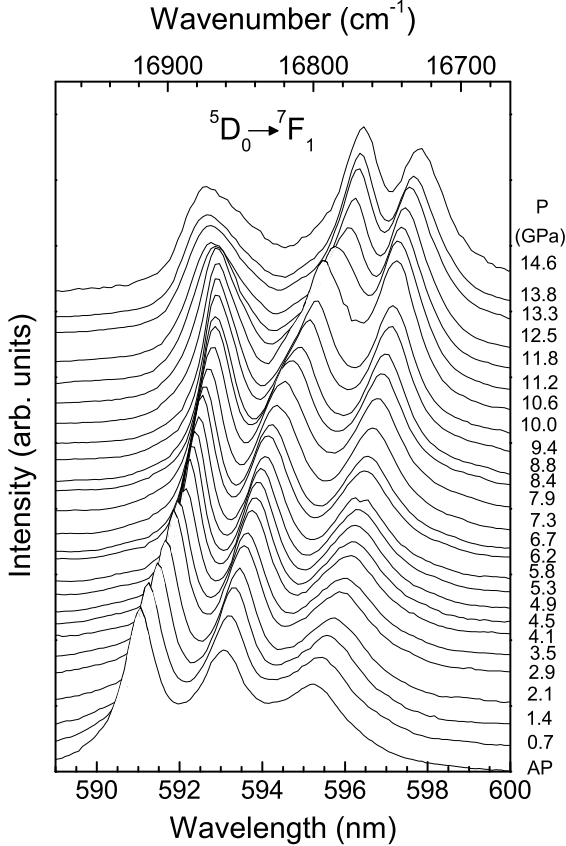
Figure 10. Emission spectra to the transition $^5D_0 \rightarrow {}^7F_1$ of α-Eu$_2$(MoO$_4$)$_3$ at different pressures.
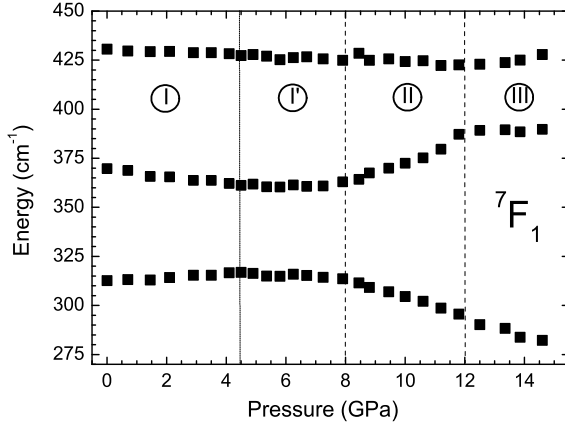
Figure 11. Shifts of the $^7F_1$ Stark levels with respect to $^7F_0$ ground level at all pressure measured.

changes: I) up to 4.5–4.9 GPa, where these three peaks also shift to the red as the $^5D_0 \rightarrow {}^7F_0$ but, at the same time, the two highest energy peaks (lowest energy Stark levels) start to reduce the gap between them, resulting in a slow decrease of the $^7F_1$ multiplet's splitting; and I') up to 8 GPa, where only the red-shifting is appreciable, with an almost constant splitting. The second stage (II) begins at 8 GPa, when the two highest energy peaks start to rapidly separate in energy with opposite directions, the highest energy peak is moved to the blue, and the central one to the red, both increasing the splitting and their FWHM till 12 GPa, indicating abrupt changes in the Eu^{3+} surrounding. Finally, the third stage (III) develops above this pressure of 12 GPa, where less changes are observed and the amorphization clearly proceeds. All these changes in the energies of the $^7F_1$ Stark levels can be directly correlated with changes in the crystal-field strength felt by the Eu^{3+} ions under pressure and these three stages are completely correlated with the compression of the crystal structure and the Raman phonons.

IV. CONCLUSIONS

We have performed an exhaustive study on the behavior of the α-phase of europium trimolybdate under high compression. A good agreement between results from several experimental techniques and theoretical calculation was found in the whole range of pressures. As a result, we have improved previous results where the amorphization process in the α and β' phases was not well differentiated.

According to the present study, from AP to 8 GPa, the compression is monotonous, uniform and isotropic. In contrast, within the pressure interval between 8 and 12 GPa, we observe anomalies in the crystal structure, and also in the evolution of the Raman and luminescence peaks. To our knowledge, these anomalies have not been previously explained. This behavior has been monitored theoretically at five pressures and it can be owed to an anisotropic compression of the MoO$_4$ tetrahedra and modifications in the Eu surrounding, resulting in a more compact packing of the structure. This is compatible with the pressure evolution of the experimental cell parameters, phonons, and luminescence peaks. Europium trimolybdate reaches the PIA at 21 GPa, without a clear indication of an intermediate phase transition. We believe that the amorphization in the α-phase is a consequence of the high distortion for the oxygen-coordination around both the Mo and Eu ions. This distortion affects the theoretical bond valence sum of the europium ion, which changes from 3 to 4.5 v.u., and thus the balance of the electrical charges in this compound.

We set the beginning of the amorphization at approximately 12 GPa, when the rate of compression of the crystal structure becomes smaller: at this pressure, there is a change in the slope of the pressure dependence for the structural parameters, phonon, and emission-peak fre-

quencies. Moreover, an increase of the number of Eu^{3+} sites, which translates into stronger crystal fields, can be predicted by the broadening of the $^5D_0 \rightarrow {^7F_0}$ emission line and the decrease of the energy red-shifting, among other effects. The onset of the PIA can be confirmed by the broadening of the Raman peaks and, finally, by their extinction at 21 GPa.

This compression process contrasts with the results of other compounds with the same structure at AP. The α-$La_2(WO_4)_3$ undergoes two phase transitions before its amorphization, which is irreversible, and the unit cell of α-$Tb_2(MoO_4)_3$ compresses by decreasing the monoclinic β-angle. We are conducting further structural studies on several related compounds featuring the α-phase, with the objective of understanding the different ways in which the PIA develops and its degree of reversibility. We believe these studies will also provide information on new distinct structural effects thanks to the comparison of the behavior of the α-phase with that of the better known β'-phase.

ACKNOWLEDGMENTS

REFERENCES

[1]M. Globus, B. Grinyov, and J. K. Kim, *Inorganic Scintillators for Modern and Traditional Applications* (Institute for Single Crystals, Kharkov, 2005).
[2]A. M. Kaczmarek and R. Van Deun, Chem. Soc. Rev. **42**, 8835 (2013).
[3]C. C. Lin and R.-S. Liu, J. Phys. Chem. Lett. **2**, 1268 (2011).
[4]D. H. Templeton and A. Zalkin, Acta Crystallogr. **16**, 762 (1963).
[5]E. T. Keve, S. C. Abrahams, and J. L. Bernstein, J. Chem. Phys. **54**, 3185 (1971).
[6]L. H. Brixner, J. R. Barkley, and W. Jeitschko, *Handbook on the Physics and Chemistry of Rare Earth* (North-Holland, Amsterdam, 1979).
[7]J. A. Dharmadhikari, A. K. Dharmadhikari, and G. R. Kumar, Appl. Phys. Lett. **83**, 2527 (2003).
[8]M. Xu, Y. Yu, H. Zhang, and J. Wang, J. Rare Earths **27**, 192 (2009).
[9]W. Jeitschko, Acta Crystallogr., Sect. B **29**, 2074 (1973).
[10]J. S. O. Evans, T. A. Mary, and A. W. Sleight, J. Solid State Chem. **133**, 580 (1997).
[11]R. A. Secco, H. Liu, N. Imanaka, and G. Adachi, J. Phys.: Condens. Matter **14**, 11285 (2002).
[12]A. Jayaraman, S. K. Sharma, Z. Wang, S. Y. Wang, L. C. Ming, and M. H. Manghnani, J. Phys. Chem. Solids **54**, 827 (1993).
[13]V. Dmitriev, V. Sinitsyn, R. Dilanian, D. Machon, A. Kuznetsov, E. Ponyatovsky, G. Lucazeau, and H. P. Weber, J. Phys. Chem. Solids **64**, 307 (2003).
[14]G. Lucazeau, O. Le Bacq, A. Pasturel, P. Bouvier, and T. Pagnier, J. Raman Spectrosc. **42**, 452 (2011).
[15]C. Guzmán-Afonso, J. López-Solano, C. González-Silgo, S. F. León-Luis, E. Matesanz, and A. Mujica, High Pressure Res. **34**, 184 (2014).
[16]A. Jayaraman, S. K. Sharma, Z. Wang, and S. Y. Wang, Solid State Commun. **101**, 237 (1997).
[17]O. Le Bacq, D. Machon, D. Testemale, and A. Pasturel, Phys. Rev. B **83**, 214101 (2011).
[18]M. Maczka, A. G. S. Filho, W. Paraguassu, P. T. C. Freire, J. M. Filho, and J. Hanuza, Prog. Mater. Sci. **57**, 1335 (2012).
[19]N. P. Sabalisck, J. López-Solano, C. Guzmán-Afonso, D. Santamaría-Pérez, C. González-Silgo, A. Mujica, A. Muñoz, P. Rodríguez-Hernández, S. Radescu, X. Vendrell, L. Mestres, J. A. Sans, and F. J. Manjón, Phys. Rev. B **89**, 174112 (2014).
[20]V. V. Atuchin, A. S. Aleksandrovsky, O. D. Chimitova, T. A. Gavrilova, A. S. Krylov, M. S. Molokeev, A. S. Oreshonkov, B. G. Bazarov, and J. G. Bazarova, J. Phys. Chem. C **118**, 15404 (2014).
[21]C. Guzmán-Afonso, M. E. Torres, C. González-Silgo, N. Sabalisck, J. González-Platas, E. Matesanz, and A. Mujica, Solid State Commun. **151**, 1654 (2011).
[22]H. K. Mao, P. M. Bell, J. W. Shaner, and D. J. Steinberg, J. Appl. Phys. **49**, 3276 (1978).
[23]H. K. Mao, J. Xu, and P. M. Bell, J. Geophys. Res.: Solid Earth **91**, 4673 (1986).
[24]A. P. Hammersley, S. O. Svensson, M. Hanfland, A. N. Fitch, and D. Hausermann, High Pressure Res. **14**, 235 (1996).
[25]A. Le Bail, Powder Diffr. **20**, 316 (2005).
[26]J. Rodríguez-Carvajal, Physica B **192**, 55 (1993).
[27]P. Hohenberg and W. Kohn, Phys. Rev. **136**, B864 (1964).
[28]G. Kresse and J. Furthmüller, Phys. Rev. B **54**, 11169 (1996).
[29]G. Kresse and D. Joubert, Phys. Rev. B **59**, 1758 (1999).
[30]P. E. Blöchl, Phys. Rev. B **50**, 17953 (1994).
[31]J. P. Perdew, A. Ruzsinszky, G. I. Csonka, O. A. Vydrov, G. E. Scuseria, L. A. Constantin, X. Zhou, and K. Burke, Phys. Rev. Lett. **100**, 136406 (2008).
[32]J. Hafner, J. Comput. Chem. **29**, 2044 (2008).
[33]C. J. Pickard, B. Winkler, R. K. Chen, M. C. Payne, M. H. Lee, J. S. Lin, J. A. White, V. Milman, and D. Vanderbilt, Phys. Rev. Lett. **85**, 5122 (2000).
[34]S. L. Dudarev, G. A. Botton, S. Y. Savrasov, C. J. Humphreys, and A. P. Sutton, Phys. Rev. B **57**, 1505 (1998).
[35]N. Chetty, A. Muoz, and R. M. Martin, Phys. Rev. B **40**, 11934 (1989).
[36]A. Mujica, A. Rubio, A. Muñoz, and R. J. Needs, Rev. Mod. Phys. **75**, 863 (2003).
[37]K. Parlinski, "software phonon," (2008).
[38]J. F. Nye, *Physical properties of crystals. Their representation by Tensor and Matrices* (Oxford University Press, 1957).
[39]D. Errandonea, A. Muñoz, and J. Gonzalez-Platas, J. Appl. Phys. **115**, 216101 (2014).
[40]O. Gomis, J. A. Sans, R. Lacomba-Perales, D. Errandonea, Y. Meng, J. C. Chervin, and A. Polian, Phys. Rev. B **86**, 054121 (2012).
[41]R. Vilaplana, R. Lacomba-Perales, O. Gomis, D. Errandonea, and Y. Meng, Solid State Sci. **36**, 16 (2014).
[42]S. Klotz, J.-C. Chervin, P. Munsch, and G. L. Marchand, J. Phys. D: Appl. Phys. **42**, 075413 (2009).
[43]D. Errandonea, D. Santamaria-Perez, S. N. Achary, A. K. Tyagi,

P. Gall, and P. Gougeon, J. Appl. Phys. **109**, 043510 (2011).

[44]I. D. Brown and D. Altermatt, Acta Crystallogr., Sect. B **41**, 244 (1985).

[45]K. Boulahya, M. Parras, and J. M. González-Calbet, Eur. J. Inorg. Chem. **2005**, 967 (2005).

[46]E. Kroumova, M. I. Aroyo, J. M. Pérez-Mato, A. Kirov, C. Capillas, S. Ivantchev, and H. Wondratschek, Phase Transitions **76**, 155 (2003).

[47]D. Christofilos, G. A. Kourouklis, and S. Ves, J. Phys. Chem. Solids **56**, 1125 (1995).

[48]F. J. Manjón, D. Errandonea, N. Garro, J. Pellicer-Porres, P. Rodríguez-Hernández, S. Radescu, J. López-Solano, A. Mujica, and A. Muñoz, Phys. Rev. B **74**, 144111 (2006).

[49]R. Vilaplana, O. Gomis, F. J. Manjón, P. Rodríguez-Hernández, A. Muñoz, D. Errandonea, S. N. Achary, and A. K. Tyagi, J. Appl. Phys. **112**, 103510 (2012).

[50]G. Chen, N. A. Stamp, R. G. Haire, and J. R. Peterson, Solid State Commun. **89**, 1005 (1994).

[51]V. Lavín, T. Tröster, U. R. Rodríguez-Mendoza, I. R. Martín, and V. D. Rodríguez, High Pressure Res. **22**, 111 (2002).

[52]V. Lavín, J. E. Muñoz Santiuste, T. Tröster, U. R. Rodríguez-Mendoza, J. González-Platas, C. González-Silgo, I. R. Martín, F. Rivera-López, and S. González-Pérez, High Pressure Res. **26**, 411 (2006).

[53]D. Machon, V. P. Dmitriev, V. V. Sinitsyn, and G. Lucazeau, Phys. Rev. B **70**, 094117 (2004).

[54]B. G. Wybourne, *Spectroscopic Properties of Rare Earths* (WileyInterscience, New York, 1965).

[55]C. Görller-Walrand and K. Binnemans, *Rationalization of crystal-field parametrization*, edited by J. K. A. Gschneidner and L. Eyring, Vol. 23 (Elsevier Science B.V., Amsterdam, 1996) Chap. 155, p. 121, in Handbook on the Physics and Chemistry of Rare Earths.

[56]R. D. Peacock, in *Rare Earths*, Structure and Bonding, Vol. 22 (Springer Berlin Heidelberg, 1975) p. 83.

[57]E. W. J. L. Oomen and A. M. A. van Dongen, J. Non-Cryst. Solids **111**, 205 (1989).

[58]V. Lavín, U. R. Rodríguez-Mendoza, I. R. Martín, and V. D. Rodríguez, J. Non-Cryst. Solids **319**, 200 (2003).

[59]B. R. Judd, Phys. Rev. **127**, 750 (1962).

[60]G. S. Ofelt, J. Chem. Phys. **37**, 511 (1962).

[61]G. Nishimura and T. Kushida, J. Phys. Soc. Jpn. **60**, 683 (1991).

[62]M. Tanaka, G. Nishimura, and T. Kushida, Phys. Rev. B **49**, 16917 (1994).

[63]S. Mahlik, A. Lazarowska, B. Grobelna, and M. Grinberg, J. Phys.: Condens. Matter **24**, 485501 (2012).

[64]E. Antic-Fidancev, M. Lemaître-Blaise, and P. Caro, New J. Chem. **11**, 467 (1987).

[65]G. Nishimura and T. Kushida, Phys. Rev. B **37**, 9075 (1988).

Supporting information for: Structural Investigation of the Negative Thermal Expansion in Yttrium and Rare Earth Molybdates

Candelaria Guzmán-Afonso[1], **Cristina González-Silgo**[2], **Javier González-Platas**[2], **Manuel Eulalio Torres**[1], **Antonio Diego Lozano-Gorrín**[3], **Nanci Sabalisck**[1], **Víctor Sánchez-Fajardo**[1], **Javier Campo**[4] **and Juan Rodríguez-Carvajal**[5]

[1] Departamento de Física Básica, Universidad de La Laguna, Tenerife, Spain
[2] Departamento de Física Fundamental II, Universidad de La Laguna, Tenerife, Spain
[3] Servicio Integrado de Difracción de Rayos X, Universidad de La Laguna, Tenerife, Spain
[4] Instituto de Ciencias de Materiales de Aragón, CSIC - Universidad de Zaragoza, Spain
[5] Institute Laue-Langevin, France

E-mail: `csilgo@ull.es`

Table 1. Refinement strategies and conventional reliability factors of the Rietveld refinement reliability factors with all non-excluded points for $Y_2(MoO_4)_3$

Temperature [K]	Patt		N-P-C	R_p	R_{wp}	R_{exp}	χ^2	R_{Bragg}	$R(F^2)$
150	N	1	2557	12.6	13.7	6.58	4.32	3.65	2.37
	N	2	2557	12.4	13.7	9.51	2.07	4.47	2.79
	X	3	5104	18.8	23.6	6.76	12.1	6.24	3.05
200	N	1	2557	8.42	9.17	5.63	2.65	4.31	2.92
	N	2	2557	12.5	13.6	9.62	2.01	4.74	3.23
	X	3	5104	13.2	16.3	5.75	8.05	5.75	3.39
250	N	1	2557	8.92	9.41	5.83	2.60	4.50	3.23
	N	2	2557	13.0	13.9	10.01	1.94	4.97	3.59
	X	3	5104	13.5	16.5	5.82	8.08	5.68	3.29
300	N	1	2557	9.01	9.52	5.99	2.52	4.29	3.19
	N	2	2557	13.6	14.2	10.18	1.93	4.87	3.52
	X	3	5104	13.2	16.6	5.83	8.12	5.63	3.40
350	N	1	2557	9.36	9.73	6.13	2.52	4.46	3.36
	N	2	2557	13.8	14.4	10.37	1.94	4.92	3.64
	X	3	5104	13.3	16.6	5.89	7.92	5.47	3.57
400	N	1	2557	10.1	10.3	6.33	2.63	4.72	3.72
	N	2	2557	14.7	15.0	10.74	1.96	5.11	3.89
	X	3	5104	13.5	16.6	5.92	7.89	5.55	3.68

Table 2. Refinement strategies and conventional reliability factors of the Rietveld refinement reliability factors with all non-excluded points for $Er_2(MoO_4)_3$

Temperature [K]	Patt		N-P-C	R_p	R_{wp}	R_{exp}	χ^2	R_{Bragg}	$R(F^2)$
150	N	1	2557	12.6	13.7	6.58	4.32	5.61	3.87
	N	2	2557	17.8	18.8	11.14	2.86	6.62	4.60
	X	3	5133	12.9	15.7	6.38	6.08	6.46	3.87
200	N	1	2557	9.86	10.7	6.69	2.55	4.40	2.94
	N	2	2557	15.0	15.9	11.40	1.94	5.22	3.51
	X	3	5133	13.0	16.3	6.74	5.82	6.77	3.70
250	N	1	2557	9.82	10.4	7.03	2.19	4.51	3.16
	N	2	2557	15.2	15.8	11.89	1.78	5.43	3.86
	X	3	5133	12.7	15.4	6.76	5.19	6.25	3.48
300	N	1	2557	9.75	10.1	7.19	1.99	4.32	3.11
	N	2	2557	15.3	15.6	12.12	1.65	4.90	3.47
	X	3	5133	12.8	15.7	6.64	5.58	6.61	3.52
350	N	1	2557	9.82	10.0	7.36	1.86	4.40	3.14
	N	2	2557	15.7	15.8	12.26	1.66	5.12	3.76
	X	3	5133	12.8	15.3	6.44	5.67	6.61	3.61
400	N	1	2557	11.0	11.0	7.62	2.09	4.66	3.39
	N	2	2557	17.1	17.2	12.87	1.78	5.55	3.98
	X	3	5133	12.8	15.5	6.60	5.51	6.60	3.71

Table 3. Refinement strategies and conventional reliability factors of the Rietveld refinement reliability factors with all non-excluded points for $Lu_2(MoO_4)_3$

Temperature [K]	Patt		N-P-C	R_p	R_{wp}	R_{exp}	χ^2	R_{Bragg}	$R(F^2)$
200	N	1	2557	10.3	11.3	6.05	3.49	4.98	3.34
	N	2	2557	15.1	16.3	10.39	2.47	5.84	3.86
	X	3	5104	8.82	11.1	5.24	4.50	4.78	2.88
225	N	1	2557	9.04	9.85	6.22	2.50	4.78	3.24
	N	2	2557	14.0	15.0	10.67	1.96	5.46	3.59
	X	3	5104	9.86	12.3	6.57	3.49	4.80	3.20
250	N	1	2557	8.90	9.56	6.36	2.26	4.08	2.73
	N	2	2557	13.8	14.6	10.84	1.81	5.06	3.31
	X	3	5104	9.48	11.7	5.39	4.69	5.65	3.64
303	N	1	2557	10.6	11.0	6.79	2.64	4.33	2.87
	N	2	2557	16.1	16.4	11.51	2.04	4.93	3.40
	X	3	5104	9.61	11.8	5.43	4.74	4.82	2.89
400	N	1	2557	10.3	11.3	6.05	3.49	5.00	3.51
	N	2	2557	15.1	16.3	10.39	2.47	5.94	4.16
	X	3	5104	8.82	11.1	5.24	4.50	5.12	2.98

Table 4. Unit-cell parameters for $Y_2(MoO_4)_3$, $Er_2(MoO_4)_3$, $Lu_2(MoO_4)_3$

$Y_2(MoO_4)_3$	150 K	200 K	250 K	300 K	350 K	400 K
a	13.8827(2)	13.8858(1)	13.8861(1)	13.8881(1)	13.8890(1)	13.8894(1)
b	9.9691(1)	9.96604(8)	9.96197(8)	9.95961(8)	9.95715(8)	9.95451(8)
c	10.0629(1)	10.05879(8)	10.05317(8)	10.04945(8)	10.04587(8)	10.04225(8)

$Er_2(MoO_4)_3$	150 K	200 K	250 K	300 K	350 K	400 K
a	13.8309(1)	13.8336(1)	13.8363(1)	13.8379(1)	13.83934(9)	13.8405(1)
b	9.93805(8)	9.93615(7)	9.93310(7)	9.92991(7)	9.92789(6)	9.92551(7)
c	10.03527(9)	10.03283(8)	10.02843(7)	10.02407(7)	10.02088(7)	10.01745(7)

$Lu_2(MoO_4)_3$	200 K	225 K	250 K	303 K		400 K
a	13.70121(8)	13.70192(8)	13.70381(9)	13.70376(8)		13.70703(8)
b	9.84752(6)	9.84591(6)	9.84569(6)	9.84254(6)		9.83937(6)
c	9.94469(6)	9.94265(6)	9.94230(7)	9.93846(6)		9.93371(6)

Table 5. Atomic coordinates at 400 K "parent = reference structures"

Atom	x/a	y/b	z/c
Y1	0.3818(2)	0.2489(3)	0.9679(2)
Mo1	0.1433(2)	0.1083(3)	0.1139(2)
Mo2	0.00000	0.5281(4)	0.25000
O1	0.0315(6)	0.1709(10)	0.0651(9)
O2	0.1404(8)	-0.0661(8)	0.0882(8)
O3	0.2337(6)	0.1808(9)	0.0157(8)
O4	0.1647(7)	0.1399(9)	0.2834(9)
O5	0.0841(6)	0.4293(8)	0.3361(9)
O6	0.0653(6)	0.6310(9)	0.1428(9)
Er1	0.3815(1)	0.2489(2)	0.9678(2)
Mo1	0.1433(2)	0.1078(3)	0.1147(3)
Mo2	0.0000	0.5283(4)	0.2500
O1	0.0309(5)	0.1736(11)	0.0663(9)
O2	0.1398(9)	-0.0678(8)	0.0879(8)
O3	0.2338(6)	0.1777(9)	0.0151(9)
O4	0.1648(7)	0.1398(9)	0.2846(9)
O5	0.0837(6)	0.4280(8)	0.3360(9)
O6	0.0657(6)	0.6291(10)	0.1410(10)
Lu1	0.3813(1)	0.2490(2)	0.9669(1)
Mo1	0.1438(2)	0.1071(3)	0.1145(2)
Mo2	0.0000	0.5293(4)	0.2500
O1	0.0317(5)	0.1774(9)	0.0672(8)
O2	0.1398(7)	-0.0686(7)	0.0889(7)
O3	0.2354(5)	0.1784(8)	0.0146(7)
O4	0.1663(6)	0.1401(8)	0.2851(8)
O5	0.0847(5)	0.4270(7)	0.3352(8)
O6	0.0634(5)	0.6314(8)	0.1380(8)

Table 6. Final coordinates, shift vectors (dx,dy,dz) in fractional coordinates and total atomic displacement (in Å) respect to the structure at 400 K for $Y_2(MoO_4)_3$.

	x/a	y/b	z/c	dx	dy	dz	Dist(Å)
			150 K				
Y1	0.38163(20)	0.2486(3)	0.9673(3)	-0.00022	-0.00034	-0.00063	0.00778
Mo1	0.1436(2)	0.1074(3)	0.1148(3)	0.00022	-0.00093	0.00094	0.01358
Mo2	0.00000	0.5275(4)	0.25000	0.00000	-0.00063	0.00000	0.00631
O1	0.0303(4)	0.1727(8)	0.0736(7)	-0.00122	0.00176	0.00852	0.08913
O2	0.1397(6)	-0.0676(6)	0.0914(6)	-0.00071	-0.00149	0.00315	0.03635
O3	0.2329(5)	0.1805(7)	0.0169(7)	-0.00077	-0.00033	0.00126	0.01688
O4	0.1677(5)	0.1373(7)	0.2831(7)	0.00299	-0.00261	-0.00028	0.04911
O5	0.0838(5)	0.4264(7)	0.3350(7)	-0.00029	-0.00291	-0.00111	0.03133
O6	0.0629(5)	0.6297(8)	0.1374(8)	-0.00240	-0.00131	-0.00534	0.06458
			200 K				
Y1	0.38152(18)	0.2492(3)	0.9675(2)	-0.00033	0.00024	-0.00042	0.00660
Mo1	0.14346(19)	0.1077(3)	0.1146(2)	0.00012	-0.00062	0.00065	0.00915
Mo2	0.00000	0.5277(4)	0.25000	0.00000	-0.00042	0.00000	0.00420
O1	0.0306(5)	0.1730(8)	0.0714(7)	-0.00094	0.00204	0.00633	0.06808
O2	0.1403(6)	-0.0674(7)	0.0906(7)	-0.00011	-0.00138	0.00240	0.02781
O3	0.2338(5)	0.1801(7)	0.0162(7)	0.00003	-0.00070	0.00048	0.00850
O4	0.1672(6)	0.1382(8)	0.2831(8)	0.00256	-0.00167	-0.00027	0.03936
O5	0.0836(6)	0.4281(7)	0.3353(8)	-0.00045	-0.00124	-0.00086	0.01633
O6	0.0630(5)	0.6305(8)	0.1391(9)	-0.00239	-0.00056	-0.00368	0.05002
			250 K				
Y1	0.38146(18)	0.2488(3)	0.9674(2)	-0.00039	-0.00012	-0.00046	0.00724
Mo1	0.14333(19)	0.1079(3)	0.1146(2)	-0.00001	-0.00044	0.00069	0.00817
Mo2	0.00000	0.5282(4)	0.25000	0.00000	0.00015	0.00000	0.00151
O1	0.0304(5)	0.1704(8)	0.0701(8)	-0.00113	-0.00059	0.00500	0.05296
O2	0.1409(7)	-0.0661(7)	0.0897(7)	0.00048	-0.00001	0.00148	0.01629
O3	0.2334(5)	0.1811(8)	0.0159(7)	-0.00035	0.00028	0.00019	0.00587
O4	0.1655(6)	0.1385(8)	0.2836(8)	0.00087	-0.00138	0.00020	0.01844
O5	0.0840(6)	0.4287(7)	0.3355(8)	-0.00006	-0.00060	-0.00064	0.00886
O6	0.0639(5)	0.6307(8)	0.1396(9)	-0.00146	-0.00028	-0.00318	0.03794
			300 K				
Y1	0.38168(18)	0.2488(3)	0.9677(2)	-0.00017	-0.00017	-0.00018	0.00343
Mo1	0.14343(19)	0.1080(3)	0.1141(3)	0.00009	-0.00027	0.00017	0.00349
Mo2	0.00000	0.5279(4)	0.25000	0.00000	-0.00015	0.00000	0.00145
O1	0.0306(5)	0.1702(9)	0.0672(8)	-0.00085	-0.00075	0.00206	0.02495
O2	0.1413(7)	-0.0670(8)	0.0889(7)	0.00084	-0.00094	0.00067	0.01645
O3	0.2334(6)	0.1817(8)	0.0157(8)	-0.00028	0.00084	0.00001	0.00923
O4	0.1650(6)	0.1390(8)	0.2838(9)	0.00036	-0.00085	0.00043	0.01077
O5	0.0848(6)	0.4294(8)	0.3359(9)	0.00066	0.00007	-0.00022	0.00952
O6	0.0644(6)	0.6318(9)	0.1411(9)	-0.00096	0.00074	-0.00165	0.02250

			350 K				
Y1	0.38178(18)	0.2488(3)	0.9679(2)	-0.00007	-0.00017	-0.00005	0.00198
Mo1	0.14334(19)	0.1081(3)	0.1138(3)	0.00000	-0.00024	-0.00013	0.00268
Mo2	0.00000	0.5279(4)	0.25000	0.00000	-0.00016	0.00000	0.00161
O1	0.0309(5)	0.1711(9)	0.0655(9)	-0.00059	0.00019	0.00035	0.00916
O2	0.1407(8)	-0.0658(8)	0.0884(8)	0.00023	0.00022	0.00015	0.00415
O3	0.2337(5)	0.1810(9)	0.0162(8)	0.00002	0.00019	0.00052	0.00554
O4	0.1645(6)	0.1398(8)	0.2834(9)	-0.00019	-0.00005	0.00001	0.00270
O5	0.0844(6)	0.4291(8)	0.3354(9)	0.00028	-0.00017	-0.00077	0.00881
O6	0.0649(6)	0.6315(9)	0.1427(9)	-0.00046	0.00050	-0.00001	0.00808

Table 7. Final coordinates, shift vectors (dx,dy,dz) in fractional coordinates and total atomic displacement (in Å) respect to the structure at 400 K for $Er_2(MoO_4)_3$.

	x/a	y/b	z/c	dx	dy	dz	$Dist(Å)$
			150 K				
Er1	0.38143(17)	0.2488(3)	0.9673(2)	-0.00012	-0.00018	-0.00050	0.00559
Mo1	0.1432(3)	0.1068(3)	0.1159(3)	-0.00009	-0.00108	0.00112	0.01556
Mo2	0.00000	0.5279(5)	0.25000	0.00000	-0.00042	0.00000	0.00419
O1	0.0303(5)	0.1742(9)	0.0742(8)	-0.00063	0.00066	0.00795	0.08048
O2	0.1410(7)	-0.0693(7)	0.0922(8)	0.00126	-0.00152	0.00427	0.04863
O3	0.2323(6)	0.1784(9)	0.0156(9)	-0.00147	0.00071	0.00055	0.02218
O4	0.1685(7)	0.1366(9)	0.2859(9)	0.00367	-0.00316	0.00138	0.06134
O5	0.0843(7)	0.4256(9)	0.3328(9)	0.00068	-0.00235	-0.00314	0.04035
O6	0.0627(6)	0.6302(10)	0.1356(10)	-0.00302	0.00111	-0.00547	0.06985
			200 K				
Er1	0.38142(16)	0.2487(3)	0.96723(20)	-0.00013	-0.00023	-0.00058	0.00647
Mo1	0.1431(2)	0.1065(3)	0.1154(3)	-0.00017	-0.00133	0.00066	0.01502
Mo2	0.00000	0.5275(4)	0.25000	0.00000	-0.00079	0.00000	0.00788
O1	0.0304(5)	0.1726(8)	0.0723(7)	-0.00053	-0.00096	0.00599	0.06134
O2	0.1409(7)	-0.0695(6)	0.0905(7)	0.00115	-0.00165	0.00264	0.03499
O3	0.2328(5)	0.1789(8)	0.0155(8)	-0.00097	0.00122	0.00043	0.01863
O4	0.1678(6)	0.1378(8)	0.2857(8)	0.00299	-0.00193	0.00110	0.04687
O5	0.0840(6)	0.4272(7)	0.3336(8)	0.00033	-0.00072	-0.00235	0.02502
O6	0.0633(5)	0.6295(9)	0.1365(8)	-0.00243	0.00040	-0.00451	0.05652

			250 K				
Er1	0.38148(15)	0.2488(2)	0.96759(18)	-0.00007	-0.00015	-0.00022	0.00282
Mo1	0.1432(2)	0.1072(3)	0.1148(3)	-0.00006	-0.00060	0.00006	0.00609
Mo2	0.00000	0.5278(4)	0.25000	0.00000	-0.00047	0.00000	0.00463
O1	0.0303(4)	0.1731(8)	0.0707(7)	-0.00067	-0.00048	0.00441	0.04543
O2	0.1406(7)	-0.0692(7)	0.0901(7)	0.00080	-0.00132	0.00223	0.02820
O3	0.2335(5)	0.1790(8)	0.0166(7)	-0.00027	0.00130	0.00152	0.02033
O4	0.1666(6)	0.1392(8)	0.2847(8)	0.00174	-0.00056	0.00014	0.02477
O5	0.0829(6)	0.4263(7)	0.3348(8)	-0.00079	-0.00165	-0.00117	0.02298
O6	0.0632(5)	0.6297(9)	0.1383(9)	-0.00257	0.00062	-0.00273	0.04528
			300 K				
Er1	0.38151(14)	0.2487(2)	0.96771(18)	-0.00004	-0.00022	-0.00010	0.00251
Mo1	0.1431(2)	0.1074(3)	0.1147(3)	-0.00017	-0.00048	-0.00007	0.00541
Mo2	0.00000	0.5280(4)	0.25000	0.00000	-0.00034	0.00000	0.00337
O1	0.0306(5)	0.1733(9)	0.0689(8)	-0.00037	-0.00027	0.00262	0.02688
O2	0.1408(7)	-0.0683(7)	0.0894(7)	0.00102	-0.00050	0.00148	0.02110
O3	0.2332(5)	0.1789(8)	0.0157(8)	-0.00052	0.00118	0.00060	0.01497
O4	0.1663(6)	0.1408(8)	0.2849(8)	0.00145	0.00098	0.00036	0.02261
O5	0.0836(6)	0.4272(7)	0.3350(8)	-0.00003	-0.00076	-0.00104	0.01283
O6	0.0642(6)	0.6302(9)	0.1402(9)	-0.00148	0.00111	-0.00086	0.02474
			350 K				
Er1	0.38145(14)	0.2489(2)	0.96767(18)	-0.00010	-0.00003	-0.00014	0.00204
Mo1	0.1433(2)	0.1074(3)	0.1147(3)	0.00000	-0.00040	-0.00006	0.00405
Mo2	0.00000	0.5280(4)	0.25000	0.00000	-0.00029	0.00000	0.00288
O1	0.0307(5)	0.1738(10)	0.0670(8)	-0.00025	0.00026	0.00074	0.00861
O2	0.1408(8)	-0.0688(7)	0.0894(8)	0.00101	-0.00093	0.00151	0.02262
O3	0.2339(5)	0.1787(9)	0.0156(8)	0.00012	0.00096	0.00049	0.01084
O4	0.1662(6)	0.1393(9)	0.2850(9)	0.00133	-0.00047	0.00044	0.01946
O5	0.0829(6)	0.4283(7)	0.3366(9)	-0.00074	0.00030	0.00058	0.01212
O6	0.0645(6)	0.6309(9)	0.1412(9)	-0.00121	0.00188	0.00021	0.02516

Table 8. Final coordinates, shift vectors (dx,dy,dz) in fractional coordinates and total atomic displacement (in Å) respect to the structure at 400 K for Lu$_2$(MoO$_4$)$_3$.

	x/a	y/b	z/c	dx	dy	dz	Dist(Å)
				200 K			
Lu1	0.38116(12)	0.24897(20)	0.96660(15)	-0.00013	0.00001	-0.00031	0.00355
Mo1	0.14384(19)	0.1063(3)	0.1154(2)	0.00000	-0.00086	0.00082	0.01177
Mo2	0.00000	0.5293(4)	0.25000	0.00000	-0.00006	0.00000	0.00056
O1	0.0306(4)	0.1769(7)	0.0721(6)	-0.00106	-0.00048	0.00488	0.05088
O2	0.1401(5)	-0.0699(5)	0.0916(6)	0.00037	-0.00130	0.00271	0.03024
O3	0.2348(5)	0.1785(8)	0.0146(7)	-0.00066	0.00010	0.00002	0.00909
O4	0.1696(5)	0.1387(7)	0.2861(7)	0.00332	-0.00146	0.00099	0.04869
O5	0.0853(5)	0.4241(7)	0.3340(7)	0.00061	-0.00287	-0.00124	0.03189
O6	0.0623(5)	0.6305(8)	0.1344(7)	-0.00115	-0.00086	-0.00360	0.04004
				225 K			
Lu1	0.38122(12)	0.24893(19)	0.96678(14)	-0.00007	-0.00003	-0.00013	0.00167
Mo1	0.14386(18)	0.1066(3)	0.1151(2)	0.00002	-0.00058	0.00059	0.00816
Mo2	0.00000	0.5293(4)	0.25000	0.00000	0.00001	0.00000	0.00009
O1	0.0309(4)	0.1768(7)	0.0719(6)	-0.00074	-0.00053	0.00475	0.04855
O2	0.1407(5)	-0.0697(5)	0.0915(6)	0.00094	-0.00111	0.00259	0.03076
O3	0.2345(4)	0.1785(7)	0.0143(6)	-0.00091	0.00011	-0.00031	0.01287
O4	0.1690(5)	0.1395(7)	0.2854(7)	0.00268	-0.00068	0.00032	0.03742
O5	0.0853(5)	0.4242(6)	0.3340(7)	0.00054	-0.00278	-0.00119	0.03068
O6	0.0625(5)	0.6311(8)	0.1345(7)	-0.00098	-0.00026	-0.00352	0.03754
				250 K			
Lu1	0.38120(13)	0.2489(2)	0.96682(16)	-0.00009	-0.00005	-0.00009	0.00162
Mo1	0.14377(20)	0.1065(3)	0.1153(3)	-0.00007	-0.00064	0.00073	0.00963
Mo2	0.00000	0.5292(4)	0.25000	0.00000	-0.00013	0.00000	0.00125
O1	0.0308(4)	0.1773(7)	0.0715(6)	-0.00084	-0.00007	0.00435	0.04470
O2	0.1403(5)	-0.0702(5)	0.0907(6)	0.00050	-0.00161	0.00179	0.02481
O3	0.2346(4)	0.1783(7)	0.0148(6)	-0.00087	-0.00008	0.00021	0.01214
O4	0.1682(5)	0.1399(6)	0.2853(7)	0.00187	-0.00023	0.00026	0.02591
O5	0.0851(5)	0.4243(6)	0.3346(6)	0.00041	-0.00271	-0.00061	0.02796
O6	0.0626(4)	0.6306(7)	0.1352(7)	-0.00078	-0.00083	-0.00281	0.03105
				303 K			
Lu1	0.38123(11)	0.24884(19)	0.96679(14)	-0.00006	-0.00012	-0.00012	0.00186
Mo1	0.14383(18)	0.1070(2)	0.1150(2)	-0.00001	-0.00015	0.00050	0.00522
Mo2	0.00000	0.5293(3)	0.25000	0.00000	-0.00007	0.00000	0.00064
O1	0.0310(4)	0.1769(7)	0.0698(6)	-0.00067	-0.00044	0.00263	0.02806
O2	0.1394(6)	-0.0694(6)	0.0900(6)	-0.00037	-0.00086	0.00106	0.01443
O3	0.2346(4)	0.1777(7)	0.0148(6)	-0.00084	-0.00068	0.00020	0.01346
O4	0.1674(5)	0.1399(7)	0.2859(7)	0.00105	-0.00028	0.00080	0.01671
O5	0.0847(5)	0.4255(6)	0.3347(7)	-0.00006	-0.00148	-0.00053	0.01554
O6	0.0630(5)	0.6314(7)	0.1357(7)	-0.00040	0.00002	-0.00226	0.02308

Table 9. Temperature dependence of A-O, Mo-O bonds and angles. Symmetry operators are: (i) x, y, z+1; (ii) x+1/2, -y+1/2, -z+1; (iii) -x, y, -z+1/2; (iv) -x+1/2, -y+1/2, z+1/2; (v) -x+1/2, y+1/2, z+1; (vi) -x+1/2, y-1/2, z+1.

Distance	150 K	200 K	250 K	300 K	350 K	400 K
Y1 - O1ii	2.242(8)	2.244(8)	2.251(8)	2.247(8)	2.244(8)	2.251(9)
Y1 - O2v	2.235(8)	2.228(8)	2.238(8)	2.225(8)	2.229(9)	2.224(9)
Y1 - O3i	2.227(9)	2.218(7)	2.218(7)	2.218(8)	2.218(8)	2.219(9)
Y1 - O4iv	2.267(9)	2.270(8)	2.258(8)	2.255(9)	2.254(9)	2.253(9)
Y1 - O5iv	2.249(9)	2.264(8)	2.262(8)	2.263(9)	2.266(9)	2.263(9)
Y1 - O6vi	2.216(10)	2.230(8)	2.226(9)	2.226(9)	2.235(9)	2.236(9)

Distance	150 K	200 K	250 K	300 K	350 K	400 K
Er1 - O1ii	2.236(8)	2.240(7)	2.234(6)	2.234(7)	2.231(8)	2.232(8)
Er1 - O2v	2.221(8)	2.211(7)	2.207(7)	2.210(7)	2.204(8)	2.201(9)
Er1 - O3i	2.231(9)	2.223(7)	2.217(7)	2.219(7)	2.210(7)	2.215(9)
Er1 - O4iv	2.256(9)	2.248(8)	2.246(8)	2.236(8)	2.240(9)	2.236(9)
Er1 - O5iv	2.247(9)	2.254(8)	2.245(8)	2.248(8)	2.250(8)	2.249(9)
Er1 - O6vi	2.200(10)	2.207(9)	2.217(9)	2.222(9)	2.226(9)	2.226(10)

Distance	200 K	225 K	250 K	303 K		400 K
Lu1 - O1ii	2.208(6)	2.211(6)	2.208(6)	2.209(6)		2.211(7)
Lu1 - O2v	2.194(6)	2.195(6)	2.185(6)	2.186(6)		2.185(7)
Lu1 - O3i	2.175(7)	2.178(6)	2.179(6)	2.181(6)		2.169(7)
Lu1 - O4iv	2.220(7)	2.221(7)	2.217(7)	2.208(7)		2.209(8)
Lu1 - O5iv	2.203(7)	2.204(7)	2.202(6)	2.210(7)		2.220(8)
Lu1 - O6vi	2.178(7)	2.173(7)	2.180(7)	2.177(7)		2.191(8)

Angle	150 K	20 K	250 K	300 K	350 K	400 K
O1-Y1-O2	86.7(5)	86.5(5)	85.7(5)	85.5(5)	85.2(5)	85.1(6)
O1-Y1-O4	87.3(5)	87.8(5)	87.2(5)	87.7(5)	88.0(5)	88.3(6)
O1-Y1-O5	87.7(5)	88.3(5)	89.2(5)	90.1(5)	89.9(5)	89.9(6)
O1-Y1-O6	90.3(5)	90.0(5)	90.3(5)	90.0(5)	89.8(5)	89.9(6)
O2-Y1-O3	90.3(5)	90.4(5)	90.1(5)	89.8(5)	90.2(5)	90.4(6)
O2-Y1-O4	90.2(5)	90.4(5)	90.0(5)	89.9(5)	90.0(5)	90.0(5)
O2-Y1-O6	93.3(5)	93.0(5)	93.2(5)	92.9(5)	93.0(6)	93.1(6)
O3-Y1-O4	93.5(5)	93.3(5)	93.6(5)	93.5(5)	93.7(5)	93.5(6)
O3-Y1-O5	95.3(5)	94.9(5)	95.0(5)	94.7(5)	94.8(5)	94.6(6)
O3-Y1-O6	89.0(5)	89.1(5)	89.1(5)	89.1(5)	88.6(5)	88.5(5)
O4-Y1-O5	88.0(5)	88.3(5)	88.3(5)	88.2(5)	87.7(5)	87.9(5)
O5-Y1-O6	88.2(5)	88.1(5)	88.3(5)	88.8(6)	89.1(6)	88.8(6)

Angle	150 K	200 K	250 K	300 K	250 K	400 K
O1-Er1-O2	87.4(5)	86.7(5)	86.5(5)	86.6(5)	86.2(5)	85.6(6)
O1-Er1-O4	87.6(5)	87.7(5)	87.7(4)	88.8(5)	88.6(5)	88.3(5)
O1-Er1-O5	87.6(5)	88.3(5)	88.0(4)	88.8(5)	88.6(5)	88.9(5)
O1-Er1-O6	90.2(6)	90.3(5)	90.0(5)	90.9(5)	89.5(5)	90.0(6)
O2-Er1-O3	90.2(5)	90.2(5)	90.3(5)	90.0(5)	90.5(5)	91.3(6)
O2-Er1-O4	90.1(5)	90.1(5)	90.4(5)	90.0(5)	90.2(5)	90.1(6)
O2-Er1-O6	93.0(6)	93.2(5)	93.2(5)	93.2(5)	92.7(5)	93.4(6)
O3-Er1-O4	92.9(6)	93.0(5)	93.6(5)	93.3(5)	93.3(5)	93.9(6)
O3-Er1-O5	94.8(6)	94.8(5)	95.3(5)	94.4(5)	94.8(5)	94.2(6)
O3-Er1-O6	89.4(6)	89.2(5)	88.9(5)	88.8(5)	88.6(5)	88.0(6)
O4-Er1-O5	88.2(6)	88.4(5)	88.0(5)	87.8(5)	88.6(5)	88.0(5)
O5-Er1-O6	88.5(6)	88.2(5)	88.2(5)	88.8(5)	88.3(5)	88.3(6)

Angle	200 K	225 K	250 K	303 K		400 K
O1-Lu1-O2	87.3(4)	87.5(4)	87.4(4)	86.7(4)		86.5(5)
O1-Lu1-O4	89.1(4)	89.0(4)	88.9(4)	89.0(4)		89.3(5)
O1-Lu1-O5	87.6(4)	87.6(4)	87.5(4)	87.9(4)		88.2(5)
O1-Lu1-O2	88.9(4)	88.9(4)	88.9(4)	88.7(4)		88.2(5)
O2-Lu1-O3	90.7(4)	90.6(4)	90.7(4)	91.2(4)		91.1(5)
O2-Lu1-O4	90.7(4)	90.8(4)	90.9(4)	90.6(4)		90.5(5)
O2-Lu1-O6	92.8(4)	92.8(4)	92.9(4)	93.4(4)		92.8(5)
O3-Lu1-O4	92.7(4)	92.7(4)	93.1(4)	94.3(4)		93.7(5)
O3-Lu1-O5	94.4(5)	94.3(4)	94.4(4)	94.3(4)		94.2(5)
O3-Lu1-O6	89.4(5)	89.5(4)	89.3(4)	89.1(4)		88.9(5)
O4-Lu1-O5	88.1(4)	87.7(4)	87.7(4)	88.0(4)		88.0(5)
O5-Lu1-O6	88.3(4)	88.4(4)	88.3(4)	88.4(4)		88.4(5)

$Y_2(MoO_4)_3$	150 K	200 K	250 K	300 K	350 K	400 K
Mo1-O1	1.756(8)	1.753(8)	1.746(8)	1.750(8)	1.752(8)	1.744(9)
Mo1-O2	1.758(8)	1.762(8)	1.752(8)	1.761(8)	1.752(9)	1.756(9)
Mo1-O3	1.747(9)	1.753(7)	1.755(8)	1.754(8)	1.750(8)	1.752(9)
Mo1-O4	1.757(9)	1.754(8)	1.753(8)	1.759(8)	1.758(9)	1.756(10)
Mo2-O5iii	1.755(9)	1.751(8)	1.756(8)	1.759(9)	1.754(9)	1.755(9)
Mo2-O6iii	1.761(9)	1.748(8)	1.750(9)	1.752(9)	1.743(9)	1.741(9)
O1-Mo1-O2	108.5(7)	108.1(7)	107.4(7)	107.2(7)	107.2(8)	106.9(8)
O1-Mo1-O3	110.5(7)	110.3(6)	110.3(6)	109.7(6)	109.6(6)	109.4(8)
O1-Mo1-O4	109.2(7)	110.1(7)	110.1(7)	110.6(7)	110.7(8)	111.0(8)
O2-Mo1-O3	110.3(7)	110.4(6)	110.1(7)	110.2(7)	110.1(8)	110.0(8)
O2-Mo1-O4	108.2(7)	108.0(7)	108.3(7)	108.4(7)	108.8(7)	108.9(8)
O3-Mo1-O4	110.1(7)	109.9(7)	110.5(7)	110.6(8)	110.4(8)	110.5(8)
O5-Mo2-O5iii	109.5(7)	111.0(7)	111.2(7)	112.2(8)	111.8(8)	111.8(8)
O5-Mo2-O6	108.6(8)	108.3(7)	107.6(7)	107.1(8)	106.8(8)	106.7(8)
O5-Mo2-O6iii	110.4(8)	110.5(7)	110.8(7)	111.4(7)	112.1(8)	111.8(8)
O6-Mo2-O6iii	109.3(8)	108.3(7)	108.6(7)	107.6(7)	107.4(8)	107.9(8)

$Er_2(MoO_4)_3$	150 K	200 K	250 K	300 K	350 K	400 K
Mo1-O1	1.750(8)	1.746(8)	1.751(7)	1.750(8)	1.758(8)	1.755(8)
Mo1-O2	1.767(8)	1.767(7)	1.770(8)	1.763(8)	1.768(8)	1.764(9)
Mo1-O3	1.743(9)	1.750(8)	1.743(8)	1.745(8)	1.749(8)	1.745(9)
Mo1-O4	1.767(10)	1.770(9)	1.763(9)	1.767(9)	1.764(9)	1.757(10)
Mo2-O5iii	1.756(10)	1.751(8)	1.746(8)	1.751(8)	1.746(8)	1.754(9)
Mo2-O6iii	1.762(10)	1.758(8)	1.758(8)	1.741(9)	1.740(9)	1.738(10)
O1-Mo1-O2	109.4(7)	108.5(7)	108.8(6)	108.4(7)	108.3(7)	107.5(7)
O1-Mo1-O3	109.7(7)	110.1(6)	109.7(6)	109.5(6)	109.2(6)	109.3(7)
O1-Mo1-O4	110.1(8)	109.9(7)	110.2(7)	110.2(7)	110.8(7)	110.5(7)
O2-Mo1-O3	109.8(7)	109.9(7)	109.8(7)	109.5(7)	109.5(7)	109.0(8)
O2-Mo1-O4	107.4(7)	108.5(7)	108.3(6)	109.1(7)	108.7(7)	109.3(8)
O3-Mo1-O4	110.4(8)	109.9(7)	110.1(7)	110.1(7)	110.3(8)	111.1(8)
O5-Mo2-O5iii	109.2(8)	110.4(7)	109.5(7)	110.3(4)	110.9(8)	110.0(4)
O5-Mo2-O6	108.4(8)	108.0(7)	108.5(7)	107.6(4)	107.9(8)	108.1(4)
O5-Mo2-O6iii	110.6(8)	110.5(7)	110.6(7)	111.3(4)	111.0(7)	110.8(4)
O6-Mo2-O6iii	109.5(8)	109.6(7)	109.1(7)	108.7(4)	108.1(8)	109.1(4)

Lu$_2$(MoO$_4$)$_3$	200 K	225 K	250 K	303 K	400 K
Mo1-O1	1.754(6)	1.749(6)	1.753(6)	1.751(6)	1.749(8)
Mo1-O2	1.752(6)	1.752(6)	1.757(6)	1.755(6)	1.749(7)
Mo1-O3	1.750(7)	1.746(6)	1.746(7)	1.739(6)	1.747(8)
Mo1-O4	1.763(7)	1.758(7)	1.754(8)	1.759(7)	1.753(8)
Mo2-O5iii	1.771(7)	1.770(7)	1.770(7)	1.761(7)	1.754(8)
Mo2-O6iii	1.745(8)	1.748(8)	1.742(7)	1.745(7)	1.733(8)
O1-Mo1-O2	109.5(5)	109.7(5)	109.6(5)	108.8(6)	108.9(7)
O1-Mo1-O3	109.2(6)	109.2(5)	109.1(5)	109.1(5)	108.7(6)
O1-Mo1-O4	110.0(6)	109.7(6)	109.5(6)	109.7(6)	109.9(7)
O2-Mo1-O3	110.2(6)	110.0(5)	109.9(5)	109.9(6)	109.7(7)
O2-Mo1-O4	108.4(6)	108.4(6)	109.0(5)	109.0(6)	109.2(7)
O3-Mo1-O4	109.6(6)	109.8(6)	109.8(6)	110.4(6)	110.4(7)
O5-Mo2-O5iii	108.4(6)	108.5(6)	108.6(6)	109.1(6)	110.0(7)
O5-Mo2-O6	108.8(6)	108.8(6)	108.7(6)	108.6(6)	108.1(7)
O5-Mo2-O6iii	110.3(6)	110.4(6)	110.3(6)	110.4(6)	110.8(7)
O6-Mo2-O6iii	110.3(6)	110.0(6)	110.1(6)	109.7(6)	109.1(7)

Table 10. Temperature dependence of non bonding distance A...Mo and angles A-O-Mo.

Y$_2$(MoO$_4$)$_3$	150 K	200 K	250 K	300 K	350 K	400 K
Y...Mo1	3.997(4)	3.993(4)	3.993(4)	3.991(4)	3.988(4)	3.986(4)
Y...Mo1	3.886(5)	3.883(4)	3.887(4)	3.884(4)	3.882(4)	3.882(4)
Y...Mo1	3.888(4)	3.887(4)	3.885(4)	3.883(4)	3.883(4)	3.884(4)
Y...Mo1	3.841(4)	3.841(3)	3.839(3)	3.845(3)	3.848(4)	3.845(4)
Y...Mo2	3.881(5)	3.887(4)	3.886(4)	3.883(4)	3.883(4)	3.884(4)
Y...Mo2	3.958(4)	3.957(3)	3.951(3)	3.948(3)	3.945(3)	3.943(3)
Y-O1-Mo1	176.1(4)	175.3(4)	174.8(4)	173.3(4)	172.5(4)	172.1(4)
Y-O2-Mo1	153.2(4)	153.1(4)	153.7(4)	153.8(4)	154.3(4)	154.4(4)
Y-O3-Mo1	156.0(4)	156.1(4)	155.7(4)	155.5(4)	156.0(4)	155.8(4)
Y-O4-Mo1	145.1(4)	145.0(4)	146.0(4)	146.4(4)	146.9(4)	146.8(4)
Y-O5-Mo2	151.2(5)	150.6(4)	150.4(4)	149.6(4)	149.8(4)	150.1(4)
Y-O6-Mo2	168.6(5)	167.8(4)	167.0(4)	165.9(4)	165.1(4)	164.9(4)

Er$_2$(MoO$_4$)$_3$	150 K	200 K	250 K	300 K	350 K	400 K
Er...Mo1	3.983(5)	3.983(4)	3.980(3)	3.978(3)	3.981(3)	3.979(4)
Er...Mo1	3.873(4)	3.868(4)	3.869(4)	3.870(4)	3.867(4)	3.870(4)
Er...Mo1	3.882(5)	3.883(4)	3.877(3)	3.876(3)	3.874(3)	3.873(4)
Er...Mo1	3.822(4)	3.827(4)	3.831(4)	3.831(4)	3.829(4)	3.828(4)
Er...Mo2	3.874(4)	3.869(4)	3.873(3)	3.873(3)	3.874(3)	3.875(4)
Er...Mo2	3.944(4)	3.946(3)	3.941(3)	3.937(3)	3.938(3)	3.934(3)
Er-O1-Mo1	175.8(4)	175.4(4)	174.8(4)	173.9(4)	172.7(4)	172.4(4)
Er-O2-Mo1	152.2(4)	152.9(4)	153.1(4)	153.6(4)	153.5(4)	154.6(4)
Er-O3-Mo1	155.1(5)	155.3(4)	156.2(4)	155.7(4)	155.9(4)	155.8(4)
Er-O4-Mo1	143.5(4)	144.3(4)	145.5(4)	146.0(4)	145.7(4)	146.7(4)
Er-O5-Mo2	150.5(5)	150.4(4)	151.6(4)	150.9(4)	151.3(4)	150.8(4)
Er-O6-Mo2	169.3(5)	168.6(4)	168.1(4)	166.7(4)	166.1(4)	165.6(5)

Lu$_2$(MoO$_4$)$_3$	200 K	225 K	250 K	303 K		400 K
Lu...Mo1	3.956(3)	3.954(3)	3.955(3)	3.953(3)		3.951(3)
Lu...Mo1	3.833(3)	3.833(3)	3.833(4)	3.836(3)		3.833(3)
Lu...Mo1	3.839(3)	3.836(3)	3.838(3)	3.834(3)		3.833(3)
Lu...Mo1	3.788(3)	3.790(3)	3.789(3)	3.789(2)		3.792(3)
Lu...Mo2	3.847(3)	3.847(3)	3.846(3)	3.845(3)		3.846(3)
Lu...Mo2	3.908(3)	3.906(3)	3.906(3)	3.904(2)		3.902(3)
Lu-O1-Mo1	173.9(3)	174.0(3)	173.6(3)	173.1(3)		171.7(4)
Lu-O2-Mo1	152.3(3)	152.3(3)	152.7(3)	153.3(3)		153.8(4)
Lu-O3-Mo1	155.8(4)	155.5(3)	155.8(3)	155.9(3)		156.2(4)
Lu-O4-Mo1	143.7(3)	144.3(3)	145.0(4)	145.3(3)		146.1(4)
Lu-O5-Mo2	150.7(4)	150.7(3)	150.9(3)	150.9(3)		150.6(4)
Lu-O6-Mo2	170.0(4)	169.7(4)	169.5(3)	168.9(3)		167.9(4)

Table 11. Temperature dependence of bond valence sum of cations and polyhedron distortion.

$Y_2(MoO_4)_3$	150 K	200 K	250 K	300 K	350 K	400K
Y	3.31(3)	3.28(3)	3.28(3)	3.31(3)	3.30(3)	3.29(3)
$\nu(\%)$	0.29	0.25	0.28	0.27	0.29	0.28
Mo1	6.04(7)	6.02(6)	6.09(6)	6.01(7)	6.07(1)	6.08(7)
$\nu(\%)$	0.05	0.04	0.08	0.07	0.07	0.09
Mo2	5.98(7)	6.12(7)	6.07(7)	6.03(7)	6.14(7)	6.15(7)
$\nu(\%)$	0.04	0.08	0.12	0.25	0.32	0.30
O1	2.05(3)	2.06(3)	2.08(3)	2.07 (3)	2.06(3)	2.09(4)
O2	2.05(3)	2.05(3)	2.07(3)	2.05(4)	2.09(4)	2.08(4)
O3	2.11(4)	2.10(3)	2.09(3)	2.09(3)	2.11(4)	2.10(4)
O4	2.01(4)	2.02(4)	2.04(4)	2.02(4)	2.03(4)	2.03(4)
O5	2.04(4)	2.04(3)	2.02(3)	2.01(4)	2.03(4)	2.03(4)
O6	2.07(4)	2.10(4)	2.10(4)	2.09(4)	2.11(4)	2.12(4)

$Er_2(MoO_4)_3$	150 K	200 K	250 K	300 K	350 K	400 K
Er	3.11(3)	3.12(3)	3.14(3)	3.14(3)	3.15(3)	3.15(3)
$\nu(\%)$	0.24	0.25	0.29	0.26	0.25	0.29
Mo1	6.01(7)	5.98(3)	6.01(6)	6.01(6)	5.95(7)	6.03(7)
$\nu(\%)$	0.02	0.02	0.01	0.02	0.03	0.05
Mo2	5.97(8)	6.08(7)	6.17(7)	6.18(7)	6.23(7)	6.19(8)
$\nu(\%)$	0.04	0.05	0.03	0.12	0.12	0.19
O1	2.04(4)	2.05(3)	2.04(9)	2.04(3)	2.01(3)	2.02(3)
O2	1.99(3)	2.01(3)	2.00(3)	2.02(3)	2.01(3)	2.03(4)
O3	2.08(4)	2.06(3)	2.09(3)	2.09(3)	2.08(4)	2.09(4)
O4	1.95(4)	1.94(3)	1.97(4)	1.97(4)	1.98(4)	2.01(4)
O5	2.00(4)	2.03(4)	2.04(3)	2.02(4)	2.04(4)	2.01(4)
O6	2.04(4)	2.05(4)	2.09(4)	2.10(4)	2.09(4)	2.10(5)

$Lu_2(MoO_4)_3$	200 K	225 K	250 K	303 K		400 K
Lu	3.27(2)	3.27(2)	3.28(2)	3.28(2)		3.26(7)
$\nu(\%)$	0.19	0.19	0.21	0.22		0.20
Mo1	6.04(5)	6.03(5)	6.07(5)	6.10(5)		6.12(6)
$\nu(\%)$	0.02	0.01	0.01	0.01		0.02
Mo2	5.99(6)	5.99(6)	6.01(6)	6.07(6)		6.23(7)
$\nu(\%)$	0.02	0.02	0.03	0.03		0.09
O1	2.04(3)	2.04(3)	2.04(3)	2.05(3)		2.05(3)
O2	2.07(2)	2.07(2)	2.06(2)	2.07(3)		2.09(3)
O3	2.10(3)	2.10(3)	2.12(3)	2.14(3)		2.13(3)
O4	1.99(3)	1.99(3)	2.03(3)	2.02(3)		2.04(4)
O5	1.98(3)	1.98(3)	1.98(3)	2.01(3)		2.02(3)
O6	2.12(3)	2.12(3)	2.13(3)	2.12(3)		2.15(4)

Refinement of atomic displacements with FullProf: (example of an input file *.pcr)

Several changes are necessary in a typical input file:

    1) It must be select a job type = 6 (as in a symmetry mode analysis).

    2) It must be added a number of lines = number of free coordinates (in our case it is 25, taking into account the atom labelled Mo2 is in a Wyckoff site) with the following format:

```
Lu2(MoO4)3                    FIX xyz
!
!Nat Dis Ang Jbt Isy Str Furth      ATZ      Nvk More
   9   0   0   6   0   0  25      2630.4990   0   1
!...........................................................


V_MODES    25
! Nm Atm      Irrep        Vx         Vy         Vz        Coeff
   1  Lu1      GM1+      0.000000   0.000000   0.035587   1.000000
   2  Lu1      GM1+      0.000000   0.035929   0.000000   1.000000
   3  Lu1      GM1+      0.025792   0.000000   0.000000   1.000000
   4  Mo1      GM1+      0.000000   0.000000   0.035587   1.000000
   5  Mo1      GM1+      0.000000   0.035929   0.000000   1.000000
   6  Mo1      GM1+      0.025792   0.000000   0.000000   1.000000
   7  Mo2      GM1+      0.000000   0.050811   0.000000   1.000000
   8  O1       GM1+      0.000000   0.000000   0.035587   1.000000
   9  O1       GM1+      0.000000   0.035929   0.000000   1.000000
  10  O1       GM1+      0.025792   0.000000   0.000000   1.000000
  11  O2       GM1+      0.000000   0.000000   0.035587   1.000000
  12  O2       GM1+      0.000000   0.035929   0.000000   1.000000
  13  O2       GM1+      0.025792   0.000000   0.000000   1.000000
  14  O3       GM1+      0.000000   0.000000   0.035587   1.000000
  15  O3       GM1+      0.000000   0.035929   0.000000   1.000000
  16  O3       GM1+      0.025792   0.000000   0.000000   1.000000
  17  O4       GM1+      0.000000   0.000000   0.035587   1.000000
  18  O4       GM1+      0.000000   0.035929   0.000000   1.000000
  19  O4       GM1+      0.025792   0.000000   0.000000   1.000000
  20  O5       GM1+      0.000000   0.000000   0.035587   1.000000
  21  O5       GM1+      0.000000   0.035929   0.000000   1.000000
  22  O5       GM1+      0.025792   0.000000   0.000000   1.000000
  23  O6       GM1+      0.000000   0.000000   0.035587   1.000000
  24  O6       GM1+      0.000000   0.035929   0.000000   1.000000
  25  O6       GM1+      0.025792   0.000000   0.000000   1.000000
```

GM1+ is an irrelevant label in our case, polarized vectors Vx, Vy and Vz have normalized components referred to the high temperature cell and are along the crystal axes because, the use of cell in the distorted phase would break the orthogonality of the displacements. And coeff is a normalization coefficient; in our case is always 1. The polarization vectors are calculated in the following way, taking into account that displacements are given in absolute values (in Å) using the reference unit cell, the square of these displacements, when summed for all atoms within a primitive unit cell of the low symmetry space group, must yield 1 $Å^2$ and they are also orthogonal vectors.

3) Finally, other 25 lines must be added with the following format, which include the name of the shifts: from the first A1_GM1+ to the last A25_GM1+ (although the meaning of this label is irrelevant, in our case), values of the shifts (in angstroms), and refinement codes:

```
A_MODES    25      2
       A1_GM1+        -0.003338      461.000000
       A2_GM1+        -0.003333      471.000000
       A3_GM1+        -0.002333      481.000000
       A4_GM1+         0.014120      491.000000
       A5_GM1+        -0.004292      501.000000
       A6_GM1+        -0.000475      511.000000
       A7_GM1+        -0.001288      521.000000
       A8_GM1+         0.073957      531.000000
       A9_GM1+        -0.012313      541.000000
       A10_GM1+       -0.025977      551.000000
       A11_GM1+        0.029664      561.000000
       A12_GM1+       -0.024001      571.000000
       A13_GM1+       -0.014477      581.000000
       A14_GM1+        0.005741      591.000000
       A15_GM1+       -0.018894      601.000000
       A16_GM1+       -0.032543      611.000000
       A17_GM1+        0.022462      621.000000
       A18_GM1+       -0.007801      631.000000
       A19_GM1+        0.040859      641.000000
       A20_GM1+       -0.014959      651.000000
       A21_GM1+       -0.041259      661.000000
       A22_GM1+       -0.002223      671.000000
       A23_GM1+       -0.063403      681.000000
       A24_GM1+        0.000517      691.000000
       A25_GM1+       -0.015480      701.000000
```

6.3   Thermodynamic relations

Knowing the equation of state of a substance, important physical quantities can be deduced, likely to be measured. In our experiments, we have measured $V = V(T)$ and $P = P(V)$ and from their derivatives, it can be calculated the thermal expansion coefficient and the bulk modulus.

In the general case, the volumetric coefficient of thermal expansion is given by:

$$\alpha_V = \frac{1}{V} \left(\frac{\partial V}{\partial T} \right)_p \tag{6.1}$$

The subscript "p" indicates that the pressure is held constant during the expansion, and the subscript "V" indicates that is the volumetric (not linear) expansion. In the special case of solid materials, the pressure does not appreciably affect its size, thus, it is not necessary to specify that the pressure be held constant.

Commonly, to a first approximation, the change in length L measurements of a solid due to thermal expansion is related to temperature change by a linear expansion coefficient (with subscript "L").

$$\alpha_L = \frac{1}{L} \frac{dL}{dT} \tag{6.2}$$

Usually, solids have coefficients of thermal expansion that do not vary significantly over the range of temperatures, thus, practical calculations can be based on a constant, average value of the coefficient of expansion. Thus, the change in the linear dimension can be estimated to be:

$$\frac{\triangle L}{L} = \alpha_L \triangle T \tag{6.3}$$

This equation works well as long as the linear–expansion coefficient does not change much over the change in temperature. If it does, the equation must be integrated. For isotropic materials

the volumetric thermal expansion coefficient is three times the linear coefficient ($\alpha_V = 3\alpha_L$).

On the other hand, bulk modulus, which is the inverse of the compressibility, is defined as:

$$B = -V \left(\frac{\partial P}{\partial V}\right)_T \tag{6.4}$$

The easiest way to get an equation of state linking P and V is to assume that B is constant, i.e. it is independent of pressure and deformation of the solid, and then we simply find the Hooke's law. In this case, the volume decreases linearly with pressure. This is not a satisfactory result because it is experimentally established that as a solid is compressed, it becomes more difficult to compress. To go further, we must take into account the variations of the elastic properties of the solid with compression. The most widely used equation of state $P = P(V)$ to calculate the bulk modulus, in high–pressure experiments, is the equation of Birch–Murnaghan (Birch 1947). In order to obtain this equation the Helmholtz free energy F must be expanded in powers of the eulerian strain coefficient ϵ.

$$F = a_0 + a_1\epsilon + a_2\epsilon^2 + a_3\epsilon^3 + ... \tag{6.5}$$

where $\epsilon = \frac{1}{2}\left(1 - \left(\frac{V}{V_0}\right)^{\frac{-2}{3}}\right)$.

Expanding until the order three and by imposing the boundary conditions $P = 0$, $B = B_0$ and $\epsilon = 0$, $a_1 = 0$; we obtain the equation of Birch–Murnaghan of third order:

$$P(V) = \frac{3B_0}{2}\left[\left(\frac{V_0}{V}\right)^{\frac{7}{3}} - \left(\frac{V_0}{V}\right)^{\frac{5}{3}}\right]\left\{1 + \frac{3}{4}\left(B_0' - 4\right)\left[\left(\frac{V_0}{V}\right)^{\frac{2}{3}} - 1\right]\right\} \tag{6.6}$$

where B_0 and B_0' are:

$$B_0 = -V\left(\frac{\partial P}{\partial V}\right)_{T,V=V_0} \qquad \text{and} \qquad B_0' = \left(\frac{\partial B}{\partial P}\right)_{T,V=V_0} \tag{6.7}$$

In the case of $B' = 4$, we obtain the second order equation of state. B_0 and B_0' will be calculated by fitting the experimental curve $P(V)$. These adjustments must take into account

the following considerations: B_0 and B_0' are strongly correlated; the selection of the order of the equation is limited by the number of experimental points and the range of the measured pressures and the ratio V/V_0. Large errors in the fitting of $P(V)$ indicates whether or not this equation should be chosen.